ELUCIDATING STRUCTURE–FUNCTION RELATIONSHIPS IN APTAMER–SMALL MOLECULE INTERACTIONS THROUGH NUCLEAR MAGNETIC RESONANCE, ISOTHERMAL TITRATION CALORIMETRY, AND DIFFERENTIAL SCANNING CALORIMETRY

Rahith Ahmmed Kaiyum

A DISSERTATION SUBMITTED TO THE FACULTY OF GRADUATE STUDIES IN PARTIAL FULFILLMENT OF THE REQUIREMENTS FOR THE DEGREE OF DOCTOR OF PHILOSOPHY

GRADUATE PROGRAM IN CHEMISTRY
YORK UNIVERSITY
TORONTO, ONTARIO

August 2026

©Rahith Ahmmed Kaiyum 2026

Abstract

Aptamers are single-stranded nucleic acid sequences capable of folding into three-dimensional structures that enable selective molecular recognition. Although aptamers are often described by their affinity and specificity for a target, these properties are governed by the structural states adopted before and after ligand binding. The mechanisms linking aptamer structure, ligand recognition, and functional response remain incompletely understood. This thesis investigated aptamer–small molecule interactions beyond binding affinity alone by examining how ligand binding influences folding, stability, conformational dynamics, and molecular recognition.

The dopamine-binding aptamer was examined as a model for ligand-induced folding. Circular dichroism and NMR spectroscopy showed that dopamine promotes formation of a more ordered aptamer structure. Truncation of the terminal stem reduced dopamine affinity, as measured by ITC, indicating that peripheral structural elements contribute to stabilization of the binding-competent fold. Further characterization of the modified dopamine aptamer, RKEC1, revealed an unconventional compact structure lacking the predicted duplex and G-quadruplex motifs. This insight helped explain dopamine specificity relative to related analogues and informed the design of an electrochemical biosensor.

The MN4 cocaine-binding aptamer was used to examine ligand-induced destabilization. DSC and NMR analyses showed that local anesthetics destabilized MN4 to varying extents, demonstrating that ligand binding is not always coupled to structural stabilization. These results highlight the importance of distinguishing binding affinity from the structural consequence of binding.

The influence of ligand structure on DNA recognition was investigated using methylene blue and leucomethylene blue, a redox pair relevant to electrochemical aptamer-based sensing. Structural characterization revealed that leucomethylene blue adopts a “butterfly” conformation relative to planar methylene blue. ITC, NMR, UV–vis, and fluorescence studies showed strong, nonspecific DNA binding

by methylene blue but negligible interaction by leucomethylene blue, indicating that ligand conformation strongly influences nucleic acid recognition.

Finally, NMR spectroscopy was applied to diverse aptamer–small molecule and aptamer–ion systems to evaluate ligand-induced folding, pre-formed structure, weak binding, G-quadruplex stabilization, metal-ion responses, nonspecific DNA binding, and ligand selectivity. Overall, this thesis demonstrates that aptamer function depends not only on whether a ligand binds, but on how binding reshapes the structural and dynamic landscape of the nucleic acid.

Acknowledgements

I would first like to thank my family and friends for the love, encouragement, and support they have provided throughout my time in graduate school. Their belief in me gave me the strength to continue through the most challenging periods of this work. I would not have been able to pursue my research with the freedom and dedication that I did without their constant support. I would also like to give special thanks to Samuel Dahan Meyboom for the countless hours of consultation, encouragement, and support.

I want to extend the warmest gratitude to my soon-to-be wife Razan who has shown incredible support and love and has encouraged me throughout the journey of writing this thesis.

I sincerely thank my supervisor, Professor Philip Johnson, for accepting me into his lab and providing me with the facilities, guidance, and intellectual environment needed to grow as both a scientist and a critical thinker. The lab space and research environment that you cultivated contributed immensely to my learning and development. You were always present when I needed advice or assistance, and I am grateful for the opportunity to have been a part of your lab over the past two years.

I would also like to give special thanks to Dr. Zachary Churcher for his mentorship and for being a constant source of support and advice. During the pandemic and periods of lockdown, you came to campus numerous times to train me and teach me techniques, including NMR spectroscopy. Your patience, generosity, and willingness to help played an important role in my development as a researcher.

I also extend my gratitude to Dr. Sladjana Slavkovic and Dr. Aron Shoara for their ongoing guidance, advice, and support, and for helping me refine my abilities in the laboratory. I am especially grateful to Nusaibah Dawood, who showed me great kindness and encouragement when I first began my research. Her support during the difficult early months of my project, especially during the COVID-19 lockdowns, meant a great deal to me.

I would like to thank my committee members, Professor Sergey Krylov and Professor Jennifer Chen, for their valuable advice, feedback, and guidance throughout this work. I also thank Howard Hunter for continuously maintaining the NMR spectrometer and ensuring that it remained operational, which allowed me to complete many of the experiments presented in this thesis.

Finally, I would like to thank all past and present members of the Johnson lab for their help, support, and company. I am grateful to have been part of a lab environment filled with people who contributed not only to my research, but also to my experience as a graduate student.

Table of Contents

Abstract ..... *ii*
Acknowledgements ..... *iv*
Table of Contents ..... *vi*
List of Tables ..... *ix*
List of Figures ..... *x*
List of Abbreviations ..... *xv*
Chapter 1. Background and Introduction *1*
1.1 Introduction to aptamers **1**
1.2 SELEX **2**
1.3 Aptamer Structure **6**
1.3.1 Canonical and Non-Canonical Base Pairs 6
1.3.2 G-Quadruplexes 8
1.3.3 Triple Helices 9
1.4 Aptamer Applications **11**
1.5 Studying Aptamers **14**
1.5.1 Isothermal Titration Calorimetry 14
1.5.2 Nuclear Magnetic Resonance Spectroscopy 16
1.5.3 Differential Scanning Calorimetry 19
1.6 Thesis Project **22**
Chapter 2 Ligand-Induced Folding in a Dopamine-Binding DNA Aptamer *24*
2.1 Preface **24**
2.2 Introduction **24**
2.3 Methods and Materials **26**
2.3.1 Materials 26
2.3.2 Isothermal Titration Calorimetry 26
2.3.3 NMR Spectroscopy 27
2.3.4 CD Spectroscopy 27
2.4 Results and Discussion **27**
2.4.1 Initial NMR Studies of DA-5bp and DA-mut3 27
2.4.2 NMR and ITC studies of Dopamine Binding by DA-Mut3 28

2.4.3 Heat Capacity of Dopamine Binding by DA-Mut3 31
2.4.4 Binding and Spectroscopic Analysis of Deletion Mutants 32
2.4.5 E-AB Sensor with Long (DA-mut3-del2) and Short Aptamer (DA-mut3-del6) 38
2.5 Work Following 40
2.6 Conclusions 41
Chapter 3 Ligand-Induced Destabilization of the MN4 Cocaine-Binding Aptamer by Local Anesthetics 43
3.1 Introduction 43
3.2 Materials and Methods 46
3.2.1 Materials 46
3.2.2 Isothermal Titration Calorimetry 47
3.2.3 Nuclear Magnetic Resonance Spectroscopy 47
3.2.4 Differential Scanning Calorimetry 48
3.3 Results 48
3.3.1 NMR Studies of Ligand Binding by MN4 and MN19 48
3.3.2 ITC Studies of Ligand Binding by MN4 71
3.3.3 DSC Studies of Ligand Binding by MN4 80
3.4 Conclusions 91
Chapter 4 The Butterfly Structure of Leucomethylene Blue Results in Weak Binding to Single- or Double-Stranded DNA 94
4.1 Preface 94
4.2 Introduction 94
4.3 Materials and Methods 96
4.3.1 NMR Spectroscopy 96
4.3.2 Isothermal Titration Calorimetry (ITC) 96
4.4 Results and Discussion 97
4.4.1 NMR Spectroscopy Demonstrates Binding of MB to DNA 97
4.4.2 NMR Spectroscopy Provides No Evidence of Binding of LMB to DNA 104
4.4.3 MB Binding DNA Analysed by Isothermal Titration Calorimetry 106
4.5 Additional Work 113
4.6 Conclusions 114
Chapter 5 Solution-State NMR Studies of Aptamer–Small Molecule Binding and Conformational Dynamics 116

5.1 Introduction 116
5.2 Methods and Materials 121
5.3 NMR Characterization of the SRTN12 Serotonin-Binding Aptamer 121
5.4 NMR Characterization of the Sc-1b Scandium-Binding Aptamer 125
5.5 NMR Characterization of a Tris-Binding Tris1Δ4 Aptamer 129
5.6 NMR Characterization of Bilirubin and Biliverdin Aptamers 133
5.7 Using NMR to Distinguish Specific and Non-Specific DNA/Aptamer-Small Molecule Interactions 139
5.8 Characterization of Cobalt- and Zinc-Binding Aptamers 152
5.9 NMR Characterization of the Kanamycin-Binding Kan 6.1 Aptamer 157
5.10 NMR Characterization of the Q1 Quinine-Binding Aptamer 160
5.11 Conclusions 165
Chapter 6 Conclusions and Future Works *168*
6.1 Conclusions 168
6.2 Future Work 172
References *175*

List of Tables

Table 2.2.1. DNA sequences of the dopamine aptamers used in this study…….....25

Table 2.4.2.1. K_d values and thermodynamic parameters of ligands used in this study for binding to the dopamine binding aptamer……...……29

Table 2.4.3.1. Thermodynamic parameters of DA-Mut3 binding dopamine at different temperatures……31

Table 2.4.5.1. DNA sequences used for the fabrication of E-AB sensors……..38

Table 3.3.2.1. ITC results of the MN4 aptamer with various ligands ……...….79

Table 3.3.3.1. DSC results of the MN4 aptamer with various ligands …….89

Table 4.4.3.1. Binding affinity and thermodynamics of MB binding by the DNA constructs studied as determined by ITC…….……..…...106

List of Figures

Figure 1.2.1. Schematic of Selex Process 3

Figure 1.3.1.1. A non-exhaustive list of canonical and non-canonical base pairings. In addition to standard Watson-Crick base pairs 7

Figure 1.3.2.1. Schematic representation of a guanine tetrad illustrating the structural basis of G-quadruplex formation 8

Figure 1.3.2.2. Schematic representation of G-quadruplex formation and topology 9

Figure 1.3.3.1. Schematic representation of possible DNA base triples involved in triple-helix formation 10

Figure 1.5.1.1. Overview of the basic principles of isothermal titration calorimetry (ITC) 15

Figure 1.5.2.1. Overview of the basic principles of nuclear magnetic resonance (NMR) spectroscopy ... 17

Figure 1.5.2.2. ^{1}H-NMR spectrum of a DNA dopamine-binding aptamer bound to dopamine 18

Figure 1.5.3.1. Overview of the basic principles of differential scanning calorimetry (DSC) 20

Figure 2.2.1. Secondary structure of various dopamine-binding aptamers showing the terminal stem..... 25

Figure 2.4.1.1. TOCSY spectra of two dopamine aptamers bound to dopamine..... 28

Figure 2.4.2.1. ITC thermograms showing the interaction of (a) DA-mut3 and (b) DA-mut3-del7 with dopamine..... 29

Figure 2.4.2.2. NMR spectra showing the imino proton resonances during a titration of the (a) DA-mut3 or (b) DA-mut3-del7 aptamer with dopamine 30

Figure 2.4.3.1. Temperature dependence of enthalpy for DA-mut3 binding to dopamine 32

Figure 2.4.4.1. Dopamine binding by various truncations of the DA-mut3 aptamer..... 36

Figure 2.4.4.2. The ^{1}H NMR spectra of the DA-mut3, DA-mut3-del1, and DA-mut3-del7 constructs 37

Figure 2.4.4.3. CD spectra of DA-mut3..... 38

Figure 2.4.5.1. Electrochemical aptamer-based biosensor scheme..... 39

Figure 2.4.5.2. Phase change of DA-mut3-del2 and DA-mut3-del6 aptamers 40

Figure 3.1.1. Chemical structures of the anesthetics investigated..... 46

Figure 3.3.1.1. ^{1}H-NMR spectra showing the imino proton resonances during a titration of MN4 with benzocaine 50

Figure 3.3.1.2. ^{1}H-NMR spectra showing the imino proton resonances during a titration of MN4 with tetracaine 52

Figure 3.3.1.3. ^{1}H-NMR spectra showing the imino proton resonances during a titration of MN4 with articaine 54

Figure 3.3.1.4. ^{1}H-NMR spectra showing the imino proton resonances during a titration of MN4 with bupivacaine 55

Figure 3.3.1.5. ^{1}H-NMR spectra showing the imino proton resonances during a titration of MN4 with lidocaine 56

Figure 3.3.1.6. ^{1}H-NMR spectra showing the imino proton resonances during a titration of MN4 with mepivacaine 57

Figure 3.3.1.7. ^{1}H-NMR spectra showing the imino proton resonances during a titration of MN4 with prilocaine 58

Figure 3.3.1.8. ^{1}H-NMR spectra showing the imino proton resonances during a titration of MN4 with procaine 59

Figure 3.3.1.9. ^{1}H-NMR spectra showing the imino proton resonances during a titration of MN19 with benzocaine 61

Figure 3.3.1.10. ^{1}H-NMR spectra showing the imino proton resonances during a titration of MN19 with tetracaine 62

Figure 3.3.1.11. ^{1}H-NMR spectra showing the imino proton resonances during a titration of MN19 with articaine 64

Figure 3.3.1.12. ^{1}H-NMR spectra showing the imino proton resonances during a titration of MN19 with bupivacaine 65

Figure 3.3.1.13. ^{1}H-NMR spectra showing the imino proton resonances during a titration of MN19 with lidocaine 66

Figure 3.3.1.14. ^{1}H-NMR spectra showing the imino proton resonances during a titration of MN19 with mepivacaine 67

Figure 3.3.1.15. ^{1}H-NMR spectra showing the imino proton resonances during a titration of MN19 with prilocaine 68

Figure 3.3.1.16. ^{1}H-NMR spectra showing the imino proton resonances during a titration of MN19 with procaine 69

Figure 3.3.1.17. Temperature-dependent ^{1}H-NMR spectra of the MN4 aptamer 70

Figure 3.3.2.1. ITC thermogram of the interaction between MN4 and benzocaine 72

Figure 3.3.2.2. ITC thermogram of the interaction between MN4 and tetracaine 73

Figure 3.3.2.3. ITC thermogram showing the interaction of MN4 with articaine 74

Figure 3.3.2.4. ITC thermogram showing the interaction of MN4 with bupivacaine. 75

Figure 3.3.2.5. ITC thermogram showing the interaction of MN4 with lidocaine 76

Figure 3.3.2.6. ITC thermogram showing the interaction of MN4 with mepivacaine. 77

Figure 3.3.2.7. ITC thermogram showing the interaction of MN4 with prilocaine 78

Figure 3.3.2.8. ITC thermogram showing the interaction of MN4 with procaine 79

Figure 3.3.3.1. DSC heat capacity profile for MN4 free and bound to benzocaine 82

Figure 3.3.3.2. DSC heat capacity profile for MN4 free and bound to tetracaine. 83

Figure 3.3.3.3. DSC heat capacity profile for MN4 free and bound to articaine. 84

Figure 3.3.3.4. DSC heat capacity profile for MN4 free and bound to bupivacaine 85

Figure 3.3.3.5. DSC heat capacity profile for MN4 free and bound to lidocaine 86

Figure 3.3.3.6. DSC heat capacity profile for MN4 free and bound to mepivacaine 87

Figure 3.3.3.7. DSC heat capacity profile for MN4 free and bound to prilocaine 88

Figure 3.3.3.8. DSC heat capacity profile for MN4 free and bound to procaine. 89

Figure 3.3.3.9. A plot of the ΔG_{bind} acquired from ITC 91

Figure 4.2.1. Methylene Blue and its Reduced Form, Leucomethylene Blue 94

Figure 4.4.1.1. ^{1}H NMR spectra showing the titration of poly(dGdC) DNA with methylene blue 98

Figure 4.4.1.2. ^{1}H-NMR spectra showing the titration of poly(dAdT); poly(dA); poly(dC); poly(dG); poly(dT) DNA with methylene blue. 103

Figure 4.4.2.1. ^{1}H-NMR spectra showing the titration of SDT into poly(dAdT) 105

Figure 4.4.3.1. ITC thermograms showing the titration of MB in poly(dA); poly(dAdT); poly(dT); poly(dC); poly(dG); poly(dGdC) DNA 112

Figure 5.3.1. Predicted secondary structure of the SRTN12 aptamer 122

Figure 5.3.2. ^{1}H-NMR titration of the SRTN12 serotonin-binding aptamer with increasing equivalents of serotonin 124

Figure 5.4.1. The predicted secondary structure of the Sc-1b scandium binding aptamer……126

Figure 5.4.2. ^{1}H-NMR titration of the scandium (III)-binding aptamer with increasing equivalents of Sc^{3+} 128

Figure 5.5.1. Predicted secondary structure of Tris1Δ4 and chemical structure of Tris-HCl. 130

Figure 5.5.2. ^{1}H-NMR titration of the Tris1Δ4 aptamer with increasing equivalents of Tris 131

Figure 5.6.1. The predicted secondary structures of biliverdin-binding aptamer Bili1 and of the bilirubin-binding aptamer BR3. The chemical structures of biliverdin and bilirubin 134

Figure 5.6.2. ^{1}H-NMR titration of the Bili1 aptamer with bilirubin 135

Figure 5.6.3. ^{1}H-NMR titration of the Bili1 aptamer with biliverdin 136

Figure 5.6.4. ^{1}H-NMR titration of the BR3 aptamer with bilirubin 137

Figure 5.6.5. ^{1}H-NMR titration of the BR3 aptamer with biliverdin 138

Figure 5.7.1. Chemical structure of amodiaquine 140

Figure 5.7.2. Structures of the nucleic acid constructs used in this study 141

Figure 5.7.3. ^{1}H-NMR titration of the SS1 aptamer with amodiaquine 142

Figure 5.7.4. ^{1}H-NMR titration of the SS2 aptamer with amodiaquine 143

Figure 5.7.5. ^{1}H-NMR titration of the SS3 aptamer with amodiaquine 144

Figure 5.7.6. ^{1}H-NMR titration of the SS4 aptamer with amodiaquine 145

Figure 5.7.7. ^{1}H-NMR titration of a generic three-way junction nucleic acid with amodiaquine 147

Figure 5.7.8. ^{1}H-NMR titration of the DDD dodecamer DNA with amodiaquine 148

Figure 5.7.9. ^{1}H-NMR titration of the SJH hexamer DNA with amodiaquine 149

Figure 5.8.1. The predicted secondary structures of the Co-1 and Zn-1 aptamers..... 153

Figure 5.8.2. ^{1}H-NMR titration of the Zn-1 aptamer with increasing equivalents of Zn^{2+} 154

Figure 5.8.3. ^{1}H-NMR titration of the Co-1 aptamer with increasing equivalents of Zn^{2+} 155

Figure 5.9.1. The predicted secondary structure of the Kan 6.1 aptamer 157

Figure 5.9.2. ^{1}H-NMR titration of the Kanamycin 6.1 aptamer with increasing equivalents of kanamycin 158

Figure 5.10.1. The predicted secondary structure of the Q1 aptamer 161

Figure 5.10.2. ^{1}H-NMR titration of the Q1 aptamer with increasing equivalents of quinine 162

Figure 5.10.3. ^{1}H-NMR titration of the Q1 aptamer with increasing equivalents of cocaine. 163

List of Abbreviations

(A)	Adenine
B_0	Magnetic field strength
(C)	Cytosine
(c)	Sigmoidicity factor
CE-SELEX	Capillary Electrophoresis SELEX
FID	Free Induction Decay
(G)	Guanine
ΔG	Change in Gibbs free energy of binding
ΔG_{unf}	Change in Gibbs free energy of unfolding
ΔH	Change in Enthalpy of binding
ΔH_{unf}	Change in Enthalpy of unfolding
ΔS	Change in Entropy of binding
ΔS_{unf}	Change in Entropy of unfolding
DNA	Deoxyribonucleic Acid
dsDNA	Double-Stranded Deoxyribonucleic Acid
E-AB	Electrochemical-Aptamer Biosensor
ITC	Isothermal Titration Calorimetry
K_d	Dissociation constant
kDa	Kilodalton
k_{off}	Dissociation rate constant
k_{on}	Association rate constant
MS	Mass Spectrometry
(n)	Binding stoichiometry
NECEEM	Non-Equilibrium Capillary Electrophoresis of Equilibrium Mixtures

NMR	Nuclear Magnetic Resonance
PCR	Polymerase Chain Reaction
RNA	Ribonucleic Acid
SELEX	Systematic Evolution of Ligands by Exponential Enrichment
SRM	Selected Reaction Monitoring
ssDNA	Single-Stranded Deoxyribonucleic Acid
(T)	Thymine
VEGF	Vascular Endothelial Growth Factor

Chapter 1. Background and Introduction

1.1 Introduction to aptamers

Deoxyribonucleic acid (DNA) is traditionally thought of as the primary carrier of genetic information, commonly depicted as a double-stranded helical molecule composed of complementary base pairs. However, in addition to its role in encoding genetic information, nucleic acids are also capable of adopting diverse structural and functional roles, including participation in regulatory pathways as riboswitches.[1–3] Aptamers are short single-stranded nucleic acid molecules characterized by their ability to fold into defined three-dimensional structures capable of binding target molecules with high affinity and specificity. Because aptamer folding is highly sequence-dependent, diverse conformations can be generated that facilitate recognition of a broad range of targets.[4] The selection of aptamers was first demonstrated independently in 1990 by three groups. Tuerk and Gold identified RNA sequences capable of binding T4 DNA polymerase, while Ellington and Szostak selected RNA molecules that bound organic dyes.[5,6] Joyce and Robertson selected for variant forms of an RNA enzyme that catalyzed sequence-specific phosphoester transfer reactions involving RNA substrates. After multiple rounds of selection, an RNA enzyme that cleaved DNA more efficiently than the wild-type enzyme was isolated.[7] These foundational studies led to the development of Systematic Evolution of Ligands by Exponential Enrichment (SELEX), an iterative process used to enrich ligand-binding aptamers from large randomized nucleic acid libraries.

Although DNA and RNA aptamers share many structural similarities, they differ chemically by the presence of a 2′-hydroxyl group on the ribose sugar in RNA, which is absent in DNA. This seemingly small chemical difference has important consequences for aptamer folding, nuclease susceptibility, chemical stability, and structural diversity. Unmodified DNA-based aptamers are generally more stable than their RNA counterparts. For example, the in vitro half-life of an RNA aptamer may be on the order of several seconds, whereas a DNA-based aptamer may persist between 30–60 minutes in plasma. The chemical instability of RNA aptamers is primarily due to the 2’-hydroxyl group which is susceptible to hydrolysis.[8,9] In vivo, RNA aptamers often require chemical modification to improve resistance to degradation by

endoribonucleases such as RNases. Common strategies include modification at the 2′-position of pyrimidines, either during library design or through incorporation of modified nucleotides during selection and amplification. These modifications can substantially enhance stability, making RNA aptamers comparable to, or even more stable than, DNA aptamers.[10–12]

Aptamers can bind a wide range of targets, including small molecules, proteins, prions, toxins, and cell-surface markers, with high affinity and specificity. Their molecular recognition capabilities have drawn frequent comparisons to antibodies, which have historically served as primary affinity reagents for detecting molecular markers in forensic analysis, disease diagnosis, food and agricultural monitoring, and viral outbreak surveillance. However, aptamers offer several distinct advantages over antibodies, including in vitro selection, reproducible chemical synthesis, broad target compatibility, small size, low immunogenicity, and the ability to tune binding properties through sequence or chemical modification. Despite their small molecular weight (typically 5-30 kDa), aptamers can bind their targets with affinities ranging from the picomolar to low nanomolar range. Additionally, aptamers can undergo reversible thermal denaturation, whereas thermal denaturation remains a concern for antibody use.[13–15]

1.2 SELEX

New aptamers are selected through an iterative in vitro process known as Systematic Evolution of Ligands by Exponential Enrichment, or SELEX, which enriches functional nucleic acid sequences from large, randomized libraries.[16] The process starts with introducing a target ligand to a library containing over 10^{15} unique oligonucleotide sequences. The sequences retain conserved primer sequences at the 5’ and 3’ ends for subsequent PCR amplification. Unbound or weakly interacting sequences are removed and sequences that bind the target ligand are collected and PCR amplified. This generates a new sub-library of oligonucleotides with varying affinities for the ligand which is then put through the entire process again. The cycle can be repeated 10 to 20 times, with each cycle producing an increasingly enriched library of oligomers, until a highly enriched pool meeting pre-determined criteria is obtained. These criteria can

include functionality under specific ligand concentrations, salt concentrations, buffer compositions, temperatures, or pH conditions. A general scheme of the SELEX process can be seen in Figure 1.2.1.

Several parameters affect the number of cycles required to obtain functional binding sequences. These include the structure and charge of the ligand, the initial library of oligomers and the aptamer characteristics that one selects for. Consequently, even small changes in selection parameters can produce variation in the sequences isolated.[17] Since its development in the 1990s, SELEX has undergone numerous modifications to address its traditionally labor-intensive and time-consuming nature, as well as the lack of guarantee that an aptamer with the desired characteristics will be successfully selected and isolated. One of the primary steps of SELEX involves the separation of interacting and non-interacting sequences and recently the use of magnetic bead-based SELEX has attracted significant interest as a convenient, efficient, and rapid separation strategy.[18,19] For example, Hong et al. reported the selection of an Ebola virus aptamer in only three rounds, in part through optimization of partitioning using magnetic SELEX.[20,21]

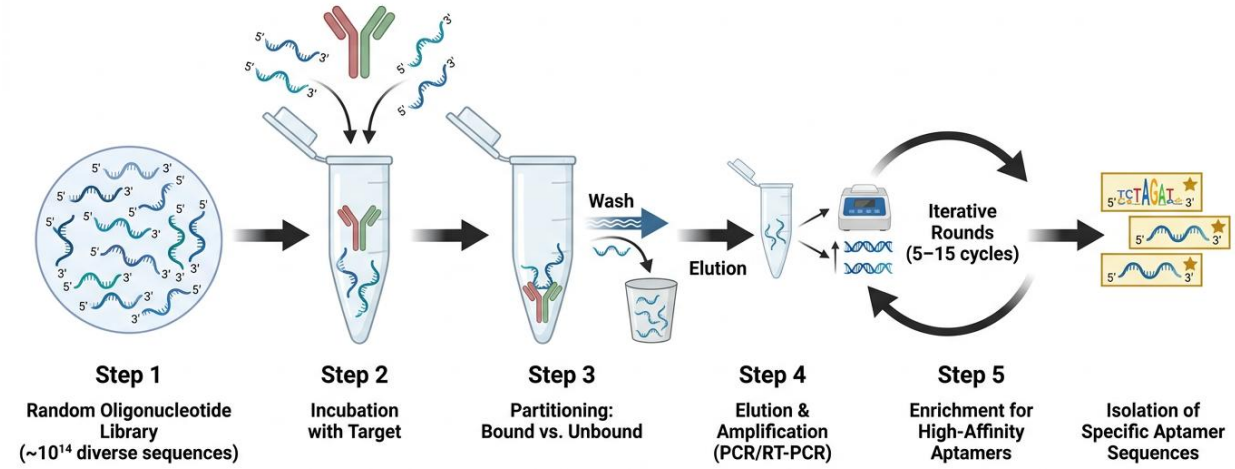

Figure 1.2.1. Schematic of SELEX Process. A ligand of interest is exposed to an initial library of oligomers. Non-binding sequences are eluted and removed whereas the interacting sequences are isolated, amplified and re-introduced to the ligand of interest. This process is repeated several times until sequences with desired criteria are collected and sequenced.

Negative SELEX has become a common component of aptamer selection strategies and greatly improves the specificity of sequences from the selection process. Negative SELEX considers interactions that may occur between an enriched population of oligomers, and the chromatography columns or other purification supports upon which aptamers are generally selected. In one study, incorporation of a negative

selection step after three positive selection rounds increased aptamer affinity by approximately 10-fold.[22] Kim *et al*. used negative selection with magnetic beads when selecting an aptamer to bind to the commonly used anti-inflammatory drug ibuprofen, removing approximately 56% of ssDNA sequences suspected of interacting with the magnetic support beads.[23]

The practical value of an aptamer depends not only on affinity, but also on specificity for the intended target. Consequently, it has become common to include a counterselection step in the SELEX process. Counter SELEX aims to isolate sequences that selectively recognize the ligand of interest by exposing the enriched nucleic acid pool to structurally related analogues of the target ligand. The enriched pool is incubated with chemically similar analogues of the ligand of interest, allowing sequences that show evidence of off–target interactions to be discarded. Jenison *et al*. selected an RNA aptamer for caffeine and upon performing counter selection, were able to isolate a sequence that had an affinity for caffeine 10,000-fold greater than theophylline, which only differed in the absence of a methyl group on its imidazole ring.[24]

SELEX modifications also extend to the assay itself and an example of this is Capillary Electrophoresis SELEX (CE-SELEX). A traditional SELEX procedure can take more than 15 rounds to isolate an effective aptamer, which is time-intensive and there is no guarantee that a sequence with the desired characteristics can be isolated. CE-SELEX was first developed by Mendonsa and Bowser in 2004 as a rapid aptamer selection method that uses capillary electrophoresis to separate bound nucleic acid–target complexes from unbound sequences according to electrophoretic mobility which proved to be a highly effective separation technique. This technique greatly improved efficiency of selecting new aptamers by reducing the number of rounds from more than 15 down to 1-4 rounds, reducing the labor and time investment.[25,26]

In 2006, further improvements to the aptamer selection process were made by limiting the DNA amplification bias which occurs after successive rounds of PCR. Non-Equilibrium Capillary Electrophoresis of Equilibrium Mixtures (NECEEM) is a highly efficient technique which separates aptamer-ligand complexes from unbound sequences. In addition to aptamer selection, NECEEM can provide quantitative information on aptamer–ligand binding, including the equilibrium dissociation

constant (K_d), association rate constant (k_{on}), and dissociation rate constant (k_{off}). Under appropriate experimental conditions, this approach can also support thermodynamic analysis of binding parameters such as changes in ΔH and entropy ΔS. This method can substantially reduce the time required for aptamer selection from several weeks or months to a matter of hours. However, one limitation of NECEEM is its reduced applicability to small-molecule targets, where the electrophoretic mobility difference between bound and unbound sequences is often below the detection limit.[27–29]

To improve the applicability of selected aptamers under cellular conditions, Cell-SELEX, originally developed in 2003 by Daniles *et al*., has been used to select aptamers targeting intracellular and transmembrane proteins.[30] In this approach, whole cells are used as the selection targets rather than purified molecules. Cell-SELEX offers several advantages including aptamer selection against proteins in their native cellular context, under conditions that more closely resemble the intended biological application. Additionally, prior knowledge of the specific molecular targets present on the cell surface is not required before selection. Consequently, tuning the interactions between the target and the aptamer becomes much more difficult without knowledge of the target's characteristics.

Capture-SELEX is another modification of the traditional SELEX workflow that is particularly useful for small-molecule targets. In this approach, the nucleic acid library is hybridized to a short complementary biotinylated capture strand, which enables immobilization on a streptavidin-coated solid support. Sequences capable of binding free target molecules may undergo target-induced structural changes that promote dissociation from the complementary strand. This strategy is advantageous for small-molecule aptamer selection as small molecules often have limited functional groups for biotinylation and immobilization. By immobilizing the oligonucleotide library instead of the target, this limitation can be circumvented. However, immobilization of the nucleic acid sequence may introduce interactions or structural constraints that differ from those of the free oligonucleotide in solution, and these effects must be considered during the selection process. A limitation of Capture-SELEX is the potential for false-positive enrichment resulting from the immobilization strategy. Since the library is often tethered to solid support through reversible hybridization with a complementary capture strand, weakly bound sequences can

dissociate spontaneously due to dynamic binding equilibria. As a result, sequences may be released and collected even without target-induced binding or conformational change, complicating the identification of true ligand-binding aptamers.[31] Capture-SELEX is one of several SELEX variants developed to address limitations of the original workflow; other derivative methods include graphene oxide (GO)-SELEX[32–34] and in vivo SELEX.[35,36]

1.3 Aptamer Structure

1.3.1 Canonical and Non-Canonical Base Pairs

Aptamers derive their function from the 3-dimensional structures they adopt. The primary sequence encodes the information required for aptamer folding. The role that three-dimensional structure plays in facilitating the binding between an aptamer and its target cannot be overstated and continues to be a prevalent avenue of investigation into aptamer functionality.[37,38] These structures are stabilized by a combination of canonical Watson-Crick base pairs, non-canonical base pairing interactions, base stacking and tertiary contacts. DNA contains two purine bases, adenine (A) and guanine (G) and two pyrimidine bases, cytosine (C) and thymine (T). DNA folding is stabilized by hydrogen bonding, base stacking and electrostatic interactions, which together promote the formation of energetically favourable secondary and tertiary structure. Canonical Watson–Crick base pairing occurs through hydrogen bonding between complementary bases, with adenine pairing with thymine and cytosine pairing with guanine. These interactions, together with base stacking and electrostatic effects, contribute to the formation of stable secondary structures, including duplex helical DNA. In aptamers, however, target recognition often depends not only on canonical base pairing but also on non-canonical interactions and tertiary contacts that generate unique binding pockets. Non-canonical base pairs are sometimes referred to as mismatches in the context of duplex DNA as illustrated in Figure 1.3.1.1. These interactions expand the conformational repertoire of DNA beyond conventional duplex structures and contribute to the formation of higher-order architectures, local structural distortions and binding pockets. Such base-pairing diversity is particularly important in aptamers, where non-canonical interactions can stabilize unique three-dimensional folds and facilitate target-specific molecular recognition.

DNA helices can adopt several conformations including A-form, B-form and Z-form, with B-form being the most common under physiological conditions. In helical DNA, the negatively charged sugar-phosphate backbone is positioned along the exterior of the helix, while stacked base pairs occupy the interior. The edges of these base pairs are exposed through their major and minor grooves, where distinct patterns of hydrogen-bond donors, hydrogen-bond acceptors and hydrophobic groups provide chemical signatures that can be recognized by biomolecules such as proteins.[39]

Most protein-DNA complexes involve B-form DNA and are often accompanied by moderate bending or local structural distortion. These conformational changes can be compensated by favourable contacts between exposed DNA functional groups and the interacting biomolecule. Similar principles are relevant to aptamer recognition, where both canonical and non-canonical base pairing interactions can shape binding pockets and expose functional groups that contribute to target specificity.

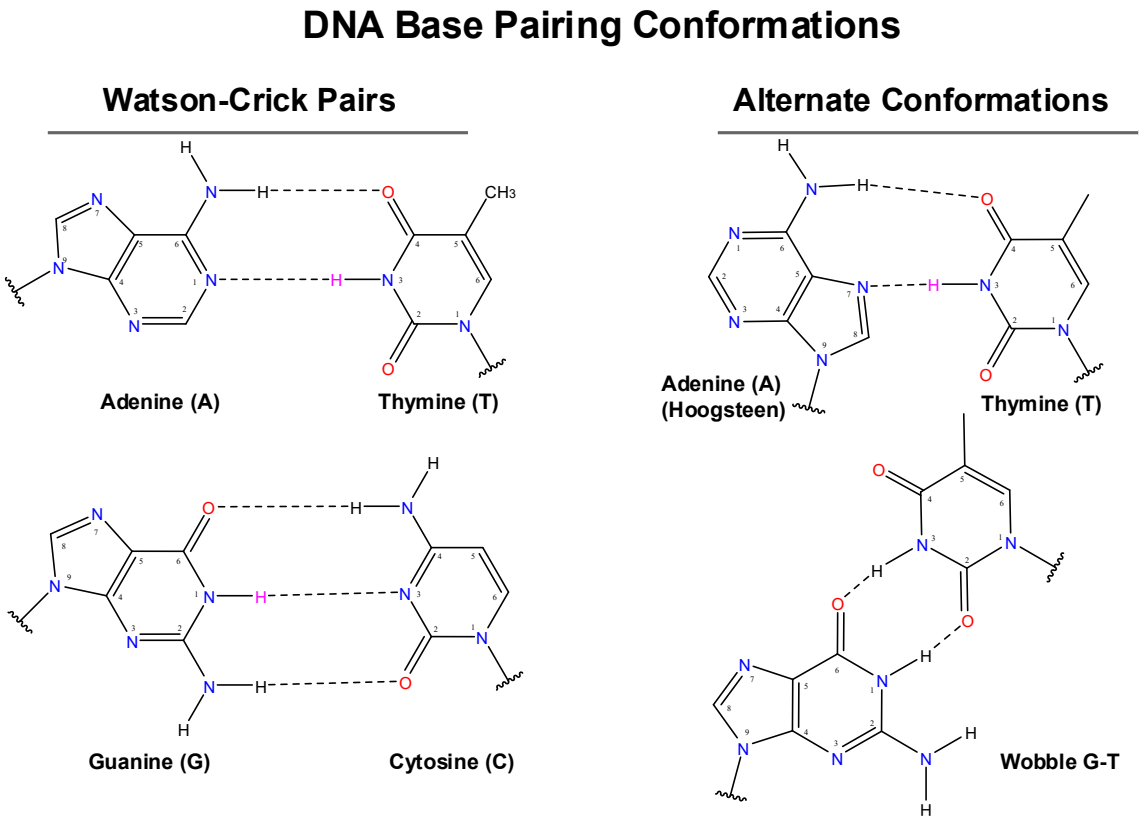

Figure 1.3.1.1. A non-exhaustive list of canonical and non-canonical base pairings. In addition to standard Watson-Crick base pairs, nucleobases can interact through alternative hydrogen-bonding arrangements involving the Watson-Crick, Hoogsteen and sugar edges. Nitrogen atoms are highlighted in blue. Oxygen atoms are highlighted in red. Imino protons are highlighted in magenta. Covalent bonds are denoted by solid lines. Hydrogen bonds are denoted by dashed lines.

1.3.2 G-Quadruplexes

In addition to canonical duplex formation, nucleic acid sequences can adopt a variety of structural motifs that contribute to their overall three-dimensional architecture. These motifs include hairpin stem-loops, symmetric and asymmetric bulges flanked by helical regions, pseudoknots, and G-quadruplexes.[40,41] A common non-canonical structure found in several well-characterized aptamers is the G-quadruplex, which is comprised of an assembly of 2 or more stacked guanine-tetrads. Each tetrad consists of 4 guanine bases arranged in a planar fashion and stabilized through Hoogsteen hydrogen bonding (Figure 1.3.2.1). Monovalent cations, most commonly potassium or sodium, are typically coordinated within the central channel between stacked tetrads, where they stabilize the G-quadruplex by interacting with the guanine 6th position carbonyl groups. G-quadruplexes are highly polymorphic structures that can adopt diverse folding topologies and play important roles in biological processes such as replication, transcription, and translation.[42–44] In aptamers, G-quadruplex formation can contribute to target binding by generating compact binding pockets, stabilizing ligand-bound conformations, or promoting conformational switching upon target recognition.

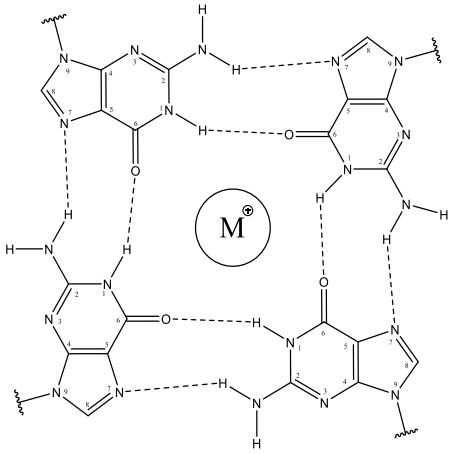

Figure 1.3.2.1. Schematic representation of a guanine tetrad illustrating the structural basis of G-quadruplex formation. Four guanine bases are arranged in a planar square configuration and are stabilized through Hoogsteen hydrogen bonding to form a G-tetrad. A monovalent cation, typically potassium (K^+) or sodium (Na^+), is coordinated within the central cavity of the tetrad, where it stabilizes the structure through interactions with the O6 carbonyl oxygens of the guanine bases.

The structural versatility of G-quadruplexes arises from the variation in strand orientation and loop arrangement observed across different topologies. G-quadruplexes may adopt parallel, antiparallel, or

mixed/hybrid topologies. In parallel G-quadruplexes, all four strands are oriented in the same 5′ to 3′ direction. In antiparallel G-quadruplexes, strands are oriented in opposing directions, with some strands running 5′ to 3′ and others running 3′ to 5′. Mixed or hybrid topologies contain both parallel and antiparallel strand orientations, often with three strands oriented in one direction and one strand oriented in the opposite direction (Figure 1.3.2.2). G-quadruplex formation is an important structural determinant of target recognition in several aptamers, including the thrombin-binding aptamer, ochratoxin-binding aptamer, and serotonin-binding aptamer.[45–47]

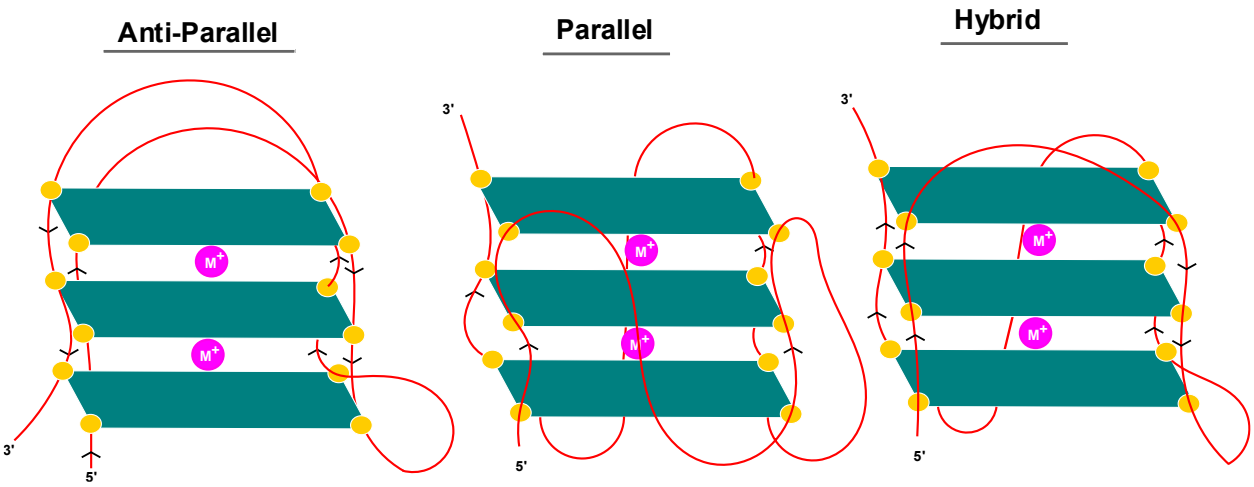

Figure 1.3.2.2. Schematic representation of G-quadruplex formation and topology. G-quadruplexes are non-canonical nucleic acid structures formed through the stacking of guanine tetrads, in which four guanine bases are arranged in a planar configuration and stabilized by Hoogsteen hydrogen bonding. Monovalent cations, such as K^+ or Na^+, can coordinate within the central channel and further stabilize the stacked tetrads. Depending on strand orientation and loop arrangement, G-quadruplexes can adopt parallel, antiparallel, or hybrid topologies. These structural variations contribute to the conformational diversity of nucleic acids and can play important roles in aptamer folding, stability, and target recognition.

1.3.3 Triple Helices

DNA bases contain multiple hydrogen-bonding edges that allow them to participate in interactions beyond canonical Watson–Crick base pairing. Under appropriate structural conditions, three nucleobases can interact to form a base triple. Consecutive base triples can give rise to stable secondary structures known as triple helices, which commonly form when a third nucleic acid strand binds within the major groove of Watson–Crick duplex DNA. In these structures, the third strand forms hydrogen bonds with the duplex through Hoogsteen or reverse Hoogsteen interactions (Figure 1.3.3.1).[48] These base triples often require a

purine within the Watson–Crick duplex to serve as the central base, as purines provide sufficient hydrogen-bonding capacity to interact with both the Watson–Crick partner and the third-strand base. Examples of aptamers that exhibit triple-helical architecture include the codeine-binding aptamer and an adenosine-binding aptamer reported by Patel et al., the latter of which was successfully incorporated into a biosensor with a reported limit of detection of 50 nM.[49,50]

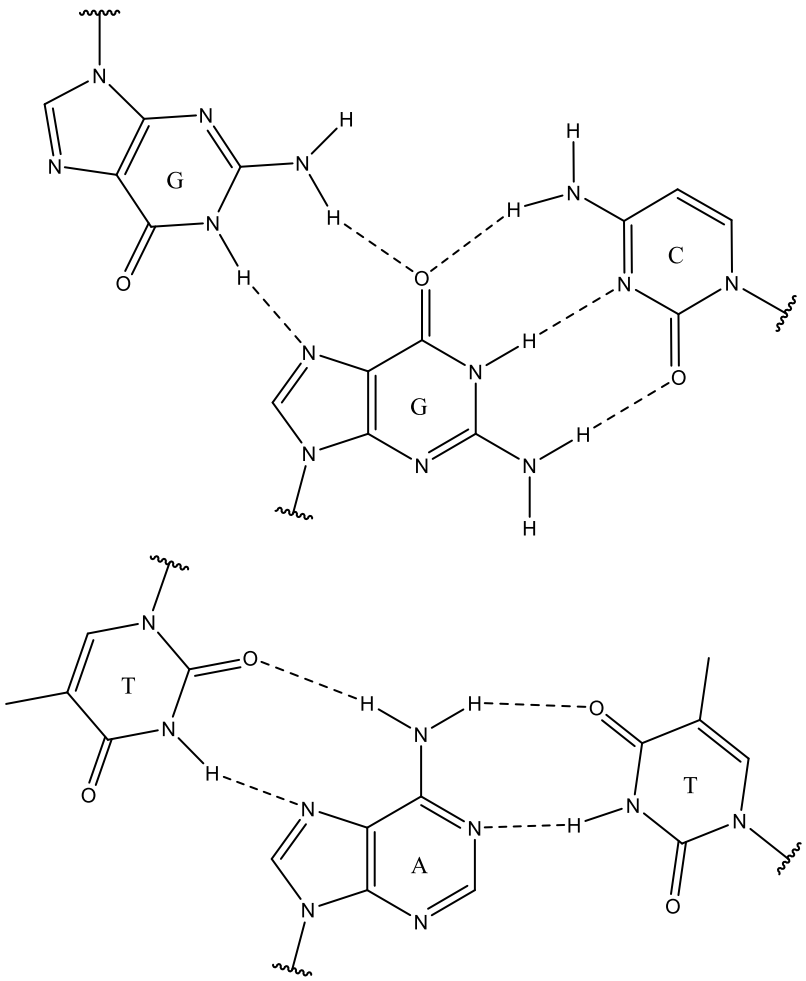

Figure 1.3.3.1. Schematic representation of possible DNA base triples involved in triple-helix formation. Base triples arise when a third nucleobase interacts with a Watson–Crick base pair through Hoogsteen or reverse Hoogsteen hydrogen bonding, typically within the major groove of duplex DNA. These interactions generate three-base assemblies that can extend along a nucleic acid sequence to form stable triple-helical structures.

1.4 Aptamer Applications

Aptamers have garnered substantial interest due to their ability to bind diverse molecular targets with high affinity and specificity. However, widespread development and commercialization of aptamers was constrained by patents that existed on the aptamer selection process (See section on SELEX). Following the expiration of key patents in 2012, there has been rapid growth in efforts to develop and commercialize aptamers as diagnostic tools, therapeutics and biosensors.[51]

Aptamers have found important applications in therapeutics, diagnostics, and biosensing, which continue to drive innovation in aptamer selection and engineering. An anti-VEGF aptamer pegaptanib sodium (brand name Macugen) was approved by the FDA for the treatment of neovascular age-related macular degeneration, demonstrating the therapeutic potential of aptamer-based molecules. In addition to this approved therapy, several aptamer-based therapeutic candidates have been investigated for clinically significant diseases, including type 2 diabetes, cardiovascular disease, leukemia, and coronary artery disease, with candidates at various stages of clinical development.[52,53]

Clinical interest in aptamers stems in part from their potential to address several limitations associated with antibody-based therapeutics. These advantages include streamlined development, reproducible chemical synthesis, broad target compatibility, lower immunogenicity, and the ability to introduce chemical modifications that improve stability and pharmacokinetic properties. Traditional antibody development requires immunization of a host organism, isolation of antibody-producing cells, and fusion of these cells with rapidly proliferating myeloma cells to generate hybridomas.[54] Each step in this process can be time- and labor-intensive and may suffer from batch-to-batch variability. In contrast, aptamers can be produced through solid-phase chemical synthesis, enabling sequence-defined production with high reproducibility and batch-to-batch consistency.[55,56]

The in vitro nature of aptamer selection also expands the range of possible therapeutic targets. Since antibody generation generally requires a host immune response against a target antigen, developing antibodies against toxic compounds or agents that impair immune function can be challenging. Aptamers, however, can be selected entirely in vitro, allowing them to be generated against a wide range of targets,

including toxins and poorly immunogenic molecules.[57] Additionally, aptamers generally exhibit low immunogenicity relative to many protein-based therapeutics and have been evaluated in several in vivo studies for physiological applications.[58,59] DNA and RNA aptamers can also be chemically modified to improve resistance to enzymatic degradation, thereby enhancing their stability, integrity, and bioavailability under physiological conditions.[60]

Aptamers have found broad utility as biosensing elements in optical, electrochemical, and mass-sensitive detection platforms. In electrochemical aptamer-based assays, an aptamer is typically immobilized on the surface of an electrode, where target binding produces a measurable change in electrochemical signal. In redox-reporter-based sensors, the aptamer is modified with an electroactive moiety capable of undergoing electron transfer with the electrode surface. Ligand binding can induce a conformational change that alters the distance or orientation of the redox reporter relative to the electrode, producing a measurable change in current or redox signal. This mechanism enables target recognition to be directly converted into an electrochemical readout.[61]

Grabowska et al. developed an aptamer-based electrochemical assay for detecting cardiac biomarkers associated with myocardial infarction. In this system, an azide-terminated aptamer selected to bind cardiac troponin I was immobilized onto a graphene oxide film using Cu(I)-catalyzed "click" chemistry. This platform demonstrated the utility of aptamer-functionalized electrode surfaces for sensitive biomarker detection in clinically relevant applications.[62]

Mass-sensitive sensing platforms can also be integrated with aptamers, although their application to small-molecule detection may be limited as low molecular weight targets often produce relatively small changes in mass and therefore weaker analytical signals. In contrast, aptamer-assisted mass spectrometry approaches have shown utility for detecting larger biomolecular targets, particularly proteins. Selected reaction monitoring (SRM), a targeted mass spectrometry-based technique, offers high selectivity and sensitivity for protein detection. Using this technique, Radko et al. used an aptamer selected against SMAD4 to detect low-abundance proteins in blood plasma.[63] The integration of aptamers with mass spectrometry modalities, including liquid chromatography–mass spectrometry, liquid chromatography–

tandem mass spectrometry, and matrix-assisted laser desorption/ionization time-of-flight mass spectrometry, has therefore become an area of interest for expanding aptamer-based detection across diverse biological and analytical systems.[64–66]

A major challenge in aptamer-based sensor development is that target binding is often assumed rather than rigorously verified under conditions relevant to sensor function. This has contributed to a broader concern in the aptasensor field: many reported sensors are developed from aptamer constructs whose solution-phase target binding has not been independently validated. Krylov et al.[67] recently described this issue as a widespread omission of aptamer–target binding verification in aptasensor development and proposed the need for a "K_d gate," defined as an auditable, construct-matched determination of target affinity in homogeneous, non-denaturing solution under sensing-relevant conditions. This recommendation emphasizes that aptamer performance should be established before incorporation into a sensing platform, rather than inferred from sensor output alone.

This concept is directly relevant to the work presented in this thesis. Aptamer function depends not only on whether a sequence produces a measurable assay response, but on whether the aptamer binds its intended target specifically and whether binding produces a defined structural or thermodynamic response. Without independent validation, apparent sensor performance may arise from interface effects, reporter behavior, nonspecific interactions, or artifacts introduced by immobilization. Therefore, solution-phase characterization methods such as ITC, NMR, DSC, CD, UV–vis absorbance, and fluorescence are essential for distinguishing true aptamer–ligand recognition from format-dependent sensor responses. In this context, the studies presented in this thesis contribute to the broader effort to move aptamer research beyond black-box binding descriptions and toward a mechanistic understanding of aptamer structure, affinity, specificity, and sensor-relevant function.

Overall, the broad applicability of aptamers in therapeutics, diagnostics, electrochemical sensing, optical detection, and mass spectrometry-based assays highlights their versatility as molecular recognition elements. These applications are enabled by the ability of aptamers to bind diverse targets with high affinity and specificity, while also being chemically synthesized, modified, and integrated into different assay

platforms. As a result, continued development of aptamer technologies depends not only on improved selection methods, but also on a deeper understanding of the structural and thermodynamic principles that govern aptamer–target recognition.

1.5 Studying Aptamers

1.5.1 Isothermal Titration Calorimetry

Many techniques have been developed to characterize aptamer–ligand interactions, each providing distinct information about binding affinity, thermodynamics, structure, or conformational change. Isothermal titration calorimetry (ITC) is widely used to quantify the strength and thermodynamic properties of aptamer–ligand binding and is considered a gold-standard technique for measuring biomolecular interactions. A key advantage of ITC is that it does not require chemical modification, immobilization, or labeling of either binding partner, allowing aptamer–ligand interactions to be studied indirectly in free solution.[68] In a typical ITC experiment, the ligand is loaded into a syringe and titrated into a sample cell containing the aptamer while the system is maintained under isothermal conditions. Interactions between the aptamer and ligand result in heat which is measured throughout the duration of the experiment. Integration of the heats associated with each injection produces a binding isotherm that can be fit to an appropriate binding model. From these data, thermodynamic parameters such as the binding affinity, dissociation constant (K_d), binding stoichiometry (n), enthalpy change (ΔH), Gibbs free energy change (ΔG), and entropy change (ΔS) can be determined (Figure 1.5.1.1). These parameters provide insight into the energetic contributions that govern aptamer–ligand interactions. For example, a favourable enthalpy change may reflect the formation of hydrogen bonds, electrostatic interactions, van der Waals contacts, or base-stacking interactions upon ligand binding. In contrast, favourable entropy may arise from desolvation, release of counterions, or displacement of ordered water molecules. Entropic penalties may also occur when ligand binding restricts the conformational flexibility of the aptamer. Therefore, ITC can help distinguish whether aptamer binding is primarily enthalpy-driven, entropy-driven, or governed by a combination of

both. This information is useful because two aptamer–ligand systems may have similar binding affinities but very different thermodynamic signatures, reflecting different underlying binding mechanisms.

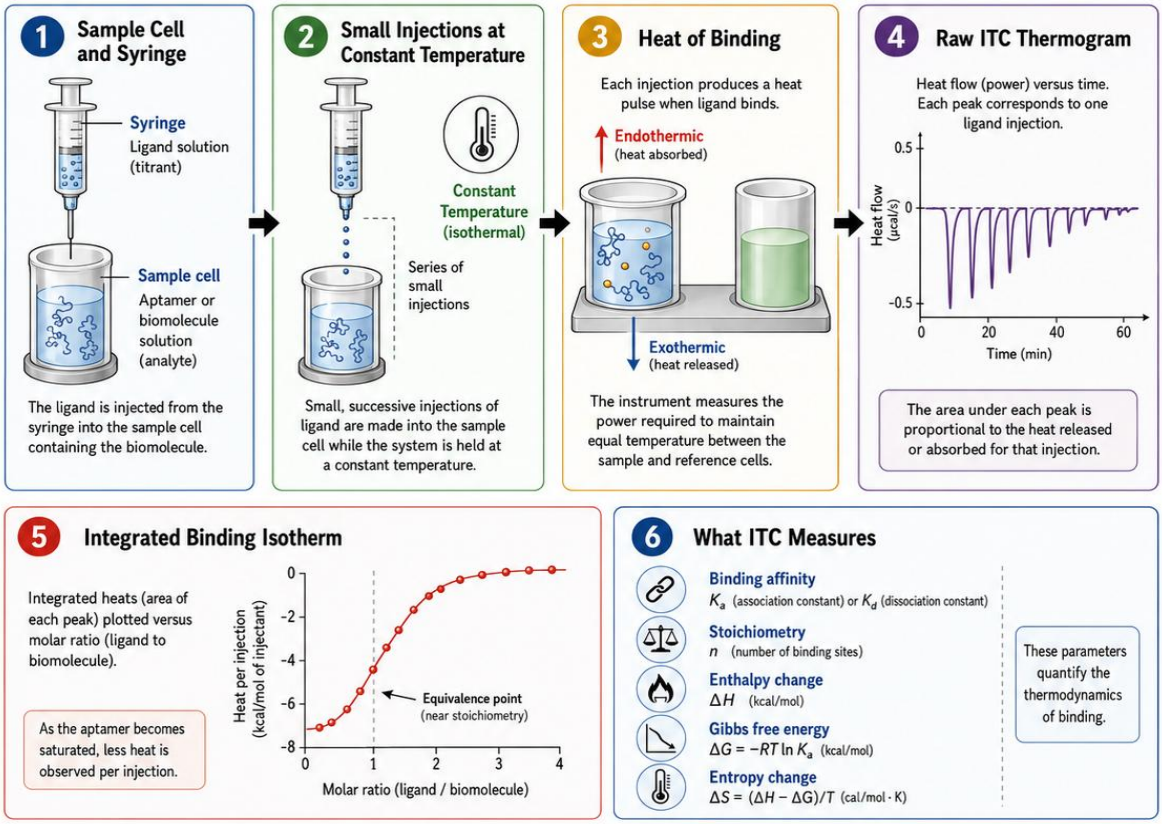

Figure 1.5.1.1. Overview of the basic principles of isothermal titration calorimetry (ITC). In an ITC experiment, a ligand solution is loaded into a syringe and sequentially titrated into a sample cell containing the aptamer or biomolecule of interest while the system is maintained under isothermal conditions. Each injection produces a heat signal as binding occurs, reflecting either heat released or absorbed during formation of the aptamer–ligand complex. The instrument measures the power required to maintain equal temperature between the sample and reference cells, generating a raw thermogram of heat flow as a function of time. Integration of the heat associated with each injection produces a binding isotherm, which can be fit to an appropriate model to determine binding affinity, stoichiometry, enthalpy change, Gibbs free energy, and entropy change. ITC therefore provides a direct, label-free method for quantifying the thermodynamic basis of biomolecular recognition in solution.

An important consideration in ITC experimental design is the optimal range of the (c)-value, which reflects the relationship between the binding affinity, the concentration of the binding partner in the sample cell, and the binding stoichiometry. The (c)-value is commonly defined as ($c = nK_a[M]$), where (n) is the binding stoichiometry, (K_a) is the association constant, and ([M]) is the concentration of the macromolecule or aptamer in the cell. Ideally, the (c)-value should fall within a range of 10-100 which produces a sigmoidal binding isotherm with a clear transition from unbound to saturated binding.[68] If the (c)-value is too low,

which often occurs for weak interactions, the binding curve becomes shallow and thermodynamic parameters may be difficult to determine accurately. If the (c)-value is too high, which can occur for very tight interactions, the transition becomes too steep, and the affinity may be difficult to resolve directly. Therefore, aptamer and ligand concentrations must often be optimized to ensure that the binding isotherm falls within a measurable range. This is particularly important for aptamer–small molecule systems, where affinities can vary widely and weak binding, low heat release, or complex binding behavior can complicate data fitting.

1.5.2 Nuclear Magnetic Resonance Spectroscopy

Nuclear magnetic resonance (NMR) spectroscopy is broadly divided into solid-state and solution-state approaches, the latter of which is going to be the focus in this thesis. Solution-state NMR is particularly useful for studying biomolecules and biomolecular interactions because it can be applied to systems for which crystalline structures are unavailable and allows molecules to be examined under solution conditions.[69,70] Experimental parameters such as pH, temperature, ionic strength, ligand concentration, and buffer composition can often be varied, making NMR well suited for comparative studies of biomolecules under native, ligand-bound, and destabilizing conditions.

In a typical NMR experiment, a sample containing NMR-active nuclei is placed in a strong static magnetic field, B_0. The sample itself must contain an NMR-active nucleus such as those that have spin quantum number ½. Commonly studied nuclei include ^{1}H, ^{13}C, ^{15}N and ^{31}P, all of which are frequently used in biomolecular NMR studies.[69,70] In the presence of the magnetic field B_0, nuclear spins become polarized, producing a net magnetization vector aligned with the external magnetic field. The sample is then irradiated with one or more radiofrequency pulses, which perturb the net magnetization away from equilibrium. After excitation, the magnetization precesses around the vector of B_0 at the resonance, or Larmor, frequency. The precessing transverse magnetization induces an oscillating current in the receiver coil, generating a time-domain signal known as the free induction decay (FID). The FID is then converted into a frequency-domain NMR spectrum through a Fourier Transform (FT), producing the familiar

spectrum in which individual resonances report on distinct chemical environments of the nucleus of interest (Figure 1.5.2.1).[69,71]

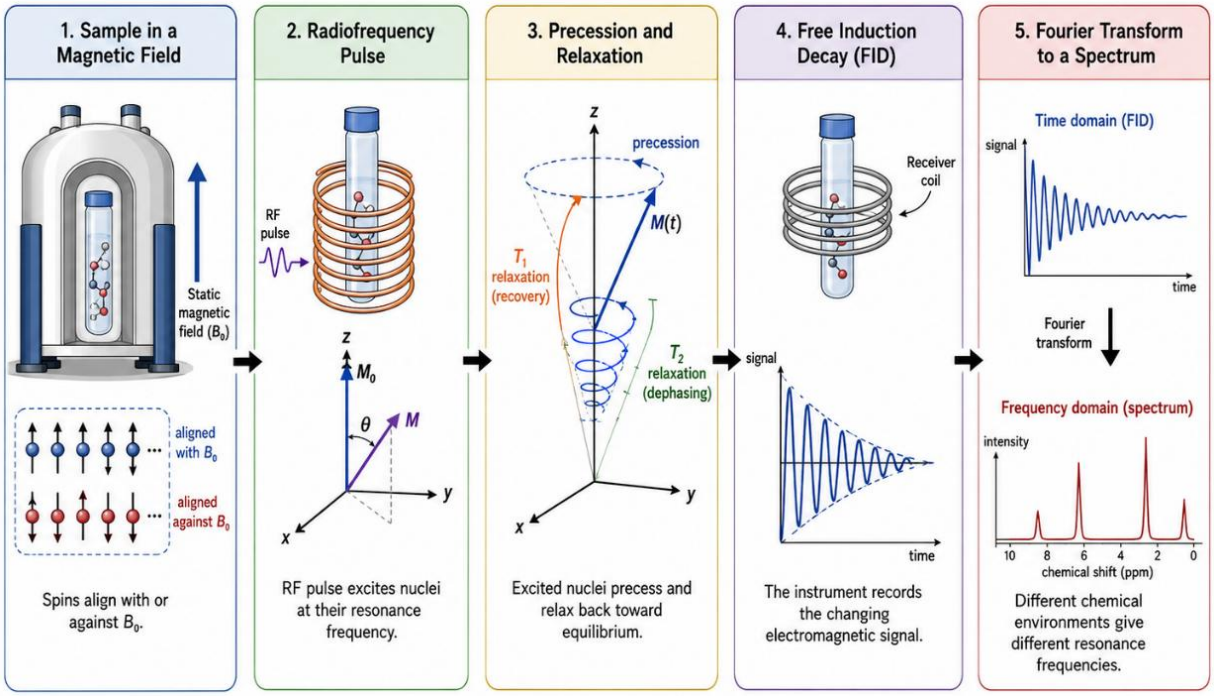

Figure 1.5.2.1. Overview of the basic principles of nuclear magnetic resonance (NMR) spectroscopy. A sample containing NMR-active nuclei is placed in a strong static magnetic field (B_0), causing nuclear spins to align with or against the field and generate a net magnetization. Application of a radiofrequency pulse excites the nuclei and tips the net magnetization away from equilibrium. The excited magnetization then precesses around B_0 while relaxing back toward equilibrium through $T_1$and T_2relaxation processes. This precessing transverse magnetization induces a detectable time-domain signal, known as the free induction decay (FID), in the receiver coil. Fourier transformation of the FID converts the signal into a frequency-domain NMR spectrum, where individual resonances reflect nuclei in distinct chemical environments.

NMR is a non-destructive technique, allowing multiple experiments to be performed on the same sample under different conditions. This is especially valuable for aptamer studies, where spectra can be collected as a function of temperature, ligand concentration, ion concentration, or buffer composition to monitor changes in folding, stability, and binding. In solution-state NMR studies of aptamers, the imino proton region is often examined first because these resonances are usually well separated from the more crowded aromatic and sugar proton regions of the spectrum and can provide rapid information about aptamer structure and ligand-induced structural changes (Figure 1.5.2.2).[72] Imino proton signals are typically observed when guanine or thymine imino protons are protected from rapid exchange with solvent,

most commonly through Watson–Crick base pairing, non-canonical base pairing, G-quadruplex formation, or other stabilizing tertiary interactions.[72,73] The chemical shift of imino proton resonances provides useful structural information. Watson–Crick base-paired imino protons are generally observed downfield, commonly between approximately 12 and 14 ppm, while imino protons involved in non-canonical base pairs, G-quadruplexes, or other tertiary interactions are often observed further upfield, typically around 10–12 ppm.[73] As a result, changes in the number, intensity, linewidth, or chemical shift of imino proton resonances can provide insight into aptamer folding, base-pair formation, ligand-induced stabilization, conformational exchange, and structural destabilization.

Structural elements of an aptamer in both the free and ligand-bound states can be investigated through assignment of these imino resonances. Once assigned, imino proton signals can provide information about base-paired stem regions, non-canonical interactions, ligand-induced structural changes, and the extent of hydrogen-bonded structure present in the aptamer. Two-dimensional NMR experiments, particularly NOESY experiments, are commonly used to support resonance assignments by identifying dipolar coupling (through-space) interactions between nearby protons, including imino–imino cross-peaks that help define base-pair connectivity in nucleic acids.[74] In this way, NMR provides a direct solution-state method for examining how aptamer structure changes upon ligand binding and is therefore a powerful tool for investigating aptamer structure–function relationships.

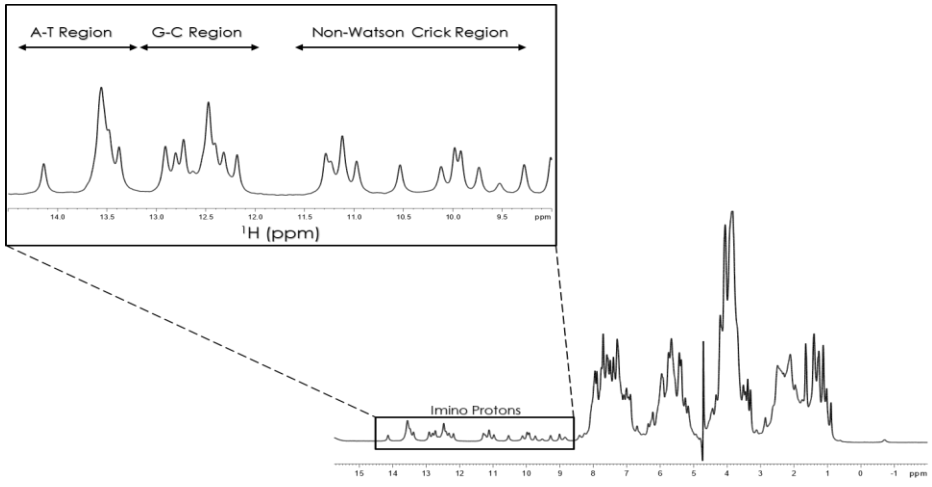

Figure 1.5.2.2. 1D ^{1}H-NMR spectrum of a DNA dopamine-binding aptamer bound to dopamine with the imino region highlighted and various types of imino protons chemical shifts outlined.

1.5.3 Differential Scanning Calorimetry

Differential scanning calorimetry (DSC) is an analytical technique used to characterize the thermal stability and unfolding behavior of biomolecules. While ITC measures the heat associated with binding under isothermal conditions, DSC monitors the heat required to thermally unfold or denature a molecule as temperature is gradually increased. In the context of aptamer studies, DSC is particularly useful because ligand binding often alters the stability of aptamers through structural changes. By comparing the thermal unfolding profile of an aptamer in the absence and presence of ligand, DSC can reveal whether ligand binding stabilizes, destabilizes, or otherwise changes the folding landscape of the aptamer.[75,76]

In a typical DSC experiment, the aptamer sample is placed in a sample cell, while a matched reference cell contains the corresponding matrix. Both cells are heated at a pre-determined scan rate over a defined temperature range. As the aptamer unfolds, melts, or undergoes a structural transition, additional heat is required to disrupt base pairing, base stacking, and tertiary interactions. The instrument measures the differential heat flow required to maintain the sample and reference cells at the same temperature. This produces a thermogram, usually represented as excess heat capacity as a function of temperature. The major feature in a DSC thermogram is the thermal transition associated with unfolding or melting of the biomolecule. The midpoint of this transition is referred to as the melt temperature or transition midpoint (T_m) and is commonly used as a measure of thermal stability (Figure 1.5.3.1). A higher T_m generally indicates that a structure is more thermally stable, whereas a lower T_m indicates reduced thermal stability. Integration of the thermal transition can also provide the calorimetric enthalpy of unfolding (ΔH_{unf}), which reflects the total heat absorbed during the transition. DSC can also provide information about heat capacity changes (ΔC_p), transition cooperativity, and whether unfolding occurs through a simple two-state process or through more complex intermediate states.

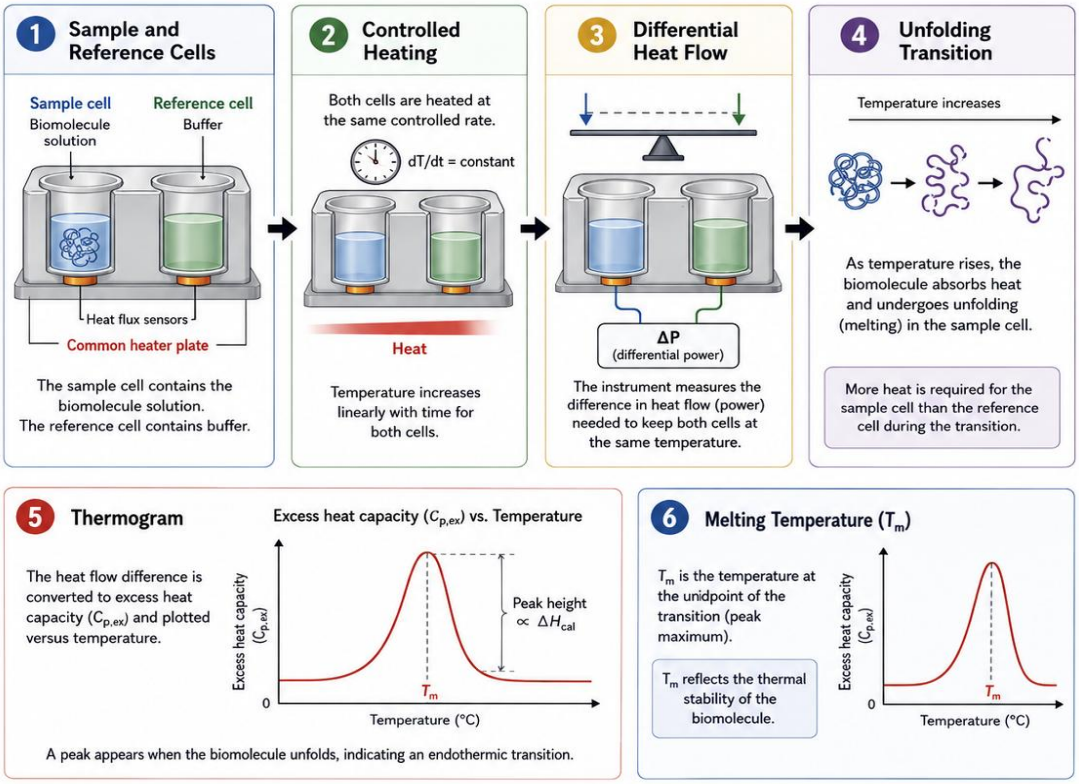

Figure 1.5.3.1. Overview of the basic principles of differential scanning calorimetry (DSC). In DSC, a sample cell containing the aptamer or biomolecule solution and a reference cell containing matched matrix are heated at a controlled rate. As temperature increases, unfolding or melting of the biomolecule requires additional heat relative to the reference cell. The instrument measures the differential heat flow required to maintain both cells at the same temperature, producing a thermogram of excess heat capacity as a function of temperature. The midpoint of the thermal transition, commonly reported as the melt temperature (T_m), provides a measure of thermal stability, while the shape and area of the transition can provide information about unfolding enthalpy and cooperativity. Shifts in the thermogram upon ligand addition can reveal whether ligand binding stabilizes or destabilizes the aptamer structure.

Despite its utility, DSC also has important limitations to consider. DSC provides information about global thermal stability, but it does not identify which specific nucleotides or structural elements are affected by ligand binding. As a result, DSC cannot independently define the binding site or provide high-resolution structural information. Interpretation can also be complicated when unfolding is partially or completely irreversible, when transitions overlap, when the aptamer forms multiple conformations, or when ligand binding produces complex non-two-state behavior. In addition, changes in T_m cannot be interpreted as direct measurements of binding affinity. A ligand may bind tightly but produce only a small thermal shift, while another ligand may produce a larger stability change despite weaker affinity. Therefore, DSC

is most powerful when combined with complementary techniques such as ITC, NMR spectroscopy, CD spectroscopy, UV–vis absorbance, or fluorescence.

Overall, DSC provides a direct, label-free method for assessing the thermal stability of aptamers and the effect of ligand binding on aptamer unfolding. By measuring changes in T_m, unfolding enthalpy, and transition shape, DSC can reveal whether ligand binding stabilizes or destabilizes the aptamer and whether unfolding occurs through a cooperative or heterogeneous process. In this thesis, DSC was particularly useful for evaluating how small-molecule ligands altered the thermal stability of aptamer structures, providing an important thermodynamic complement to NMR and ITC analyses.

1.6 Aptamer Structure Prediction

Recent advances in computational structure prediction have changed how biomolecular structure is approached. Tools such as AlphaFold and related deep-learning methods have demonstrated that artificial intelligence can generate highly accurate structural models for many proteins, and newer platforms have extended this capability beyond single proteins to include complexes involving nucleic acids, small molecules, ions, and modified residues. AlphaFold 3, for example, was developed to predict structures of biomolecular assemblies that include proteins, DNA, RNA, ligands, and ions, representing an important step toward unified modelling of biological interactions.[77]

For aptamer research, these advances are especially promising. Aptamers often rely on ligand-induced folding, noncanonical base pairing, long-range tertiary contacts, G-quadruplex formation, and dynamic conformational equilibria. Recent studies have begun evaluating whether AlphaFold 3 can directly model DNA and RNA aptamers and aptamer–target complexes. These studies suggest that AlphaFold 3 can capture some aptamer folds, including certain G-quadruplex-like and noncanonical structural features, but performance remains uneven, particularly for structures involving pseudoknots, long-range nucleobase interactions, and systems underrepresented in structural databases. This further drives home the point of needing additional solved structures to improve the seed data necessary to train these systems.[78]

However, predicted aptamer structures should be interpreted as hypotheses rather than definitive structural models. Aptamers are often conformationally dynamic, and ligand binding may stabilize only a subset of structures within a broader ensemble. This is particularly important for small-molecule-binding aptamers, where recognition can involve subtle changes in base pairing, stacking, loop organization, local dynamics, ion coordination, or ligand-induced folding. As a result, a predicted lowest-energy secondary structure or docked ligand pose may not accurately represent the experimentally populated binding-competent state. Reviews of aptamer modelling emphasize that computational workflows are most useful when combined with experimental validation, such as NMR spectroscopy, X-ray crystallography, calorimetry, chemical probing, or other biophysical methods.[79,80]

Within this context, prediction software, AI-based modelling, and molecular simulations should be viewed as complementary to experimental structural characterization. Computational models can guide experiments by suggesting plausible folds and ligand-binding modes, but experimental methods are required to determine whether ligand binding actually induces folding, remodels a pre-existing structure, stabilizes a defined complex, or produces nonspecific interactions. This distinction is central to aptamer characterization because binding affinity alone does not reveal the structural mechanism of recognition. Therefore, integrating computational prediction with solution-state methods such as NMR provides a stronger framework for understanding aptamer function, where models generate testable structural hypotheses and experiments determine which conformational states are actually populated in solution.

1.7 Thesis Project

The overall goal of this thesis was to investigate how nucleic acid structure governs the function of aptamers in small-molecule and ion recognition. Although aptamers are commonly described by their affinity and selectivity for a target, these properties ultimately arise from the conformations available to the nucleic acid and the structural changes that occur upon ligand binding. In many cases, aptamer–small molecule interactions are treated as a functional “black box,” where a sequence is selected, binding is measured, and the aptamer is then applied in a sensor or recognition platform without a detailed

understanding of the structural mechanism underlying target recognition. This limited structural understanding can make it difficult to rationally optimize aptamers, predict specificity and cross-reactivities, or determine why some aptamers perform well in sensing platforms while others do not.

This thesis aimed to shed light on this black box by examining aptamer–ligand interactions beyond binding affinity alone. Specifically, this work investigated how small molecules and ions influence aptamer folding, structural stability, conformational dynamics, and specificity. Across the systems studied, ligand binding was shown to produce a range of structural outcomes, including ligand-induced folding, stabilization of pre-existing structure, ligand-induced destabilization, weak but detectable structural perturbation, and non-specific DNA binding. These findings demonstrate that aptamer function cannot be fully understood by asking only whether a ligand binds; it is also necessary to determine what structural consequence binding has on the aptamer.

To address this, complementary biophysical and structural techniques were used, including NMR spectroscopy, isothermal titration calorimetry, differential scanning calorimetry, circular dichroism, UV–vis absorbance, and fluorescence spectroscopy. Together, these methods provided insight into both the thermodynamic and structural basis of aptamer recognition. Particular emphasis was placed on NMR spectroscopy because of its ability to directly monitor solution-state structural changes in aptamers upon ligand addition. By comparing free and ligand-bound states, this thesis sought to determine whether binding produces a defined folded complex, stabilizes an existing conformation, causes structural destabilization, or reflects broader non-specific nucleic acid interactions.

Overall, this thesis sought to map the structure–function relationships that underlie aptamer recognition of small molecules and ions. By clarifying how ligand binding reshapes aptamer structure and dynamics, this work provides insight that can guide future aptamer selection, validation, optimization, and biosensor design.

Chapter 2 Ligand-Induced Folding in a Dopamine-Binding DNA Aptamer

2.1 Preface

All work presented in this chapter has been published in the article below [81]

- Kaiyum, Y. A., Hoi Pui Chao, E., Dhar, L., Shoara, A. A., Nguyen, M. D., Mackereth, C. D., Dauphin-Ducharme, P., & Johnson, P. E. (2024). Ligand-Induced Folding in a Dopamine-Binding DNA Aptamer. *ChemBioChem*, *25*(23).
- Contributions for sections 2.4.1 – 2.4.4. were done by Y. A. Kaiyum.

2.2 Introduction

Aptamers are single-stranded nucleic acid molecules that are selected to bind a particular molecule. Small molecule-binding aptamers are especially well-studied as they are often used in biosensor development.[82] An example of these applications are the electrochemical aptamer-based (E-AB) biosensors that are now employed for in vivo use.[83] It is postulated that a key requirement of aptamers that allows them to function as an E-AB sensor is that aptamers undergo ligand-induced structure formation, where new secondary structure forms upon ligand addition and binding. This ligand-induced structure formation has been observed in several aptamers including the short stem 1 version of the cocaine-binding aptamer (MN19)[84] as well as other aptamer small-molecule systems.[85] However, little is known about the nature of the structural change that facilitates sensor function. The extent of structural formation required and whether this new structure must develop near the surface to which the aptamer is bound remain unresolved questions.

The dopamine DNA aptamer selected by Stojanovic and co-workers is interesting to study as its target ligand is an important neurotransmitter (Figure 2.2.1) and the aptamer was shown to be structure-switching based on changes in the circular dichroism (CD) spectrum between the free and bound forms of the aptamer.[46] Following its initial report, a number of biosensor applications have subsequently used this aptamer.[86] This original aptamer (DA-5bp) was predicted to form a structured region built on a stem of five base pairs before the predicted CA mismatch (Figure 2.2.1). This putative CA mismatch in the stem can be replaced by a TA base pair to generate the variant identified as Mut3 with no loss in affinity.[87] Additionally, it has been shown that Mg^{2+} is needed for maximal ligand binding affinity.[86–88] While Mg^{2+} plays an

important role in RNA structure, it has not been seen to play as large a role in DNA aptamer structure and function.

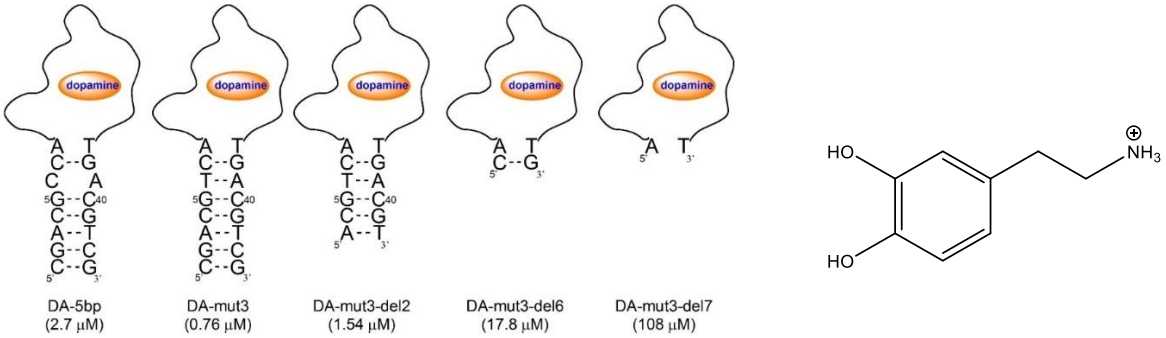

Figure 2.2.1. Secondary structure of various dopamine-binding aptamers showing the terminal stem. The DA-5bp contains a C−A mismatch which is changed to a Watson-Crick T−A pairing in the DA-mut3. The affinity of each aptamer to dopamine is indicated, based on ITC data (Table 2.2.1). On the right is the chemical structure of dopamine in the protonated state, the dominant form of the ligand throughout this study.

To better understand the function of the dopamine aptamer and its use in E-AB biosensors, the affinity and structure of a series of aptamer variants were investigated as the terminal stem that contains the 5' and 3' termini was progressively shortened. A table containing the sequences of each of these variants is in Table 2.2.1. The affinity of each variant to dopamine was analysed by ITC and the structural response to dopamine binding was investigated utilizing CD spectroscopy and NMR spectroscopy techniques. A general trend of the aptamer having a weaker affinity as the terminal stem is shortened was observed and all the dopamine aptamer constructs studied exhibited ligand-induced structure formation as demonstrated by numerous new signals appearing in the imino region of the ^{1}H-NMR spectrum. Additionally, it is only when the terminal stem is shortened by six base pairs that a functional E-AB biosensor is obtained.

Table 2.2.1. DNA sequences of the dopamine aptamers used in this study

Sequence name	Sequence (5' to 3')
DA-3BP	ACGTCAGTTTGAAGGTTCGTTCGCAGGTGTGGAGTGACGT
DA-5BP	CGACGCCAGTTTGAAGGTTCGTTCGCAGGTGTGGAGTGACGTCG
DA-mut3	CGACGTCAGTTTGAAGGTTCGTTCGCAGGTGTGGAGTGACGTCG
DA-mut3-del1	GACGTCAGTTTGAAGGTTCGTTCGCAGGTGTGGAGTGACGTC
DA-mut3-del2	ACGTCAGTTTGAAGGTTCGTTCGCAGGTGTGGAGTGACGT
DA-mut3-del3	CGTCAGTTTGAAGGTTCGTTCGCAGGTGTGGAGTGACG
DA-mut3-del4	GTCAGTTTGAAGGTTCGTTCGCAGGTGTGGAGTGAC
DA-mut3-del5	TCAGTTTGAAGGTTCGTTCGCAGGTGTGGAGTGA
DA-mut3-del6	CAGTTTGAAGGTTCGTTCGCAGGTGTGGAGTG
DA-mut3-del7	AGTTTGAAGGTTCGTTCGCAGGTGTGGAGT

2.3 Methods and Materials

2.3.1 Materials

Aptamer samples (Table 2.2.1) were obtained from Integrated DNA Technologies (IDT, Coralville, Iowa) with standard desalting and used without further purification. The veracity of the DNA was verified by mass spectrometry performed by the manufacturer. DNA samples were dissolved in distilled, deionized water and then exchanged three times in a 3-kDa molecular weight cut-off concentrator with 1 M NaCl and washed at least three times with distilled deionized water. All DNA samples were exchanged with the appropriate buffer three times before use. Aptamer concentrations were determined by absorbance spectroscopy using the extinction coefficients provided by IDT. All small molecule ligands were obtained from Sigma Aldrich. Stock solutions of compounds for binding experiments were prepared by dissolving the appropriate weight of dopamine into 20 mM sodium phosphate, 140 mM NaCl, 2 mM $MgCl_2$, pH 7.4 (buffer A). This buffer was chosen to match the conditions of a prior ITC study.[89] Dopamine-hydrochloride (Catalog number – H8502) was purchased from Sigma Aldrich.

2.3.2 Isothermal Titration Calorimetry

ITC binding experiments were performed using a MicroCal VP-ITC instrument in a manner similar to what we previously described.[68] Samples were degassed before analysis with a MicroCal Thermo Vac unit. All experiments were corrected for the heat of dilution of the titrant. Titrations were performed with the aptamer samples in the cell, and the ligand as the titrant, loaded in the needle. All aptamer samples were heated in a 95 °C water bath for 3 minutes and cooled in an ice water bath prior to use in a binding experiment to allow the DNA aptamer to anneal in an intramolecular fashion.

The binding experiments were performed at 20 °C with the aptamer solution at 20–85 μM aptamer concentration using a dopamine concentration of 0.312 to 1.326 mM. Dopamine was diluted to experimental concentrations with buffer A. All binding experiments were performed at 20 °C and consisted of an initial delay of 60 s, first injection of 2 μL and 300 s delay. Subsequent 34 injections were 8 μL, spaced every 300 s to allow for adequate mixing and equilibration before subsequent injections. The first point was removed from all data sets due to the different injection volume and delay parameters. ITC data

following a one-site binding model were fit using the manufacturer provided Origin 7 software. The isobaric heat capacity (ΔC_p) of dopamine-binding by the DA-mut3 aptamer was determined by measuring the thermodynamics of binding over a temperature range of 5 to 30 °C with an aptamer solution of 20 μM in buffer A.

2.3.3 NMR Spectroscopy

NMR experiments on aptamer samples were performed using a 600 MHz Bruker Avance spectrometer equipped with a ^{1}H-^{13}C-^{31}P triple-resonance probe in a similar fashion as previously described.[72] All NMR spectra were acquired in buffer A in $1H_2O/^{2}H_2O$ (90 %/10 %) at 5 °C. Water suppression was achieved through the use of excitation sculpting.[90] Total Correlation Spectroscopy (TOCSY) experiments were performed with a 70.65 ms mixing time at 20 °C in 99.96 % $^{2}H_2O$. Aptamer concentrations for NMR studies varied from 0.25 to 1.0 mM. Dopamine was prepared in buffer A immediately prior to use to limit dopamine polymerization.

2.3.4 CD Spectroscopy

CD spectroscopy was performed using a Jasco J-810 instrument at 20 °C with a quartz two-compartment cuvette with a pathlength of 10 mm and the ellipticity was measured in millidegrees (mdeg). Dopamine was added into the free aptamer until a 4 to 1 ligand to aptamer molar ratio was achieved. Aptamer concentrations in the cuvette were 100 μM in buffer A. All spectra were baseline corrected using buffer A. Spectra were recorded from 20–320 nm with a scan rate of 100 nm min^{-1} and a 1.0 nm bandwidth.

2.4 Results and Discussion

2.4.1 Initial NMR Studies of DA-5bp and DA-mut3

NMR spectroscopy was performed on the DA-5bp and DA-mut3 aptamer constructs both free and bound to dopamine to gauge their suitability for further NMR-based studies. A TOCSY spectrum of each complex in $^{2}H_2O$ was collected. An H5-H6 correlation peak for each cytosine in the sequence indicates a single bound conformation, with nine signals expected for the DA-5bp sample. However, for the DA-5bp aptamer-dopamine complex, 11 signals were detected (Figure 2.4.1.1), which was more than expected.

Additionally, these signals had varying intensities indicating that multiple conformations are present in the bound DA-5bp complex. For the DA-mut3–dopamine complex, eight signals were expected from the eight cytosines in this aptamer. As shown in Figure 2.4.1.1 there were eight observed signals, as expected from the number of cytosines in this construct, indicating that only one conformation is present in the DA-mut3-bound complex. Consequently, the DA-mut3 construct was selected for further study.

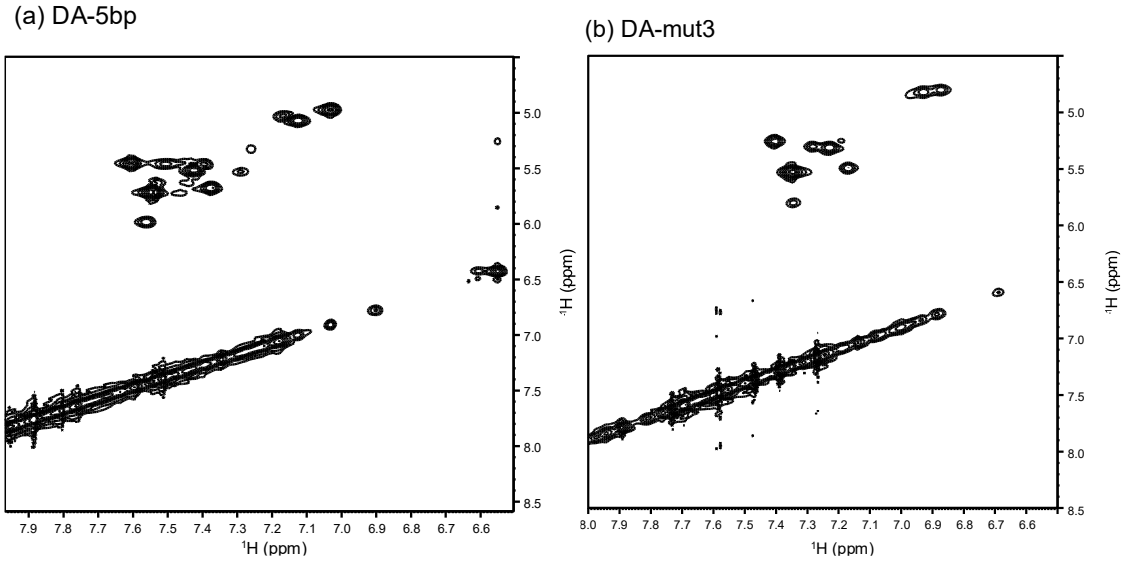

Figure 2.4.1.1. TOCSY spectra of two dopamine aptamers bound to dopamine showing the H5-H6 region. The DNA is prepared in 140 mM NaCl, 20 mM sodium phosphate (pH 7.4), 99.96% D_2O at 20°C.

2.4.2 NMR and ITC studies of Dopamine Binding by DA-Mut3

Binding of dopamine to the DA-mut3 aptamer was analysed using ITC methods. The DA-mut3 construct binds dopamine with an affinity of (0.76±0.04) μM in an enthalpically driven process coupled with an unfavourable entropy of binding (Figure 2.4.2.1a; Table 2.4.2.1). These binding values compare favourably with those reported in previous studies of this variant.[87] The c-value for ITC experiments with the DA-mut3 construct was 26 indicating high reliability in the data.[91] The importance of Mg^{2+} to the binding of dopamine was assessed by performing ITC in the absence of added Mg^{2+} and in the presence of 5 mM EDTA that should bind any Mg^{2+} present. Without Mg^{2+} present the affinity weakens to (2.0±0.1) μM, again consistent with previous studies showing that the presence of Mg^{2+} increases affinity.[86,87]

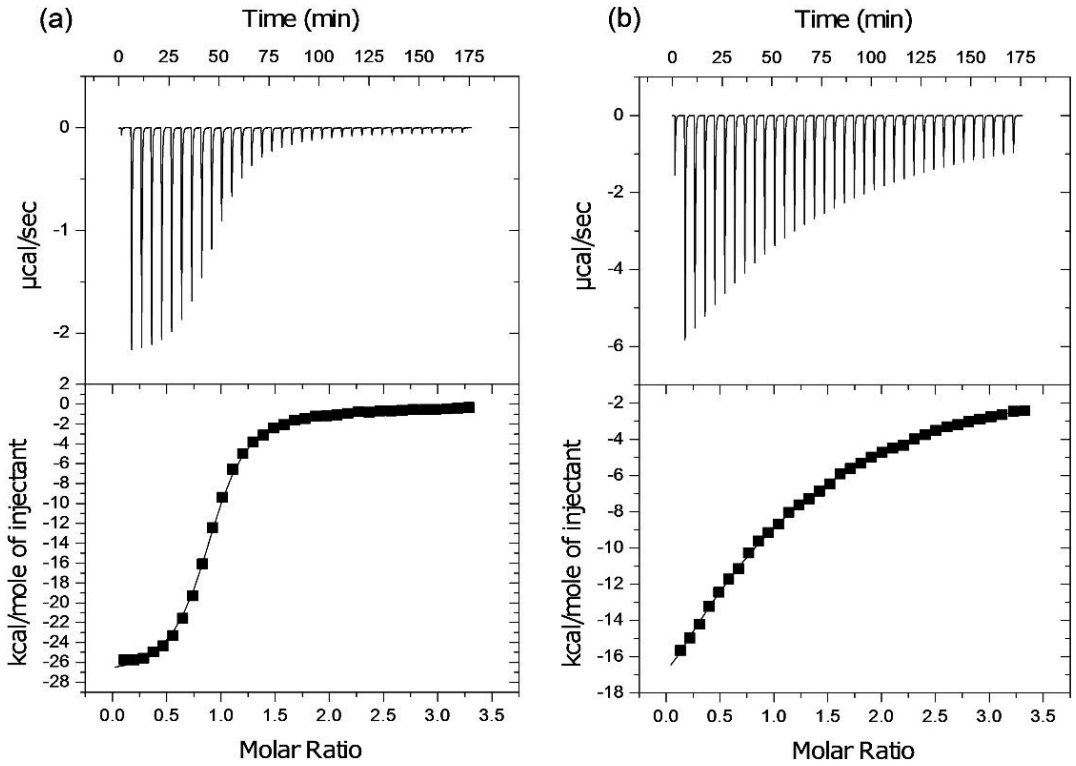

Figure 2.4.2.1. ITC thermograms showing the interaction of (a) DA-mut3 and (b) DA-mut3-del7 with dopamine. Heats of dilution were subtracted from the thermograms prior to performing fitting. For each figure, the top represents the titration data showing the resultant heat from each injection of dopamine into aptamer solution and the bottom represents the integrated heats after correcting for the heat of dilution. The sigmoidal nature of the curve in (a) indicated one-site binding with a K_d of 0.77 µM and a ΔH of −27.0 kcal/mol for the DA-mut3 binding dopamine. For the DA-mut3-del7 aptamer binding dopamine the K_d value is 108 µM and the ΔH is −41 kcal/mol. ITC experiments were conducted at 20 °C with an aptamer concentration of 20 µM and a dopamine concentration of 312 µM. Both aptamer and ligand were dissolved in 20 mM sodium phosphate (pH 7.4), 140 mM NaCl, 2 mM $MgCl_2$.

Table 2.4.2.1. K_d values and thermodynamic parameters of ligands used in this study for binding to the dopamine binding aptamer[a]

	K_d (µM)	ΔH (kcal mol^{-1})	-TΔS (kcal mol^{-1})	ΔG (kcal mol^{-1})
DAMut3	0.76 ± 0.04	-27.0 ± 0.2	18.7 ± 0.2	-8.21 ± 0.03
DAMut3[b]	2.01 ± 0.11	-22.2 ± 0.4	14.6 ± 0.4	-7.64 ± 0.03
DAMut3 Del1	1.96 ± 0.07	-23.4 ± 0.2	15.7 ± 0.2	-7.66 ± 0.02
DAMut3 Del2	1.54 ± 0.08	-32.3 ± 0.4	24.5 ± 0.4	-7.80 ± 0.03
DAMut3 Del3	1.68 ± 0.06	-29.7 ± 0.1	22.0 ± 0.1	-7.74 ± 0.02
DAMut3 Del4	2.7 ± 0.2	-35.3 ± 0.3	27.8 ± 0.2	-7.47 ± 0.03
DAMut3 Del5	17.9 ± 0.7	-41.7 ± 0.5	35.3 ± 0.5	-6.37 ± 0.02
DAMut3 Del6	17.8 ± 0.6	-45.5 ± 0.7	39.1 ± 0.7	-6.37 ± 0.02
DAMut3 Del7	108 ± 3	-41 ± 1	36 ± 1	-5.31 ± 0.02

The values reported are averages of two individual experiments. [a] Data acquired at 20 °C in buffer A (20 mM sodium phosphate, 140 mM NaCl, 2 mM $MgCl_2$, pH 7.4) except where marked. [b] Data acquired at 20 °C in buffer B (20 mM sodium phosphate, 140 mM NaCl, 5 mM EDTA, pH 7.4).

Binding of dopamine by the DA-mut3 aptamer was also studied using NMR spectroscopy. The 1-D ^{1}H-NMR spectrum were recorded of unbound DA-mut3 and NMR spectra in the presence of an increasing amount of dopamine (Figure 2.4.2.2a). In the free state, DA-mut3 displayed 6–8 signals in the downfield part of the imino region (12–14.5 ppm) indicating the presence of 6–8 Watson-Crick base pairs. There was also a single broad peak at ~10.3 ppm. The total number of signals in the unbound spectrum is much lower than the possible number of imino signals from all the thymine and guanine nucleosides, 29 in total. Together, these observations suggest that a stem consisting of Watson-Crick base pairs exists in the free DA-mut3 aptamer and that there is a large unstructured region.

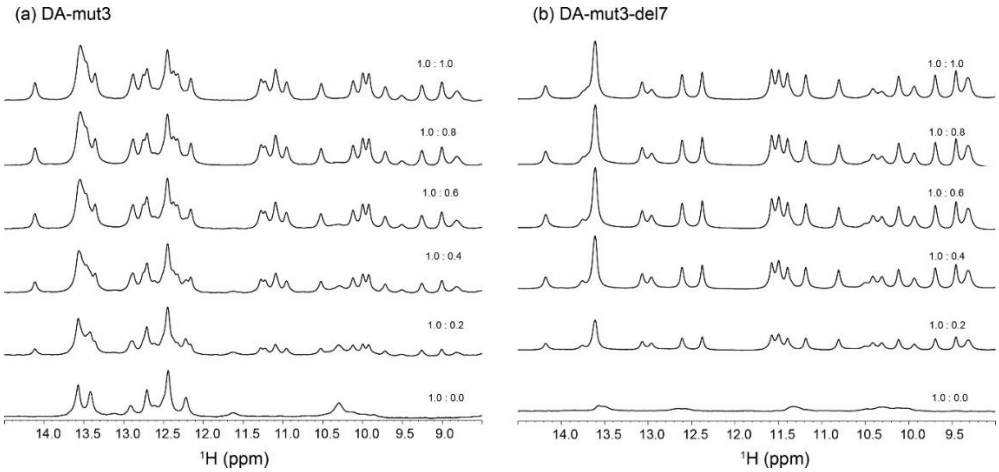

Figure 2.4.2.2. NMR spectra showing the imino proton resonances during a titration of the (a) DA-mut3 or (b) DA-mut3-del7 aptamer with dopamine. Numbers on the right-hand side of the spectrum indicate the molar ratio of aptamer to dopamine. Experiments were conducted with an aptamer concentration of 0.5 mM in 20 mM sodium phosphate, 140 mM NaCl, 2 mM $MgCl_2$, pH 7.4, 90 % $^{1}H_2O$-10 % $^{2}H_2O$ at 5 °C.

Upon the addition of dopamine, a large number of signals appear in both the Watson-Crick region and the non-Watson-Crick region (8.5–12 ppm) of the imino ^{1}H spectrum. This indicated that a large amount of new structure forms with dopamine binding and, since many signals are in the 8.5–12 ppm range, many non-Watson-Crick base pairs are formed in this new structure. Few or none of the signals in the Watson-Crick region of the free spectrum change chemical shift with ligand binding, indicating the stem plays little or no direct role in binding.

2.4.3 Heat Capacity of Dopamine Binding by DA-Mut3

To confirm that ligand-induced structure formation occurs, the change in heat capacity (ΔC_p) for DA-mut3 binding dopamine was measured by running ITC at different temperatures (Table 2.4.3.1).

Table 2.4.3.1. Thermodynamic parameters of DA-Mut3 binding dopamine at different temperatures

Temperature (°C)	ΔH (kcal mol^{-1})
5	-19.98 ± 0.07
10	-26.1 ± 0.1
10	-13.8 ± 0.2
10	-16.9 ± 0.1
15	-24.40 ± 0.07
20	-18.9 ± 0.1
25	-38.7 ± 0.4
25	-42.4 ± 0.2
30	-32 ± 1
30	-29 ± 1
30	-40.8 ± 0.9

The error values reported are from the fit.
Data acquired using ITC methods in buffer A (20 mM sodium phosphate, 140 mM NaCl, 2 mM $MgCl_2$, pH 7.4).

The ΔC_p value for aptamers that undergo ligand-induced folding is more negative than for aptamers not undergoing ligand-induced folding.[84,92] The ΔCp value was obtained from the slope of a plot of ΔH of binding versus temperature (Figure 2.4.3.1). For DA-mut3 binding dopamine , the ΔC_p value is (−880 ± 270) cal mol^{-1} K^{-1}. This large negative value is in the range observed for other aptamers that undergo ligand-induced structure formation[84,92,93] indicating that a large amount of structure in the DA-mut3 aptamer is formed upon dopamine binding, consistent with the NMR titration data. This observation of ligand-induced structure formation is consistent with prior claims of ligand-induced structural change based on the change in the CD spectrum of the free and dopamine-bound original DA-5bp aptamer shown by Nakatsuka et al.[46,86] Liu *et al.* also suggested structural change with dopamine binding occurs based on the behaviour of the aptamer in a gold nanoparticle assay.[89]

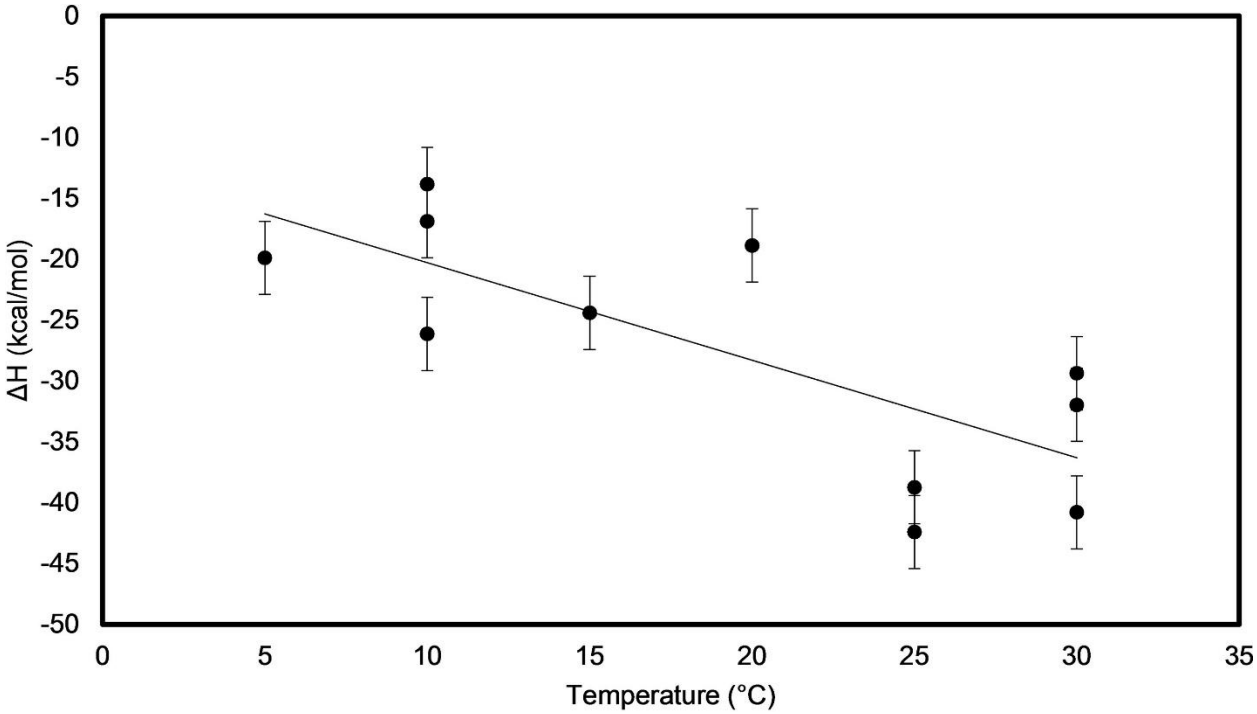

Figure 2.4.3.1. Temperature dependence of enthalpy for DA-mut3 binding to dopamine. This plot provides a ΔC_p value for DA-mut3 binding dopamine of (−880±270) cal mol^{-1} K^{-1}. Buffer conditions were 20 mM sodium phosphate, 140 mM NaCl, 2 mM $MgCl_2$, pH 7.4.

2.4.4 Binding and Spectroscopic Analysis of Deletion Mutants

To further determine the role played by the stem in ligand binding we analysed the binding ability and NMR spectra of a series of deletion mutants of the DA-mut3 aptamer (Figure 2.2.1; Figure 2.4.2.1b; Figure 2.4.2.2b; Figure 2.4.4.1). Seven deletion mutants were analysed, each with consecutive single base pair removed from the 5'-3' terminus of DA-mut3 (Figure 2.2.1). The binding affinities of the deletion mutants stay relatively constant for the DA-mut3-del1 to DA-mut3-del4 constructs. In contrast, a major affinity decrease to ~18 μM for DA-mut3-del5 and DA-mut3-del6, as shown by a loss in the sigmoidal nature of the ITC thermogram, is further followed by a large affinity decrease to 108 μM for DA-mut3-del7 (Table 2.4.2.1). For the DA-mut3-del7 construct, the ITC experiments were acquired at a c-value of 0.8 indicating that the exact value of the K_d determined would be less reliable for this construct than the longer constructs.[91] Nevertheless, it is clear that the DA-mut3-del7 binds dopamine with significantly weaker affinity than DA-mut3.

The imino ^{1}H spectra of DA-mut3-del1, DA-mut3-del2, DA-mut3-del3 and DA-mut3-del4 are similar to the free spectrum of DA-mut3 in that there are some sharp Watson-Crick signals observed and a broad peak seen at ~10.3 ppm. For DA-mut3-del5, DA-mut3-del6 and DA-mut3-del7 there are only a few broad and weak signals present in the unbound NMR spectrum indicating little structure is formed in these unbound aptamer constructs (Figure 2.4.2.2b; Figure 2.4.4.1). It is likely that the stem goes from being formed in the free DA-mut3-del4 to being not formed in the unbound DA-mut3-del5. This change is consistent with the sharp drop in affinity going from DA-mut3-del4 to DA-mut3-del5. Upon the addition of dopamine, many sharp new signals appear, similar to what is seen in DA-mut3. This demonstrates that all of these aptamers show a large amount of new structure formation with ligand binding. This finding is consistent with the ITC data showing that these deletion constructs all bind dopamine. From the similarity of the chemical shifts of all the NMR spectra of the aptamers studied, it was concluded that a highly similar dopamine-bound structure is formed by all these constructs (Figure 2.4.4.2).

The measured thermodynamic parameters for the series of dopamine aptamer deletion mutants allow comparisons to be made with the trends seen here with what has previously been observed with the cocaine-binding aptamer deletion mutants. The dopamine aptamer constructs with the shortest stems display the weakest observed binding. This trend was also observed with deletion mutants of the cocaine-binding aptamer.[94] Similarly, for both aptamers, the constructs with the shortest stem have the most negative ΔH values for binding and the highest values of $-T\Delta S$ for binding. This trend of weaker binding, a more negative ΔH, and a more positive $-T\Delta S$ may result from more structural change with ligand binding occurring with the shorter stem aptamers. Ligand binding drives the aptamer folding event for both the short stem 1 cocaine-binding aptamer (MN19) and the dopamine binding aptamers. During this process, some of the binding free energy goes into "paying the cost" of aptamer folding with the rest observed as apparent K_d value. This results in the shorter stem aptamers consistently having a weaker measured K_d value. For the more negative ΔH and more positive $-T\Delta S$ values seen with the shorter stem aptamers this is consistent with more folding occurring with ligand binding for both the dopamine aptamers here and the previously obtained cocaine binding aptamers data.[94,95]

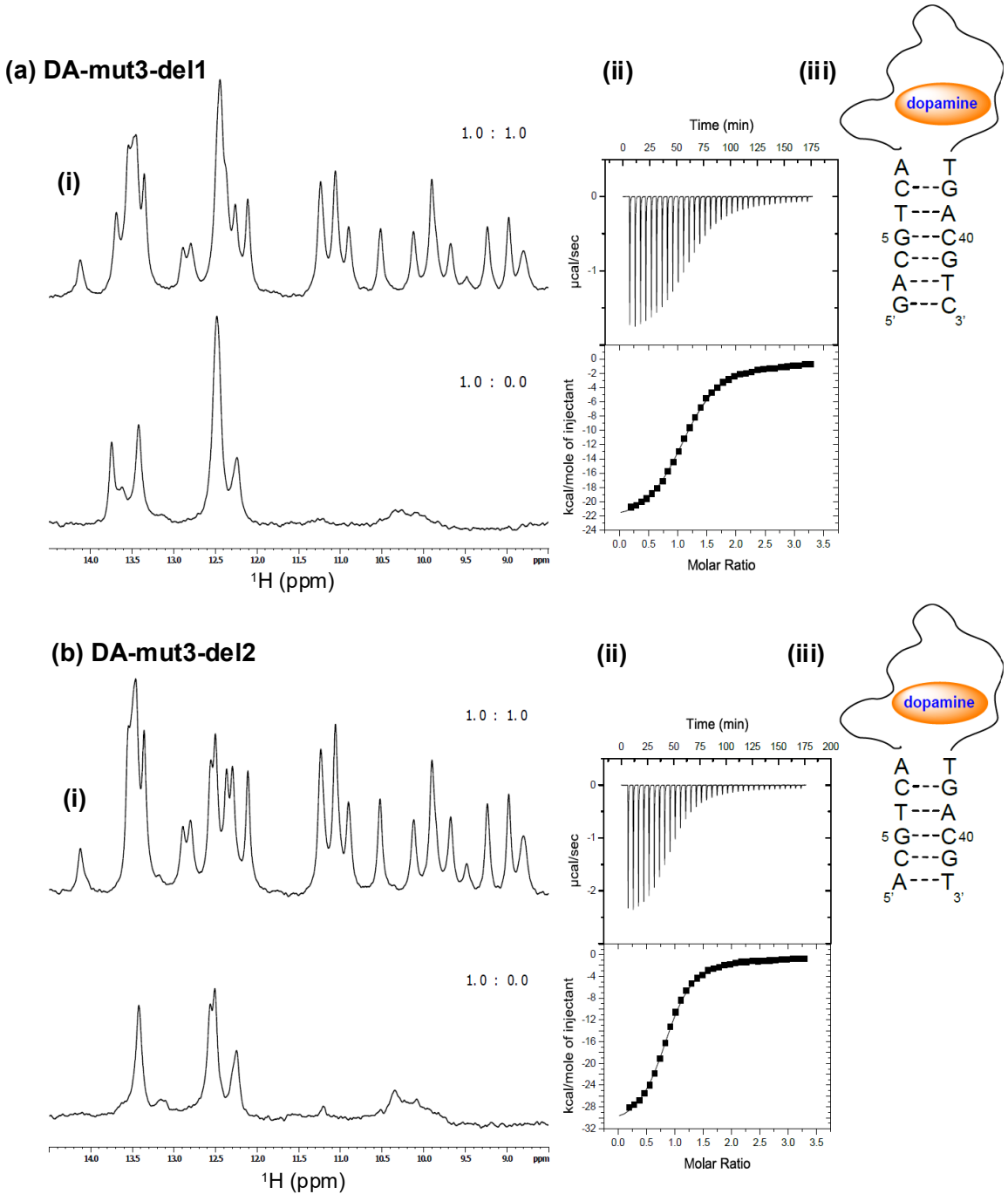
(a) DA-mut3-del1
(i)
1.0 : 1.0
1.0 : 0.0
14.0 13.5 13.0 12.5 12.0 11.5 11.0 10.5 10.0 9.5 9.0 ppm
¹H (ppm)
(ii)
Time (min)
0 25 50 75 100 125 150 175
µcal/sec
kcal/mole of injectant
0.0 0.5 1.0 1.5 2.0 2.5 3.0 3.5
Molar Ratio
(iii)
dopamine
A T
C---G
T---A
5 G---C 40
C---G
A---T
G---C
5' 3'
(b) DA-mut3-del2
(i)
1.0 : 1.0
1.0 : 0.0
14.0 13.5 13.0 12.5 12.0 11.5 11.0 10.5 10.0 9.5 9.0 ppm
¹H (ppm)
(ii)
Time (min)
0 25 50 75 100 125 150 175 200
µcal/sec
kcal/mole of injectant
0.0 0.5 1.0 1.5 2.0 2.5 3.0 3.5
Molar Ratio
(iii)
dopamine
A T
C---G
T---A
5 G---C 40
C---G
A---T
5' 3'

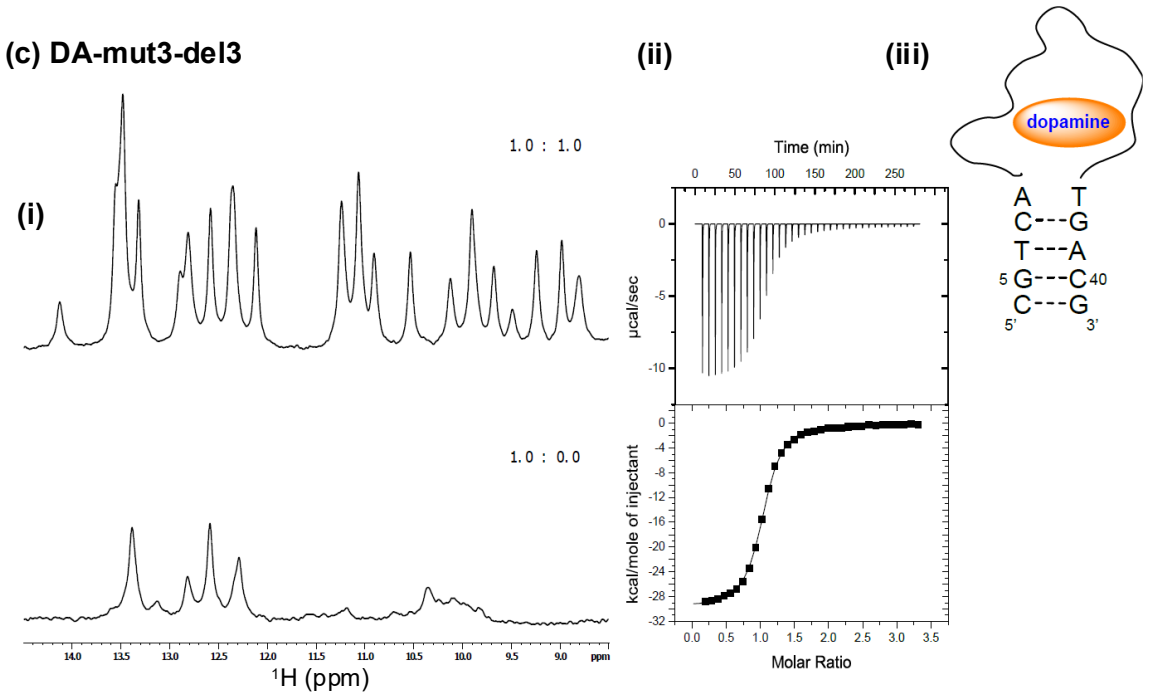
(c) DA-mut3-del3
(i)
1.0 : 1.0
1.0 : 0.0
14.0 13.5 13.0 12.5 12.0 11.5 11.0 10.5 10.0 9.5 9.0 ppm
¹H (ppm)
(ii)
Time (min)
0 50 100 150 200 250
µcal/sec
0 -5 -10
kcal/mole of injectant
0 -4 -8 -12 -16 -20 -24 -28 -32
0.0 0.5 1.0 1.5 2.0 2.5 3.0 3.5
Molar Ratio
(iii)
dopamine
A T
C---G
T---A
5 G---C 40
C---G
5' 3'

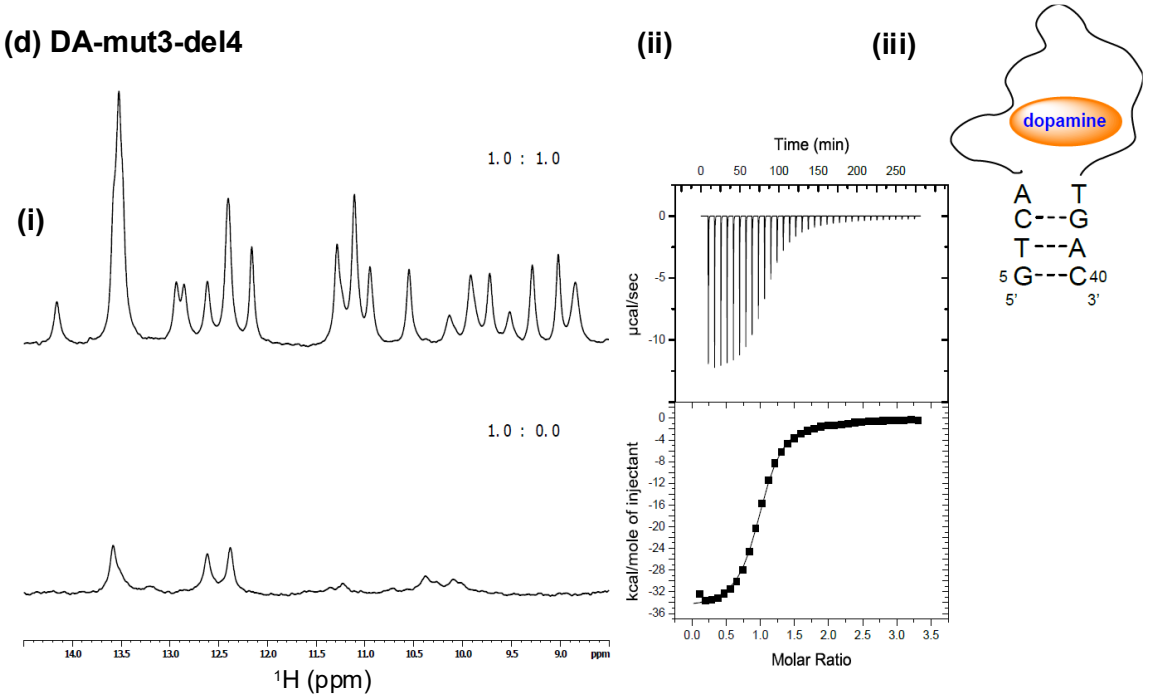
(d) DA-mut3-del4
(i)
1.0 : 1.0
1.0 : 0.0
14.0 13.5 13.0 12.5 12.0 11.5 11.0 10.5 10.0 9.5 9.0 ppm
¹H (ppm)
(ii)
Time (min)
0 50 100 150 200 250
µcal/sec
0 -5 -10
kcal/mole of injectant
0 -4 -8 -12 -16 -20 -24 -28 -32 -36
0.0 0.5 1.0 1.5 2.0 2.5 3.0 3.5
Molar Ratio
(iii)
dopamine
A T
C---G
T---A
5 G---C 40
5' 3'

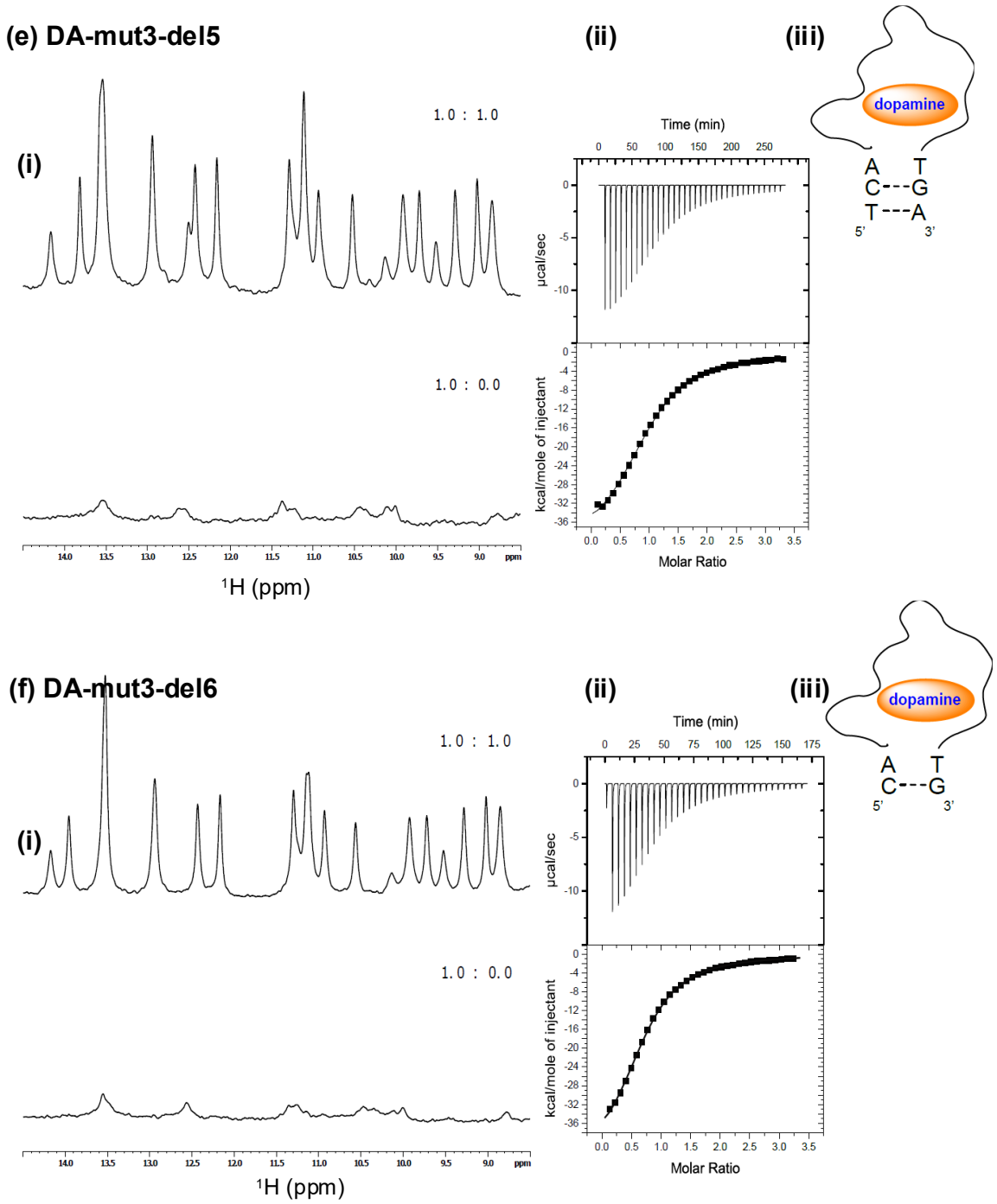

Figure 2.4.4.1. Dopamine binding by various truncations of the DA-mut3 aptamer (a-f). In each (i) binding is monitored by one-dimensional ^{1}H NMR. The imino proton region is shown along with molar ratios of aptamer to dopamine. Experiments were conducted at 5°C with 500 µM DNA aptamer sample in 20 mM sodium phosphate, 140 mM NaCl, 2 mM $MgCl_2$, pH 7.4 with 10% ^2H_2O. (ii) ITC binding thermograms representing the interactions between the truncated DA-mut3 aptamer and dopamine. The top of each thermogram is the raw titration data showing the heat resulting from each injection of ligand into an aptamer solution. The bottom shows the integrated heat plot after correcting for the heat of dilution. ITC data were acquired at 20°C in the same buffer conditions as with NMR experiments with an aptamer concentration of 20 µM and ligand concentration of 0.312 mM. (iii) Secondary structure diagrams of the various truncations of the DA-mut3 aptamer.

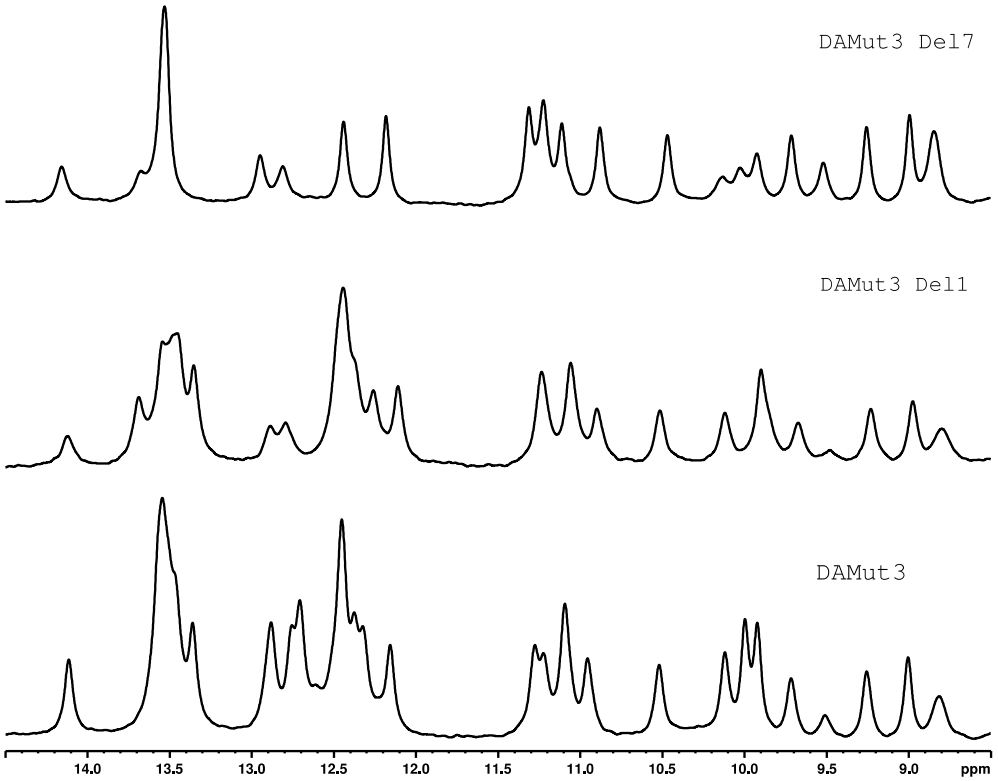

Figure 2.4.4.2. The ^{1}H NMR spectra of the DA-mut3, DA-mut3-del1, and DA-mut3-del7 constructs. The spectral width is focused on the imino region comparing the dopamine-bound states of each of these aptamers. The three aptamers appear to share many peaks in common indicating that they likely are forming the same structure in the bound state.

CD spectroscopy was used to assess the structures of the free and bound DA-mut3 and DA-mut3-del7 dopamine aptamers (Figure 2.4.4.3). Upon ligand binding, CD spectra of DA-mut3 demonstrates a large change in CD peak position from a maximum at 280 nm to a maximum at 265 nm. These spectra are consistent with the CD spectra of the free and unbound dopamine aptamer reported by Nakatsuka et al. demonstrating that the structures are similar.[46] For the DA-mut3-del7 construct, the free aptamer has a broad positive peak centered at 275 nm (Figure 2.4.4.3) and changes with dopamine binding to having a CD peak at 265 nm. The similarity of the CD signal for both the dopamine-bound DA-mut3-del7 and DA-mut3 constructs indicates a similarity in the structures of the two ligand-bound constructs.

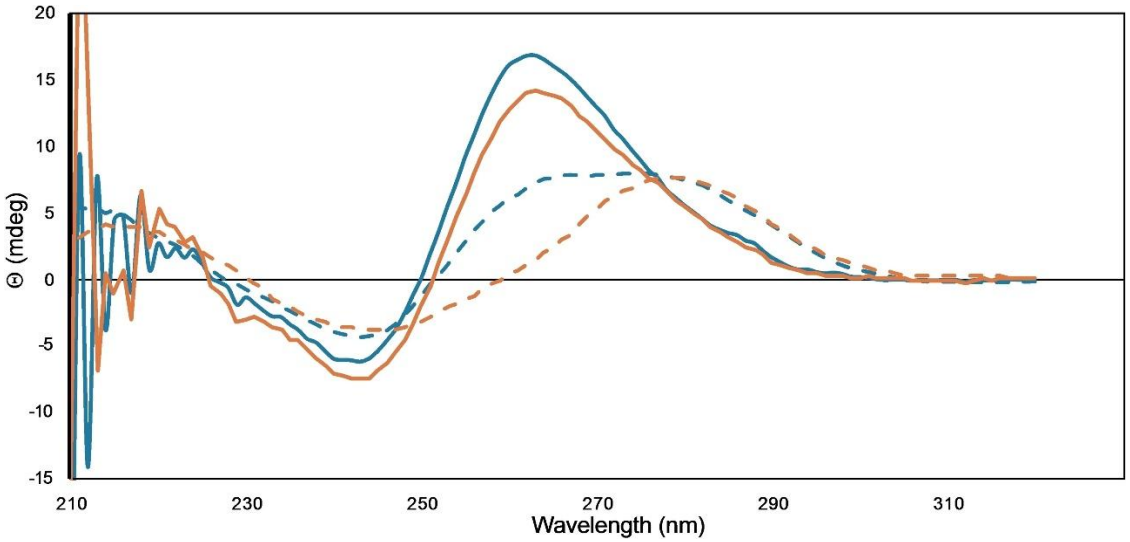

Figure 2.4.4.3. CD spectra of DA-mut3 (Orange) and DA-mut3-del7 (Blue) both free (dashed lines) and dopamine-bound (solid lines). Ellipticity is baseline corrected. Experiments were performed with an aptamer concentration of 100 µM in 20 mM sodium phosphate, 140 mM NaCl, 2 mM $MgCl_2$, pH 7.4 and without or with 4x molar-equivalences of dopamine.

2.4.5 E-AB Sensor with Long (DA-mut3-del2) and Short Aptamer (DA-mut3-del6)

The following section was completed by collaborators Minh-Dat Nguyen and Philippe Dauphin-Ducharme from the University of Sherbrooke. The DA-mut3-del6 truncated variant of the dopamine aptamer produced a functional electrochemical aptamer-based (E-AB) biosensor. This was assessed by adapting a variant of the dopamine aptamer possessing a longer or shorter stem (DA-mut3-del2 and DA-mut3-del6) into the E-AB sensing platform. The DA-mut3-del2 construct was chosen as its affinity for dopamine is slightly higher than for DA-mut3-del1. The DA-mut3-del6 construct was chosen as it is the construct with the shortest stem before affinity for dopamine is significantly reduced in DA-mut3-del7. Adaptation of the variants involved functionalizing their 3' and 5' extremities with a methylene blue redox reporter and a thiol anchor so that they can be interrogated electrochemically and attached to a monolayer-coated gold electrode, respectively (Table 2.4.5.1)

Table 2.4.5.1. DNA sequences used for the fabrication of E-AB sensors

Sequence name	5' modification	Sequence (5' to 3')	3' modification
DA-mut3-del2	HO-$(CH_2)_6$-S-S-$(CH_2)_6$-O-	ACG TCA GTT TGA AGG TTC GTT CGC AGG TGT GGA GTG ACG T	-O-$(CH_2)_6$-NH-CO-$(CH_2)_2$-MB
DA-mut3-del6		CAG TTT GAA GGT TCG TTC GCA GGT GTG GAG TG	

The change in electron transfer of the redox reporter as a result of ligand addition[96] was monitored using an electrochemical impedance spectroscopy methodology (Figure 2.4.5.1)[97,98] Briefly, this involved acquiring a potentiostatic impedimetric trace when polarizing electrodes at the potential of the redox reporter that are then fitted to a known equivalent circuit comprised of four elements (solution resistance (R_{sol}), electrical double-layer formation (C_{int}), charge transfer resistance (R_{CT}) and the redox reporter pseudo-capacitance (C_{DNA})).[99] The measured charge transfer resistance was extracted and the acquisition was repeated at increasing dopamine concentrations to obtain a binding trace from which a K_d value was derived. The results indicate that the DA-mut3-del2 variant presented negligible changes in charge transfer resistance over the entire range of dopamine concentrations we used.

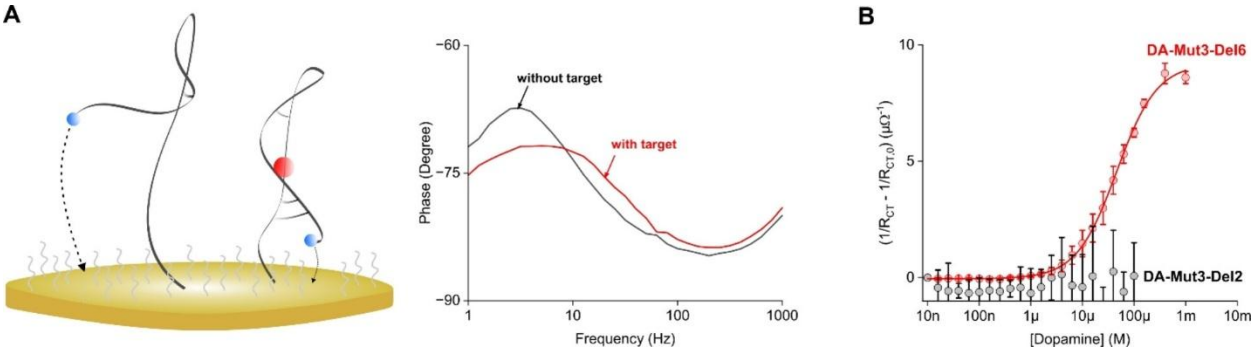

Figure 2.4.5.1. (A) Electrochemical aptamer-based biosensors are comprised of a redox-reporter-modified aptamer that is covalently attached to a gold electrode coated with a self-assembled monolayer. Target binding alters the electron transfer rate from the redox reporter to the electrode surface, which can be easily monitored by a shift in measured phase. (B) When challenged with increasing amounts of dopamine and interrogated using electrochemical impedance, we quantified changes in charge-transfer resistance (R_{CT}). We observed that the DA-mut3-del6 variant produced a target-dependent response with a K_d value of 46±2 μM in contrast to the DA-mut3-del2 variant which exhibited a negligible response. All measurements were done in 1X PBS buffer spiked with 2 mM $MgCl_2$ and 0.02 % ascorbic acid to prevent dopamine oxidation. Error bars represent the standard deviation of signals produced by at least three sensors that were independently fabricated and tested.

In contrast, the truncated variant DA-mut3-del6 showed a concentration-dependent signal to dopamine with a K_d value of (46±2) μM (Figure 2.4.5.1b). The observation of a target-dependent signal for the latter variant was attributed to the conformational destabilization brought by base truncations. This destabilization results in significantly larger differences in electron transfer rate in the unbound configuration according to observations of a shift in measured phase (Figure 2.4.5.1 and Figure 2.4.5.2).[100]

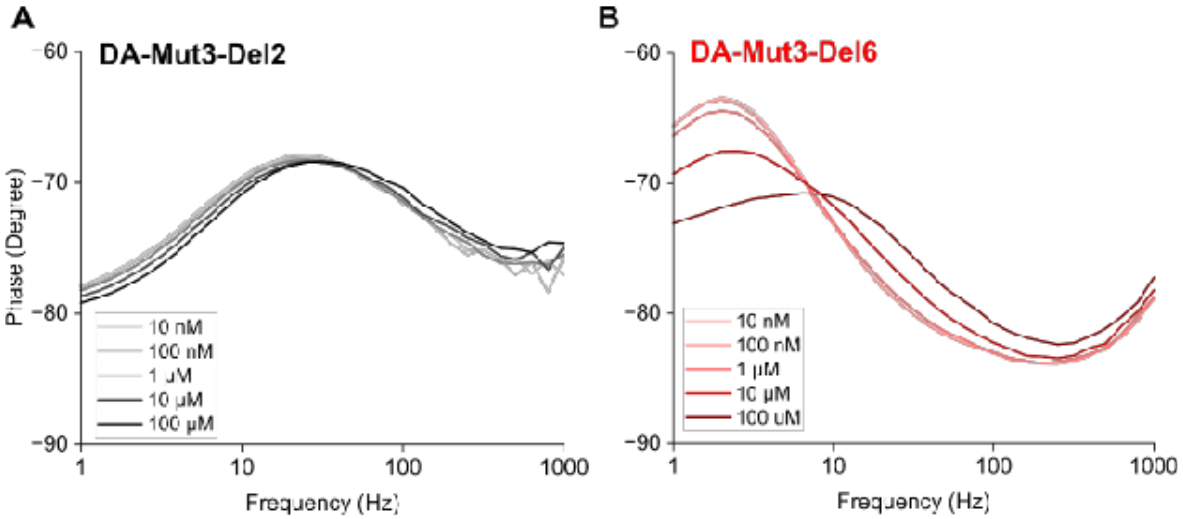

Figure 2.4.5.2. Phase change of (A) DA-mut3-del2 and (B) DA-mut3-del6 aptamers when exposed to increasing amounts of dopamine. The DA-mut3-del2 displayed minimal shift in phase in the presence of increasing dopamine concentrations, suggesting no structure switching while, in contrast, the shortened DA-mut3-del6 variant demonstrated significant changes in measured phase upon dopamine addition. It was presumed that this is in part because the shortened aptamer is more unstructured and that the ligand binding site is closer to the electrode surface, enabling improved sensor response.

The difference in K_d values (17.8 µM vs 46 µM) observed for DA-mut3-del6 binding dopamine using ITC and EIS methods, was attributed to differences arising from the solution method (ITC) versus a surface-based method (EIS). The results further corroborate the NMR evidence that the dopamine binding site appears to be located in the upper section of the aptamer and that removing 6 base pairs from the stem of the sequence does not prohibit binding.

2.5 Work Following

Since publishing this work, the DA-mut3-del7 construct has been further modified by removing three additional bases from the 5' end into a new variant referred to as the RKEC1. This variant had an improved binding affinity of about 4 µM. The improved affinity was attributed to an auto-inhibitory effect from the 5' overhang and by removing three bases from this terminus, the binding pocket was much more accessible by the dopamine ligand, improving the overall affinity. A shorter functioning sequence with an improved binding affinity made this construct an excellent candidate for further structural characterization. Working with Dr. Cameron D. Mackereth and Eric Largy, a full three-dimensional structure was determined for this construct using NMR.[101] The RKEC1 variant was determined to form a compact structure upon

ligand binding that lacks any Watson-Crick duplex region or G-quadruplex in contrast to the predicted secondary structure and previous CD studies.[46] Atomic details explained dopamine specificity against similarly structured analogues. Collaborators Minh-Dat Nguyen and Philippe Dauphin-Ducharme were able to design a functioning biosensor using a structure-guided approach where previous attempts with this sequence had failed. The aptamer structure had further suggested that DNA folding can access an extensive conformational landscape resembling RNA and thus expanding the diversity traditionally captured by predictive algorithms.

The solved three-dimensional structure was then submitted as target D1273 to the 16th Critical Assessment of Techniques for Protein Structure Prediction (CASP16). This provided a blind test of whether its three-dimensional architecture could be recovered computationally. Despite the small size of RKEC1 at only 27 nucleotides, 107 structural models were submitted by 22 groups, none of whom achieved an RMSD below 10 Å relative to the experimentally determined structure. The RMSD values ranged from 10.16 to 27.79 Å. The difficulty primarily arose from the highly unconventional architecture of RKEC1, which only contains two non-adjacent canonical Watson-Crick base pairs and instead relies extensively on noncanonical base pairing and higher-order tertiary interactions.[102] These results reinforce the conclusions of this chapter by demonstrating that sequence-based and computational models can provide useful hypothesis but may fail to capture the tertiary interactions responsible for functional aptamer folds. Experimental structural characterization therefore remains essential, particularly for synthetic DNA aptamers that occupy regions of structural space poorly represented by existing structural databases.

2.6 Conclusions

In this study, we analysed the affinity and binding thermodynamics of a series of dopamine aptamers where the terminal stem was progressively shortened. We observed a trend where the dopamine binding affinity becomes weaker as the stem is shortened. We also observed that as the terminal stem is shortened the binding enthalpy becomes more negative and binding more entropically unfavourable. These trends were previously seen for the cocaine binding aptamer and may hold for other small molecule binding

aptamers selected using capture SELEX. From the appearance of numerous new signals in the ^{1}H NMR spectra of the imino regions of each of the aptamers studied, a large amount of new structure forms with ligand binding. This observation differs from what was seen previously in other aptamers, such as the cocaine-binding aptamer, where a stem in the aptamer needs to be shortened in order to induce a ligand-induced structure switching binding mechanism.[84] A ligand-induced structure formation binding mechanism, similar to what we see here with the dopamine aptamer, was seen previously in the glucose binding aptamer[98] and is likely to be observed with other aptamers selected using capture SELEX methods. Despite the DA-mut3 dopamine aptamer, with a 7 base pair terminal stem, undergoing ligand-induced folding, only when the folding region of the aptamer is brought close to the sensor surface does the aptamer produce a functional E-AB biosensor. Proximity of the region of the aptamer undergoing structure switching to the sensor surface appears to be an important factor for designing a functional E-AB sensor.

Chapter 3 Ligand-Induced Destabilization of the MN4 Cocaine-Binding Aptamer by Local Anesthetics

- Contributions for section 3.3.1 was made by Y. A. Kaiyum.

3.1 Introduction

Aptamers are short, single-stranded DNA or RNA oligonucleotides that can fold into defined three-dimensional structures capable of recognizing molecular targets with high affinity and often with high specificity. The breadth of targets that aptamers have been selected for includes small molecules, nucleotides, cofactors, amino acids, peptides, polysaccharides, proteins, whole cells, viruses and single-celled organisms.[103–109] The process by which new aptamers are selected is referred to as SELEX (Systematic Evolution of Ligands by EXponential enrichment).[5,6] Aptamers are characterized by their ability to bind to targets with high affinity and high specificity, However, despite their widespread use, the molecular principles governing aptamer–ligand recognition remain incompletely understood, particularly for small-molecule targets where binding often depends on slight differences in ligand size, shape, charge distribution, aromaticity, and conformational flexibility.

There have been significant efforts made to explore the mechanisms that facilitate aptamer-target specificity and affinity. Investigating the thermodynamics of interactions between aptamers and their targets is a common way to further our understanding of the energetics that drive these interactions. The binding of a ligand to an aptamer is governed by the free energy of complex formation, where the observed binding affinity (K_d) is reflected in the balance between enthalpic (ΔH) and entropic (ΔS) contributions. Formation of hydrogen bonds, electrostatic interactions, π-π stacking, cation-π interactions, van der Waals contacts, metal-ion-mediated interactions and ligand-induced stabilization of base-pairing or tertiary contacts can all contribute to a more favourable binding enthalpy.[84,110] Entropic penalties are associated with loss of conformational freedom of both the aptamer and the ligand as well as ordering of solvent molecules.[84,110,111] As a result, aptamer binding affinity cannot be interpreted from the number or strength of molecular contacts and instead it reflects the net compensation between favourable enthalpy and unfavourable entropy.

Isothermal titration calorimetry (ITC) has been particularly valuable for investigating aptamer-ligand interactions as it directly provides binding affinity, stoichiometry, enthalpy, entropy and free energy in solution without the need for immobilization or labeling.[112] Recent large-scale analysis of small-molecule-binding DNA aptamers has shown that aptamer–ligand recognition is largely enthalpy-driven, with favourable enthalpic contributions frequently accompanied by unfavourable entropy changes.[110] Notably, this work also demonstrated that binding affinity and specificity are not directly interchangeable such that a high-affinity aptamer is not necessarily highly selective, and broad ligand cross-reactivity may arise when an aptamer recognizes shared physicochemical features rather than a unique molecular structure. This is consistent with the idea that aptamers must form unique three-dimensional structures to bind their targets, which largely constrain the degrees of freedom for the aptamer, resulting in a large entropy penalty.

Several well-studied aptamer systems illustrate how thermodynamics can reveal the molecular basis of target recognition. In the cocaine-binding aptamer, NMR and calorimetric studies demonstrated that binding depends strongly on aptamer secondary structure and stem stability, showing that the surrounding nucleic acid scaffold contributes directly to ligand affinity.[84,113] Additional studies further revealed that the cocaine-binding aptamer can bind off-target ligands such as quinine with substantially higher affinity than cocaine, highlighting the distinction between selection target, binding affinity, and molecular specificity.[114] Structure–affinity studies with quinine derivatives further support the idea that small changes in ligand structure can significantly alter binding affinity and recognition by the cocaine-binding aptamer.[115] Together, these studies demonstrate that small-molecule aptamers can display unexpected ligand preferences and that thermodynamic measurements are essential for identifying whether binding is driven by target-specific recognition or by broader compatibility between ligand chemical features and the aptamer binding pocket.

Although aptamer–ligand binding is frequently associated with ligand-induced folding or stabilization, ligand association does not necessarily require global stabilization of the aptamer structure. Binding can remain thermodynamically favourable even when ligand addition decreases the apparent thermal stability of the aptamer, provided that favourable local interactions within the binding site

compensate for the energetic cost of disrupting pre-existing secondary or tertiary contacts. In this scenario, ligand binding may involve hydrogen bonding, electrostatic interactions, aromatic stacking, or hydrophobic association while simultaneously weakening base-pairing, altering tertiary packing, or shifting the aptamer conformational ensemble. This distinction is important because the free energy of binding reflects the net energetic balance of ligand association, desolvation, conformational rearrangement, and structural perturbation, whereas thermal stability measurements report on the stability of the folded nucleic acid ensemble. Studies of small-molecule aptamers have shown that ligand binding can involve heterogeneous conformational populations, adaptive binding, and population-shift mechanisms rather than simple rigid-body stabilization.[116,117] Therefore, ligand-induced destabilization should not be interpreted as evidence against binding; rather, it may indicate that ligand association is coupled to structural remodeling, partial unfolding, conformational redistribution, or disruption of stabilizing aptamer interactions. However, destabilizing aptamer–target interactions remain less commonly described than classical ligand-induced stabilization mechanisms. To address this gap, we used ITC, DSC, and NMR to investigate the interactions between the cocaine-binding aptamer variants MN4 and MN19 with a series of local anesthetics (Figure 3.1.1), with the goal of defining how ligand binding influences aptamer thermodynamics, thermal stability, and structural organization.

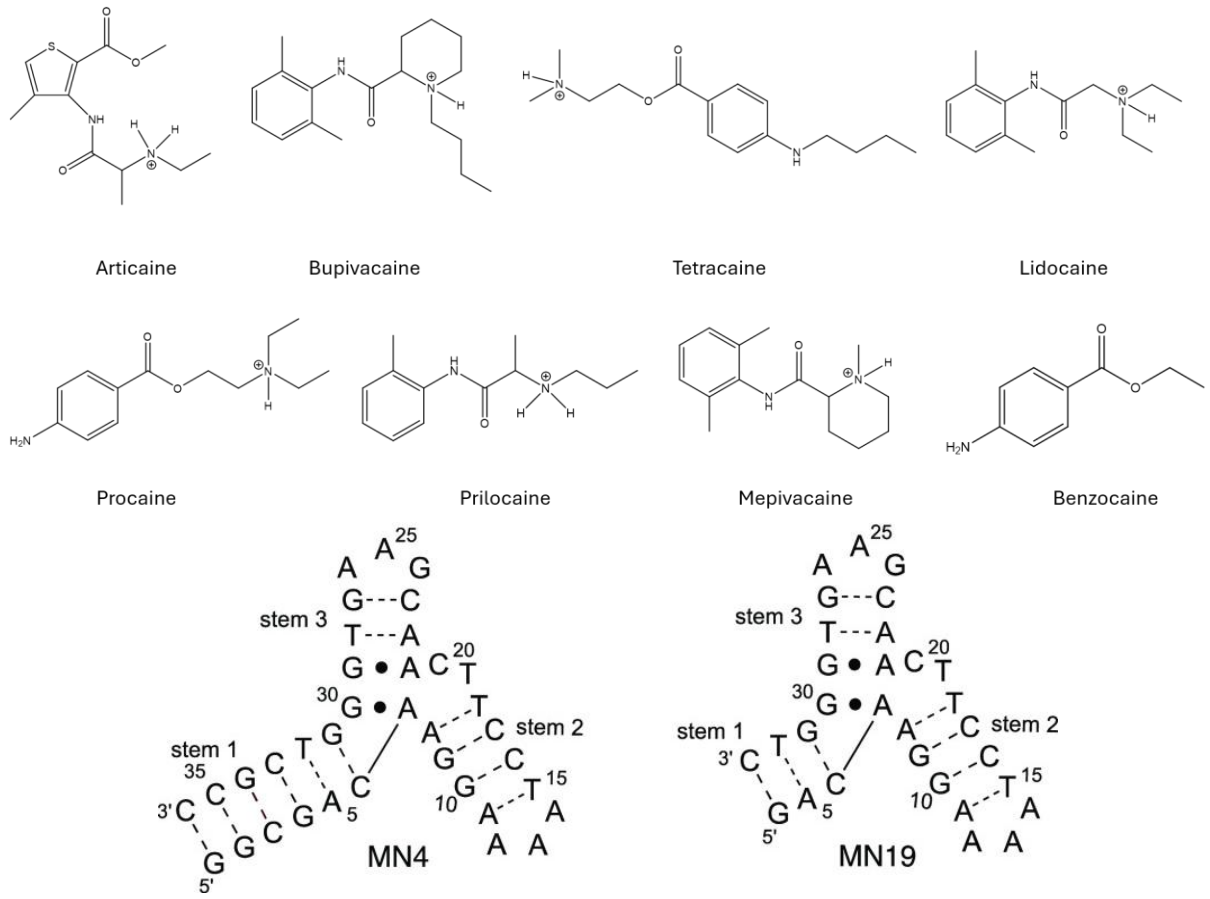

Figure 3.1.1. Chemical structures of the ligands investigated in this study—articaine, bupivacaine, tetracaine, lidocaine, procaine, prilocaine, mepivacaine, and benzocaine—alongside the predicted secondary structure of the MN4 aptamer and the MN19 aptamer. The MN4 aptamer adopts a pre-folded three-way junction consisting of stems 1–3, with nucleotide positions indicated throughout the sequence. The MN19 aptamer folds with ligand-binding.

3.2 Materials and Methods

3.2.1 Materials

All DNA samples were purchased from the Integrated DNA Technologies (Coralville, IA, USA). Quinine hemisulfate monohydrate (Catalog Number - 22640), tetracaine hydrochloride (Catalog Number – T7508), benzocaine (Catalog Number – E1501), bupivacaine hydrochloride monohydrate (Catalog Number – B5274), prilocaine hydrochloride (Catalog Number - P9547), articaine hydrochloride (Catalog Number – SML1093), mepivacaine hydrochloride (Catalog Number – PHR1955) and lidocaine hydrochloride monohydrate (Catalog Number – L5647) were purchased from Sigma Aldrich. Procaine hydrochloride (Catalog Number – A1163) was purchased from TCI America. Buffer (Buffer A hereafter) was prepared

as a 10 mM mixture of sodium phosphate monobasic and sodium phosphate dibasic adjusted to a pH of 7.4 and 150 mM sodium chloride. All solutions were prepared in Milli-Q water. The concentrations of the aptamers were determined by measuring the OD_{260} in a UV-Vis spectrometer using extinction coefficients provided by IDT.

3.2.2 Isothermal Titration Calorimetry

Isothermal titration calorimetry (ITC) data were collected using an Affinity ITC instrument (TA Instruments Inc., New Castle, DE). Prior to analysis, all samples were degassed using a MicroCal ThermoVac system. Titration experiments were conducted with DNA loaded in the sample cell and the ligand (cocaine derivatives) in the injection syringe. DNA samples were pre-treated by heating at 95 °C for 1 min, followed by rapid cooling in an ice bath for 5 min before binding measurements. DNA solutions were prepared at concentrations of 20 μM or 100 μM. Both DNA and ligand solutions were prepared in buffer A. Experiments consisted of 20 sequential injections, each delivering 2 μL of ligand solution (0.312 mM or 1.56 mM) into the sample cell at 150 s intervals, with continuous stirring at 125 rpm and a constant temperature of 20 °C. Data were analysed using NanoAnalyze software. The heat of dilution was subtracted from the raw data, and the corrected thermograms were fitted to a single-site binding model. The fitted parameters were then used to determine the binding stoichiometry (n), dissociation constant (K_d), and enthalpy change (ΔH).

3.2.3 Nuclear Magnetic Resonance Spectroscopy

NMR experiments on DNA aptamer samples were performed using a 600 MHz Bruker DRX Avance spectrometer in a manner similar to what we have previously described.[72] Prior to performing NMR experiments, samples were heated in a 90°C water bath for 3 minutes and then fast-cooled to room temperature to favour intramolecular folding. All NMR spectra were conducted with an aptamer concentration of 0.5 mM in an aqueous solution of buffer A and 10% D_2O. Ligands were dissolved in the same buffer and titrated into the aptamers to a final molar ratio of 1:5 aptamer to ligand. Water suppression was achieved using excitation sculpting.[90]

3.2.4 Differential Scanning Calorimetry

DSC thermal stability experiments were performed using a Nano DSC from TA Instruments and associated software to run all measurements. Samples of free aptamer and the aptamer-ligand complexes were prepared in buffer A. The temperature range for the DSC scans was set from 10 °C to 90 °C, with a heating rate of 1 °C min^{-1} to accurately capture the melting transitions. Ten consecutive heating–cooling runs were performed for each sample. Baseline corrections were applied using buffer-buffer scans.

3.3 Results

3.3.1 NMR Studies of Ligand Binding by MN4 and MN19

NMR spectroscopy was first used to investigate how binding of local anesthetic ligands affects the structure of the MN4 aptamer. Because NMR provides a direct solution-state readout of aptamer structure, it is well suited for identifying ligand-induced changes in the imino proton region, where resonances report on hydrogen-bonded base pairs, non-canonical interactions, and overall structural organization. By comparing the free MN4 spectrum with spectra collected in the presence of each local anesthetic, NMR allowed the structural response of MN4 to be assessed for each ligand and provided insight into whether these compounds promote similar or distinct aptamer conformations.

MN19 was also examined by NMR to determine whether the anesthetics are able to induce similar structure formation in a variant that does not have a pre-folded free state. This comparison provided an additional means of assessing whether local anesthetic binding produced similar perturbations in a structurally related aptamer or whether MN4 displayed a distinct ligand-dependent response. Together, the MN4 and MN19 NMR experiments helped establish how local anesthetic binding influences the imino proton fingerprints of cocaine-binding aptamer variants.

In particular, the imino proton region of the one-dimensional ^{1}H-NMR spectrum is highly sensitive to changes in nucleic acid base-pairing and secondary structure. Well-resolved imino resonances are typically associated with protected Watson–Crick or noncanonical base pairs, whereas peak broadening, disappearance, or chemical shift perturbations can indicate changes in hydrogen bonding, exchange

dynamics, or conformational heterogeneity. Therefore, comparison of the free MN4 spectrum with spectra collected in the presence of each local anesthetic provides insight into whether ligand binding preserves the preformed aptamer structure, induces localized structural changes, or disrupts stabilizing base-pairing interactions.

The titration of benzocaine into MN4 is shown in Figure 3.3.1.1. The bottom spectrum represents free MN4 in the absence of benzocaine and contains resonances in the imino proton region, including peaks typically associated with Watson–Crick base pairs (~13–15 ppm) as well as more upfield resonances commonly associated with non-Watson–Crick or less protected imino protons (~9–13 ppm). Assignment of peaks were previously made by Churcher et al. in 2020.[118] This spectrum is consistent with previously reported NMR data for free MN4, which indicates that the aptamer adopts a preformed structure with a characteristic resonance at 12.2 ppm assigned to G31.[114] Upon addition of benzocaine, the resonances at 13.5 and 12.2 ppm decrease in intensity and undergo line broadening. As the benzocaine concentration increases, new resonances appear at approximately 13.4 and 12.0 ppm, consistent with slow exchange between the free and benzocaine-bound states on the NMR chemical shift timescale. The shift of the G31 resonance from 12.2 to 12.0 ppm is similar to that previously observed upon quinine binding to MN4.[114] These new resonances continue to increase in intensity with additional benzocaine and reach saturation at higher ligand concentrations. The emergence of sharp, well-resolved resonances in the saturated MN4–benzocaine spectrum suggests that benzocaine binding promotes a specific, structured aptamer conformation.

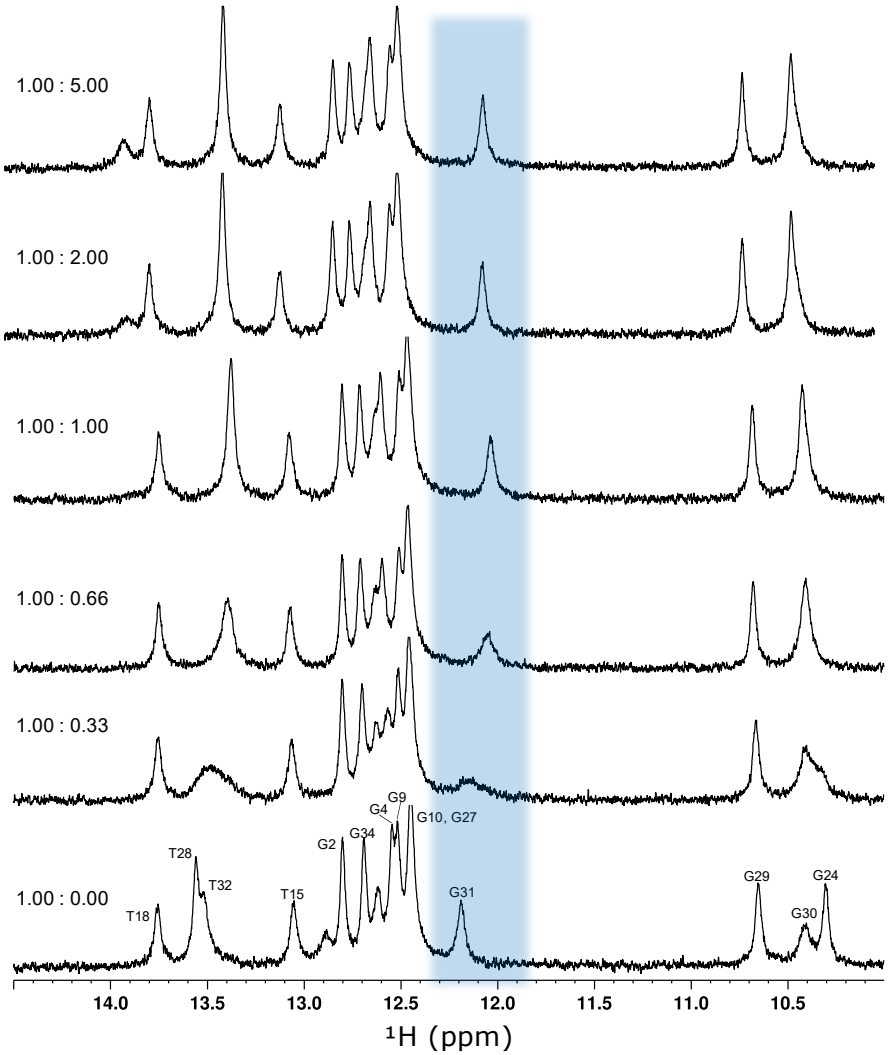

Figure 3.3.1.1. 1H-NMR spectra showing the imino proton resonances during a titration of MN4 with benzocaine. The numbers on the left-hand side of the spectrum indicate the molar ratio of MN4 to benzocaine. The G31 imino resonance shift is highlighted in blue. Experiments were conducted with an MN4 concentration of 0.5 mM in 10 mM NaHPO4, 150 mM NaCl, pH 7.4, 90% $^{1}H_2O$-10% $^{2}H_2O$ at 5 °C.

The titration of tetracaine into MN4 is shown in Figure 3.3.1.2 and reveals ligand-induced spectral changes that are broadly similar to those observed for benzocaine. Upon addition of tetracaine, new imino resonances appear while resonances corresponding to free MN4 decrease in intensity and broaden, indicating that tetracaine binding perturbs the preformed MN4 structure. The coexistence of free- and bound-state resonances at early titration points is consistent with slow exchange on the NMR chemical shift timescale. As the tetracaine concentration is increased, the free-state resonances continue to decrease in intensity until saturation, while the bound-state resonances become more prominent.

Similar to the MN4–benzocaine and MN4–quinine complexes, tetracaine binding produces a shift in the characteristic G31 resonance from approximately 12.2 ppm to a more upfield position. This recurring G31 chemical shift perturbation suggests that benzocaine, tetracaine, and quinine affect a similar region of the MN4 structure or induce a related local rearrangement near this residue. However, the saturated MN4–tetracaine spectrum is not identical to the spectra of the MN4–benzocaine or MN4–quinine complexes. In particular, the MN4–tetracaine complex contains more resonances in the region typically associated with Watson–Crick imino protons, suggesting differences in the base-pairing environment or hydrogen-bond protection of the bound-state structure. Therefore, while tetracaine appears to induce some structural features that are shared with other MN4-binding ligands, the final MN4–tetracaine complex likely represents a distinct ligand-bound conformation.

The appearance of sharp, well-resolved imino resonances in the saturated MN4–tetracaine spectrum suggests that tetracaine binding promotes or stabilizes a discrete, structured aptamer state. However, the differences between the tetracaine-, benzocaine-, and quinine-bound spectra indicate that these ligands do not generate identical MN4 conformations, despite sharing common spectral features such as the G31 resonance shift.

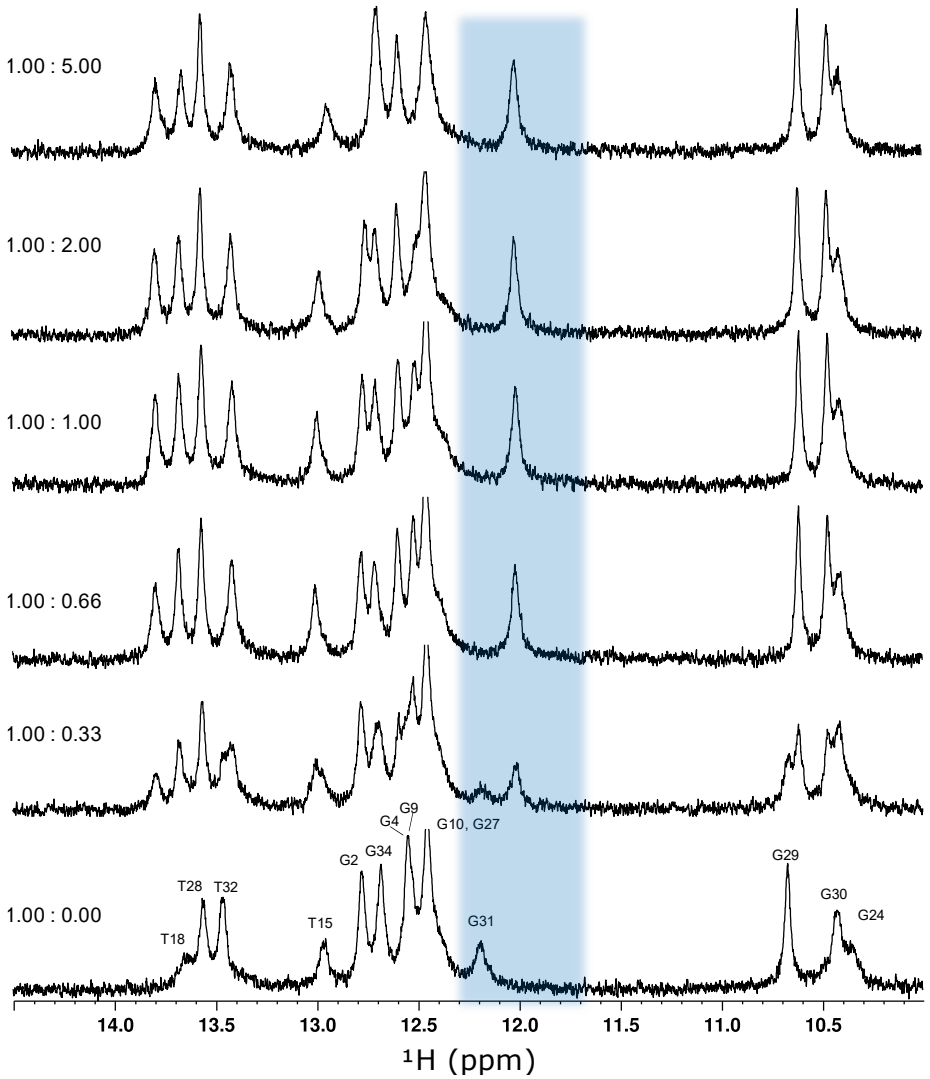

Figure 3.3.1.2. ^{1}H-NMR spectra showing the imino proton resonances during a titration of MN4 with tetracaine. The numbers on the left-hand side of the spectrum indicate the molar ratio of MN4 to tetracaine. The G31 imino resonance shift is highlighted in blue. Experiments were conducted with an MN4 concentration of 0.5 mM in 10 mM $NaHPO_4$, 150 mM NaCl, pH 7.4, 90% $^{1}H_2O$-10% $^{2}H_2O$ at 5 °C.

In addition to benzocaine and tetracaine, the remaining local anesthetics—procaine, mepivacaine, bupivacaine, articaine, lidocaine, and prilocaine—were also investigated by ^{1}H-NMR spectroscopy to assess whether they induce similar structural changes in MN4 (Figure 3.3.1.3-3.3.1.8). In each case, ligand titration produced observable changes in the imino proton region, indicating that all six ligands interact with MN4 and perturb the free structure. A common feature across the ligand series was the shift of the characteristic G31 resonance from its position in free MN4, suggesting that each ligand affects a similar region of the aptamer or induces a related local rearrangement within the MN4 binding pocket. This

recurring spectral change is consistent with the ITC data showing measurable binding for all ligands and supports the conclusion that these local anesthetics do not simply interact non-specifically with the exterior of the aptamer, but instead influence structural elements associated with the folded state of MN4.

Although the G31 resonance shift was observed across the ligand series, the final spectra of the different MN4–ligand complexes were not identical. Differences in peak number, chemical shifts, and resonance intensity suggest that each ligand promotes a related but distinct bound-state conformation. Importantly, the final titration spectra retained or generated sharp, well-resolved imino resonances, indicating the presence of protected base-paired regions and suggesting that ligand binding promotes formation of specific structured MN4 complexes. These NMR results therefore complement the ITC and DSC data by showing that, despite the ligand-induced decrease in apparent thermal stability observed by DSC, the local anesthetics still induce defined structural changes upon binding. Taken together, the data support a model in which local anesthetic binding to MN4 is coupled to structural remodeling rather than complete unfolding, with each ligand stabilizing a specific bound-state ensemble while simultaneously reducing the global thermal stability of the aptamer.

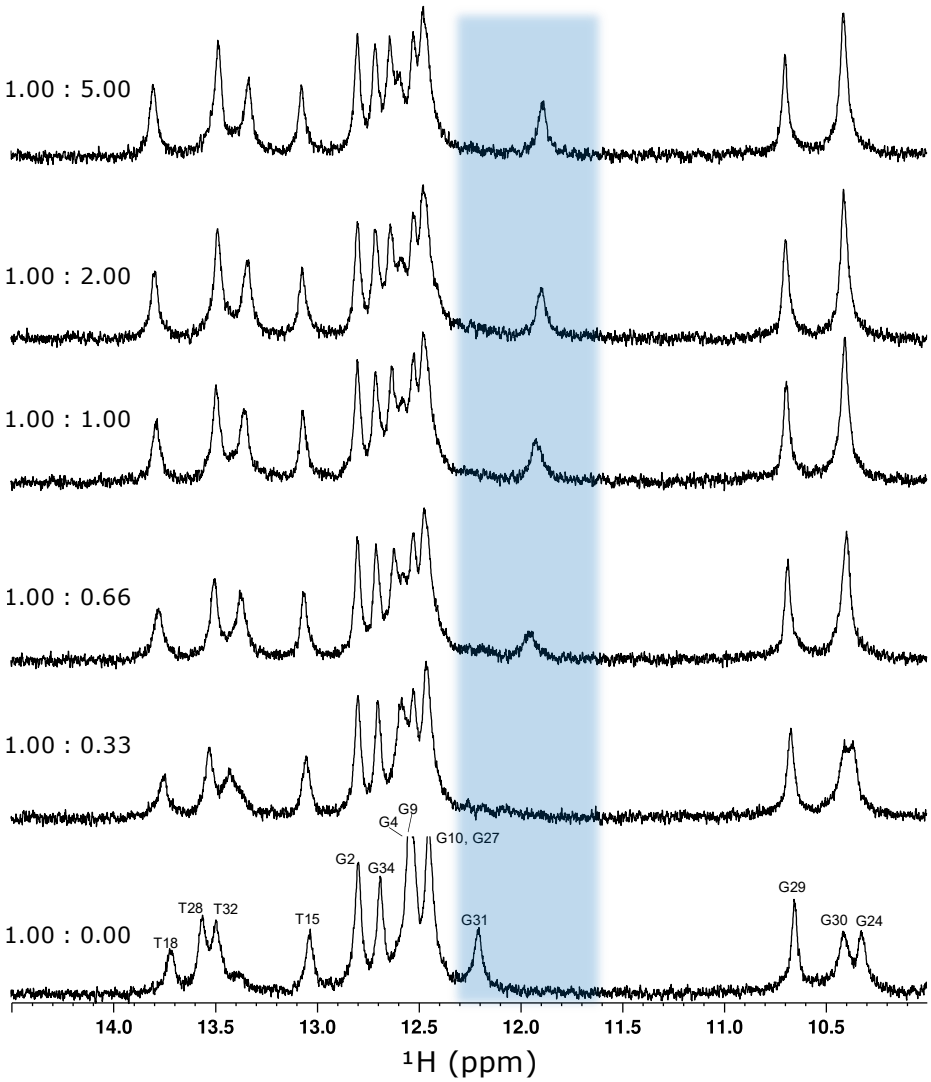

Figure 3.3.1.3. ^{1}H-NMR spectra showing the imino proton resonances during a titration of MN4 with articaine. The numbers on the left-hand side of the spectrum indicate the molar ratio of MN4 to articaine. The G31 imino resonance shift is highlighted in blue. Experiments were conducted with an MN4 concentration of 0.5 mM in 10 mM $NaHPO_4$, 150 mM NaCl, pH 7.4, 90% $^{1}H_2O$-10% $^{2}H_2O$ at 5 °C.

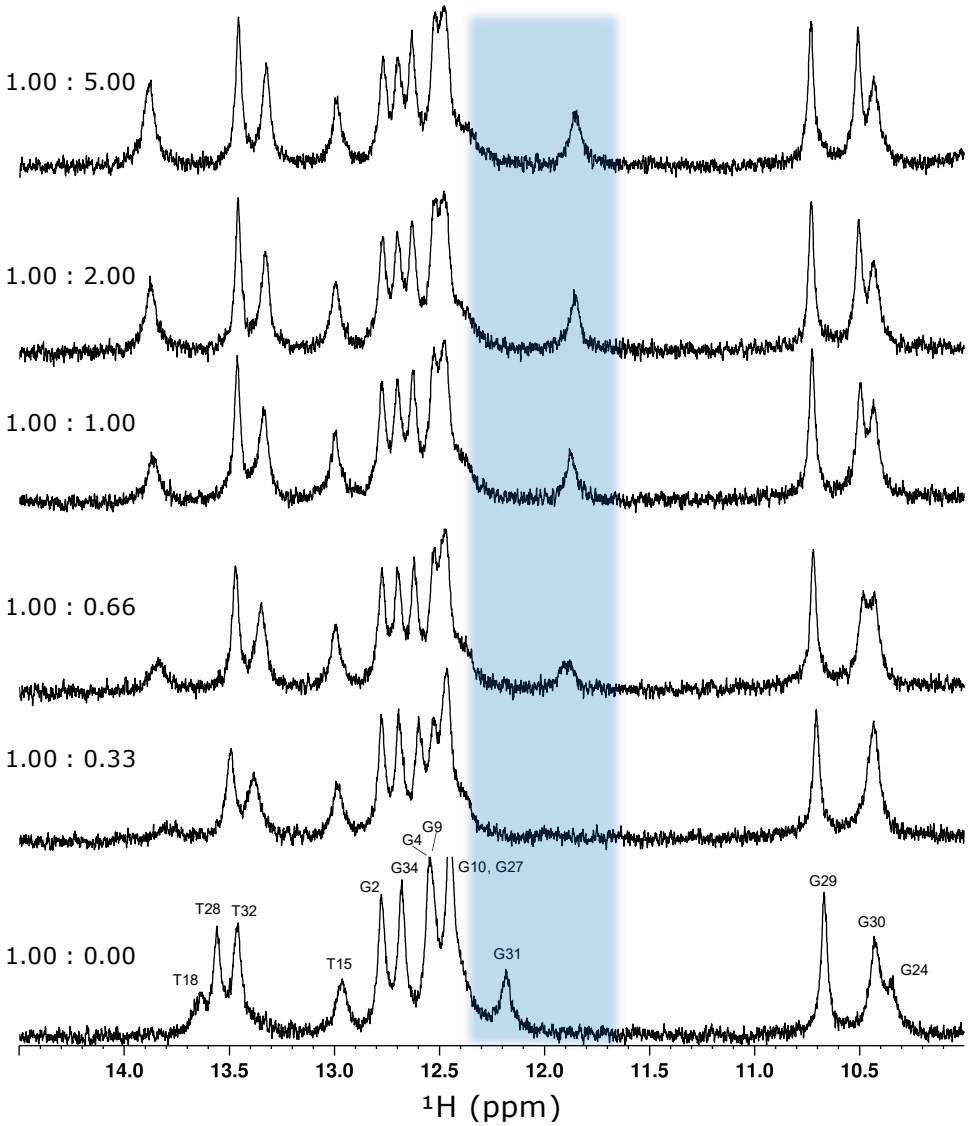

Figure 3.3.1.4. ^{1}H-NMR spectra showing the imino proton resonances during a titration of MN4 with bupivacaine. The numbers on the left-hand side of the spectrum indicate the molar ratio of MN4 to bupivacaine. The G31 imino resonance shift is highlighted in blue. Experiments were conducted with an MN4 concentration of 0.5 mM in 10 mM $NaHPO_4$, 150 mM NaCl, pH 7.4, 90% $^{1}H_2O$-10% $^{2}H_2O$ at 5 °C.

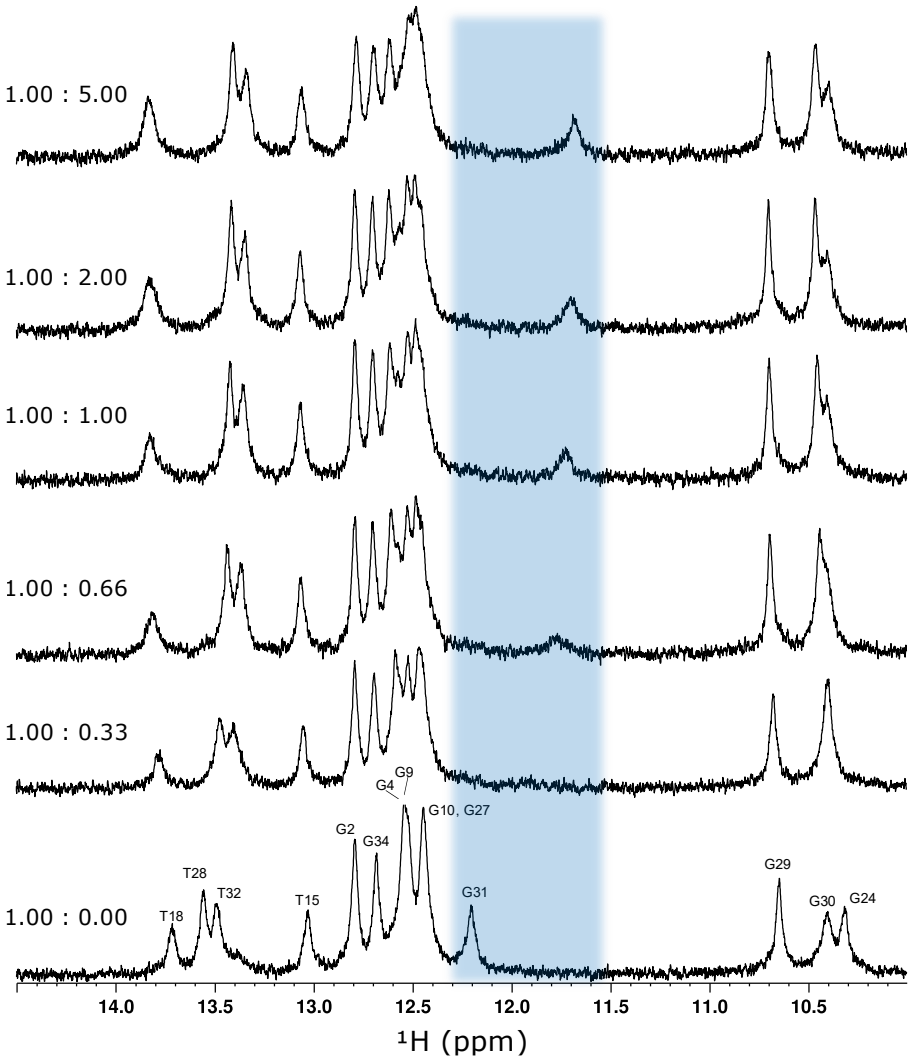

Figure 3.3.1.5. ^{1}H-NMR spectra showing the imino proton resonances during a titration of MN4 with lidocaine. The numbers on the left-hand side of the spectrum indicate the molar ratio of MN4 to lidocaine. The G31 imino resonance shift is highlighted in blue. Experiments were conducted with an MN4 concentration of 0.5 mM in 10 mM $NaHPO_4$, 150 mM NaCl, pH 7.4, 90% $^{1}H_2O$-10% $^{2}H_2O$ at 5 °C.

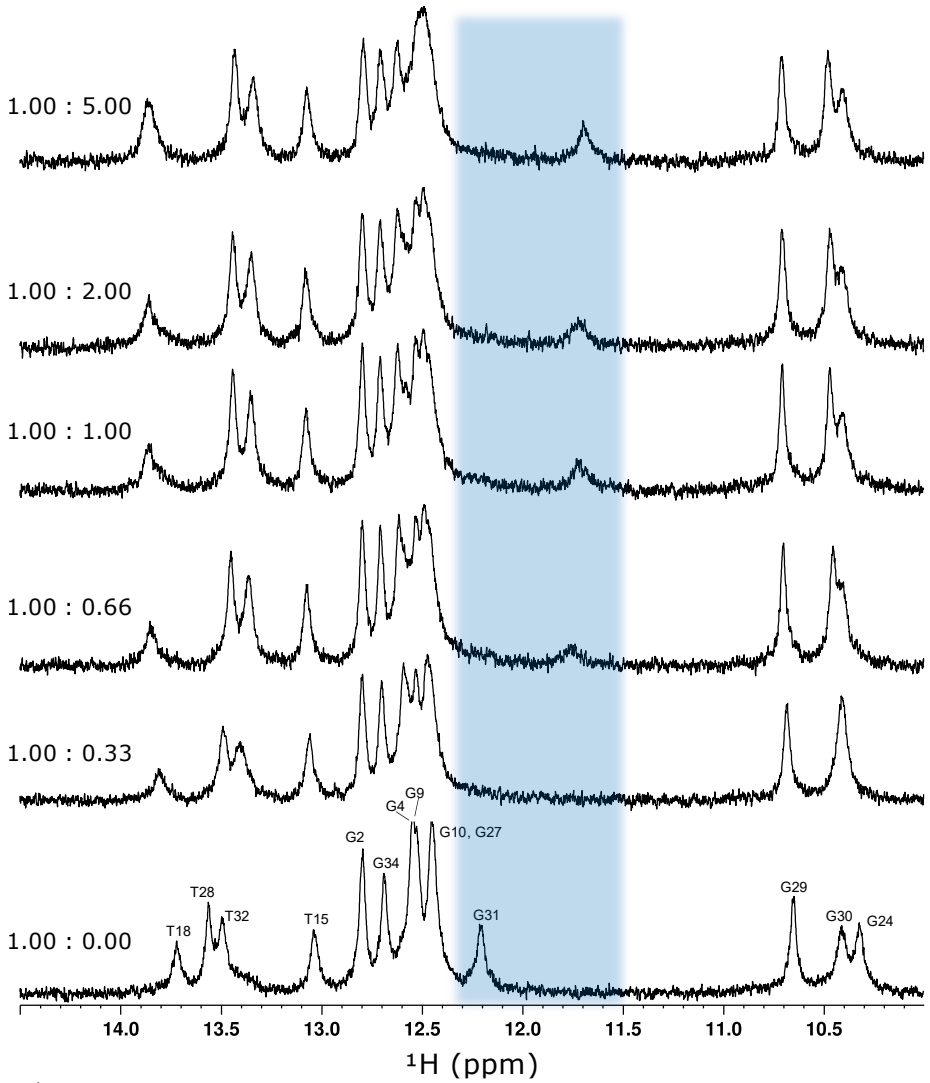

Figure 3.3.1.6. ^{1}H-NMR spectra showing the imino proton resonances during a titration of MN4 with mepivacaine. The numbers on the left-hand side of the spectrum indicate the molar ratio of MN4 to mepivacaine. The G31 imino resonance shift is highlighted in blue. Experiments were conducted with an MN4 concentration of 0.5 mM in 10 mM $NaHPO_4$, 150 mM NaCl, pH 7.4, 90% $^{1}H_2O$-10% $^{2}H_2O$ at 5 °C.

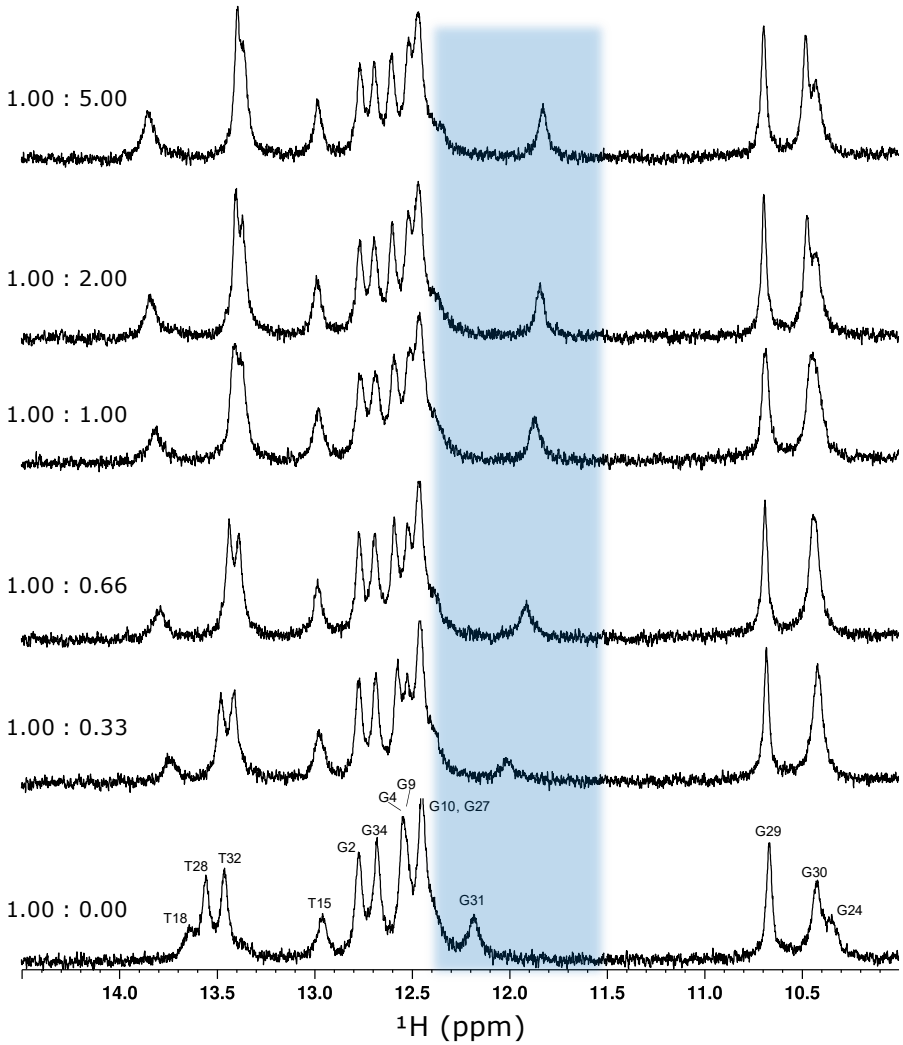

Figure 3.3.1.7. ^{1}H-NMR spectra showing the imino proton resonances during a titration of MN4 with prilocaine. The numbers on the left-hand side of the spectrum indicate the molar ratio of MN4 to prilocaine. The G31 imino resonance shift is highlighted in blue. Experiments were conducted with an MN4 concentration of 0.5 mM in 10 mM $NaHPO_4$, 150 mM NaCl, pH 7.4, 90% $^{1}H_2O$-10% $^{2}H_2O$ at 5 °C.

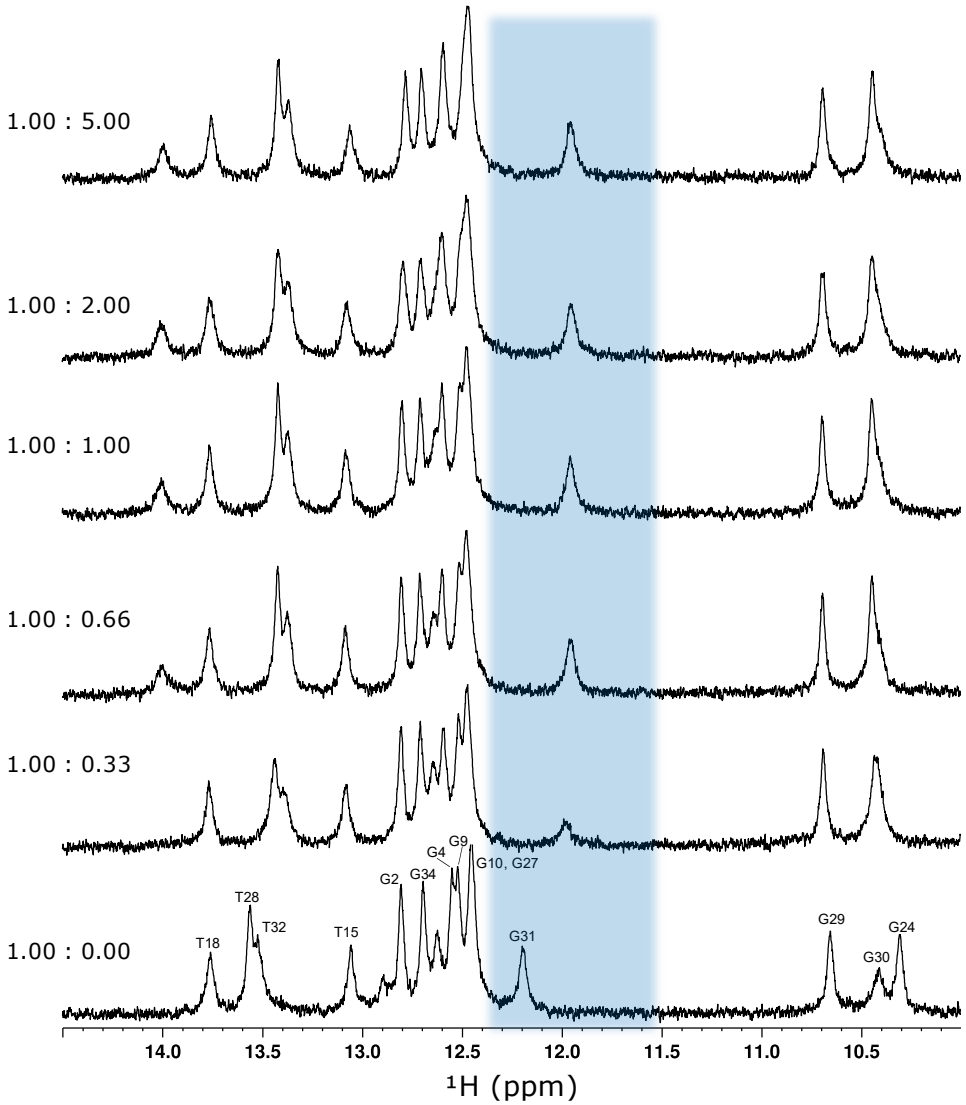

Figure 3.3.1.8. ^{1}H-NMR spectra showing the imino proton resonances during a titration of MN4 with procaine. The numbers on the left-hand side of the spectrum indicate the molar ratio of MN4 to procaine. The G31 imino resonance shift is highlighted in blue. Experiments were conducted with an MN4 concentration of 0.5 mM in 10 mM $NaHPO_4$, 150 mM NaCl, pH 7.4, 90% $^{1}H_2O$-10% $^{2}H_2O$ at 5 °C.

After examining the effects of local anesthetic binding on MN4, MN19 was also investigated by ^{1}H-NMR spectroscopy to determine whether related cocaine-binding aptamer scaffolds respond similarly to this ligand series. This provided an opportunity to assess whether the local anesthetics simply perturb pre-existing aptamer structure, as observed for MN4, or whether they can also promote folding in a less structured aptamer variant.

The ^{1}H-NMR titration of MN19 with benzocaine (Figure 3.3.1.9) indicates that ligand binding promotes substantial structural organization of the aptamer. Assignment of peaks were previously made by

Churcher et al. in 2020.[118] In the free state, MN19 shows few well-resolved imino proton resonances, suggesting that it is largely unstructured or conformationally dynamic under these conditions. This indicates that, unlike MN4, MN19 does not possess a strongly pre-formed hydrogen-bonded structure in the absence of ligand. Upon addition of benzocaine, several new imino resonances appear and increase in intensity, indicating formation or stabilization of base-paired or otherwise protected structural elements.

This spectral behavior suggests that benzocaine shifts the MN19 conformational ensemble toward a more ordered ligand-bound state. Rather than simply perturbing an existing fold, benzocaine appears to promote ligand-induced folding of MN19. Notably, the appearance of a resonance resembling the characteristic G31 peak observed in MN4 titrations suggests that MN19 may adopt a ligand-bound conformation similar to MN4, at least within this local structural environment. This similarity supports the idea that, despite differences in free-state organization, MN19 and MN4 may converge toward a related bound-state fold upon interaction with local anesthetic ligands. Overall, the benzocaine titration demonstrates that MN19 is structurally responsive to benzocaine and that ligand binding induces formation of a more ordered aptamer structure.

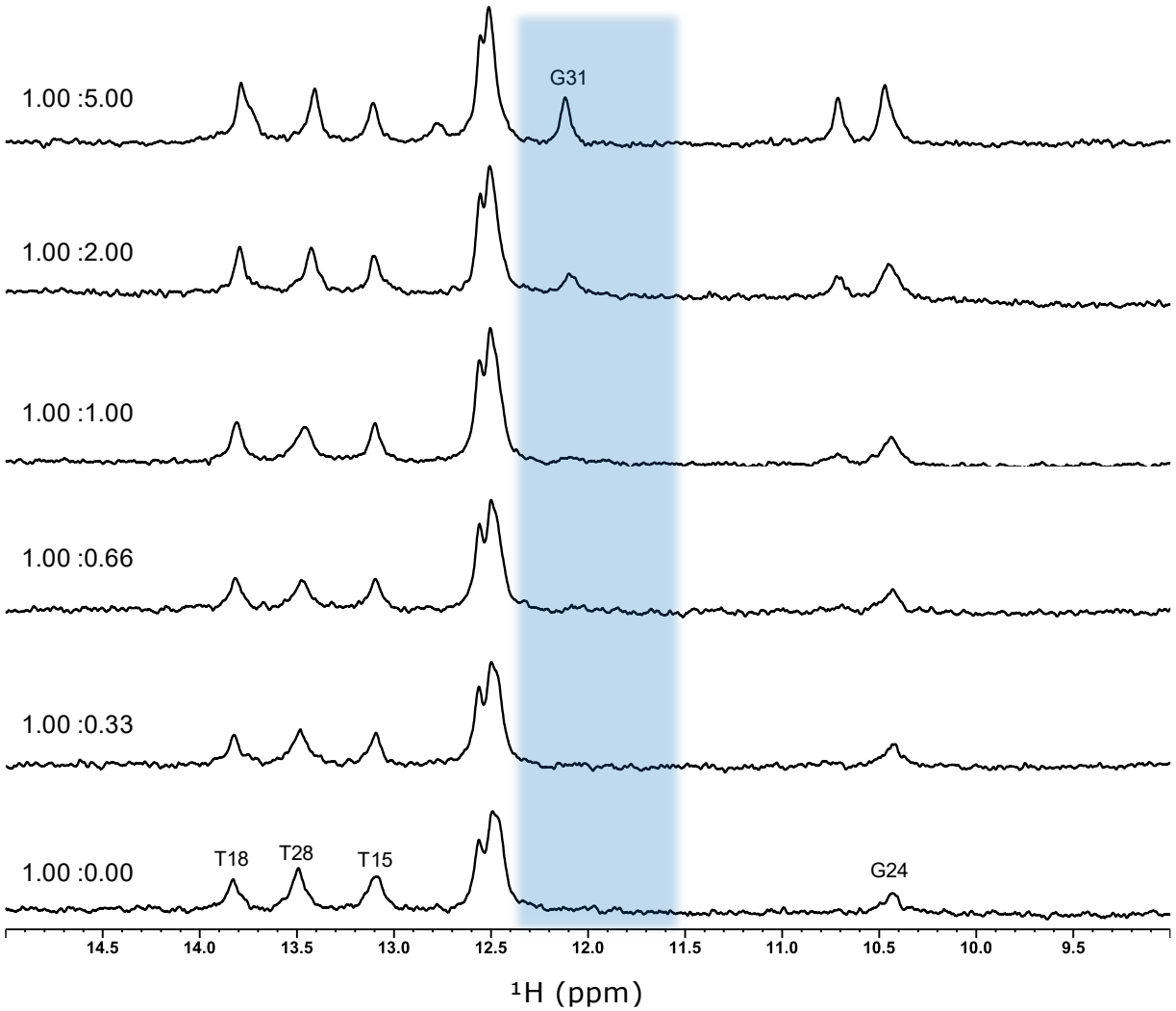

Figure 3.3.1.9. ^{1}H-NMR spectra showing the imino proton resonances during a titration of MN19 with benzocaine. The numbers on the left-hand side of the spectrum indicate the molar ratio of MN19 to benzocaine. The G31 imino resonance emergence is highlighted in blue. Experiments were conducted with an MN19 concentration of 0.5 mM in 10 mM $NaHPO_4$, 150 mM NaCl, pH 7.4, 90% $^{1}H_2O$-10% $^{2}H_2O$ at 5 °C.

The ^{1}H-NMR titration of MN19 with tetracaine (Figure 3.3.1.10) shows that ligand addition promotes clear structural organization of the aptamer. In the absence of ligand, MN19 displays only limited imino proton signal intensity, consistent with a largely unstructured or conformationally dynamic free state. This indicates that MN19 does not possess a strongly pre-formed hydrogen-bonded structure prior to ligand binding. Upon addition of tetracaine, several imino proton resonances emerge and increase in intensity, demonstrating formation or stabilization of base-paired and protected structural elements within the aptamer.

This spectral response is consistent with ligand-induced folding of MN19. Rather than simply perturbing an already folded scaffold, tetracaine appears to shift the MN19 conformational ensemble toward a more ordered ligand-bound state. The emergence of sharper and more numerous imino resonances suggests that tetracaine binding stabilizes hydrogen-bonded regions that are only weakly populated or not detectable in the free aptamer. Notably, a resonance resembling the characteristic G31 peak observed in MN4 titrations also appears upon tetracaine addition, suggesting that MN19 may adopt a bound-state fold similar to that observed for MN4. This supports the idea that MN19 and MN4, despite differing in their free-state structural organization, can converge toward a related ligand-bound conformation when complexed with local anesthetic ligands.

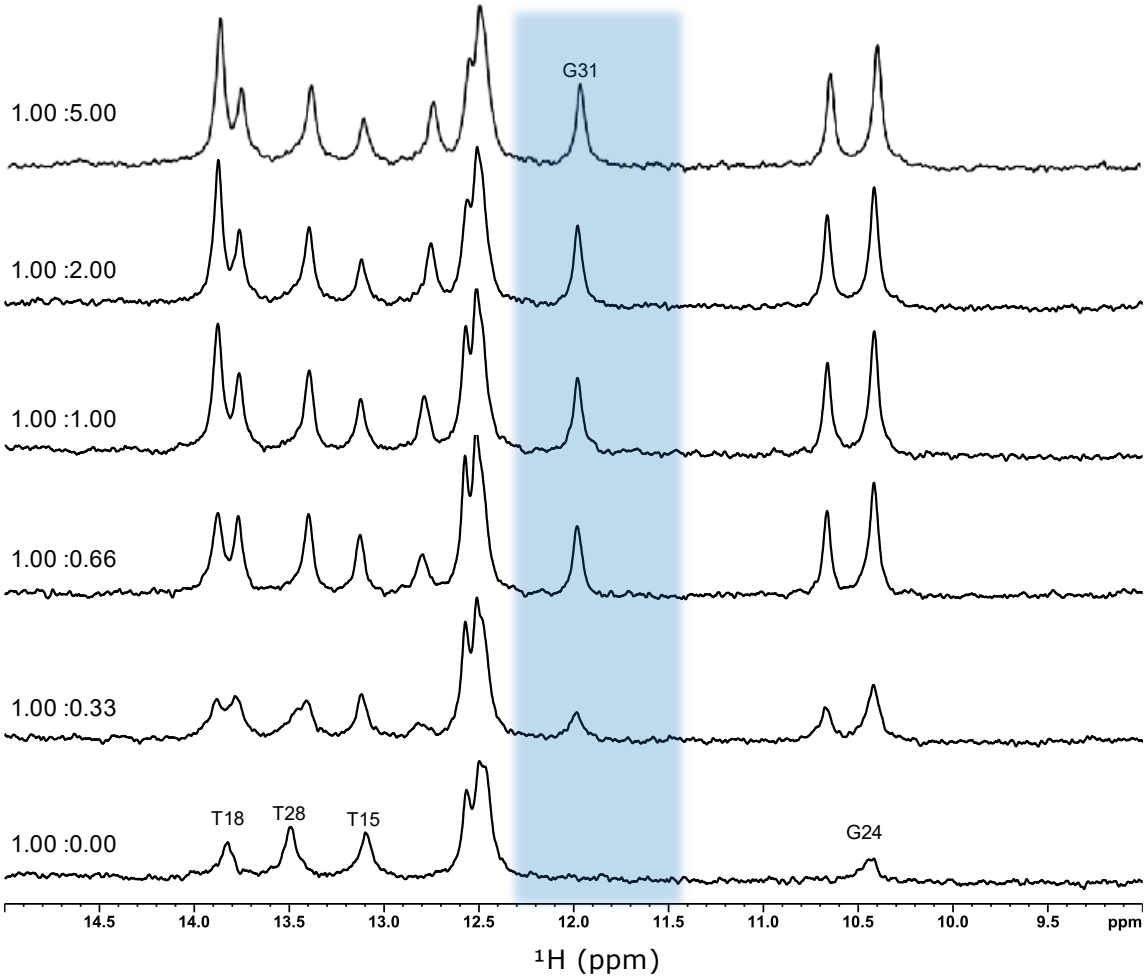

Figure 3.3.1.10. ^{1}H-NMR spectra showing the imino proton resonances during a titration of MN19 with tetracaine. The numbers on the left-hand side of the spectrum indicate the molar ratio of MN19 to tetracaine. The G31 imino resonance emergence is highlighted in blue. Experiments were conducted with an MN19 concentration of 0.5 mM in 10 mM $NaHPO_4$, 150 mM NaCl, pH 7.4, 90% $^{1}H_2O$-10% $^{2}H_2O$ at 5 °C.

The remaining local anesthetics, articaine, bupivacaine, lidocaine, mepivacaine, prilocaine, and procaine, produced broadly similar responses in MN19 (Figure 3.3.1.11 – 3.3.1.16). In each case, ligand addition resulted in the appearance of new imino proton resonances and increased spectral definition relative to the free aptamer. This behavior is consistent with ligand-induced folding or stabilization of protected base-paired and tertiary structural elements. The emergence of resonances in both the Watson–Crick and non-canonical imino regions suggests that these ligands do not merely produce local perturbations, but instead promote more extensive organization of the aptamer structure.

Although all of the anesthetic ligands promote structure formation in MN19, the final bound-state spectra are not identical. Differences in peak intensity, linewidth, and resonance distribution across the ligand series suggest that each ligand stabilizes a related but distinct MN19-bound conformation. These differences likely reflect variation in ligand size, hydrophobicity, aromatic substitution, linker composition, and charge distribution, which may influence local interactions within the binding pocket or surrounding tertiary structure. Thus, MN19 appears capable of adopting a common ligand-responsive fold while still allowing ligand-specific structural refinement.

A key shared feature across the MN19–anesthetic complexes is the appearance of a characteristic resonance corresponding to the G31 imino proton, similar to that observed in the MN4 titrations. The presence of this G31-associated peak in each MN19-bound spectrum suggests that all ligand-bound MN19 complexes share a related local structural environment around G31. Because this resonance is also characteristic of the MN4-bound state, its appearance supports the interpretation that MN19 folds into a structure related to the MN4 ligand-bound conformation upon interaction with local anesthetics.

Together, these data show that MN19 is structurally responsive to the full local anesthetic series. While free MN19 is largely dynamic or weakly structured, ligand addition promotes formation of a more ordered aptamer fold in every case examined. The shared appearance of the G31 resonance suggests convergence toward a related bound-state architecture, whereas differences among the spectra indicate ligand-specific structural variation. These results complement the MN4 NMR data by showing that local

anesthetics can perturb a pre-formed aptamer scaffold in MN4 while also inducing folding of a more dynamic related aptamer in MN19.

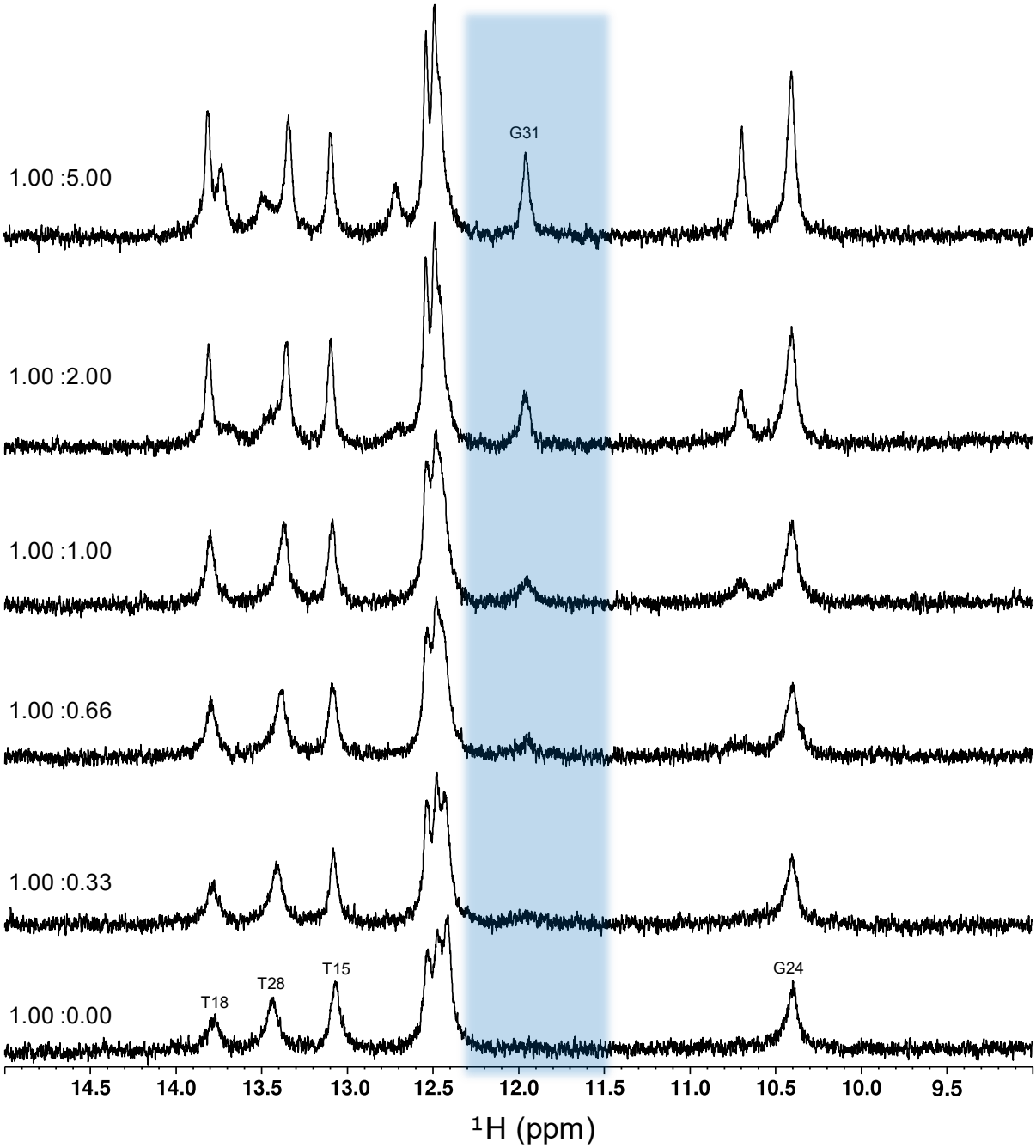

Figure 3.3.1.11. ^{1}H-NMR spectra showing the imino proton resonances during a titration of MN19 with articaine. The numbers on the left-hand side of the spectrum indicate the molar ratio of MN19 to articaine. The G31 imino resonance emergence is highlighted in blue. Experiments were conducted with an MN19 concentration of 0.5 mM in 10 mM $NaHPO_4$, 150 mM NaCl, pH 7.4, 90% $^{1}H_2O$-10% $^{2}H_2O$ at 5 °C.

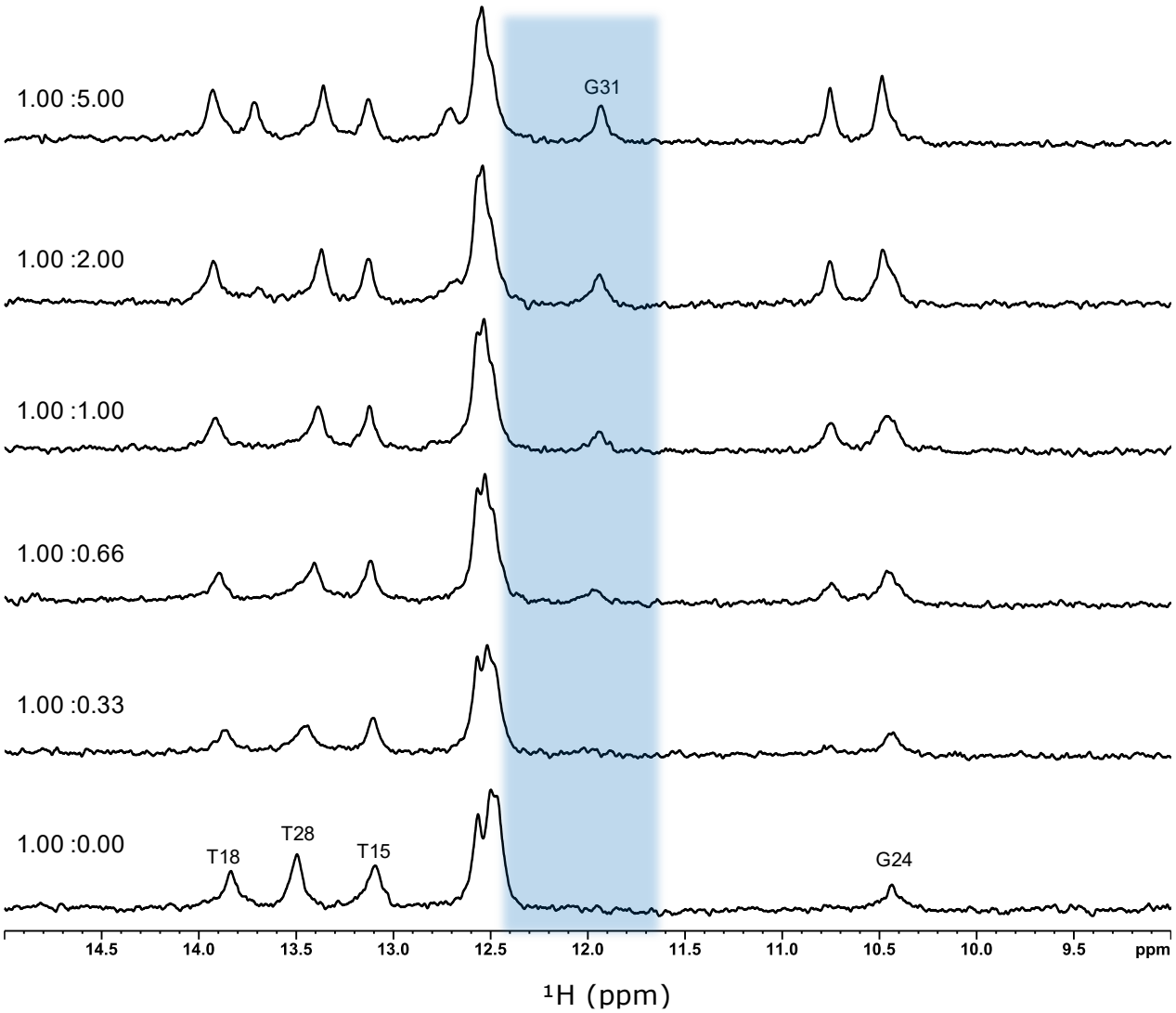

Figure 3.3.1.12. ^{1}H-NMR spectra showing the imino proton resonances during a titration of MN19 with bupivacaine. The numbers on the left-hand side of the spectrum indicate the molar ratio of MN19 to bupivacaine. The G31 imino resonance emergence is highlighted in blue. Experiments were conducted with an MN19 concentration of 0.5 mM in 10 mM $NaHPO_4$, 150 mM NaCl, pH 7.4, 90% $^{1}H_2O$-10% $^{2}H_2O$ at 5 °C.

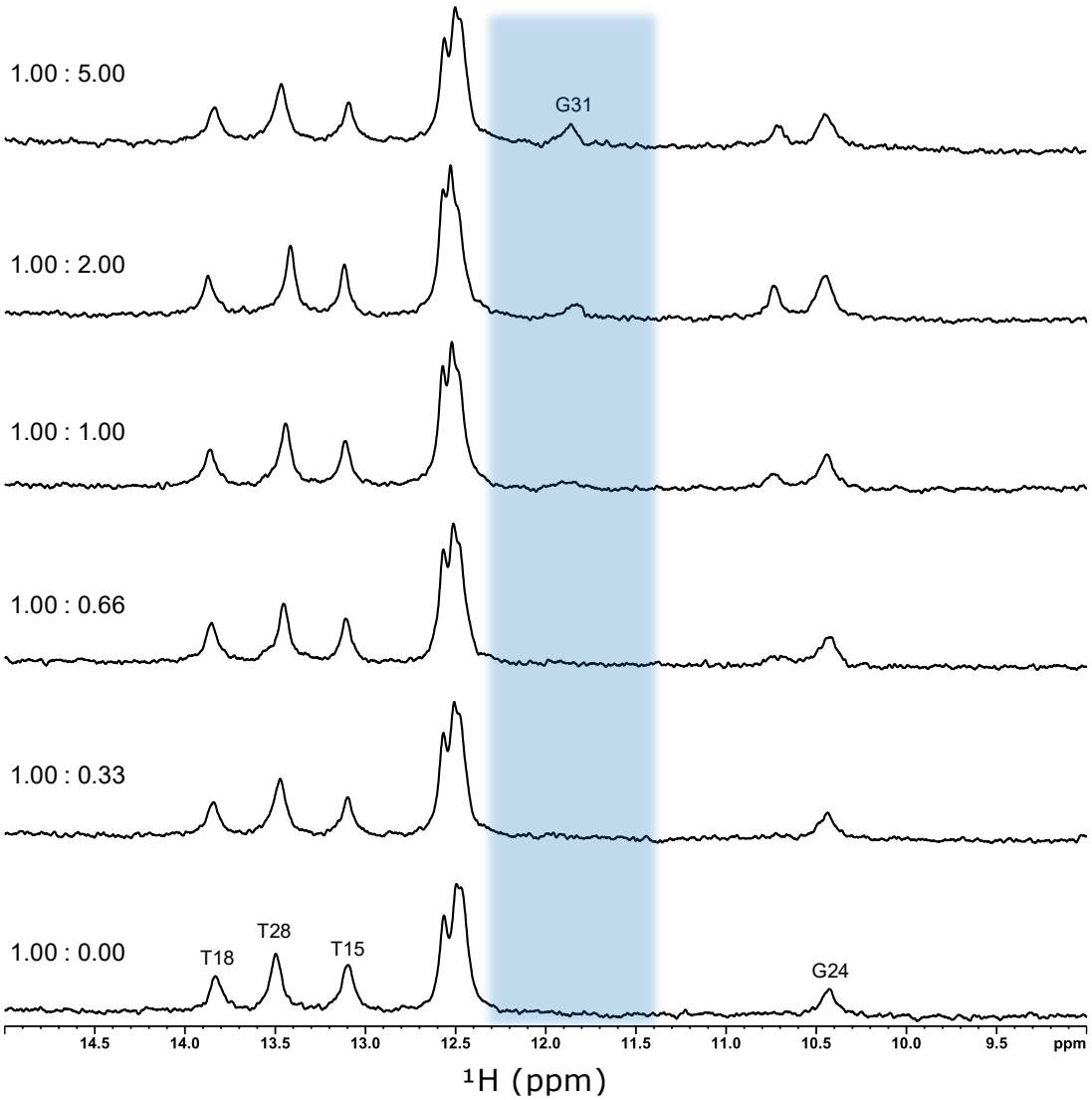

Figure 3.3.1.13. ^{1}H-NMR spectra showing the imino proton resonances during a titration of MN19 with lidocaine. The numbers on the left-hand side of the spectrum indicate the molar ratio of MN19 to lidocaine. The G31 imino resonance emergence is highlighted in blue. Experiments were conducted with an MN19 concentration of 0.5 mM in 10 mM $NaHPO_4$, 150 mM NaCl, pH 7.4, 90% $^{1}H_2O$-10% $^{2}H_2O$ at 5 °C.

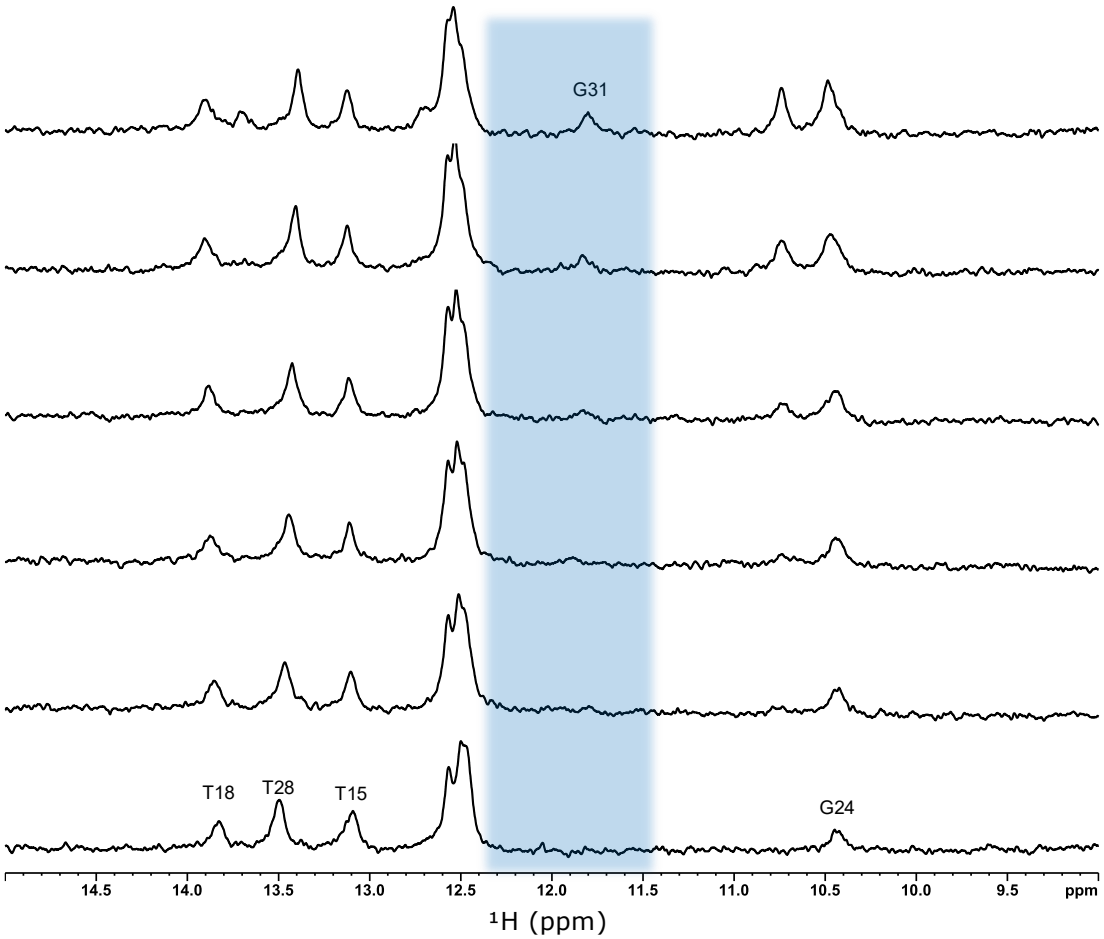

Figure 3.3.1.14. ^{1}H-NMR spectra showing the imino proton resonances during a titration of MN19 with mepivacaine. The numbers on the left-hand side of the spectrum indicate the molar ratio of MN19 to mepivacaine. The G31 imino resonance emergence is highlighted in blue. Experiments were conducted with an MN19 concentration of 0.5 mM in 10 mM $NaHPO_4$, 150 mM NaCl, pH 7.4, 90% $^{1}H_2O$-10% $^{2}H_2O$ at 5 °C.

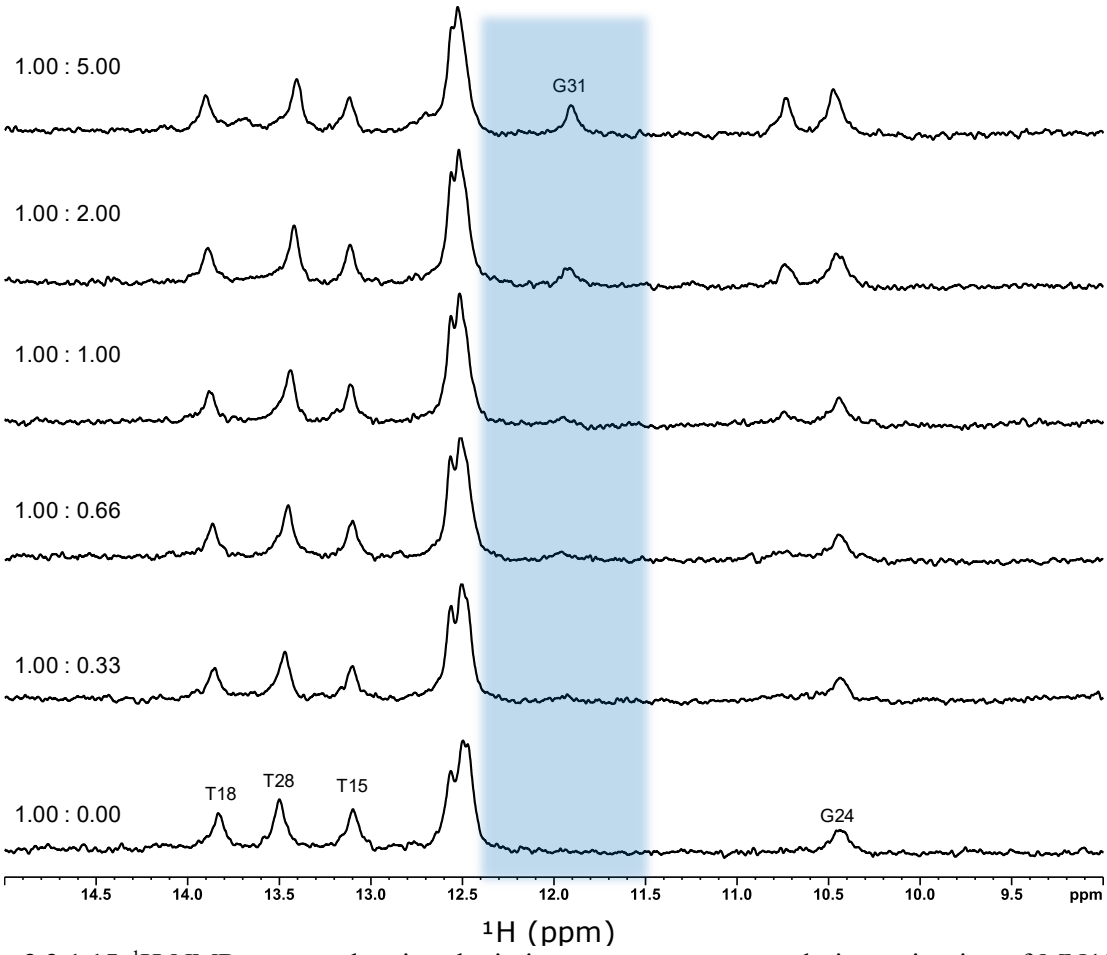

Figure 3.3.1.15. ^{1}H-NMR spectra showing the imino proton resonances during a titration of MN19 with prilocaine. The numbers on the left-hand side of the spectrum indicate the molar ratio of MN19 to prilocaine. The G31 imino resonance emergence is highlighted in blue. Experiments were conducted with an MN19 concentration of 0.5 mM in 10 mM $NaHPO_4$, 150 mM NaCl, pH 7.4, 90% $^{1}H_2O$-10% $^{2}H_2O$ at 5 °C.

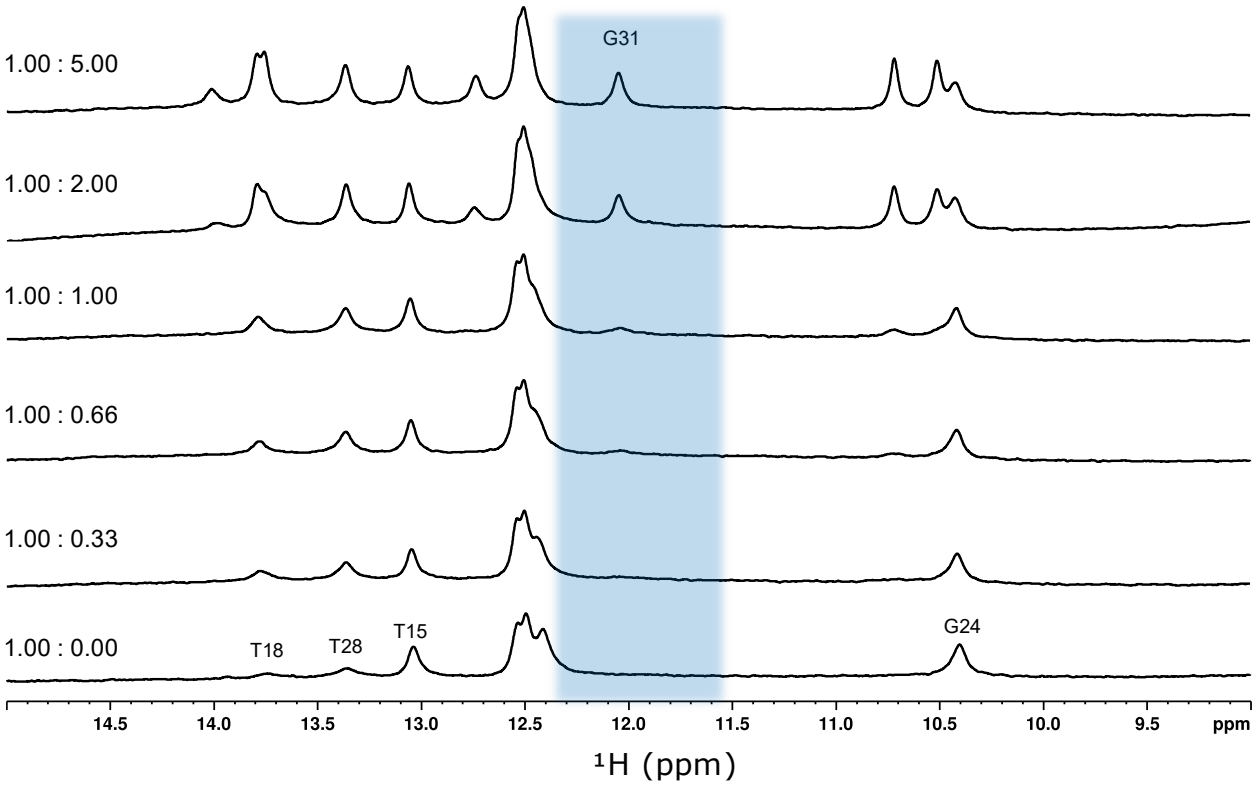

Figure 3.3.1.16. ^{1}H-NMR spectra showing the imino proton resonances during a titration of MN19 with procaine. The numbers on the left-hand side of the spectrum indicate the molar ratio of MN19 to procaine. The G31 imino resonance emergence is highlighted in blue. Experiments were conducted with an MN19 concentration of 0.5 mM in 10 mM $NaHPO_4$, 150 mM NaCl, pH 7.4, 90% $^{1}H_2O$-10% $^{2}H_2O$ at 5 °C.

To complement the DSC analysis, temperature-dependent ^{1}H-NMR experiments were performed on free MN4, the MN4–benzocaine complex, and the MN4–tetracaine complex. Benzocaine and tetracaine were selected for this analysis because they represented the two extremes of thermal destabilization observed in the DSC experiments: benzocaine produced the largest decrease in apparent T_m, whereas tetracaine produced the smallest decrease among the local anesthetics tested. Therefore, comparing these two complexes by NMR provided an opportunity to examine whether differences in global thermal destabilization observed by DSC were also reflected in the temperature-dependent behaviour of imino proton resonances.

In these experiments, one-dimensional ^{1}H-NMR spectra were collected in 5 °C increments to monitor the disappearance of imino proton resonances as a function of increasing temperature. Because imino signals report on protected base-paired regions of the aptamer, their persistence at higher temperatures provides a qualitative measure of the thermal stability of local secondary-structure elements.

The thermal NMR stack plots (Figure 3.3.1.17) showed that the imino resonances of free MN4 gradually decreased in intensity with increasing temperature and were largely absent by approximately 45 °C. A similar trend was observed for the MN4–benzocaine complex, where most imino signals also disappeared by approximately 45 °C, although some resonances appeared to persist slightly longer than in the free aptamer. In contrast, the MN4–tetracaine complex retained detectable imino resonances until approximately 50 °C, suggesting that tetracaine provides a modest increase in the persistence of protected base-paired regions compared with both free MN4 and the MN4–benzocaine complex.

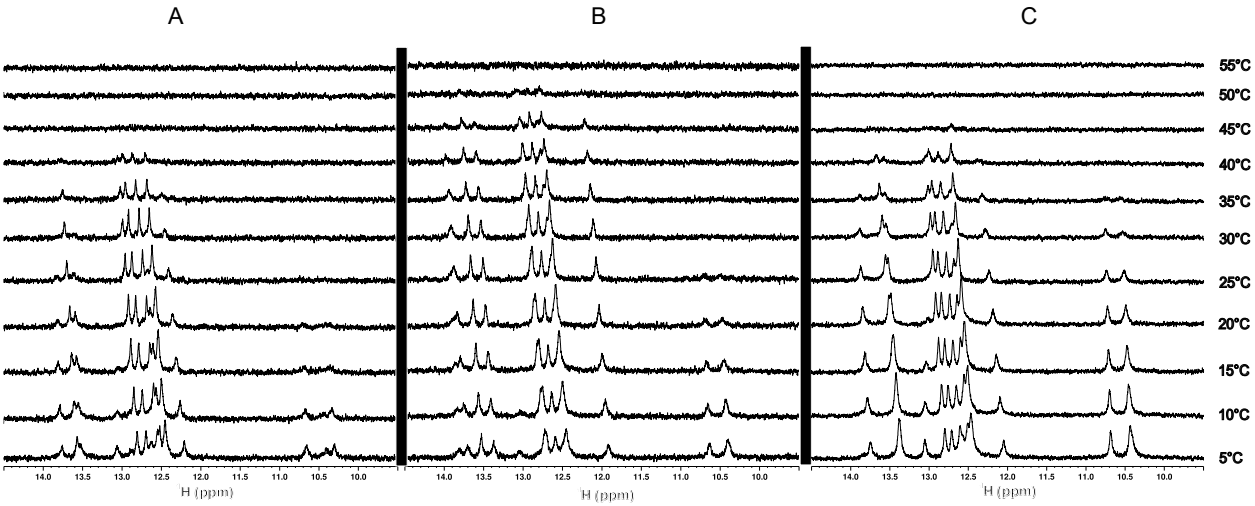

Figure 3.3.1.17. Temperature-dependent ^{1}H-NMR spectra of the MN4 aptamer in the free and complexed state with ligands. (A) Free MN4 aptamer; (B) MN4–tetracaine complex; (C) MN4–benzocaine complex. Spectra were acquired at 5 °C intervals from 5 °C to 55 °C to monitor thermally induced changes in the imino proton region. Comparison of the stacked spectra reveals differences in complex stability, with the MN4-tetracaine complex showing the greatest stability as the imino signals persist until 50 °C whereas the MN4-benzocaine complex signals only persist until 45 °C. This is in contrast to the free MN4 whose signals persist only till 40 °C.

These NMR thermal-melt results are broadly consistent with the DSC data, which showed that tetracaine produces the least destabilizing effect among the local anesthetics, whereas benzocaine causes the largest decrease in apparent melt temperature. Although DSC indicated that both benzocaine and tetracaine reduce the global thermal stability of MN4 relative to the free aptamer, the NMR data suggest that ligand binding can still preserve or promote local base-paired structure within the bound complexes. This distinction is important because DSC reports on the overall thermal unfolding behaviour of the aptamer ensemble, whereas NMR monitors specific imino-detectable structural elements. Therefore, the persistence

of selected imino resonances in the ligand-bound spectra suggests that benzocaine and tetracaine do not simply unfold MN4, but instead alter the aptamer structure in a way that retains localized protected regions while reducing the overall thermal stability of the complex.

3.3.2 ITC Studies of Ligand Binding by MN4

The binding of eight local anesthetics—tetracaine, procaine, mepivacaine, bupivacaine, articaine, lidocaine, prilocaine, and benzocaine—to MN4 was analysed using ITC. As a collaborative effort, ITC data was collected in conjunction with Lashaun Coote. The integrated binding isotherms were fit using a one-site binding model, consistent with an apparent 1:1 binding interaction between MN4 and each ligand. The resulting binding affinities and thermodynamic parameters are summarized in Table 3.3.2.1. Among the ligands investigated, benzocaine exhibited the weakest affinity for MN4, with a K_d of (22 ± 9) μM, whereas tetracaine showed the strongest affinity, with a K_d of (5.0 ± 2.3) μM (Figure 3.3.2.1, Figure 3.3.2.2). In both cases, binding was enthalpically driven and accompanied by an unfavourable entropy change, indicating that favourable aptamer–ligand interactions are partially offset by entropic penalties associated with binding. Similar one-site binding behaviour was observed for the remaining local anesthetics (Figures 3.3.2.3-3.3.2.8). Overall, the affinities of the local anesthetics were weaker than the previously reported affinity of MN4 for quinine.[114] This difference appears to be associated with the more favourable binding enthalpy reported for quinine, although the overall binding free energy reflects the combined contributions of both enthalpy and entropy. The binding thermodynamics of mepivacaine, bupivacaine, articaine, lidocaine, and prilocaine indicate that these ligands bind MN4 with favourable enthalpic and entropic contributions. However, the magnitudes of these contributions are smaller than those observed for tetracaine and procaine, which is consistent with the weaker affinities measured for this subset of ligands. The favourable entropy terms may reflect increased conformational freedom within localized regions of MN4, desolvation effects, and/or disruption of pre-existing intramolecular contacts upon ligand binding. Such behaviour would be consistent with a binding mechanism in which ligand association is coupled to partial structural destabilization or conformational redistribution rather than simple ligand-induced stabilization.

In addition, the aromatic groups present in these anesthetics may contribute to binding through π-stacking interactions with nucleobases, a recognized contributor to ligand recognition in cocaine-binding aptamer systems.[119] However, because aromaticity is shared across the ligand series, differences in affinity likely also depend on other ligand properties, including substituent size, charge, hydrophobicity, and the ability to form complementary contacts within the MN4 binding environment. The sigmoidal nature of the thermograms for each ligand indicates that each ligand binds MN4 in a one-site fashion.

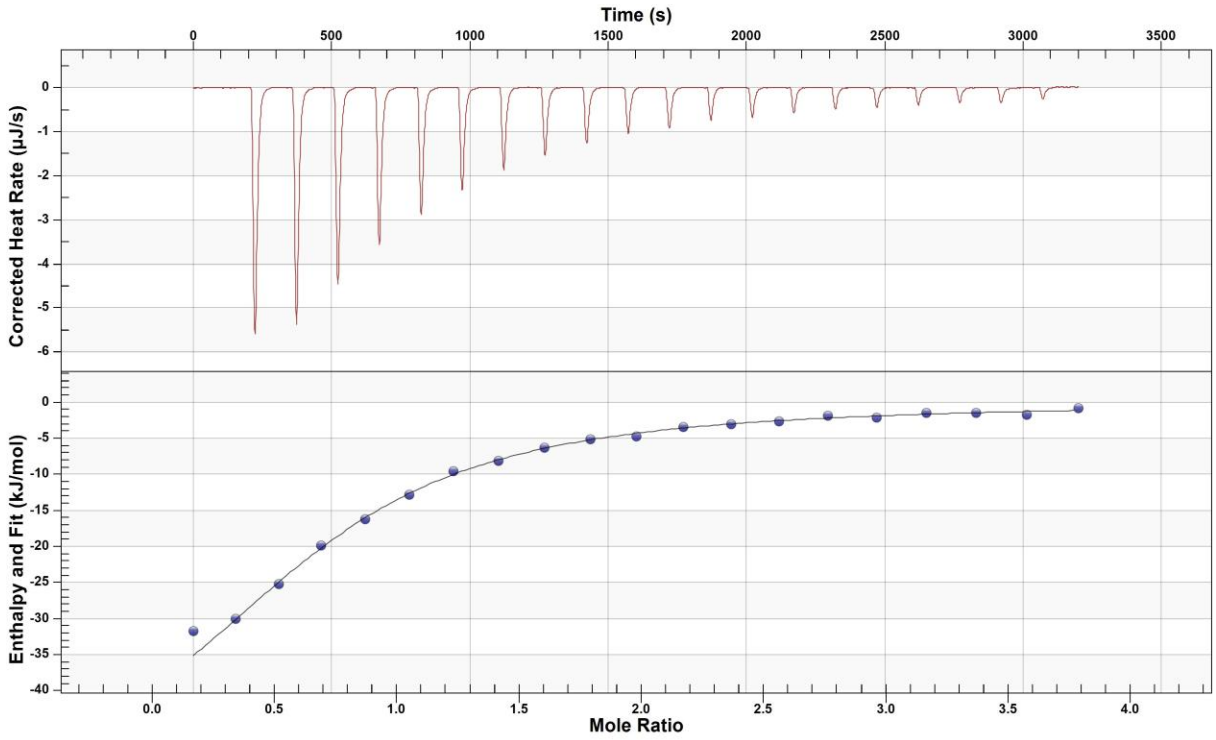

Figure 3.3.2.1. ITC thermogram of the interaction between MN4 and benzocaine. Heats of dilution were subtracted from the thermograms prior to performing fitting. The top represents the raw titration data showing the resultant heat from each injection of benzocaine into aptamer solution and the bottom represents the integrated heats after correcting for the heat of dilution. The sigmoidal nature of the curve indicated one-site binding with a K_d of 22 ± 9 µM and a ΔH_{bind} of 8.8 ± 0.7 kcal/mol. The experiment was conducted at 20 °C with an aptamer concentration of 100 µM and a benzocaine concentration of 1.56 mM. Both aptamer and ligand were dissolved in 10 mM sodium phosphate, 140 mM NaCl at pH 7.4. Data collected by Lashaun N. Coote.

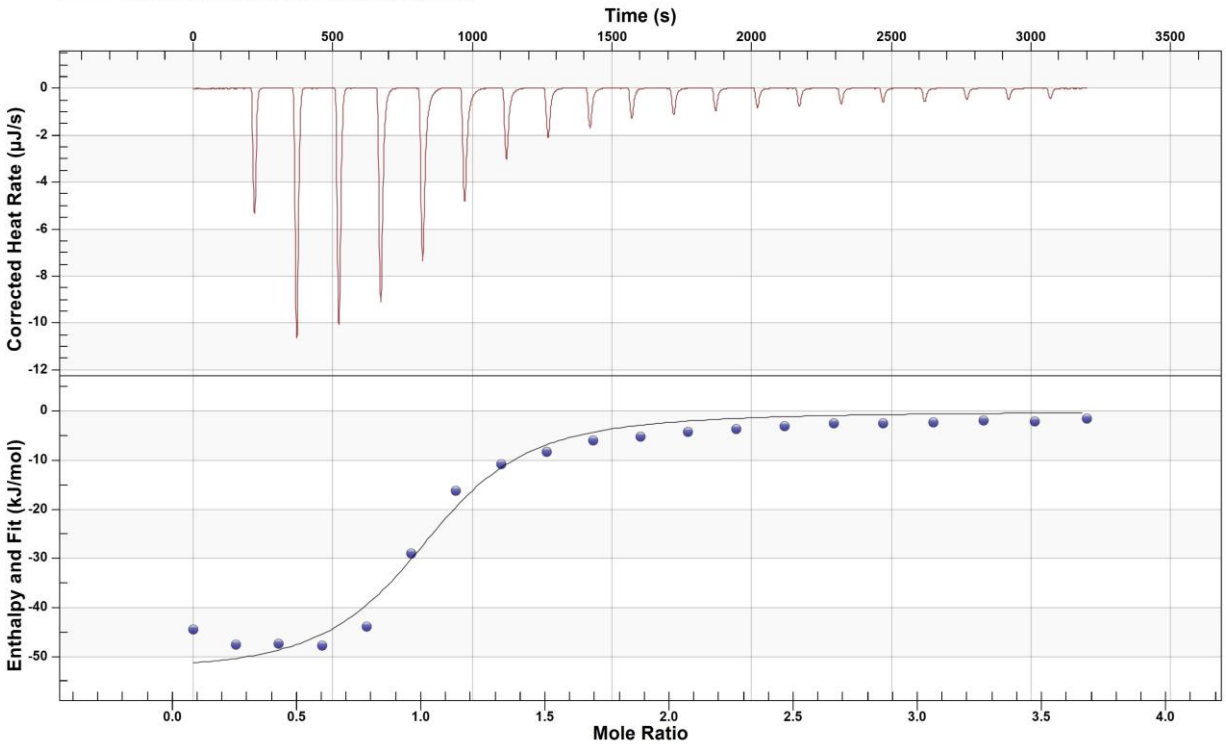

Figure 3.3.2.2. ITC thermogram of the interaction between MN4 and tetracaine. Heats of dilution were subtracted from the thermogram prior to performing fitting. The top represents the raw titration data and resultant heat from each injection of tetracaine into aptamer solution and the bottom represents the integrated heats after correcting for the heat of dilution. The sigmoidal nature of the curve indicates one-site binding with a K_d of 4.5 ± 2.3 µM and a ΔH_{bind} of -12.7 ± 0.8 kcal/mol. The experiment was conducted at 20 °C with an aptamer concentration of 100 µM and a tetracaine concentration of 1.56 mM. Both aptamer and ligand were dissolved in 10 mM sodium phosphate, 140 mM NaCl at pH 7.4. Data collected by Lashaun N. Coote.

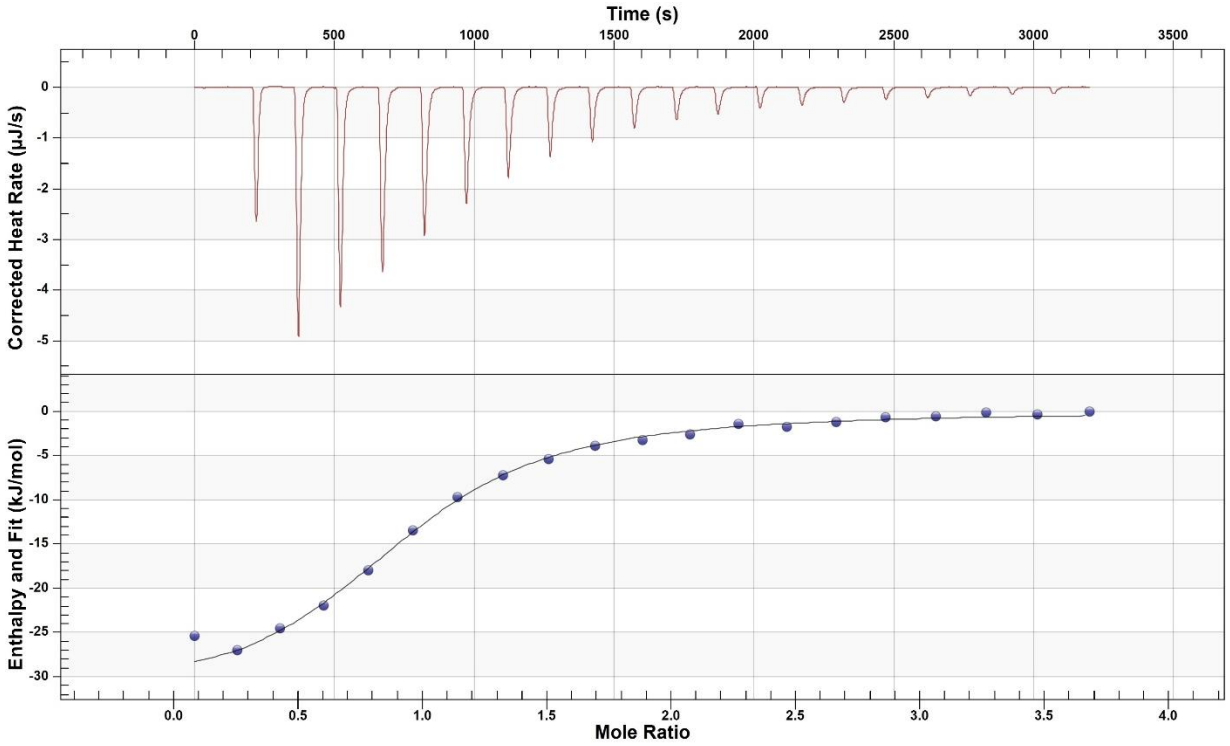

Figure 3.3.2.3. ITC thermogram showing the interaction of MN4 with articaine. Heats of dilution were subtracted from the thermogram prior to performing fitting. The top represents the raw titration data and resultant heat from each injection of articaine into aptamer solution and the bottom represents the integrated heats after correcting for the heat of dilution. The sigmoidal nature of the curve indicates one-site binding with a K_d of 12 ± 3.1 µM and a ΔH_{bind} of -6.9 ± 0.3 kcal mol^{-1}. The experiment was conducted at 20 °C with an aptamer concentration of 100 µM and an articaine concentration of 1.56 mM. Both aptamer and ligand were dissolved in 10 mM sodium phosphate, 140 mM NaCl at pH 7.4. Data collected by Lashaun N. Coote.

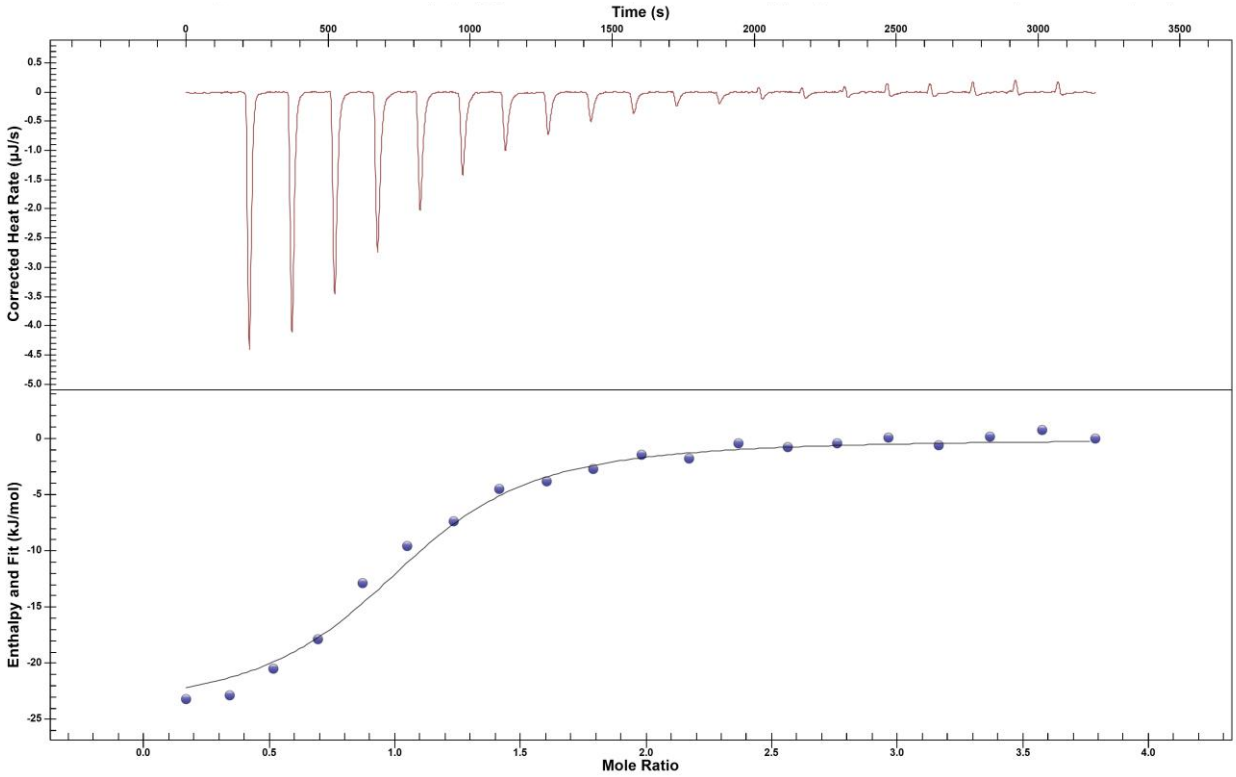

Figure 3.3.2.4. ITC thermogram showing the interaction of MN4 with bupivacaine. Heats of dilution were subtracted from the thermogram prior to performing fitting. The top represents the raw titration data and resultant heat from each injection of bupivacaine into aptamer solution and the bottom represents the integrated heats after correcting for the heat of dilution. The sigmoidal nature of the curve indicates one-site binding with a K_d of 8 ± 3.9 µM and a ΔH_{bind} of -5.7 ± 0.4 kcal mol^{-1}. The experiment was conducted at 20 °C with an aptamer concentration of 100 µM and a bupivacaine concentration of 1.56 mM. Both aptamer and ligand were dissolved in 10 mM sodium phosphate, 140 mM NaCl at pH 7.4. Data collected by Lashaun N. Coote.

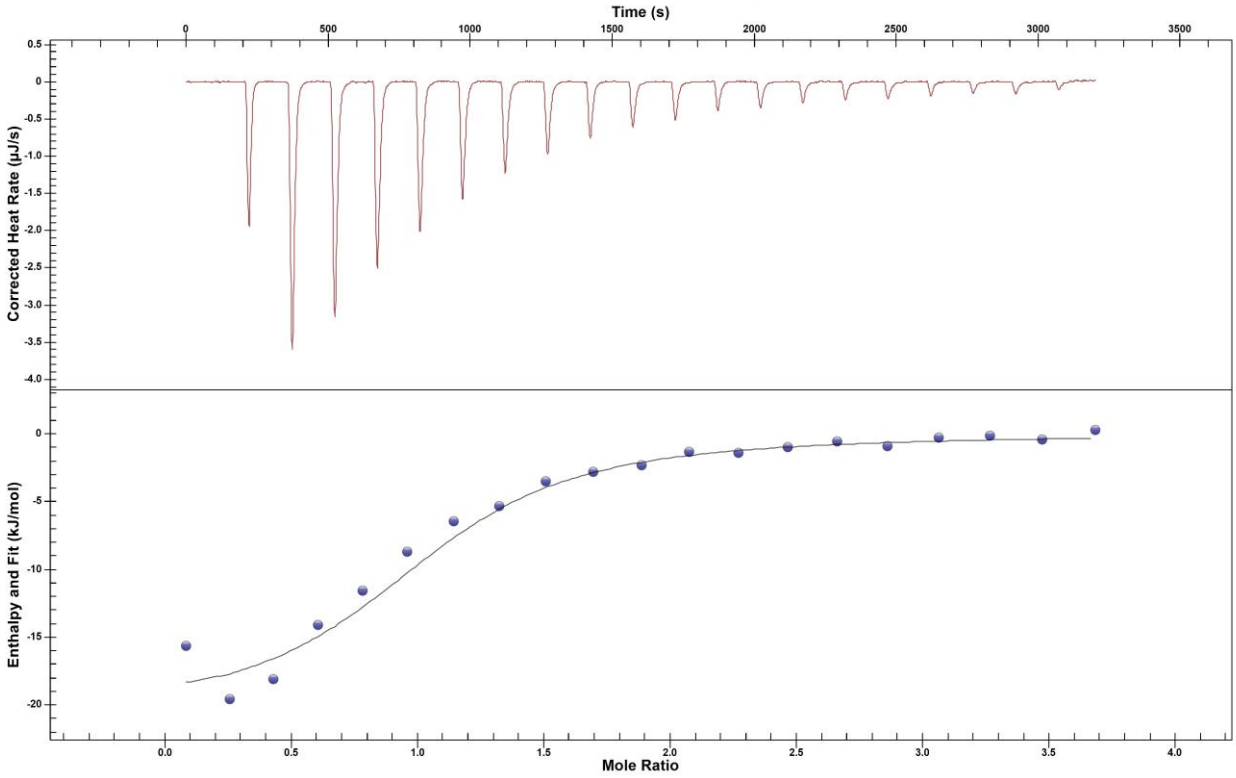

Figure 3.3.2.5. ITC thermogram showing the interaction of MN4 with lidocaine. Heats of dilution were subtracted from the thermogram prior to performing fitting. The top represents the raw titration data and resultant heat from each injection of lidocaine into aptamer solution and the bottom represents the integrated heats after correcting for the heat of dilution. The sigmoidal nature of the curve indicates one-site binding with a K_d of 12 ± 6.9 µM and a ΔH_{bind} of -5.0 ± 0.4 kcal mol^{-1}. The experiment was conducted at 20 °C with an aptamer concentration of 100 µM and a lidocaine concentration of 1.56 mM. Both aptamer and ligand were dissolved in 10 mM sodium phosphate, 140 mM NaCl at pH 7.4. Data collected by Lashaun N. Coote.

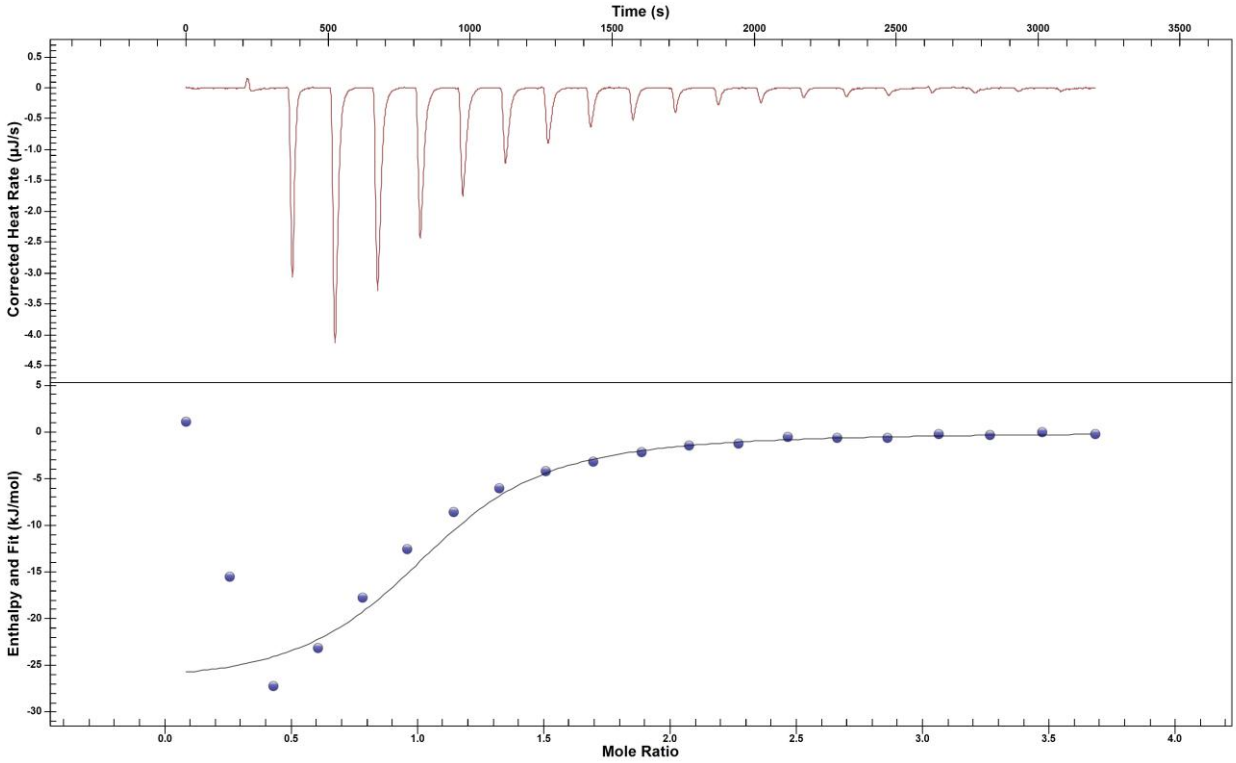

Figure 3.3.2.6. ITC thermogram showing the interaction of MN4 with mepivacaine. Heats of dilution were subtracted from the thermogram prior to performing fitting. The top represents the raw titration data and resultant heat from each injection of mepivacaine into aptamer solution and the bottom represents the integrated heats after correcting for the heat of dilution. The sigmoidal nature of the curve indicates one-site binding with a K_d of 7 ± 3.4 µM and a ΔH_{bind} of -6.7 ± 0.6 kcal mol^{-1}. The experiment was conducted at 20 °C with an aptamer concentration of 100 µM and a mepivacaine concentration of 1.56 mM. Both aptamer and ligand were dissolved in 10 mM sodium phosphate, 140 mM NaCl at pH 7.4. Data collected by Lashaun N. Coote.

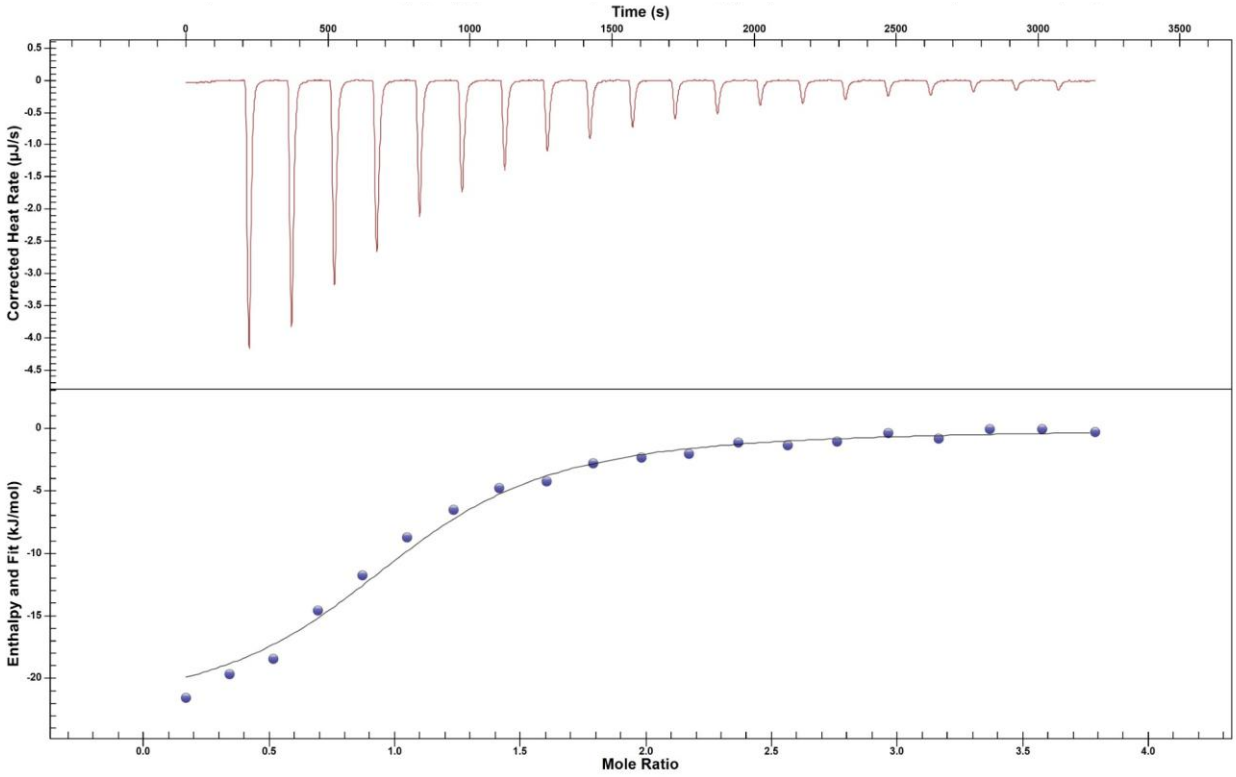

Figure 3.3.2.7. ITC thermogram showing the interaction of MN4 with prilocaine. Heats of dilution were subtracted from the thermogram prior to performing fitting. The top represents the raw titration data and resultant heat from each injection of prilocaine into aptamer solution and the bottom represents the integrated heats after correcting for the heat of dilution. The sigmoidal nature of the curve indicates one-site binding with a K_d of 13 ± 3.6 µM and a ΔH_{bind} of -5.5 ± 0.3 kcal mol^{-1}. The experiment was conducted at 20 °C with an aptamer concentration of 100 µM and a prilocaine concentration of 1.56 mM. Both aptamer and ligand were dissolved in 10 mM sodium phosphate, 140 mM NaCl at pH 7.4. Data collected by Lashaun N. Coote.

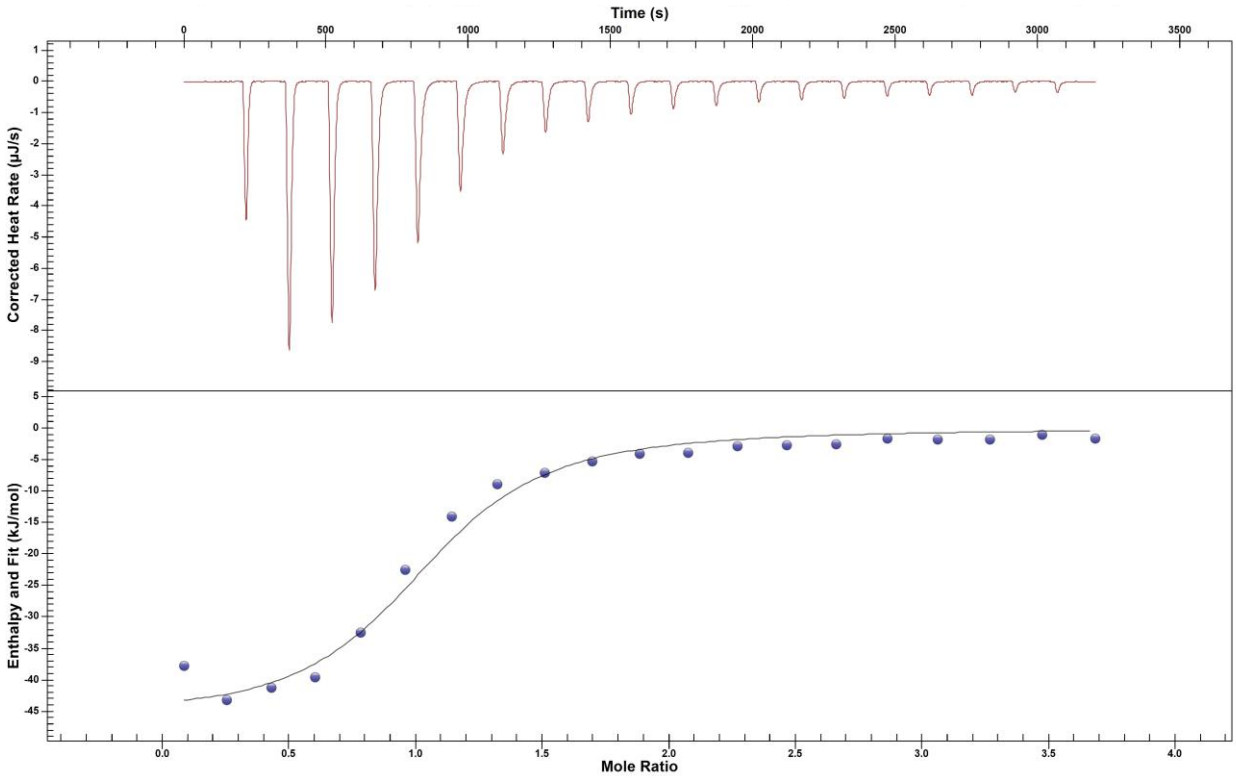

Figure 3.3.2.8. ITC thermogram showing the interaction of MN4 with procaine. Heats of dilution were subtracted from the thermogram prior to performing fitting. The top represents the raw titration data and resultant heat from each injection of procaine into aptamer solution and the bottom represents the integrated heats after correcting for the heat of dilution. The sigmoidal nature of the curve indicates one-site binding with a K_d of 7 ± 2.8 µM and a ΔH_{bind} of -10.9 ± 0.7 kcal mol^{-1}. The experiment was conducted at 20 °C with an aptamer concentration of 100 µM and a procaine concentration of 1.56 mM. Both aptamer and ligand were dissolved in 10 mM sodium phosphate, 140 mM NaCl at pH 7.4. Data collected by Lashaun N. Coote.

Table 3.3.2.1. ITC results of the MN4 aptamer with various ligands. K_d values and thermodynamic parameters of ligands used in this study for binding to the MN4 aptamer[a]

	K_d (µM)	ΔH_{bind} (kcal mol^{-1})	$-T\Delta S_{bind}$ (kcal mol^{-1})	ΔG_{bind} (kcal mol^{-1})
Quinine[b]	1.3 ± 0.9	-17 ± 2.1	10 ± 2.1	-7.9 ± 0.4
Tetracaine	5 ± 2.3	-12.7 ± 0.8	5.5 ± 0.9	-7.1 ± 0.3
Procaine	7 ± 2.8	-10.9 ± 0.7	4.1 ± 0.7	-7.0 ± 0.3
Mepivacaine	7 ± 3.4	-6.7 ± 0.6	-0.3 ± 0.6	-7.0 ± 0.3
Bupivacaine	8 ± 3.9	-5.7 ± 0.4	-1.1 ± 0.5	-6.8 ± 0.3
Articane	12 ± 3.1	-6.9 ± 0.3	-0.3 ± 0.30	-6.6 ± 0.2
Lidocaine	12 ± 6.9	-5.0 ± 0.4	-1.6 ± 0.55	-6.6 ± 0.3
Prilocaine	13 ± 3.6	-5.5 ± 0.3	-1.1 ± 0.4	-6.6 ± 0.2
Benzocaine	22 ± 9	-8.8 ± 0.7	2.6 ± 0.7	-6.3 ± 0.2

[a] Data acquired at 20 °C in buffer A (10 mM sodium phosphate, 140 mM NaCl, pH 7.4) and an aptamer concentration of 100 µM and a ligand concentration of 1.56 mM, except where noted.
[b] Performed with an aptamer concentration of 20 µM and a ligand concentration of 0.312 mM.

3.3.3 DSC Studies of Ligand Binding by MN4

To complement the ITC binding studies, DSC was used to examine how local anesthetic binding influences the thermal stability of MN4. As a collaborative effort, DSC data was collected in conjunction with Dang Yen Ha Pham. While ITC provides information on binding affinity and the thermodynamic forces that drive complex formation, DSC reports on the thermal unfolding behaviour of the free and bound aptamer and can therefore reveal whether ligand association stabilizes or destabilizes the folded nucleic acid structure. This distinction is important as ligand binding does not necessarily result in global stabilization of the aptamer; favourable local aptamer–ligand interactions may occur alongside disruption of pre-existing base-pairing, altered tertiary packing, or changes in conformational heterogeneity.

The thermal unfolding profile of MN4 was first measured in the absence of ligand to establish the baseline stability of the free aptamer. MN4 was then analysed in the presence of each local anesthetic to determine whether ligand binding altered the melt temperature, unfolding enthalpy, or overall shape of the DSC thermogram. Changes in these parameters were used to assess whether each ligand stabilizes the folded aptamer structure, destabilizes the aptamer, or induces a more complex thermal response consistent with structural remodeling or conformational redistribution.

The DSC-derived thermal parameters for each MN4–ligand system are summarized in Table 3.3.3.1. Free MN4 exhibited a melt temperature (T_m) of (54.39 ± 0.04) °C, consistent with thermal unfolding of the preformed structure reported for this aptamer in previous studies.[113] In contrast to quinine, which increased the T_m of MN4 to (63.4 ± 0.1) °C, all local anesthetics decreased the apparent T_m of MN4 relative to the free aptamer. This indicates that local anesthetic binding is associated with thermal destabilization of MN4 rather than ligand-induced stabilization.

The extent of destabilization varied substantially across the ligand series. Benzocaine produced the largest decrease in apparent T_m, lowering the transition temperature to (34.84 ± 0.04) °C (Figure 3.3.3.1, Table 3.3.3.1). This substantial shift to lower temperature suggests that benzocaine binding strongly perturbs stabilizing interactions within the free MN4 structure. Bupivacaine also produced pronounced destabilization, with a T_m of (39.53 ± 0.04) °C. These lower transition temperatures were accompanied by

reduced DSC-derived unfolding free energies, with ΔG_{unf} values of (17 ± 4) kJ mol^{-1} for the MN4–benzocaine complex and (19 ± 9) kJ mol^{-1} for the MN4–bupivacaine complex. These values suggest that the benzocaine- and bupivacaine-bound states are less resistant to thermal unfolding than free MN4.

By comparison, tetracaine and procaine produced the smallest decreases in thermal stability, with T_m values of (52.1 ± 0.1) °C and (52.3 ± 0.5) °C, respectively (Figure 3.3.3.2 and Figure 3.3.3.8). The proximity of these transitions to that of free MN4 suggests that these ligands preserve more of the stabilizing interactions within the aptamer than the other local anesthetics tested. Notably, despite differences in their ITC-derived binding affinities and enthalpic/entropic signatures, all local anesthetics reduced the apparent thermal stability of MN4 (Figure 3.3.3.3-3.3.3.7). These findings indicate that favourable ligand binding can occur alongside global destabilization of the aptamer, consistent with a mechanism in which local aptamer–ligand contacts are coupled to disruption, remodeling, or conformational redistribution of the pre-existing MN4 structure.

The contrasting behaviour of quinine highlights the distinct nature of local anesthetic binding. Previous DSC studies of the MN4–quinine complex showed that quinine stabilizes MN4, increasing the T_m by approximately 9 °C relative to free MN4.[120] This behaviour is consistent with a classical ligand-induced stabilization model, in which ligand binding stabilizes the folded aptamer structure. In contrast, the local anesthetics investigated here bind MN4 while decreasing its apparent thermal stability, suggesting a less conventional binding mode involving structural perturbation rather than global stabilization.

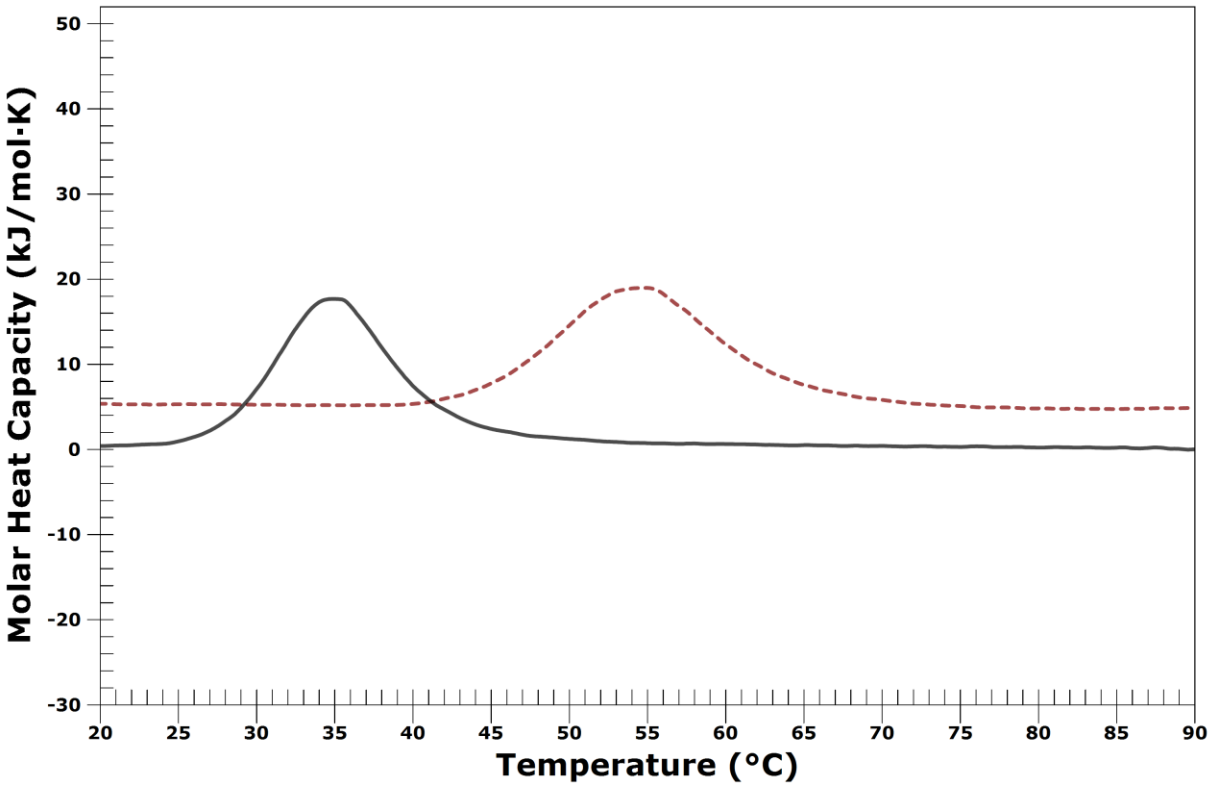

Figure 3.3.3.1. DSC heat capacity profile for MN4 free (dashed line) and bound to benzocaine (black line). Samples were equilibrated for 600 seconds prior to heating and cooling cycles. Samples were heated and cooled at a rate of 1°C/min for each scan. When bound to benzocaine, the melt temperature (T_m) of the complex is (34.84 ± 0.04) °C which is lower than that of free MN4, indicating a reduction in thermal stability upon complexation. Data collected by Dang Yen Ha Pham.

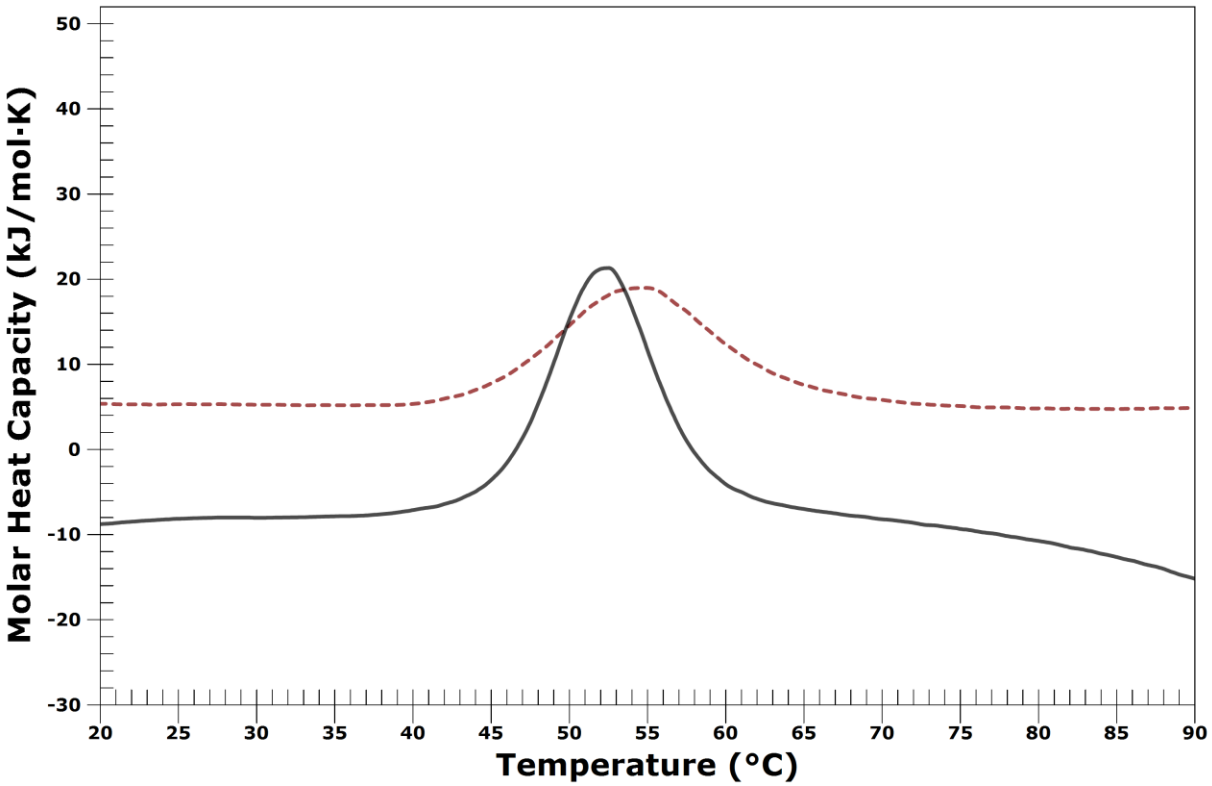

Figure 3.3.3.2. DSC heat capacity profile for MN4 free (dashed line) and bound to tetracaine (black line). Samples were equilibrated for 600 seconds prior to heating and cooling cycles. Samples were heated and cooled at a rate of 1°C/min for each scan. When bound to tetracaine, the melt temperature (T_m) of the complex is (52.1 ± 0.1) °C which is lower than that of free MN4, indicating reduced thermal stability upon complexation. Data collected by Dang Yen Ha Pham.

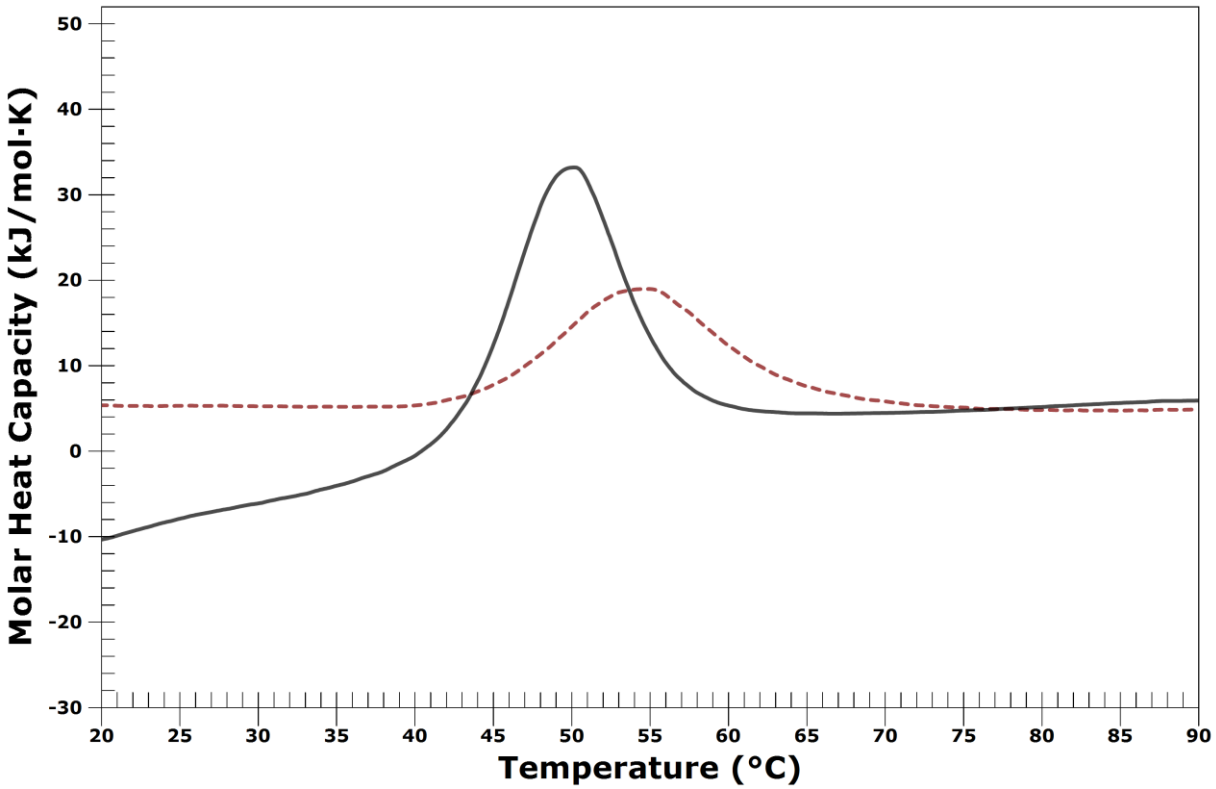

Figure 3.3.3.3. DSC heat capacity profile for MN4 free (dashed line) and bound to articaine (black line). Samples were equilibrated for 600 seconds prior to heating and cooling cycles. Samples were heated and cooled at a rate of 1°C/min for each scan. When bound to articaine, the melt temperature (T_m) of the complex is (49.8 ± 0.1) °C which is lower than that of free MN4, indicating a reduction in thermal stability upon complexation. Data collected by Dang Yen Ha Pham.

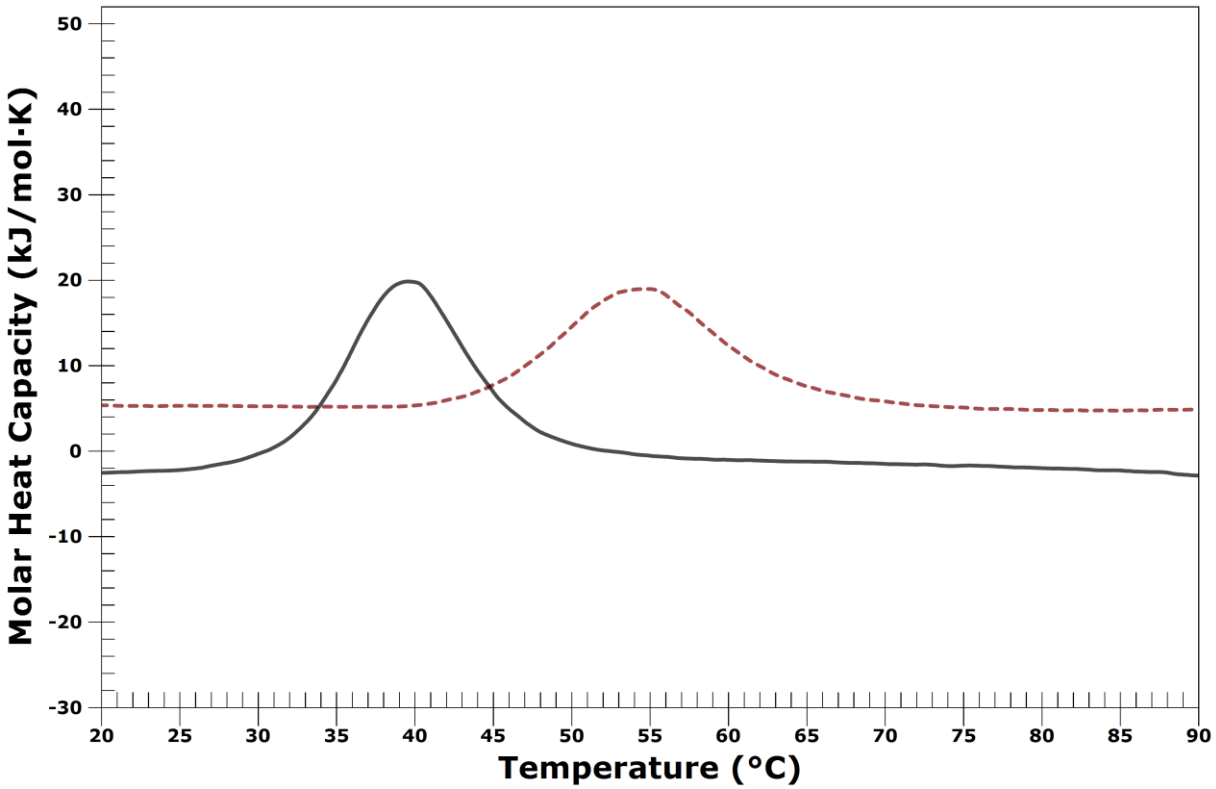

Figure 3.3.3.4. DSC heat capacity profile for MN4 free (dashed line) and bound to bupivacaine (black line). Samples were equilibrated for 600 seconds prior to heating and cooling cycles. Samples were heated and cooled at a rate of 1°C/min for each scan. When bound to bupivacaine, the melt temperature (T_m) of the complex is (39.53 ± 0.04) °C which is lower than that of free MN4, indicating a reduction in thermal stability upon complexation. Data collected by Dang Yen Ha Pham.

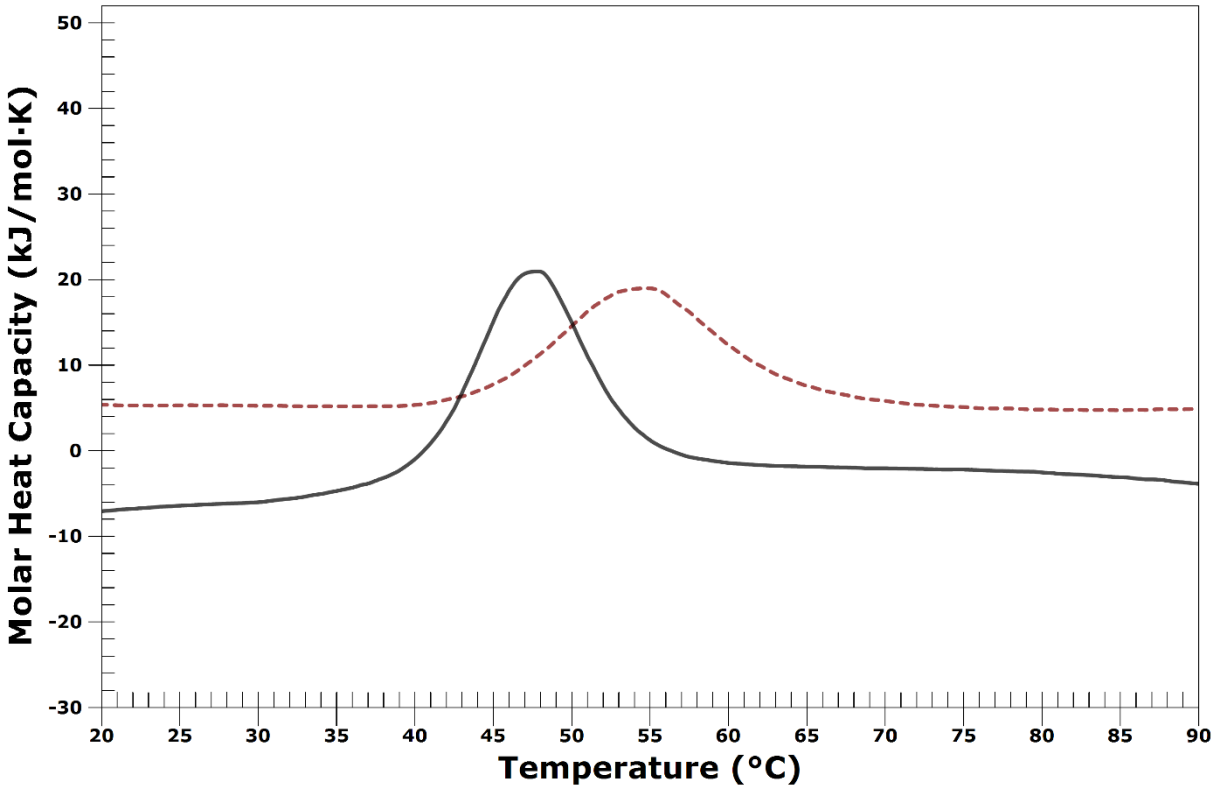

Figure 3.3.3.5. DSC heat capacity profile for MN4 free (dashed line) and bound to lidocaine (black line). Samples were equilibrated for 600 seconds prior to heating and cooling cycles. Samples were heated and cooled at a rate of 1°C/min for each scan. When bound to lidocaine, the melt temperature (T_m) of the complex is (47.5 ± 0.04) °C which is lower than that of free MN4, indicating a reduction in thermal stability upon complexation. Data collected by Dang Yen Ha Pham.

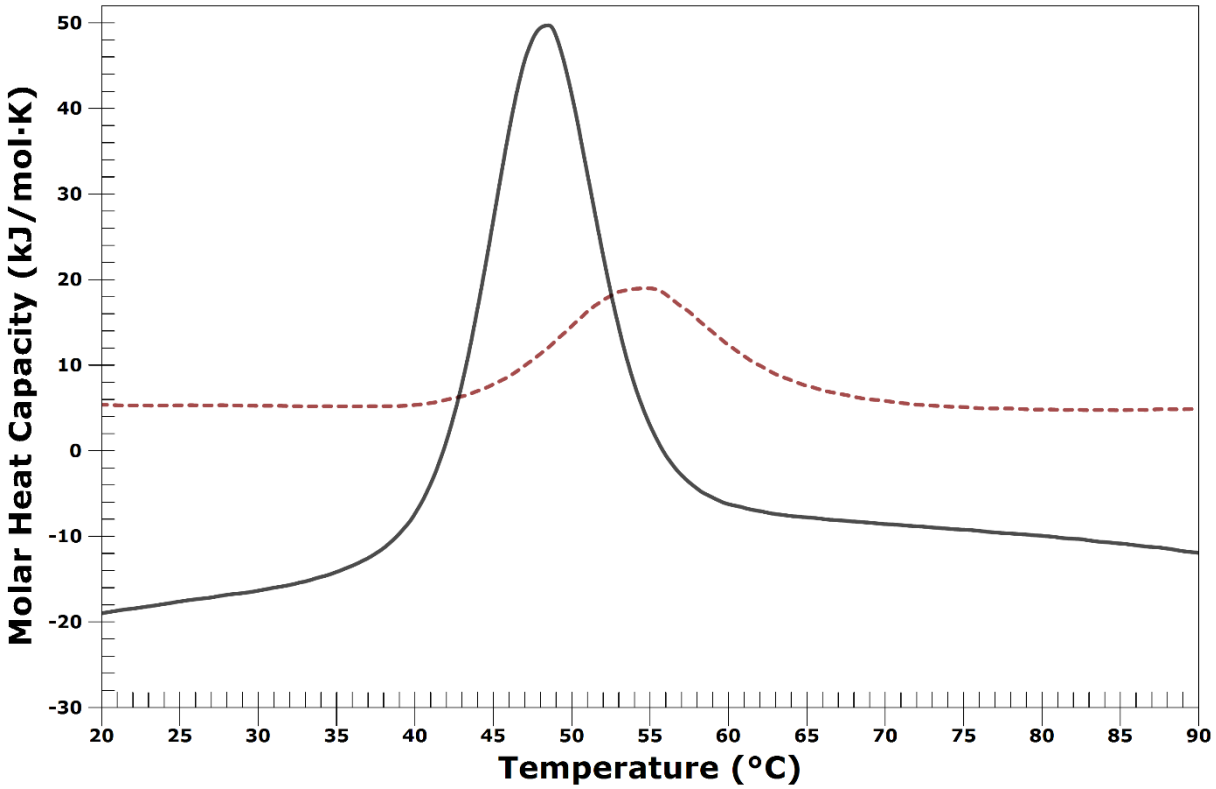

Figure 3.3.3.6. DSC heat capacity profile for MN4 free (dashed line) and bound to mepivacaine (black line). Samples were equilibrated for 600 seconds prior to heating and cooling cycles. Samples were heated and cooled at a rate of 1°C/min for each scan. When bound to mepivacaine, the melt temperature (T_m) of the complex is (48.21 ± 0.05) °C which is lower than that of free MN4, indicating a reduction in thermal stability upon complexation. Data collected by Dang Yen Ha Pham.

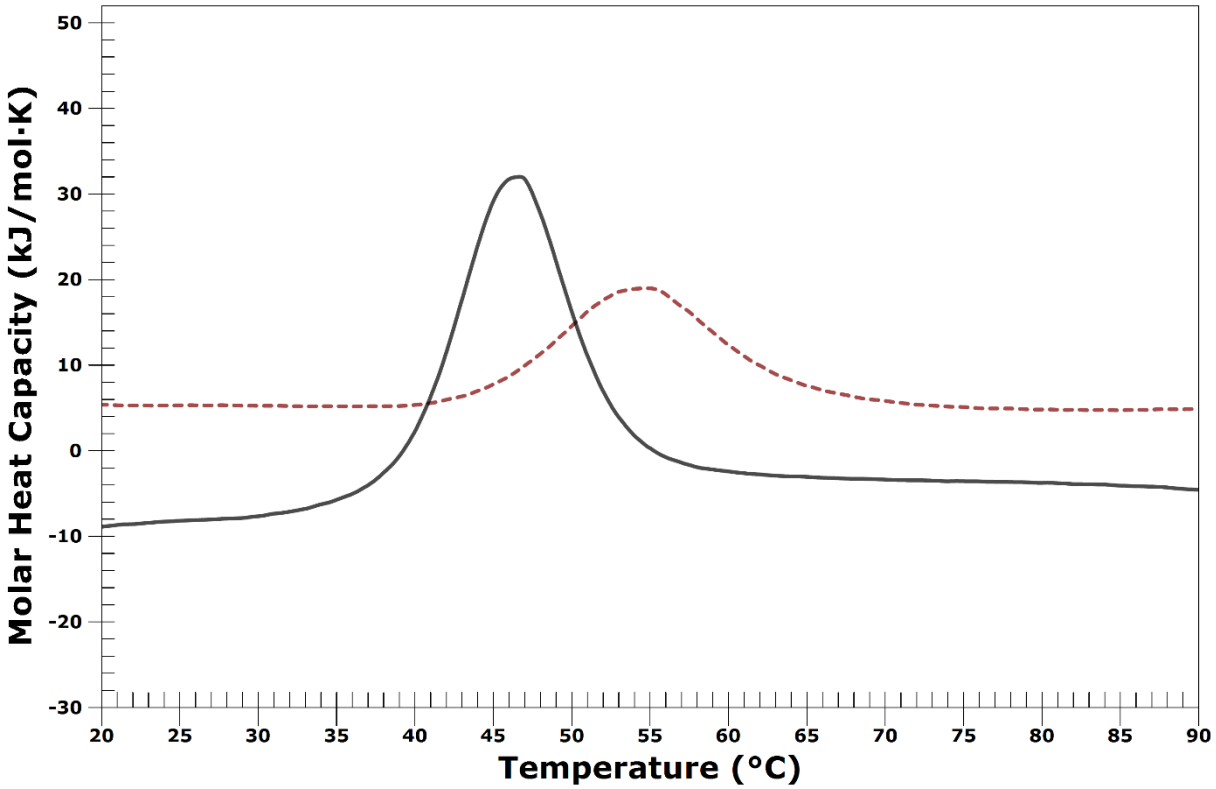

Figure 3.3.3.7. DSC heat capacity profile for MN4 free (dashed line) and bound to prilocaine (black line). Samples were equilibrated for 600 seconds prior to heating and cooling cycles. Samples were heated and cooled at a rate of 1°C/min for each scan. When bound to prilocaine, the melt temperature (T_m) of the complex is (46.34 ± 0.05) °C which is lower than that of free MN4, indicating a reduction in thermal stability upon complexation. Data collected by Dang Yen Ha Pham.

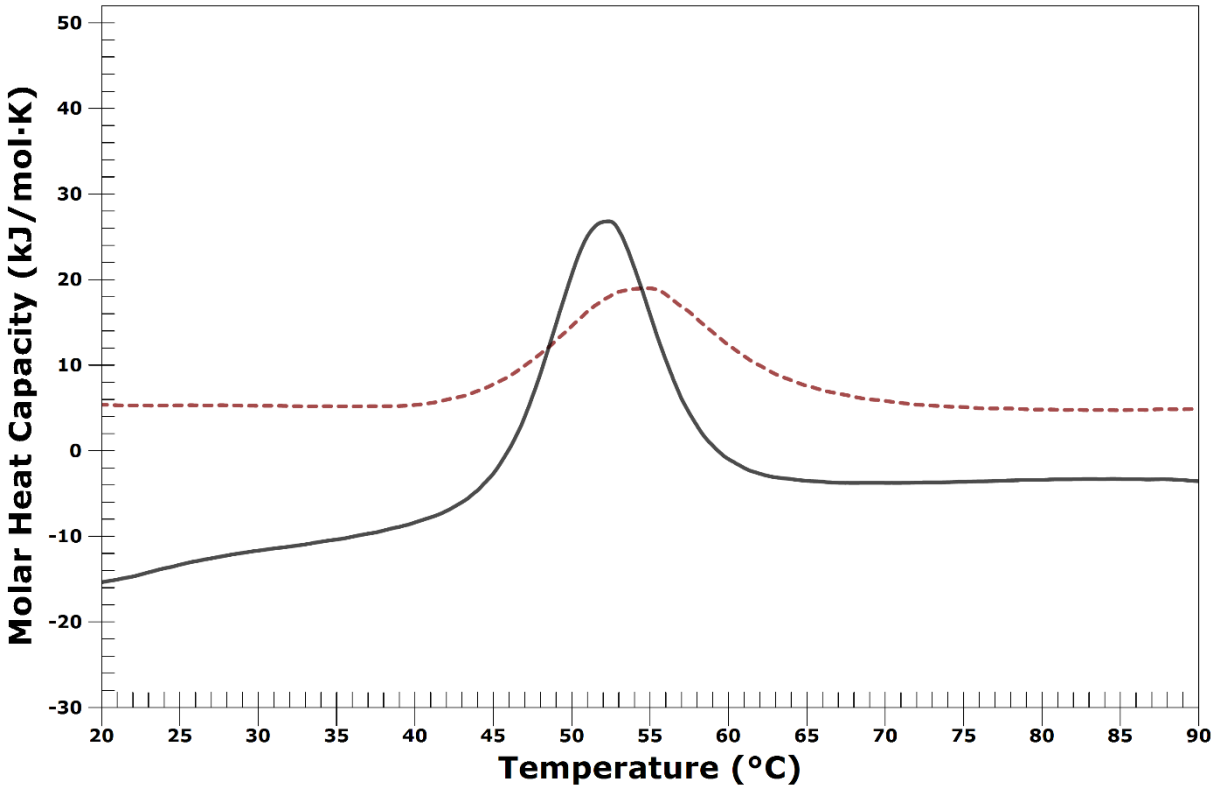

Figure 3.3.3.8. DSC heat capacity profile for MN4 free (dashed line) and bound to procaine (black line). Samples were equilibrated for 600 seconds prior to heating and cooling cycles. Samples were heated and cooled at a rate of 1°C/min for each scan. When bound to procaine, the melt temperature (T_m) of the complex is (52.3 ± 0.5) °C which is lower than that of free MN4, indicating a reduction in thermal stability upon complexation. Data collected by Dang Yen Ha Pham.

Table 3.3.3.1. DSC results of the MN4 aptamer with various ligands in 10 mM $NaHPO_4$, 140 mM NaCl at pH 7.4 and 3 atm pressure. Data acquired with an aptamer concentration of 180 µM and a ligand concentration of 1.8 mM, except where noted. Heating rate of 1°C / min.

	T_m (°C)	ΔH_{unf} (kJ mol^{-1})	ΔS_{unf} (kJ mol^{-1} K^{-1})	ΔG_{unf} (kJ mol^{-1})
MN4	54.39 ± 0.04	273 ± 2	0.82 ± 0.03	29 ± 2
MN4 + Quinine[a]	63.4 ± 0.1	405 ± 15	1.20 ± 0.05	52 ± 20
MN4 + Tetracaine[b]	52.1 ± 0.1	397.8 ± 0.2	1.223 ± 0.001	39.2 ± 0.4
MN4 + Procaine	52.3 ± 0.5	393 ± 8	1.21 ± 0.02	39 ± 11
MN4 + Articaine	49.8 ± 0.1	363 ± 2	1.12 ± 0.01	33 ± 3
MN4 + Mepivacaine	48.21 ± 0.05	367 ± 3	1.14 ± 0.01	32 ± 5
MN4 + Lidocaine	47.5 ± 0.1	358 ± 1	1.117 ± 0.003	31 ± 1
MN4 + Prilocaine	46.34 ± 0.05	360 ± 1	1.125 ± 0.004	30 ± 2
MN4 + Bupivacaine	39.53 ± 0.04	310 ± 6	0.99 ± 0.02	19 ± 9
MN4 + Benzocaine	34.84 ± 0.04	346 ± 3	1.12 ± 0.01	17 ± 4

The values reported are averages of 5 individual experiments with the standard deviation as the reported error. ΔG_{unf} values were calculated at 20 °C.

[a] Data taken from [120]

[b] Data acquired with a ligand concentration of 0.9 mM.

Comparison of the ITC-derived free energy of binding with the DSC-derived change in melt temperature provided insight into how ligand affinity relates to MN4 thermal stability. Although all local anesthetics decreased the apparent T_m of MN4 relative to the free aptamer, the magnitude of this destabilization varied across the ligand series. The ITC-derived free energy of binding for each MN4-ligand complex was plotted as a function of the DSC-derived decrease in T_m for each complex relative to free MN4 (Figure 3.3.3.9). The moderate positive correlation suggests that more favourable binding free energy generally corresponded to smaller decreases in T_m, with tetracaine showing the strongest binding and one of the least destabilizing effects, while benzocaine showed the weakest binding and the largest decrease in T_m. This relationship suggests that ligands with stronger affinity may be more structurally compatible with the MN4 binding environment, allowing them to form favourable aptamer–ligand contacts while preserving more of the stabilizing interactions within the aptamer. Conversely, weaker-binding ligands may require greater disruption or conformational remodeling of MN4 to associate with the aptamer. Thus, the correlation between ΔG_{bind} and ΔT_m supports the conclusion that local anesthetic binding is ligand-dependent and that the extent of thermal destabilization reflects how well each ligand is accommodated by the preformed MN4 structure. Because ΔG_{bind} and ΔT_m describe different thermodynamic processes, this relationship should be interpreted qualitatively rather than as evidence of direct energetic equivalence between binding and unfolding.

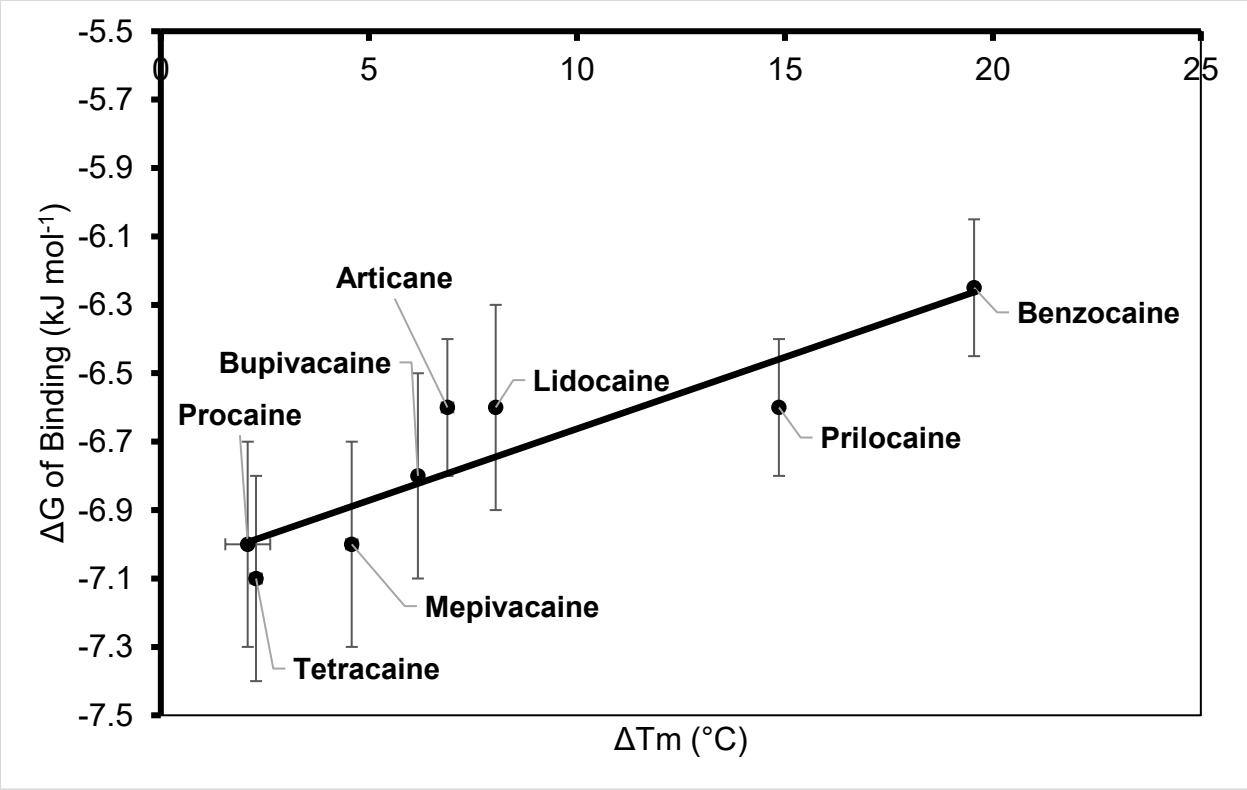

Figure 3.3.3.9. A plot of the ΔG_{bind} acquired from ITC as a function of the change in T_m between free MN4 and each MN4-ligand complex. The positive correlation suggests that more favourable ΔG_{bind} values correspond to smaller decreases in T_m values, indicating that tighter-binding ligands better preserve MN4 thermal stability, despite all local anesthetics inducing some degree of destabilization.

3.4 Conclusions

This study demonstrates that MN4 is capable of binding a structurally diverse series of local anesthetics, including benzocaine, tetracaine, procaine, mepivacaine, bupivacaine, articaine, lidocaine, and prilocaine. ITC analysis showed that all ligands bind MN4 with micromolar affinity and are consistent with an apparent 1:1 binding interaction. Among the anesthetics investigated, tetracaine exhibited the strongest affinity, whereas benzocaine showed the weakest affinity. The thermodynamic signatures varied across the ligand series, indicating that structurally related local anesthetics do not interact with MN4 through an identical energetic mechanism. Some ligands were primarily enthalpically driven with unfavourable entropy, whereas others showed both favourable enthalpic and entropic contributions, suggesting that differences in local contacts, desolvation, conformational rearrangement, and aptamer dynamics contribute to binding.

DSC analysis revealed a clear distinction between local anesthetic binding and the previously characterized MN4–quinine interaction. Whereas quinine stabilizes MN4 and increases its melt temperature relative to the free aptamer, all local anesthetics decreased the apparent T_m of MN4. This indicates that local anesthetic binding is associated with global thermal destabilization rather than classical ligand-induced stabilization. The extent of destabilization varied substantially across the ligand series, with benzocaine producing the largest decrease in apparent T_m and tetracaine producing one of the smallest decreases. These findings show that ligand binding and aptamer stabilization are not necessarily coupled. Instead, favourable ligand association can occur alongside reduced global thermal stability, suggesting that local anesthetic binding may disrupt, remodel, or redistribute stabilizing interactions within the preformed MN4 structure.

Comparison of the ITC-derived free energy of binding with the DSC-derived change in melt temperature provided further insight into the relationship between ligand affinity and thermal destabilization. Although all local anesthetics reduced the apparent T_m of MN4, more favourable binding free energies were generally associated with smaller decreases in T_m. Tetracaine, which exhibited the most favourable ΔG_{bind} among the local anesthetics, produced one of the least destabilizing effects, whereas benzocaine, which showed the weakest binding, produced the largest decrease in T_m. This relationship suggests that stronger-binding ligands are better accommodated within the MN4 binding environment and preserve more of the stabilizing interactions present in the free aptamer. In contrast, weaker-binding ligands may require greater disruption or remodeling of the pre-existing MN4 structure to associate with the aptamer. Therefore, while local anesthetic binding is generally associated with thermal destabilization, the magnitude of this destabilization appears to be inversely related to binding strength.

NMR spectroscopy provided further evidence that local anesthetic binding induces defined structural changes in MN4. Titration of benzocaine and tetracaine into MN4 produced new imino resonances and slow-exchange behaviour between free and bound states, consistent with formation of discrete ligand-bound conformations. A recurring shift of the characteristic G31 resonance was observed not only for benzocaine and tetracaine, but also across the broader local anesthetic series, indicating that these ligands perturb a similar region of the MN4 structure. However, the final spectra of the different

MN4–ligand complexes were not identical, suggesting that each ligand promotes a related but distinct bound-state ensemble. The presence of sharp, well-resolved imino resonances in the saturated complexes indicates that ligand binding does not simply unfold MN4; rather, local anesthetics promote specific structural rearrangements while retaining protected base-paired regions.

Temperature-dependent NMR experiments on free MN4, MN4–benzocaine, and MN4–tetracaine further supported this interpretation. Benzocaine and tetracaine were selected because they represented the extremes of thermal destabilization observed by DSC. The imino resonances of free MN4 and the MN4–benzocaine complex were largely lost by approximately 45 °C, whereas the MN4–tetracaine complex retained detectable imino resonances until approximately 50 °C. Although these NMR thermal-melt experiments provide a qualitative measure of local structural persistence rather than a direct Tm measurement, the results are consistent with DSC data showing that tetracaine is less destabilizing than benzocaine. Together, the DSC and NMR results indicate that local anesthetic binding reduces the global thermal stability of MN4 while still allowing formation or retention of localized structured regions.

Overall, these findings support a binding model in which local anesthetics interact with MN4 through local aptamer–ligand contacts that induce structural remodeling rather than global stabilization of the aptamer fold. The shared G31 resonance shift suggests that the anesthetics engage or perturb a common structural region of MN4, while differences in final NMR spectra, binding thermodynamics, and thermal stability indicate ligand-specific effects on the bound-state ensemble. This work highlights an important nonclassical mode of aptamer–small molecule recognition in which measurable ligand binding occurs alongside aptamer destabilization. More broadly, the results emphasize the value of combining ITC, DSC, and NMR to distinguish binding affinity, thermal stability, and structural organization in aptamer–ligand systems.

Chapter 4 The Butterfly Structure of Leucomethylene Blue Results in Weak Binding to Single- or Double-Stranded DNA

4.1 Preface

All work presented in this chapter has been published in the article below [121]

- Batchelor, R. H., Kaiyum, Y. A., Chao, E. H. P., Tenorio, N., Ofori, C., Bird, S. A., Brand, H. E. A., Auckett, J. E., Karouei, M. H., Richardson, K., Vlcek, V., Johnson, P. E., Gooding, J. J., & Bonham, A. J. (2025). The Butterfly Structure of Leucomethylene Blue Results in Weak Binding to Single- or Double-Stranded DNA. *Journal of Physical Chemistry B*, *129*(47), 12110–12119.
- The work presented here was completed by Kaiyum, Y. A.

4.2 Introduction

The small molecule methylene blue (MB) (Figure 4.2.1) has been used in a wide variety of scientific, medical, and veterinary applications[122–124] since its discovery and description in the late 19th century.[125,126] Critically, a class of sensors called electrochemical aptamer-based (E-AB) biosensors rely on MB as the electrically active reporter moiety.[127–130] Thus, an improved understanding of how MB interacts with other components of the E-AB system would inform better biosensor design and help explain or avoid unexpected side processes. MB interacts with a variety of molecules including double-stranded DNA and single-stranded DNA.[130–132] Numerous groups have explored the mechanisms of how MB interacts with both double-stranded and single-stranded DNA using laboratory and modeling methods.[133–142] MB is known to bind DNA via several binding modes, including both intercalation and electrostatic driven interactions[143], with the preferred mode of MB binding dependent on a combination of the salt concentration, the MB/dsDNA ratio, and the base composition, as MB has a known preference for guanine bases.[130] These investigations have included how MB binding to DNA impacts the photophysical properties of MB, such as hypochromism and bathochromism,[144,145] and quenching of MB fluorescence.[146,147]

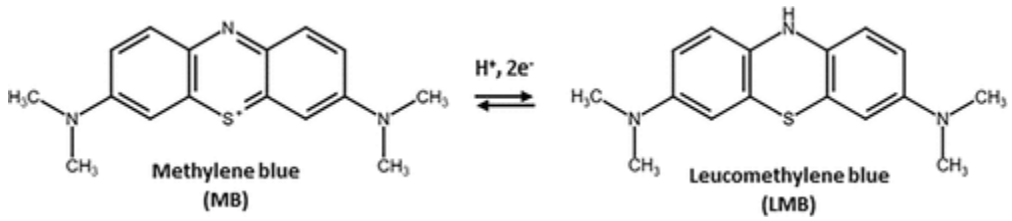

Figure 4.2.1. Methylene Blue (MB) and its Reduced Form, Leucomethylene Blue (LMB)

MB can be reduced to leucomethylene blue (LMB) (Figure 4.2.1) electrochemically,[148,149] and chemically using reducing agents such as glutathione,[150] nicotinamide adenine dinucleotide,[151] ascorbic acid, glucose, sodium sulfite,[152] and tris(2-carboxyethyl)phosphine hydrochloride (TCEP).[153] E-AB biosensors, and many other MB-based sensors, typically rely on the repeated reduction of MB and reoxidation of the resultant LMB during electrochemical interrogation to generate a current.[61,130] Therefore, understanding the possible interactions of LMB with double-stranded and single-stranded DNA is important to improve sensor systems that utilize MB and DNA.

However, LMB has not been as deeply investigated as MB. This lack of investigation is likely partially driven by experimental difficulties working with LMB, as it readily reoxidizes to MB in ambient conditions.[154] To date, there are two reports in the literature on the photophysical properties of LMB in aqueous solution,[154,155] and four on how LMB interacts with DNA.[128,156–158] An examination of LMB/DNA interactions and their structural cause has not been reported. In particular, while MB is well-characterized as planar,[159] LMB has been reported to be nonplanar based on quantum modeling.[160] The predicted nonplanarity, in combination with the neutral charge of LMB, creates the expectation that the binding affinity of LMB for DNA should be weaker than that of MB. However, neither robust evidence of the nonplanarity, the binding affinity of LMB for DNA, nor the photophysical impact of LMB bound to DNA have been described.

Toward that end, a multifaceted approach investigating LMB and its interactions with single- and double-stranded DNA was performed. As part of a large collaborative effort, quantum modeling studies of LMB and for the first time, X-ray crystallographic data of LMB was collected. Additionally, we characterize the interaction of MB and LMB with double-stranded and single-stranded DNA constructs via absorbance, fluorescence, nuclear magnetic resonance (NMR), and isothermal titration calorimetry (ITC)-based methods. Together, these observations support the hypothesis that the nonplanar, “butterfly,” structure of LMB results in greatly reduced binding affinity for single- and double-stranded DNA compared with MB binding.

4.3 Materials and Methods

4.3.1 NMR Spectroscopy

NMR data were acquired on a 600 MHz Bruker AvanceIII Spectrometer as well as a 700 MHz Bruker Neo Spectrometer in a manner similar to what has been previously described.[72] All one-dimensional ^{1}H NMR spectra were acquired in an aqueous solution of 10 mM phosphate buffer at pH 7.0 in $^{1}H_2O/^{2}H_2O$ (90%/10%) at 5 °C. Water suppression was achieved using excitation sculpting.[90] The DNA concentration for NMR studies was 0.5 mM. Methylene Blue (Catalog Number – M9140) and sodium dithionite (Catalog Number – 71699) were purchased from Millipore Sigma. The MB was dissolved in the same buffer as the DNA. MB was chemically reduced to LMB by treatment with 5 mM sodium dithionite for 5 min before measurement. Each of the six DNA sequences was initially titrated with MB until a 1:5 DNA to MB ratio was achieved. ^{1}H NMR spectra were acquired at 1, 3, and 5 molar equivalences of MB added. Following this, 10 equivalences of sodium dithionite were added to reduce the MB to LMB, and a final acquisition was performed within 15 min. The sodium dithionite was prepared in the same buffer as the DNA.

4.3.2 Isothermal Titration Calorimetry (ITC)

ITC data was acquired on a MicroCal PEAQ-ITC 200 instrument using standard procedures.[161] Samples were degassed before analysis with a MicroCal ThermoVac unit. All experiments were corrected for heat of dilution of titrant. Titrations were performed with the DNA in the cell and the ligand (either MB or LMB) as the titrant in the syringe. All DNA samples were heated in a 95 °C water bath for 1 min and cooled in an ice–water bath prior to use in a binding experiment. The binding experiments were performed at 20 °C with the DNA solutions prepared at 100 μM concentration. Both DNA and ligands were prepared in a 10 mM phosphate buffer at pH 7.0. Each experiment consisted of an initial delay of 60 s, a first injection of 2 μL, and a 300 s delay. The subsequent 19 injections were 2 μL, spaced every 150 s to allow for adequate mixing and equilibration before another injection. The first point was removed from all data sets due to

different delay parameters. ITC data following a one-site binding model were fitted using the manufacturer-provided Malvern Panalytical PEAQ-ITC analysis software.

ITC of Poly(dA), Poly(dG), Poly(dT) and Poly(dAdT) were performed on an Affinity ITC System (TA Instruments Inc., New Castle, DE). A typical binding experiment consisted of 20 successive injections. Each injection of 2 μL of 1.56 mM MB was titrated into the cell at an interval of 150 s with 125 rpm stirring at 20 °C. Data analysis was performed with NanoAnalyze software, and the heat of dilution was then subtracted to fit the data to the appropriate single-site binding model. The fitted data was then used to calculate the values of n, K_d and ΔH.

4.4 Results and Discussion

4.4.1 NMR Spectroscopy Demonstrates Binding of MB to DNA

NMR spectroscopy was used to assess the binding of MB to the six DNA constructs studied. For each of the DNA constructs, MB was added in 3 additions to a final molar ratio of 5:1 (MB/DNA). The effect of MB on the NMR spectra of each of the constructs was then investigated. In general, if the addition of ligand results in changes in the NMR spectrum this is evidence of binding.[162–164]

For the poly(dGdC) construct (Figure 4.4.1.1) in the free DNA the downfield imino protons are observed at 12.5–13.0 ppm indicating Watson–Crick base pair formation. There are also numerous other protons observed upfield from the imino protons, as expected for a DNA sample.[165] Upon the addition of MB, there is a decrease in the intensity of all NMR signals including the disappearance of the imino signals. This signal disappearance is attributed to the binding of MB by the DNA. The spectra suggest that MB intercalates randomly into the poly(dGdC) construct, with multiple MB molecules potentially binding a single dsDNA molecule. Therefore, a single bound complex does not form, rather an ensemble of different complexes that are in exchange with other forms. This results in the disappearance of the NMR signals as opposed to observing a single bound complex with a well-defined NMR spectrum. It was noted that for the poly(dGdC) construct there were no observable NMR signals from either the bound or free MB suggesting that the ligand is also exchanging. Similar behavior was observed in the NMR spectra of DNA aptamer

structures as well as the Dickerson-Drew dodecamer with the addition of quinine-based antimalarial compounds such as amodiaquine and chloroquine.[166] The other DNA constructs behaved in a similar manner with MB addition as the poly(dGdC) construct with only some subtle difference (Figure 4.4.1.2).

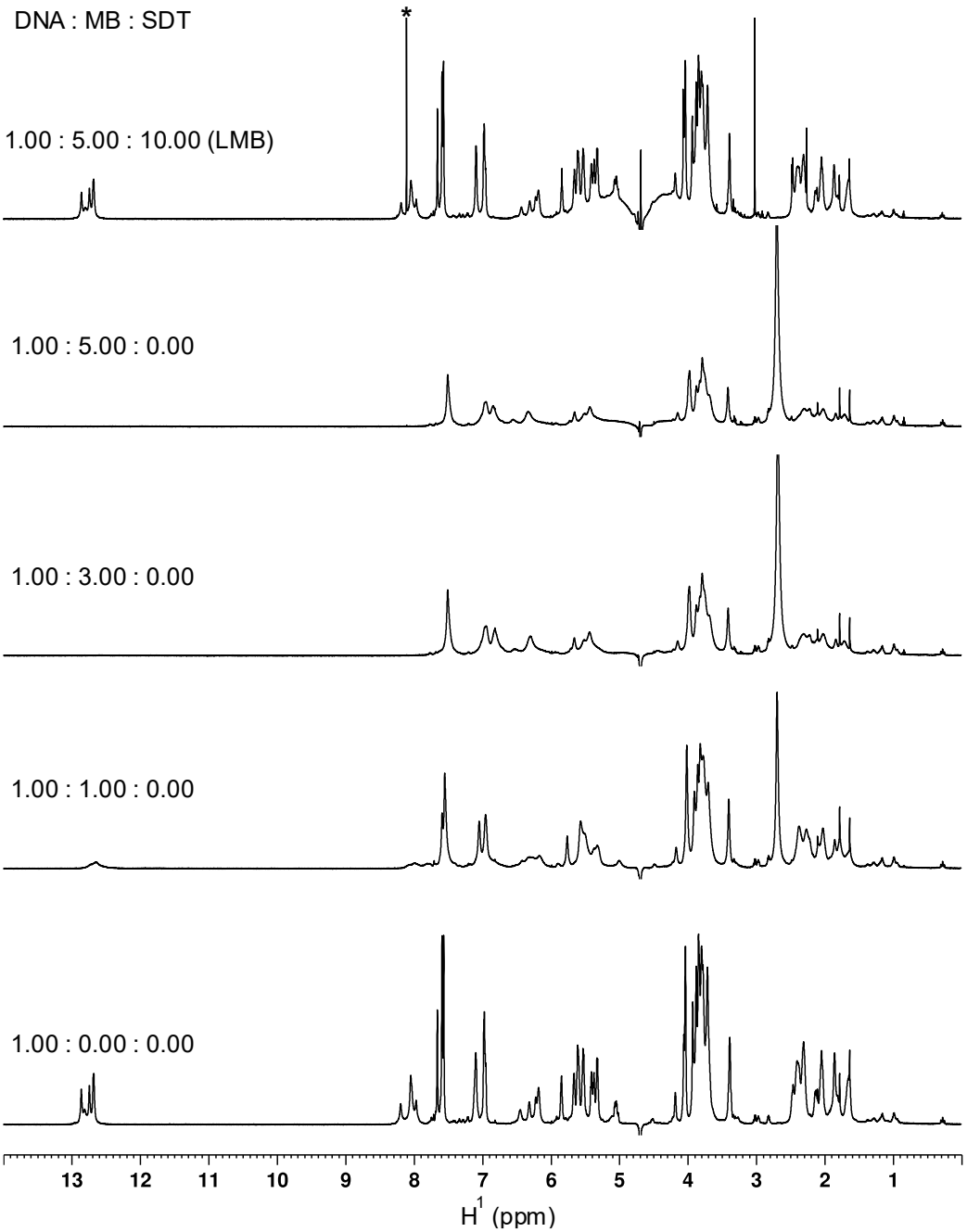

Figure 4.4.1.1. ^{1}H NMR spectra showing the titration of poly(dGdC) DNA with methylene blue (MB). Upon the addition of sodium dithionite (SDT) the MB is converted to LMB. Numbers on the left-hand side indicate the molar ratio of DNA/MB/SDT. A signal due to LMB is indicated with an asterisk. Experiments were conducted with a DNA concentration of 0.5 mM in 10 mM phosphate buffer, pH 7.4. in 90% $^{1}H_2O$/10% $^{2}H_2O$ at 5 °C

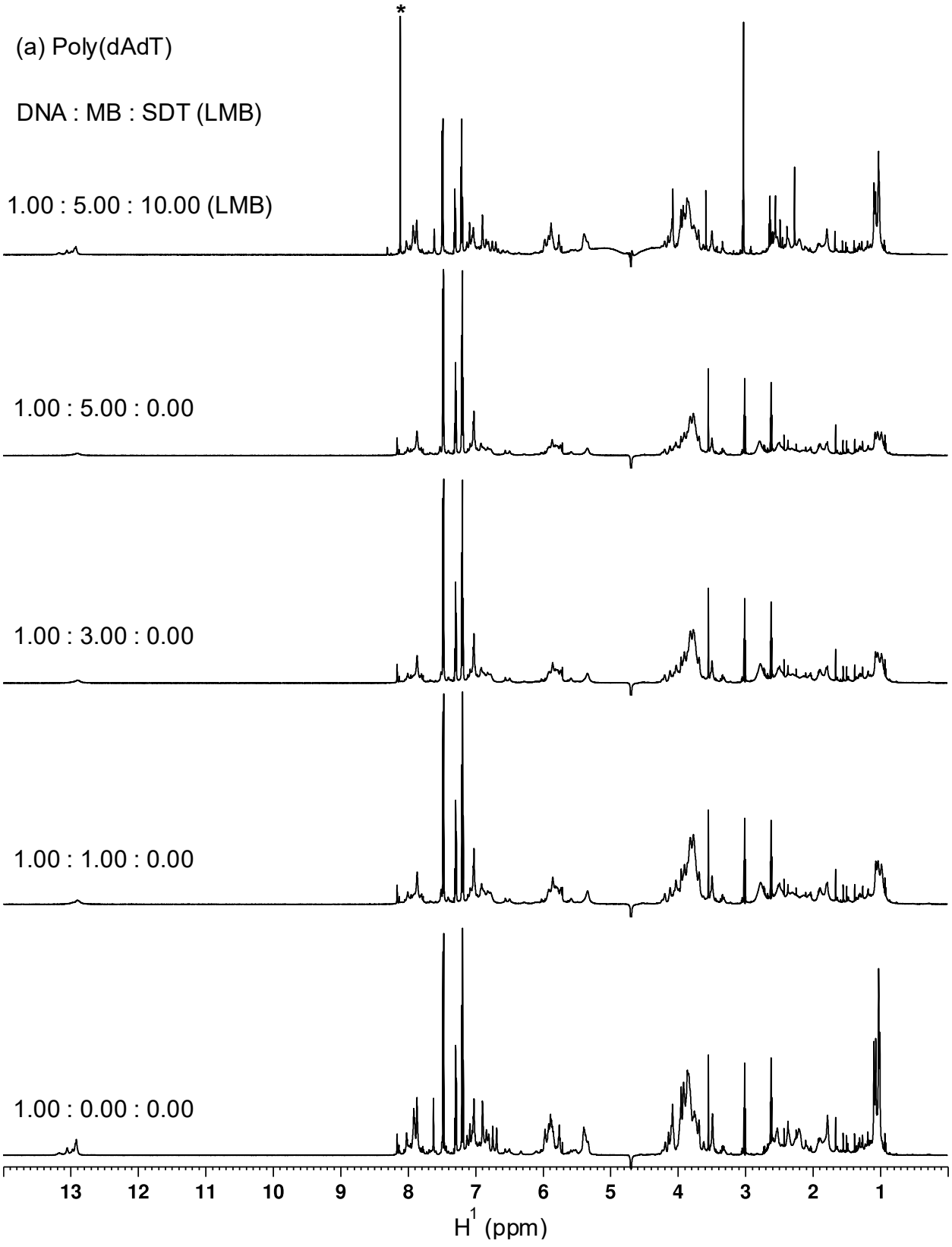
(a) Poly(dAdT)
DNA : MB : SDT (LMB)
1.00 : 5.00 : 10.00 (LMB)
1.00 : 5.00 : 0.00
1.00 : 3.00 : 0.00
1.00 : 1.00 : 0.00
1.00 : 0.00 : 0.00
*
13
12
11
10
9
8
7
6
5
4
3
2
1
H1 (ppm)

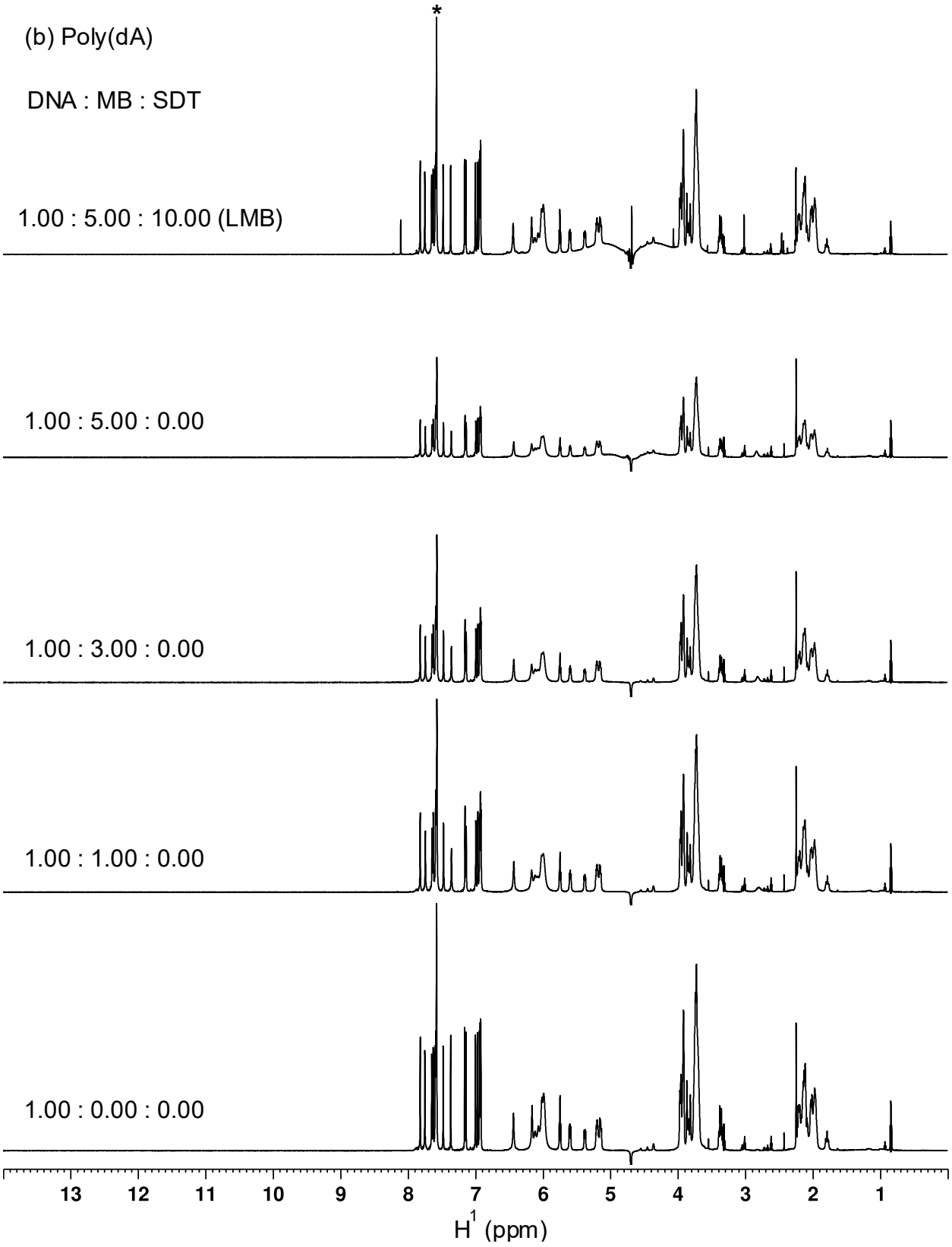
(b) Poly(dA)
DNA : MB : SDT
1.00 : 5.00 : 10.00 (LMB)
1.00 : 5.00 : 0.00
1.00 : 3.00 : 0.00
1.00 : 1.00 : 0.00
1.00 : 0.00 : 0.00
*
13
12
11
10
9
8
7
6
5
4
3
2
1
H1 (ppm)

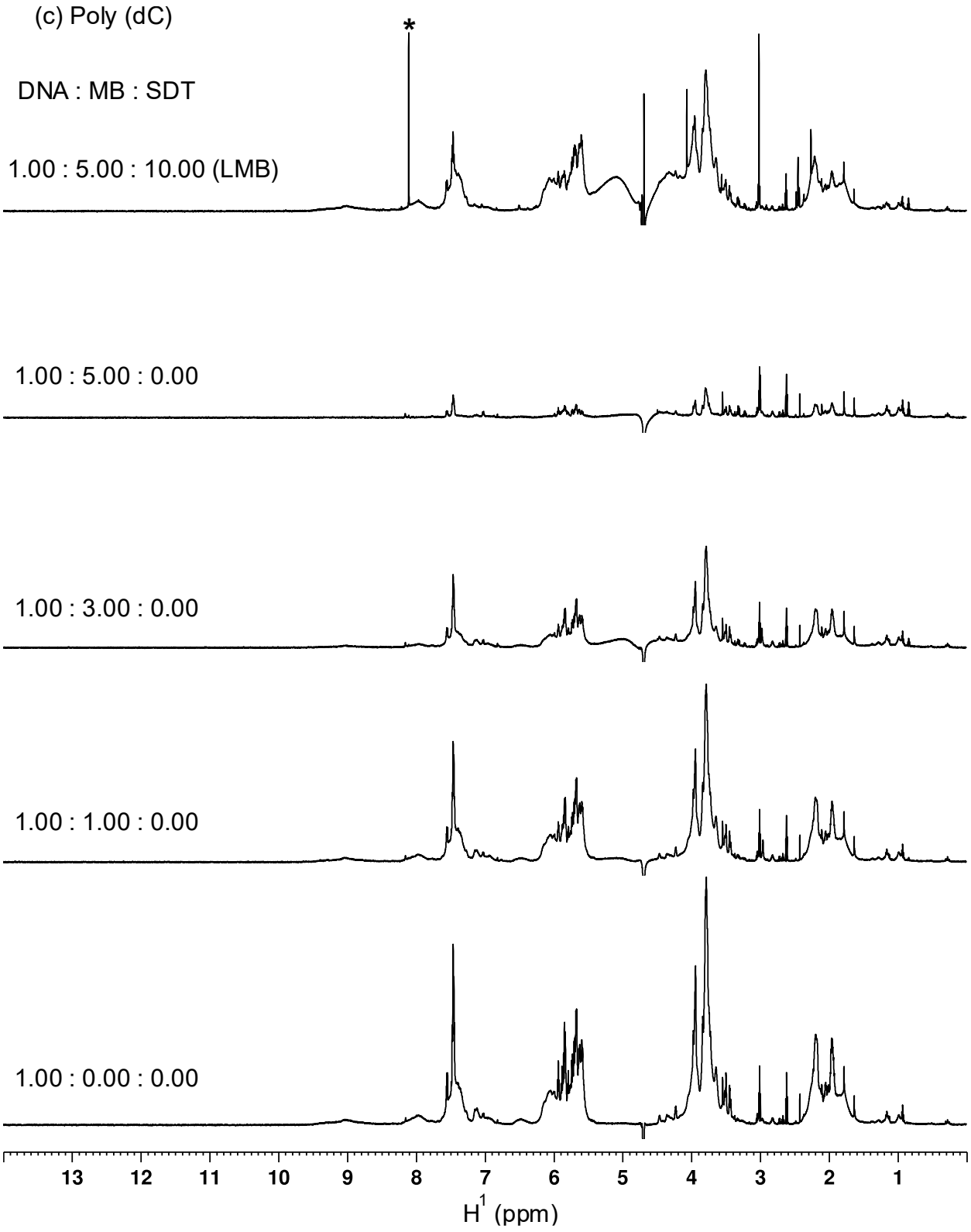
(c) Poly (dC)
DNA : MB : SDT
1.00 : 5.00 : 10.00 (LMB)
*
1.00 : 5.00 : 0.00
1.00 : 3.00 : 0.00
1.00 : 1.00 : 0.00
1.00 : 0.00 : 0.00
13
12
11
10
9
8
7
6
5
4
3
2
1
H1 (ppm)

(d) Poly(dG)

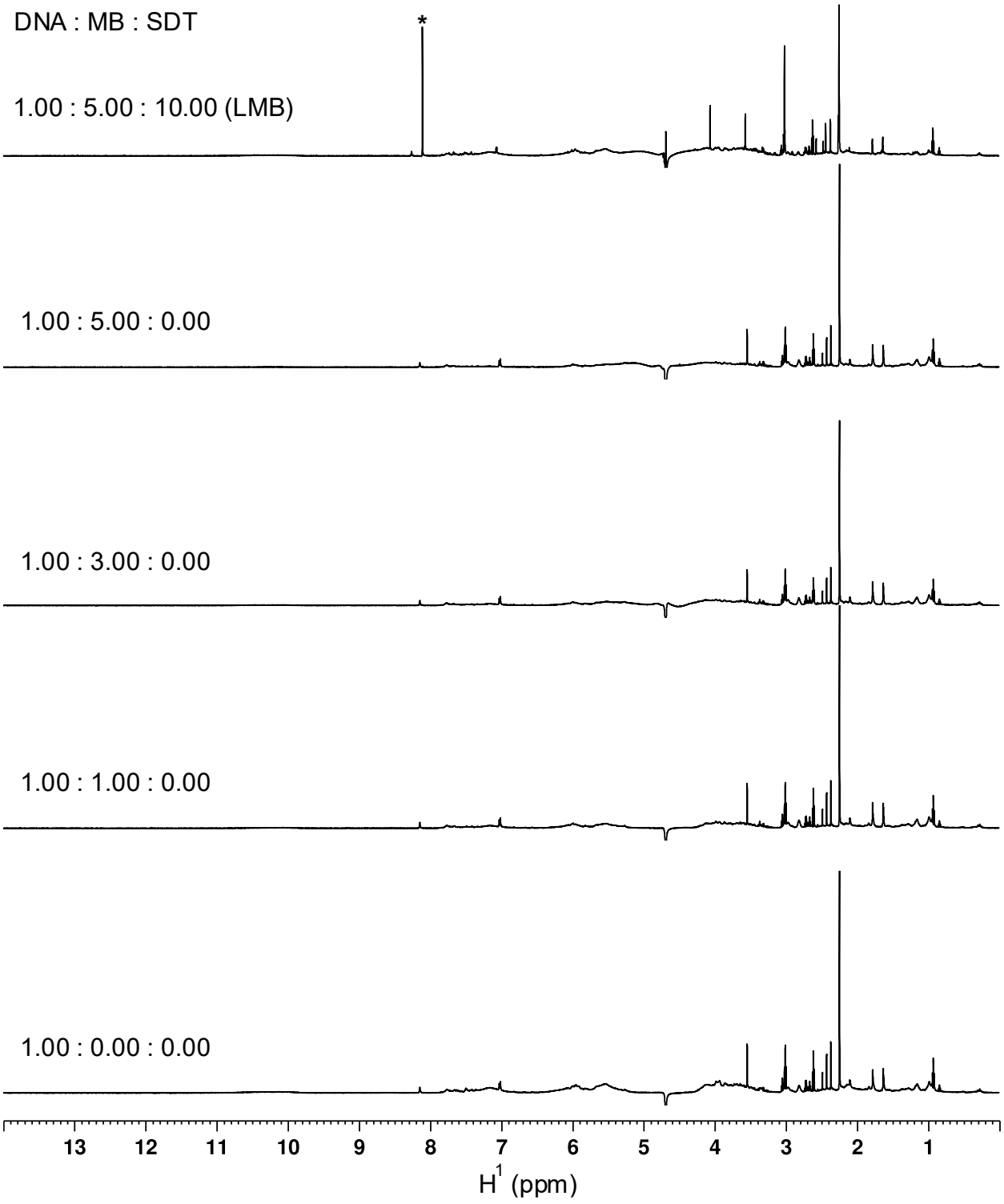
DNA : MB : SDT
*
1.00 : 5.00 : 10.00 (LMB)
1.00 : 5.00 : 0.00
1.00 : 3.00 : 0.00
1.00 : 1.00 : 0.00
1.00 : 0.00 : 0.00
13
12
11
10
9
8
7
6
5
4
3
2
1
H1 (ppm)

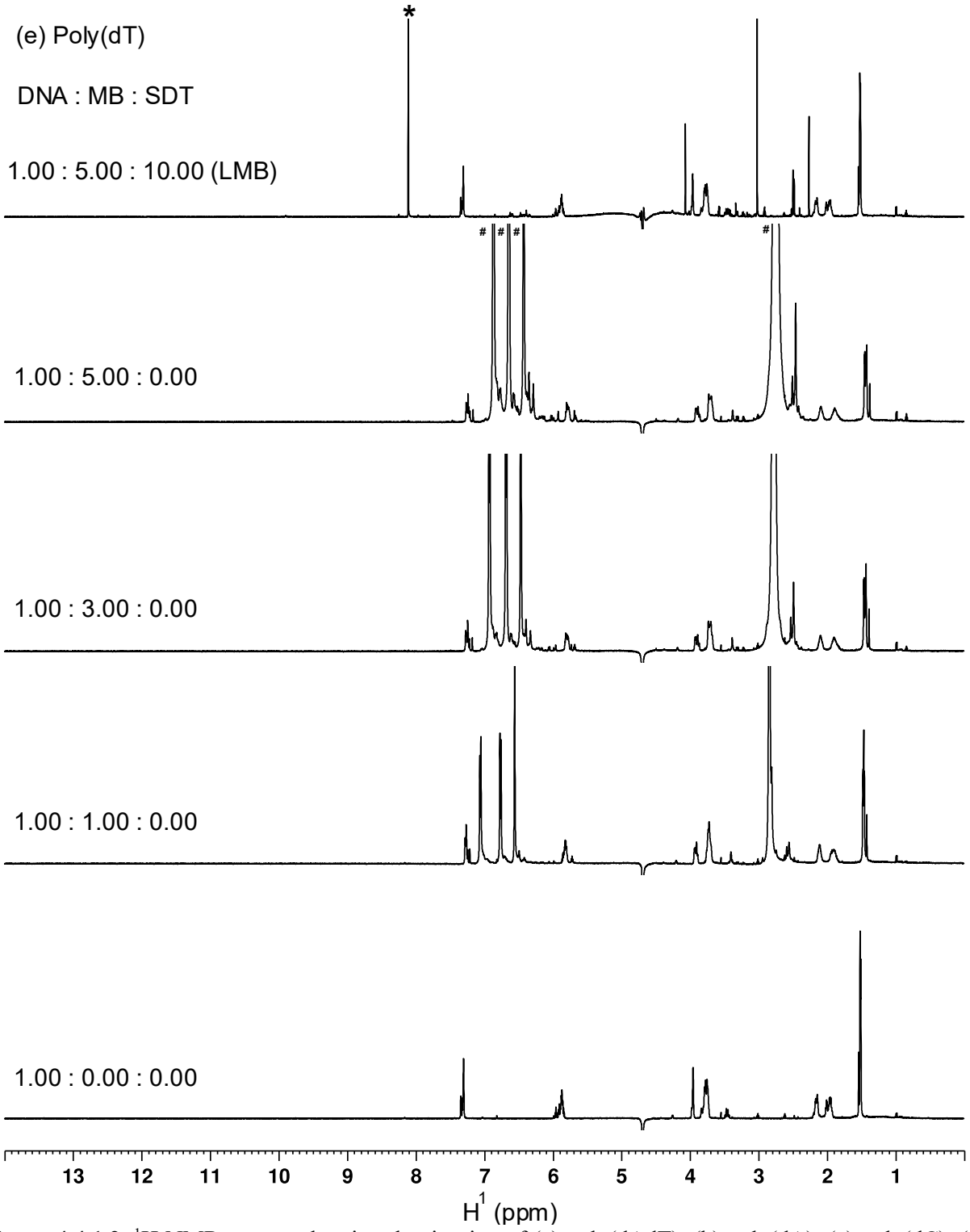

Figure 4.4.1.2. ^{1}H-NMR spectra showing the titration of (a) poly(dAdT); (b) poly(dA); (c) poly(dC); (d) poly(dG); (e) poly(dT) DNA with methylene blue (MB). With the addition of sodium dithionite (SDT) the MB is converted to LMB. Numbers on the left-hand side indicate the molar ratio of DNA:MB:SDT. A signal due to LMB is indicated with an asterisk. In (e) signals due to MB are indicated with a #. All experiments were conducted with a DNA concentration of 0.5 mM in 10 mM phosphate buffer, pH 7.4 in 90% $^{1}H_2O$/10% $^{2}H_2O$ at 5 °C.

For the poly(dAdT) sample the most notable signals to disappear with MB binding are the upfield methyl signals from the dT nucleotides. For the poly(dG), poly(dA) and poly(dC) we observe a general decrease in signal intensity due to MB randomly binding the DNA, likely through stacking interactions instead of through intercalation. For the poly(dT) sample we again observe a reduction in signal intensity, possibly most noticeable in the upfield methyl signal, indicating binding of MB. For this sample we do see in the NMR spectra the signals from MB possibly indicating that this DNA binds MB more weakly than the other DNA constructs or that fewer molecules of MB bind this DNA at the same molar ratios. These MB NMR signals are indicated by a pound symbol (*) in the NMR spectrum (Figure 4.4.1.2e).

4.4.2 NMR Spectroscopy Provides No Evidence of Binding of LMB to DNA

To investigate the possible binding of LMB to the six DNA constructs, we again used NMR spectroscopy. For each of the DNA samples bound to MB, we added a 10-fold molar excess of sodium dithionite compared to MB (Figure 4.4.2.1). For each sample, upon the addition of sodium dithionite the dark blue MB color disappeared, and the solution turned colorless, indicating the conversion of MB to LMB. In the case of the poly(dT) sample where we observed the NMR signals from MB, these signals disappeared. Additionally, in each of the samples of DNA with the *in situ*-generated LMB we observed a distinctive NMR signal from LMB also indicating that LMB is being generated (indicated with an asterisk in Figure 4.4.1.2a-e). For all the DNA samples, with the generation of LMB, the NMR signals of the free DNA returned indicating that LMB does not bind these DNA molecules. As a control, an equivalent amount of sodium dithionite was added to a sample of only DNA and we did not observe any spectral changes indicating that the reducing agent does not interact with the DNA (Figure 4.4.2.1) This was not the case with TCEP where the addition of TCEP to DNA resulted in many changes in the NMR spectra of DNA samples.

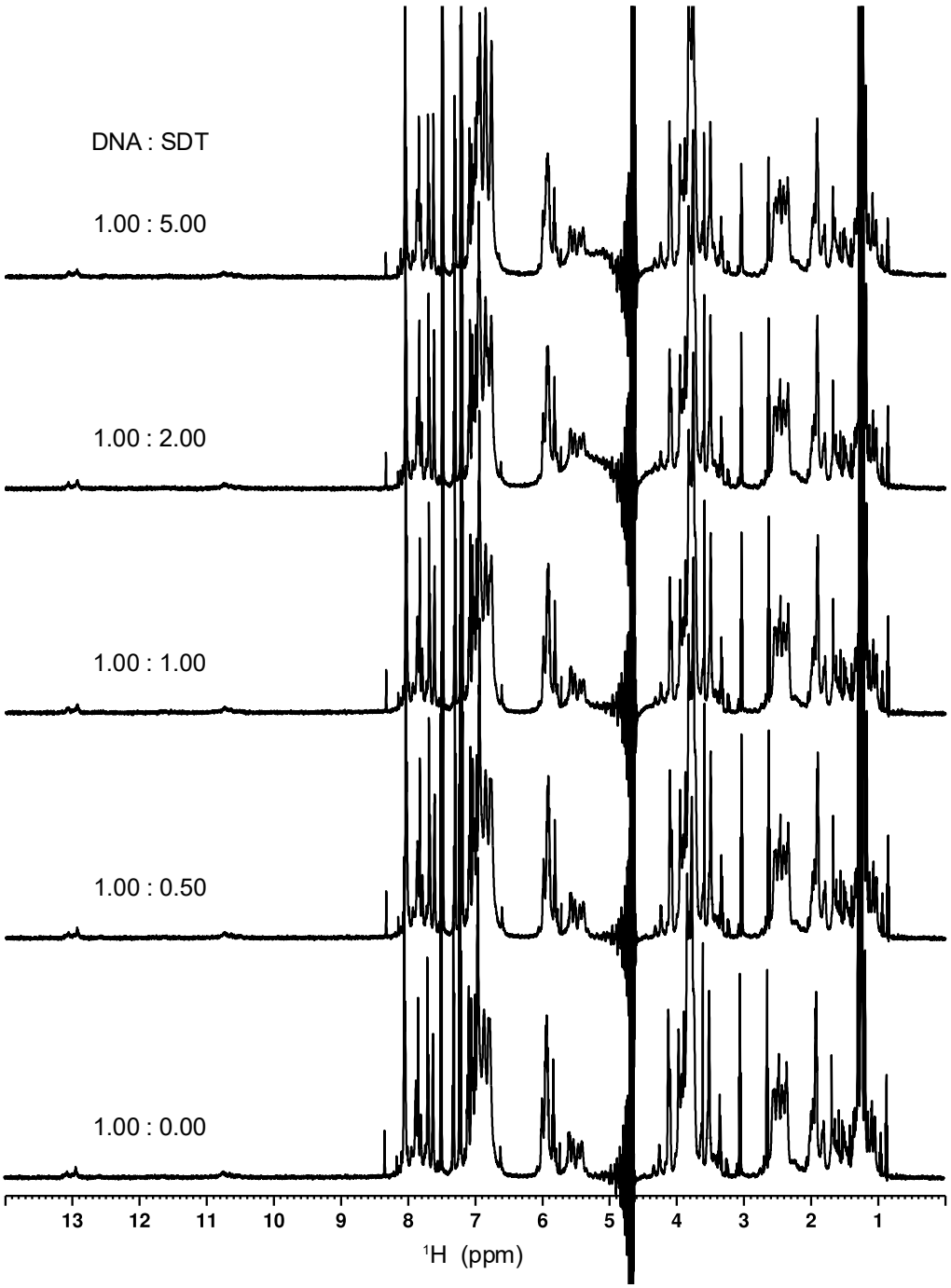

Figure 4.4.2.1. ^{1}H-NMR spectra showing the titration of SDT into poly(dAdT). Numbers on the left-hand side indicate the molar ratio of DNA:SDT. All experiments were conducted with a DNA concentration of 0.5 mM in 10 mM phosphate buffer, pH 7.4 in 90% $^{1}H_2O$/10% $^{2}H_2O$ at 5 °C.

4.4.3 MB Binding To DNA Analysed by Isothermal Titration Calorimetry

To measure the affinity of MB by the six DNA constructs, ITC was performed in cooperation with collaborator Emily Hoi Pui Chao. ITC is a label-free method used to determine the affinity and binding thermodynamics of interacting molecules including DNA with small molecules.[167,168] ITC has been previously used to analyze the interaction of MB with calf thymus DNA and long deoxynucleotide polymers.[169,170] For all six DNA constructs studied, ITC results indicated binding between the DNA and MB (Figure 4.4.3.1 a-f). All the data were fitted to a 1:1 binding model and the affinity and binding thermodynamics are shown in Table 4.4.3.1. As the DNA and MB interact via multiple modes of interaction,[143] it was noted that the reported values in Table 4.4.3.1 should be thought of as apparent K_d values for the entire set of binding interactions taking place between each DNA and MB.

Table 4.4.3.1. Binding affinity and thermodynamics of MB binding by the DNA constructs studied as determined by ITC[a]

DNA Construct	K_d (μM)	ΔH (kcal/mol)	-TΔS (kcal/mol)
Poly (dA)	1.8 ± 0.4	4.4 ± 0.5	–12.2 ± 0.6
poly(dC)[b]	0.3 ± 0.5	–2.5 ± 0.3	–6.2
poly(dG)	15 ± 12	1.5 ± 0.1	–8.2 ± 0.6
poly(dT)	23 ± 1	1.0 ± 0.2	–7.2 ± 0.2
poly(dAdT)	0.9 ± 0.6	1.0 ± 0.2	–9.3 ± 0.7
poly(dGdC)[b]	11 ± 6	0.9 ± 0.2	–7.6

[a]Data acquired in 10 mM sodium phosphate (pH 7.4) at 20 °C. Reported Errors are the standard deviation from 2-3 experiments except for:
[b]Where the data is from one run and the error reported is the error in the fit.

(a) Poly (dA)

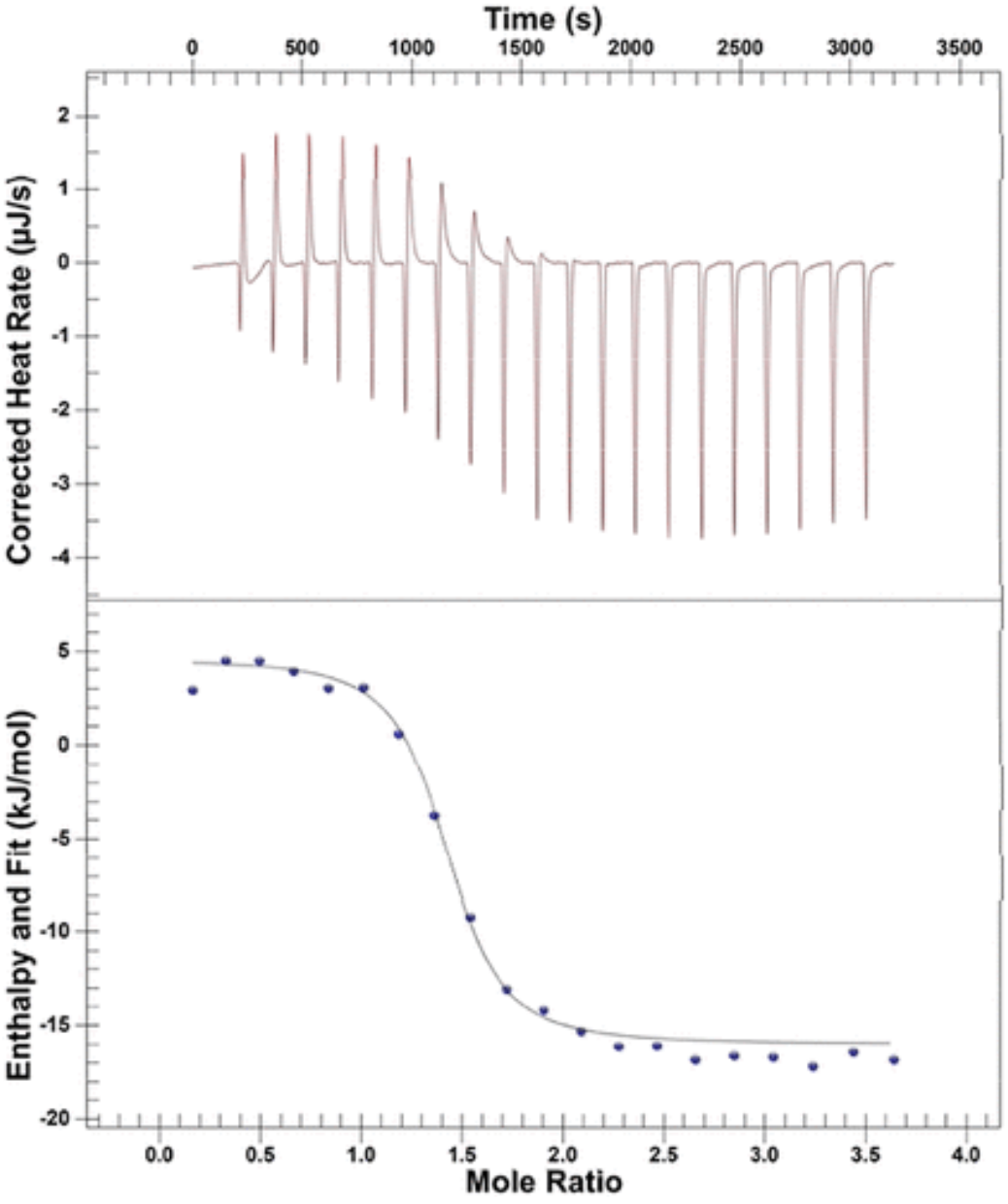
Time (s)
0
500
1000
1500
2000
2500
3000
3500
Corrected Heat Rate (µJ/s)
2
1
0
-1
-2
-3
-4
Enthalpy and Fit (kJ/mol)
5
0
-5
-10
-15
-20
0.0
0.5
1.0
1.5
2.0
2.5
3.0
3.5
4.0
Mole Ratio

(b) Poly (dAdT)

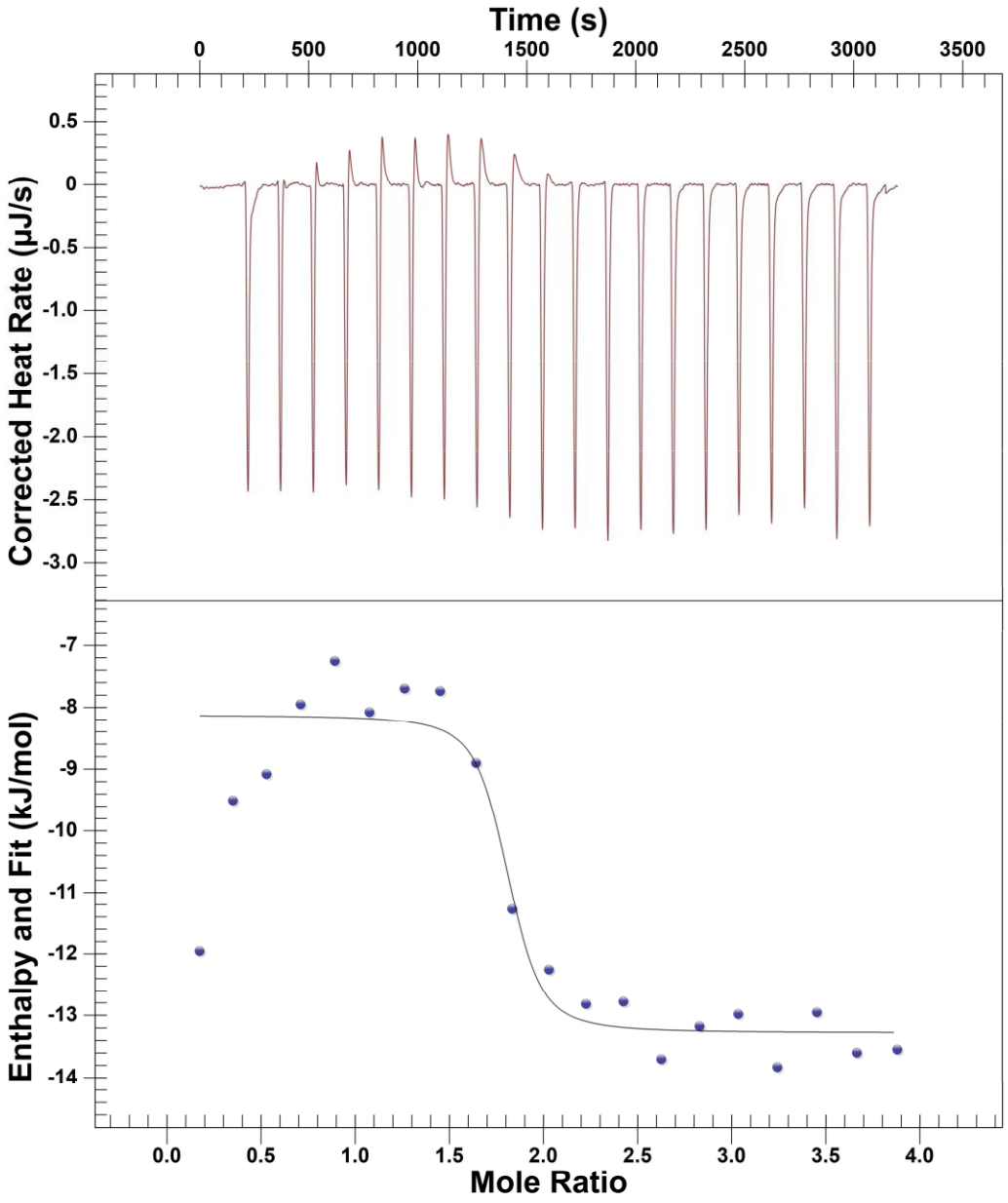
Time (s)
0
500
1000
1500
2000
2500
3000
3500
Corrected Heat Rate (µJ/s)
0.5
0
-0.5
-1.0
-1.5
-2.0
-2.5
-3.0
Enthalpy and Fit (kJ/mol)
-7
-8
-9
-10
-11
-12
-13
-14
0.0
0.5
1.0
1.5
2.0
2.5
3.0
3.5
4.0
Mole Ratio

(c) Poly (dT)

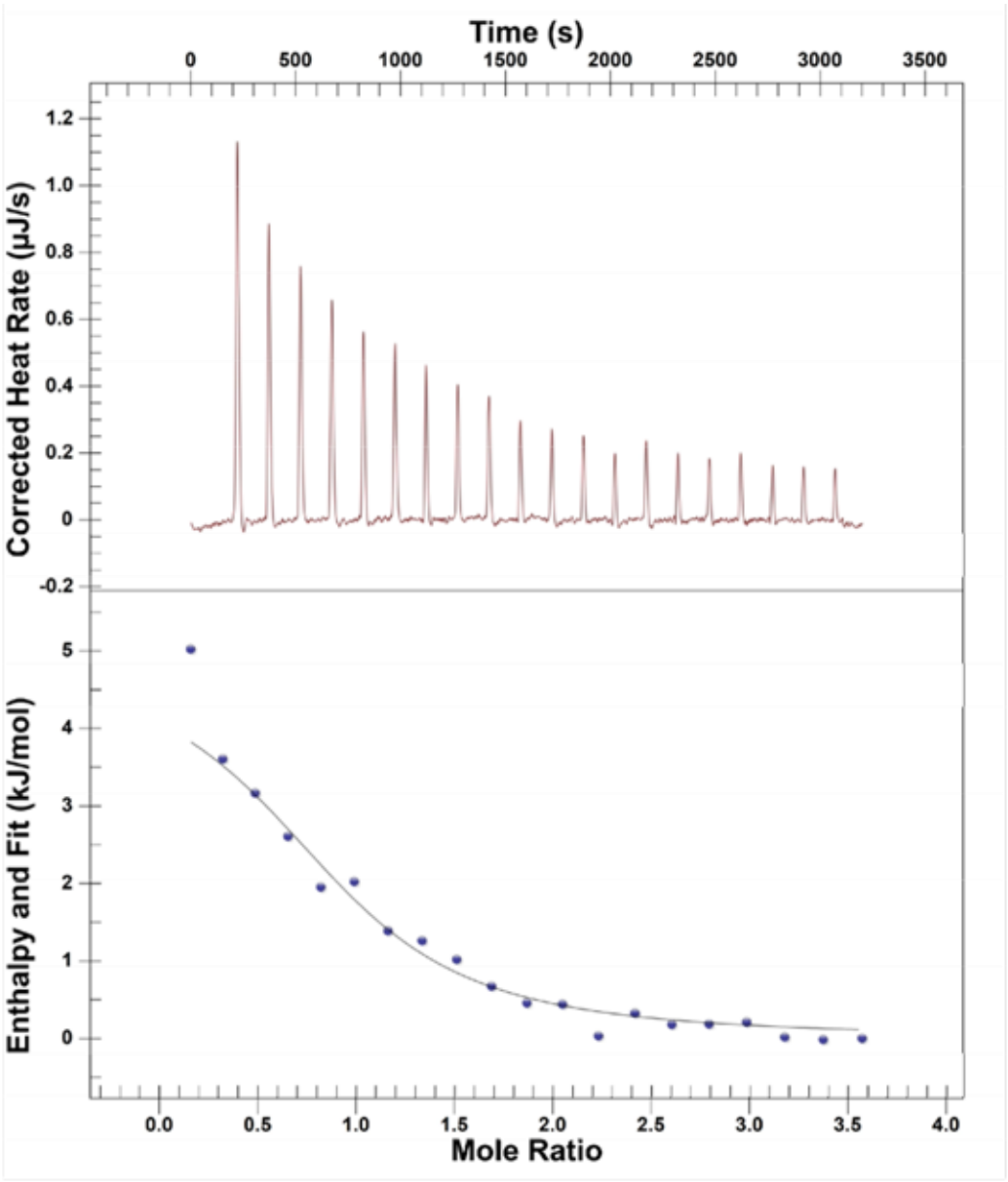
Time (s)
0
500
1000
1500
2000
2500
3000
3500
Corrected Heat Rate (µJ/s)
1.2
1.0
0.8
0.6
0.4
0.2
0
-0.2
Enthalpy and Fit (kJ/mol)
5
4
3
2
1
0
0.0
0.5
1.0
1.5
2.0
2.5
3.0
3.5
4.0
Mole Ratio

(d) Poly (dC)

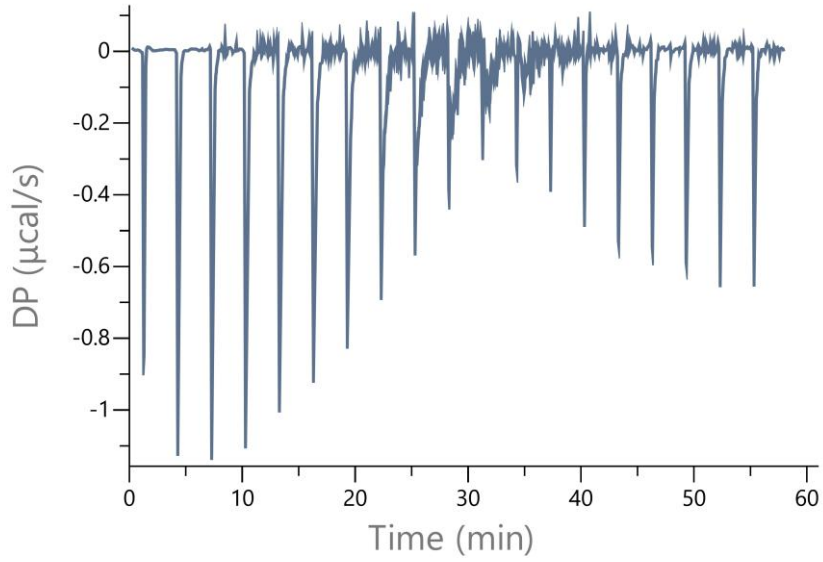
DP (µcal/s)
0
-0.2
-0.4
-0.6
-0.8
-1
0
10
20
30
40
50
60
Time (min)

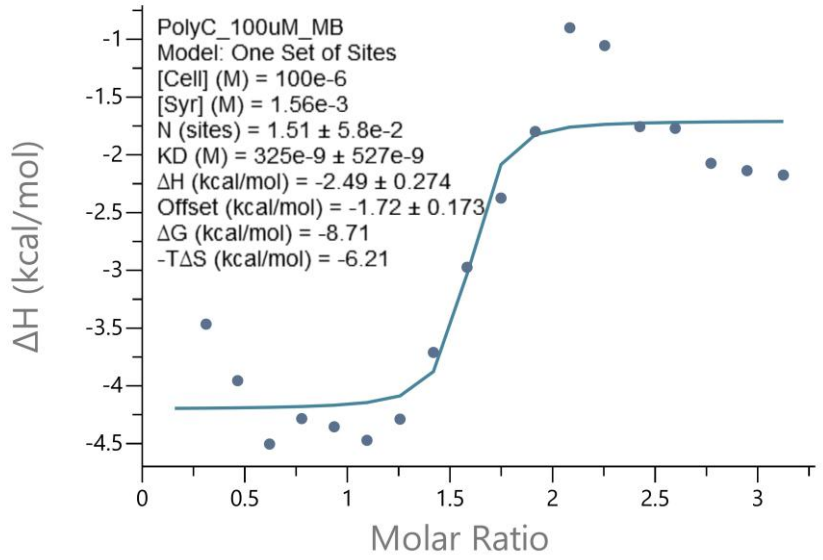
PolyC_100uM_MB
Model: One Set of Sites
[Cell] (M) = 100e-6
[Syr] (M) = 1.56e-3
N (sites) = 1.51 ± 5.8e-2
KD (M) = 325e-9 ± 527e-9
ΔH (kcal/mol) = -2.49 ± 0.274
Offset (kcal/mol) = -1.72 ± 0.173
ΔG (kcal/mol) = -8.71
-TΔS (kcal/mol) = -6.21
ΔH (kcal/mol)
-1
-1.5
-2
-2.5
-3
-3.5
-4
-4.5
0
0.5
1
1.5
2
2.5
3
Molar Ratio

(e) Poly (dG)

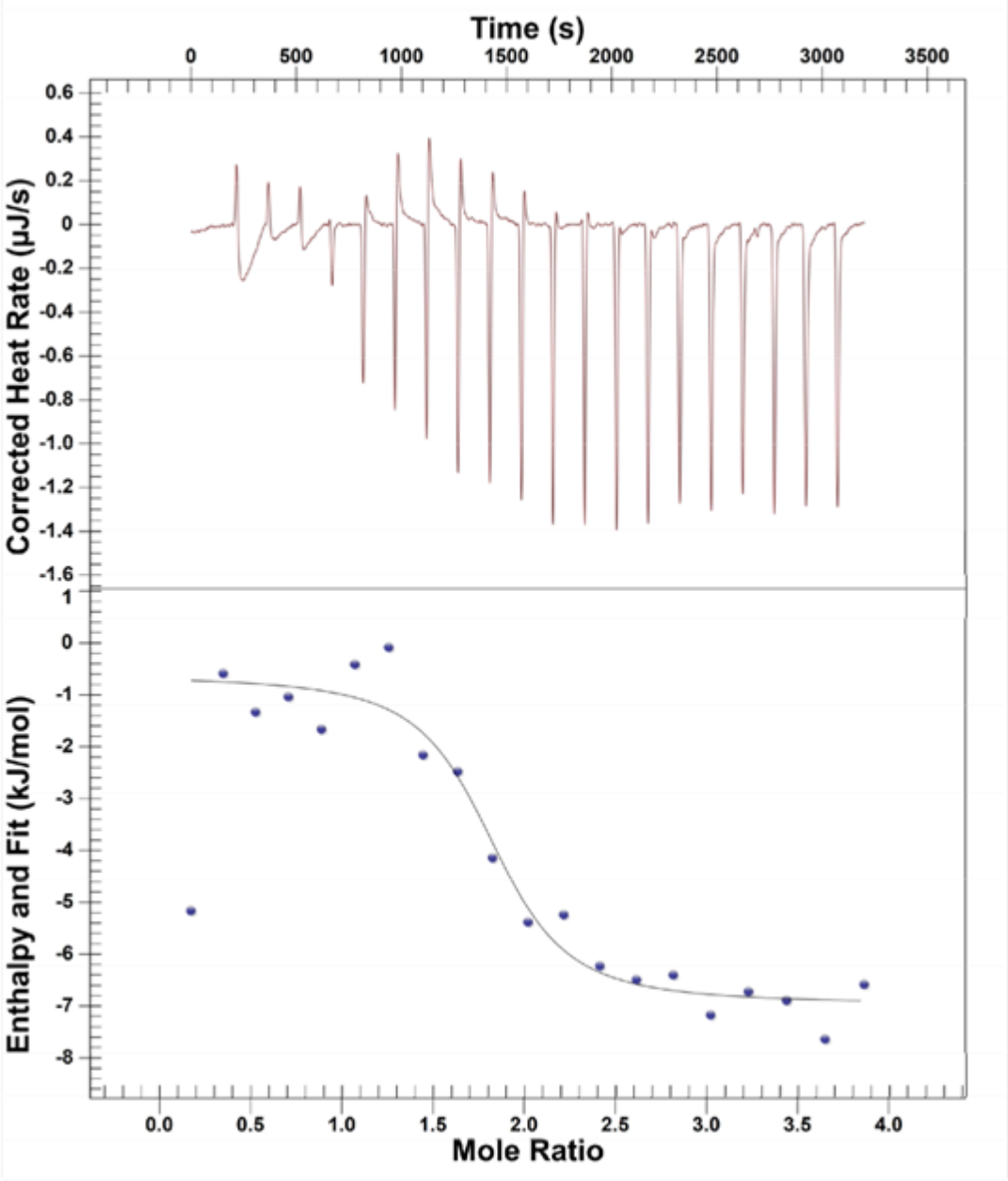
Time (s)
0
500
1000
1500
2000
2500
3000
3500
Corrected Heat Rate (µJ/s)
0.6
0.4
0.2
0
-0.2
-0.4
-0.6
-0.8
-1.0
-1.2
-1.4
-1.6
Enthalpy and Fit (kJ/mol)
1
0
-1
-2
-3
-4
-5
-6
-7
-8
0.0
0.5
1.0
1.5
2.0
2.5
3.0
3.5
4.0
Mole Ratio

(f) Poly (dGdC)

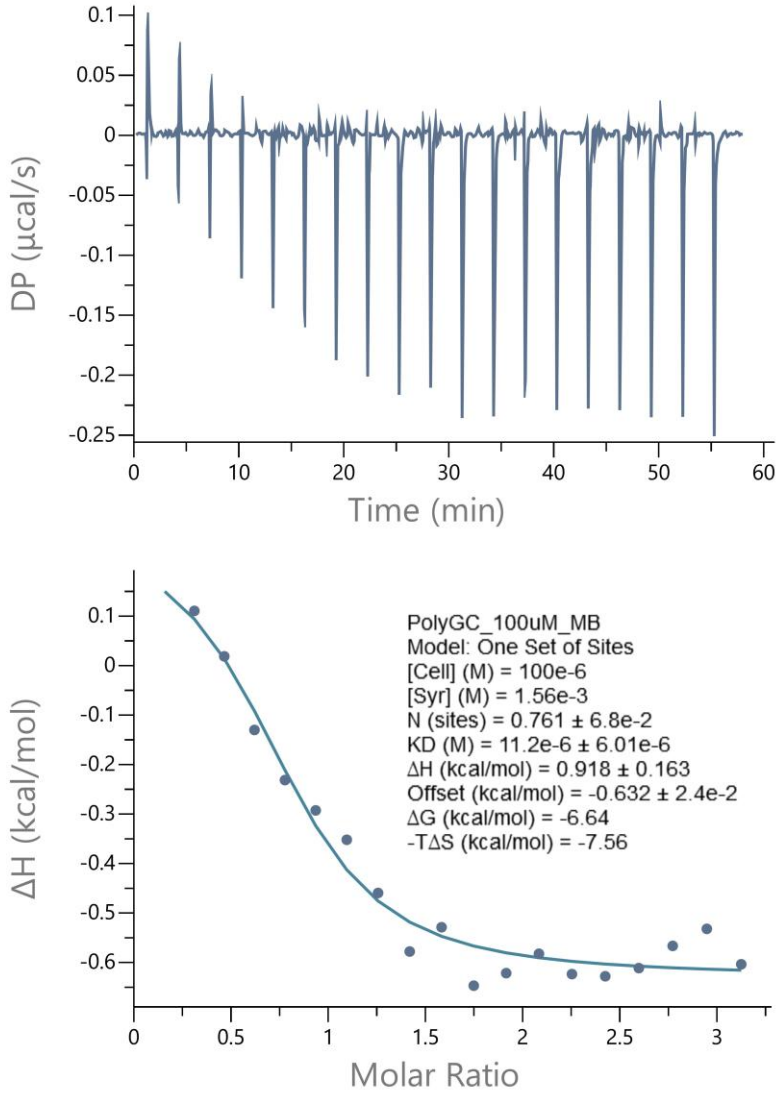

Figure 4.4.3.1. ITC thermograms showing the titration of MB in (a) poly(dA); (b) poly(dAdT); (c) poly(dT); (d) poly(dC); (e) poly(dG); poly(dGdC) DNA with methylene blue (MB). Experiments were conducted with a DNA concentration of 0.1 mM in 10 mM phosphate buffer, pH 7.4, measured at 20 °C.

For all DNA constructs studied, affinity is in the low micromolar range with binding weakly endothermic (except for poly(dC) which is weakly exothermic) and entropically favourable. MB binding by these DNA molecules is therefore an entropically driven process. The low heats of binding made data acquisition difficult despite working at a high concentration of DNA (100 µM). The results are in good agreement with the previous reports for MB binding calf thymus and long deoxypolynucleotides where the authors report low micromolar affinity with a favourable binding entropy.[169,170] The previous studies

reported weak exothermic binding compared to the weak endothermic binding observed in this study. This difference is likely due to the difference in DNA length where the DNA constructs used in this study are 10 nucleotides long compared to being thousands of nucleotides long.

Our results here with MB nonspecifically binding DNA differ from what is known about the thermodynamics of the specific binding of DNA aptamers with their ligands. In general, specific aptamer-ligand interactions are strongly exothermic with an unfavourable binding entropy.[171,172] A recent study by Xiao and co-workers examined a large data set of ITC results of aptamer-ligand interactions and found that aptamers with the most exothermic binding and greatest entropy penalty have high specificity.[110] The results collected in this study agree with this as MB binding by DNA is endothermic and entropically driven for a nonspecific interaction. The use of ITC to quantitate the interaction of LMB with the six DNA constructs was explored. However, it was not feasible to use ITC methods to measure LMB/DNA interactions as the control experiment of titrating the chemical reducing agent alone (no MB present) into DNA consistently produced a strong signal. It was anticipated that this signal was caused by oxidation of the reducing agent as it was titrated into the ITC cell. This 'oxidation' signal was always detected despite multiple attempts to match the ITC cell and syringe conditions. Attempts were made with several reducing agents including TCEP, dithiothreitol, ascorbic acid and sodium dithionite without success.

4.5 Additional Work

This project was conducted as a collaborative study, with complementary experimental approaches used to examine MB and LMB interact with nucleic acid structures. In addition to the binding and structural studies described above, Andrew J. Bonham contributed fluorescence and absorbance spectroscopy data that further supported the distinct DNA-binding behavior of MB and LMB. His results showed that MB interacts with both single-stranded and double-stranded DNA constructs, particularly guanine-containing sequences, producing concentration-dependent decreases in absorbance and fluorescence intensity. The absorbance behavior also supported different binding modes depending on DNA structure: MB binding to single-stranded DNA produced little change in the absorbance maximum, consistent with electrostatic association, whereas binding to double-stranded DNA produced a bathochromic shift consistent with

intercalative binding. In contrast, LMB produced little to no change in absorbance or fluorescence in the presence of the DNA constructs tested, supporting the conclusion that reduction of MB to LMB greatly weakens its interaction with DNA. These fluorescence and absorbance results therefore complemented the ITC and NMR findings by independently demonstrating that MB binds generic DNA structures while LMB exhibits negligible DNA association under the conditions examined.

Structural analysis of LMB was performed by Kelsey Richardson and Vojtech Vlcek, whose quantum modeling and X-ray crystallography studies provided a structural explanation for the weak DNA-binding behavior of LMB. Their modeling confirmed that LMB is significantly nonplanar, with calculated planarity parameters and a bend angle of approximately 147° between the two halves of the molecule. This nonplanar geometry was further supported by X-ray crystallography of LMB chloride crystals, which showed a pronounced central bend of approximately 150° around the sulfur and central nitrogen atoms. Although minor differences were observed between the calculated and crystal structures, likely due to crystal packing, crystallization conditions, and counterion effects, both approaches demonstrated that LMB adopts a bent "butterfly" conformation rather than the planar structure associated with MB. This structural difference provides a molecular basis for the reduced DNA affinity of LMB. While planar MB can interact with duplex DNA through intercalation between stacked base pairs, the bent geometry of LMB would make intercalation energetically unfavourable. These structural findings therefore support the experimental binding data by showing that reduction of MB to LMB changes the three-dimensional shape of the molecule in a way that limits its ability to associate with DNA.

4.6 Conclusions

Overall, these results demonstrate that the redox state and three-dimensional conformation of methylene blue strongly influence its interaction with nucleic acids. Across the experimental approaches used in this study, MB consistently showed measurable association with DNA, whereas LMB showed little to no detectable DNA binding under the conditions examined. ITC experiments demonstrated that MB binds both single-stranded and duplex DNA constructs. Similarly, NMR spectroscopy showed that addition

of MB perturbed DNA imino proton resonances, consistent with DNA binding and structural disruption or exchange, whereas LMB produced minimal spectral changes. These observations indicate that reduction of MB to LMB substantially weakens its ability to associate with nucleic acid structures.

The optical spectroscopy data further supported this conclusion. UV–vis absorbance and fluorescence experiments showed concentration-dependent changes upon addition of DNA to MB, including decreased absorbance and fluorescence intensity. These effects were most pronounced for guanine-containing DNA constructs and were consistent with prior reports of MB interactions with both single- and double-stranded DNA. The absorbance behavior also suggested that MB can engage DNA through different binding modes depending on nucleic acid architecture. Binding to single-stranded DNA produced little bathochromic shift, consistent with electrostatic or surface-associated interactions, whereas binding to duplex DNA produced a red-shifted absorbance maximum, supporting an intercalative binding mode. In contrast, LMB showed little to no change in absorbance or fluorescence in the presence of the same DNA constructs, further demonstrating its reduced affinity for DNA.

The structural and computational analyses provide a molecular explanation for these differences. Quantum modeling and X-ray crystallography showed that LMB adopts a significantly nonplanar, bent "butterfly" conformation, with an approximately 150° bend across the molecule. This geometry contrasts with the planar aromatic structure of MB, which is well suited for stacking interactions and intercalation between DNA base pairs. Because LMB is bent, insertion into duplex DNA would be energetically unfavourable, providing a structural basis for its weak DNA-binding behavior. Together, the ITC, NMR, UV–vis, fluorescence, crystallographic, and modeling data support a unified model in which planar MB readily associates with DNA through multiple binding modes, while reduced, nonplanar LMB has greatly diminished capacity for nucleic acid binding. These findings are particularly relevant to electrochemical aptamer-based sensors, where MB is widely used as a redox reporter and where redox-dependent changes in reporter structure and DNA affinity may influence signal transduction.

Chapter 5 Solution-State NMR Studies of Aptamer–Small Molecule Binding and Conformational Dynamics

- Work presented in this chapter was completed by Kaiyum, Y. A.

5.1 Introduction

Aptamers are sequence-defined nucleic acid receptors whose function is governed by the relationship between primary sequence, three-dimensional structure, conformational dynamics, and target recognition. Since the development of SELEX by Tuerk and Gold and the independent demonstration of in vitro selection by Ellington and Szostak, aptamers have been selected against a wide range of targets, including ions, metabolites, small molecules, proteins, and whole cells.[5,6] Although aptamers are often discussed in terms of their binding affinity and specificity, these properties ultimately arise from the structural ensembles that the nucleic acid can access. For small-molecule-binding aptamers, this relationship is especially important because ligand recognition often depends on localized binding pockets, non-canonical base-pairing interactions, conformational switching, and subtle changes in secondary or tertiary structure.[173,174] Therefore, understanding aptamer function requires methods that can probe not only whether binding occurs, but also how ligand binding changes the structure and dynamics of the aptamer.

Small-molecule aptamers present unique challenges for structural and biophysical characterization. Compared with protein–aptamer complexes, aptamer–small molecule interactions often involve targets with limited molecular surface area and relatively few functional groups available for hydrogen bonding, stacking, or electrostatic interactions. As a result, binding may depend on highly specific local arrangements of nucleobases, transient structural states, or ligand-induced stabilization of pre-existing conformations. In many cases, aptamers selected against small molecules do not behave as rigid lock-and-key receptors. Instead, ligand recognition can involve conformational selection, induced fit, or population-shift mechanisms in which ligand binding redistributes the conformational ensemble of the aptamer.[173,175] These mechanisms are difficult to define using binding affinity alone. A measured dissociation constant can establish the apparent strength of an interaction, but it does not identify the structural elements responsible

for binding, the nucleotides involved in recognition, or the extent to which ligand binding stabilizes or remodels the aptamer fold.

Nuclear magnetic resonance (NMR) spectroscopy is particularly well suited to address these questions because it provides site-specific information on nucleic acid structure and dynamics under solution conditions. Unlike methods that require crystallization, immobilization, or labeling, NMR can monitor aptamers in free solution and can often detect both free and ligand-bound conformations. This is especially valuable for aptamer–small molecule systems, where functionally important conformations may be transient, weakly populated, or exchange on timescales that are difficult to observe using other structural methods.[70,72] NMR has long been used to investigate nucleic acid structure, including base pairing, stacking, conformational exchange, and tertiary interactions.[176] In the context of aptamers, NMR can provide information at several levels, ranging from rapid one-dimensional screening of ligand-induced spectral changes to detailed two-dimensional and multidimensional experiments used for resonance assignment and structural analysis.

One of the most useful starting points for studying nucleic acid aptamers by NMR is the imino proton region of the one-dimensional proton spectrum. Imino protons are exchangeable protons associated primarily with guanine and thymine or uracil bases. When these protons are protected from solvent exchange through stable base pairing or tertiary interactions, they can be observed as distinct resonances, typically in the downfield region of the proton spectrum. The presence, disappearance, broadening, or chemical shift movement of imino resonances can therefore report on base-pair formation, local stability, ligand-induced folding, and conformational exchange.[73,177] For aptamers that undergo structural switching upon ligand binding, the imino region can provide a rapid and sensitive readout of whether ligand binding induces new base pairs, stabilizes pre-existing base pairs, or disrupts secondary structure. This makes one-dimensional imino proton NMR particularly valuable for screening related ligands, comparing aptamer variants, and identifying changes in folding behavior.

In addition to imino proton analysis, chemical shift perturbation experiments provide a powerful way to identify regions of an aptamer affected by ligand binding. Upon ligand addition, resonances

corresponding to nucleotides near the binding site or involved in ligand-induced structural rearrangements may shift, broaden, split, appear, or disappear. These spectral changes can be interpreted in relation to exchange regime, binding kinetics, conformational heterogeneity, and local structural changes.[178] In fast-exchange systems, resonances may move gradually as ligand concentration increases, whereas slow-exchange systems may show separate resonances for free and bound states. Intermediate exchange can lead to significant peak broadening or loss of signal. These behaviors provide mechanistic information beyond affinity measurements and can help distinguish direct binding events from nonspecific interactions or global structural perturbations.

Two-dimensional NMR experiments provide additional structural information that can be used to characterize aptamer folds and aptamer–ligand complexes in greater detail. NOESY experiments identify through-space proton–proton contacts and are central to determining nucleic acid structures in solution. In aptamer systems, NOE patterns can reveal base stacking, loop organization, ligand contacts, and tertiary interactions that define the binding pocket. TOCSY experiments can assist with spin-system identification, particularly for ligand resonances or sugar proton assignments, while heteronuclear experiments using isotopically labeled samples can improve resolution and facilitate assignment in larger or more complex nucleic acid systems. These methods have been central to several landmark aptamer structures, including ATP- and AMP-binding RNA aptamers, where NMR revealed compact ligand-binding architectures involving internal loops, bulges, and specific ligand contacts.[179–182]

NMR has also played an important role in understanding DNA aptamer structure. The thrombin-binding DNA aptamer is one of the best-known examples, with NMR studies demonstrating that it folds into a compact G-quadruplex structure containing stacked guanine tetrads.[183,184] Subsequent comparisons between NMR and crystallographic structures emphasized that aptamer folds can be sensitive to experimental conditions, metal ions, and complex formation, highlighting the importance of solution-based characterization.[185] These early studies established NMR as a critical approach for revealing how DNA aptamers adopt non-canonical structures that are directly linked to function.

For small-molecule-binding DNA aptamers, NMR has been especially useful for distinguishing between ligand-induced folding, pre-folding, and nonspecific binding. The cocaine-binding aptamer provides a useful model system in this regard. Combined NMR and isothermal titration calorimetry studies showed that stem length influences the binding mechanism, with shorter constructs exhibiting greater ligand-induced folding behavior.[84] Related studies demonstrated that the same aptamer scaffold can bind chemically distinct ligands such as quinine, levamisole, and antimalarial compounds, with NMR providing evidence for ligand-induced structural changes, competition between ligands, and weak binding interactions that may be difficult to quantify by calorimetry alone.[114,166,186,187] These examples illustrate how NMR can reveal whether ligands share a common binding site, whether binding induces similar structural responses, and whether apparent affinity reflects specific aptamer recognition or broader nucleic acid-binding behavior.

NMR also complements thermodynamic methods such as isothermal titration calorimetry. ITC provides quantitative binding parameters, including binding affinity, enthalpy, entropy, and stoichiometry, but it does not directly reveal the structural origin of these parameters. NMR can provide the structural context needed to interpret thermodynamic data by identifying which regions of the aptamer are affected by binding and whether the interaction is accompanied by folding, stabilization, destabilization, or conformational exchange. For example, studies of the ATP-binding DNA aptamer have combined thermodynamic and NMR data to support population-shift binding mechanisms and cooperative ligand binding.[175] Similarly, NMR-detected titrations can be particularly useful when interactions are weak, when heats of binding are small, or when multiple binding modes complicate calorimetric analysis.[70,72,187]

Beyond structural assignment, NMR can provide insight into aptamer dynamics. Aptamers are not static receptors; they exist as conformational ensembles whose populations and exchange rates can influence ligand recognition. Changes in peak intensity, linewidth, exchange behavior, and temperature-dependent spectra can provide information about local flexibility and base-pair stability. Imino proton exchange experiments have been used to study base-pair opening and lifetimes in nucleic acids, allowing researchers to connect structural stability with dynamic behavior.[177,182] In aptamer–ligand systems, this is

particularly important because ligand binding may stabilize specific base pairs near the binding site, reduce local dynamics, or reorganize the conformational ensemble without producing a complete global refolding event. Temperature-dependent NMR experiments can further reveal whether ligand binding stabilizes or destabilizes aptamer structure, providing a useful complement to thermal melt experiments and calorimetric measurements. The value of NMR is also evident when validating aptamers for analytical and biosensing applications. Aptamer-based sensors, including electrochemical aptamer-based sensors, often rely on ligand-induced structural switching or changes in conformational dynamics to generate signal.[188] However, not all reported aptamers bind their proposed targets under the conditions required for sensor function, and several studies have emphasized the need for multifaceted validation of aptamer–target interactions.[189] NMR can contribute to this validation by confirming whether ligand binding produces reproducible, concentration-dependent spectral changes and whether those changes are consistent with specific molecular recognition. This is particularly important for small-molecule aptamers, where nonspecific interactions with nucleic acid structures can lead to misleading interpretations if only a single assay format is used.

This chapter focuses on the use of NMR spectroscopy to investigate a series of aptamer–small molecule systems studied throughout this thesis. The chapter first considers the types of information that can be obtained from NMR experiments, including ligand-induced structural changes, base-pair formation, chemical shift perturbations, conformational exchange, and thermal stability. It then applies these concepts to specific aptamer–ligand systems to examine how NMR can distinguish specific binding from nonspecific interactions, compare the effects of structurally related ligands, and reveal how small molecules influence aptamer folding and function. Together, these studies demonstrate that NMR is not simply a structural tool, but a central method for elucidating the structure–function relationships that govern aptamer–small molecule recognition.

5.2 Methods and Materials

All DNA samples for analysis were purchased from Integrated DNA Technologies (IDT, Coralville, Iowa) with standard desalting as purification. The identity of aptamer samples was confirmed by mass spectrometry performed by the manufacturer. The DNA was dissolved in ~1 mL distilled deionized H_2O (ddH_2O) and then exchanged three times against 1 or 2 M NaCl using 3 kDa molecular weight cutoff Amicon-style concentrators to compete off any unwanted substances bound to the nucleic acid. The DNA concentration was measured using UV spectroscopy and the known extinction coefficient provided by the manufacturer. Serotonin hydrochloride (Catalog Number – H9523)), Amodiaquine dihydrochloride (Catalog Number – A2799) and Scandium (III) chloride hydrate (Catalog Number - 307858) were purchased from Millipore-Sigma (Oakville, ON, Canada). Zinc chloride was purchased from Fisher Scientific (Catalog Number – UN2331). Kanamycin sulfate (Catalog Number - KAN201) was purchased from Bioshop. Bilirubin (Catalog Number – B4126) was purchased from Sigma Aldrich (MO, USA). Biliverdin (Catalog Number – 36337) was purchased from Cayman CHEMICAL (MI, USA). Tris hydrochloride (Catalog Number – 9310) was purchased from Sigma Aldrich.

NMR experiments were conducted on either a 600 MHz Bruker Avance or a 700 MHz Bruker Avance-III spectrometer in a manner previously described.[72] Prior to performing NMR experiments, samples were heated in a 90 °C water bath for 3 min then fast-cooled on ice to favour intramolecular folding. 1D ^{1}H spectra of the imino proton region were acquired in the appropriate buffers for each aptamer or DNA sequence.

5.3 NMR Characterization of the SRTN12 Serotonin-Binding Aptamer

Serotonin is a biologically important monoamine neurotransmitter involved in neurological, gastrointestinal, cardiovascular, and endocrine signaling pathways. As a result, molecular recognition elements capable of selectively detecting serotonin are of significant interest for biosensing and analytical applications. Aptamers are well suited for this purpose because their sequence-dependent folding can generate binding pockets capable of recognizing small molecules with high affinity and specificity.

However, the development of small-molecule-binding aptamers remains challenging because these targets often provide limited surface area and fewer functional groups for molecular recognition compared with larger biomolecular targets. Consequently, small-molecule aptamer function often depends on subtle conformational rearrangements, ligand-induced folding, or stabilization of weakly populated structural states.[173,174,189]

The SRTN12 aptamer (Figure 5.3.1) represents an improved serotonin-binding aptamer derived from earlier serotonin aptamer development efforts. The original serotonin-binding aptamer, reported by Stojanovic and co-workers in 2018, demonstrated that serotonin recognition by nucleic acid aptamers could be used in field-effect transistor-based sensing platforms.[46] However, subsequent work has highlighted that aptamer performance in sensor formats is closely linked to ligand-induced conformational change and the ability of the aptamer to undergo a reproducible structural response upon target binding.[190] Therefore, structural characterization of improved serotonin-binding aptamers is essential for determining whether enhanced function arises from stronger ligand binding, more efficient structural switching, or stabilization of a defined ligand-bound fold.

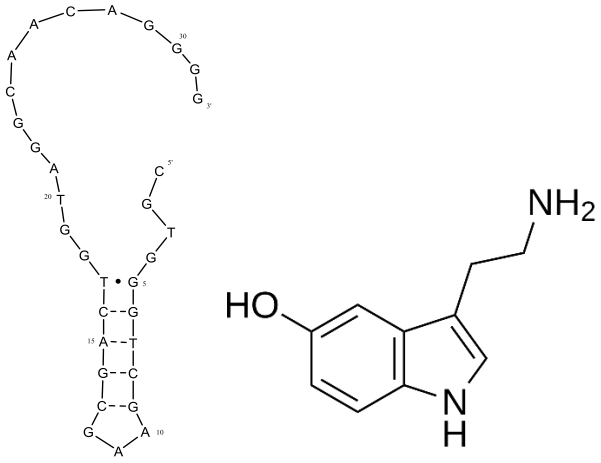

Figure 5.3.1. Predicted secondary structure of the SRTN12 aptamer. Dots represent non-Watson-Crick base pairs and dashed lines represent Watson-Crick base pairs. Chemical structure of serotonin.

In the absence of serotonin, SRTN12 exhibits weak and poorly resolved imino proton resonances, suggesting that the free aptamer is largely unfolded, weakly structured, or conformationally heterogeneous (Figure 5.3.2). This indicates that the aptamer does not strongly populate a single stable secondary structure

in the free state. Instead, SRTN12 likely exists as an ensemble of dynamic conformations in which many exchangeable imino protons remain exposed to solvent and are therefore broadened beyond detection. This type of spectral behavior is consistent with aptamer systems in which ligand binding is coupled to structural ordering rather than simple binding to a pre-formed rigid binding pocket. Upon titration of serotonin into SRTN12, substantial spectral changes are observed in the imino proton region. Increasing serotonin concentration leads to the emergence of multiple new resonances and a progressive increase in peak intensity and resolution. These changes indicate that serotonin binding promotes formation or stabilization of hydrogen-bonded structural elements within the aptamer. The gradual development of well-defined imino resonances is consistent with a ligand-induced folding mechanism in which serotonin shifts the conformational ensemble toward a more ordered bound state. This suggests that serotonin does not merely associate nonspecifically with SRTN12 but instead promotes a reproducible structural transition in the aptamer. The distribution of emergent peaks is also informative. Several resonances appear in the downfield region commonly associated with structured nucleic acids, while prominent signals in the approximately 10–12 ppm region are consistent with imino protons involved in Hoogsteen hydrogen-bonding networks characteristic of G-quadruplex formation.[191–193] G-quadruplexes are non-canonical nucleic acid structures formed through stacked guanine tetrads and are often stabilized by monovalent cations, particularly potassium ions, which coordinate within the central channel of the quadruplex.[191,193–195] The spectral response of SRTN12 is therefore consistent with the formation of a more structured ligand-bound conformation that may contain a G-quadruplex or G-quadruplex-like motif.

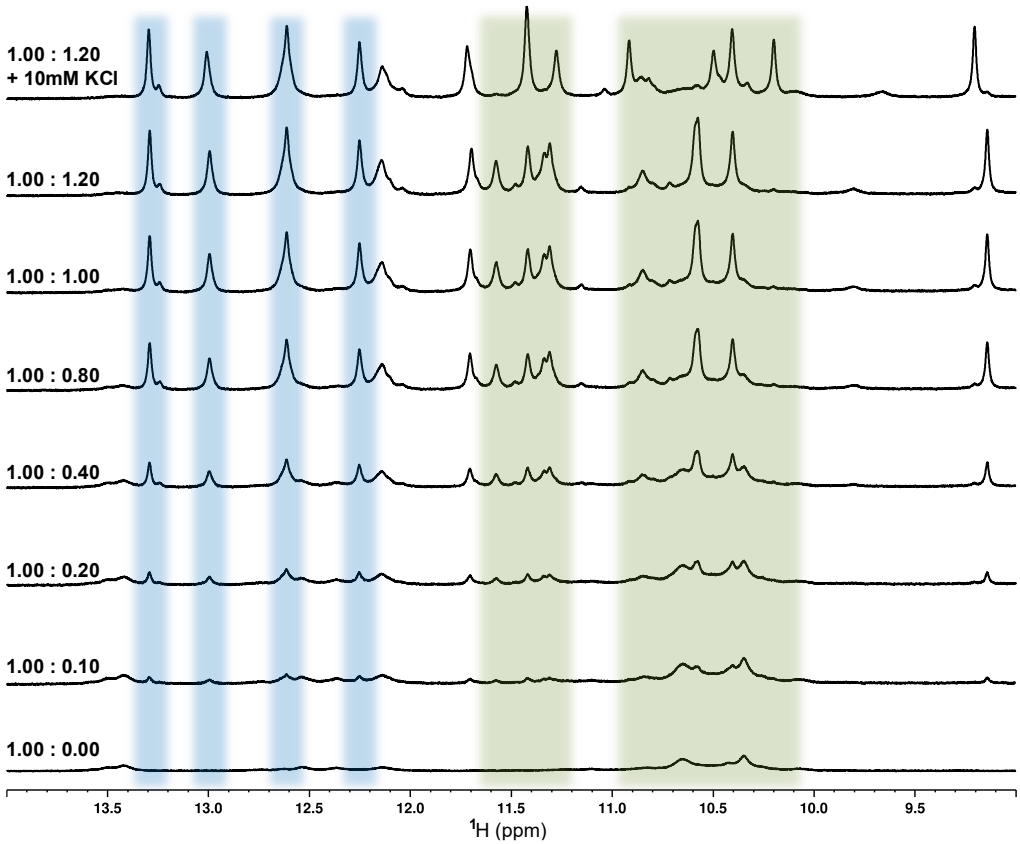

Figure 5.3.2. ^{1}H-NMR titration of the SRTN12 serotonin-binding aptamer with increasing equivalents of serotonin. The free aptamer exhibits weak and poorly resolved imino proton resonances, consistent with a largely unfolded or conformationally heterogeneous state. Addition of serotonin results in the emergence and sharpening of multiple imino proton signals, indicating ligand-induced formation or stabilization of hydrogen-bonded secondary structure. Further addition of KCl enhances peak resolution and produces additional resonances, consistent with potassium-dependent stabilization of a G-quadruplex or G-quadruplex-like folded state. Imino proton resonances in the approximately 10–12 ppm region are commonly associated with guanine imino protons involved in Hoogsteen hydrogen-bonded G-tetrads. Peaks that appear with serotonin addition are highlighted in blue. Peaks that are altered by further addition of KCl are highlighted in green.

This is further supported by the addition of KCl. Following serotonin titration, addition of KCl results in further sharpening of existing imino proton resonances and the emergence of additional peaks. Potassium-dependent sharpening is strongly suggestive of stabilization of a G-rich folded state because K^+ is known to preferentially stabilize G-quadruplex structures by coordinating between stacked guanine tetrads.[191,193–195] The enhanced spectral resolution observed after KCl addition suggests that potassium reduces conformational heterogeneity and stabilizes a more defined folded state of the serotonin-bound aptamer. This behavior supports a model in which serotonin binding promotes folding of SRTN12, while potassium further stabilizes the resulting G-quadruplex-like architecture.

Collectively, the data indicates that SRTN12 undergoes a pronounced ligand-induced structural transition upon serotonin binding. The weak imino proton signals observed for the free aptamer suggest limited stable secondary structure in the absence of ligand, whereas serotonin titration produces new and sharpened resonances consistent with formation of a more ordered hydrogen-bonded structure. The additional stabilization observed upon KCl addition provides further evidence for involvement of a potassium-stabilized G-quadruplex or G-quadruplex-like motif in the bound state. These findings demonstrate the utility of NMR spectroscopy for identifying ligand-induced folding events in small-molecule-binding aptamers and support the conclusion that SRTN12 function is closely linked to serotonin-dependent structural stabilization.

5.4 NMR Characterization of the Sc-1b Scandium-Binding Aptamer

Metal ion-binding aptamers represent an important class of functional nucleic acids because they provide sequence-defined receptors capable of recognizing targets that are difficult to distinguish using conventional biomolecular recognition strategies. Unlike proteins or larger organic ligands, metal ions are small, highly solvated, and often lack extended molecular surfaces for forming diverse non-covalent contacts. As a result, metal ion recognition by aptamers frequently depends on precise spatial organization of nucleobases, backbone phosphates, solvent molecules, and folded structural motifs that together create a suitable coordination environment.[196–198] This presents a unique challenge for aptamer selection and characterization, particularly for trivalent metal ions such as Sc^{3+}, where binding can be influenced by ionic radius, charge density, hydration, and competition with other cations in solution.[196,199] These observations make scandium-binding aptamers useful systems for examining how nucleic acids organize structure around highly charged inorganic targets.

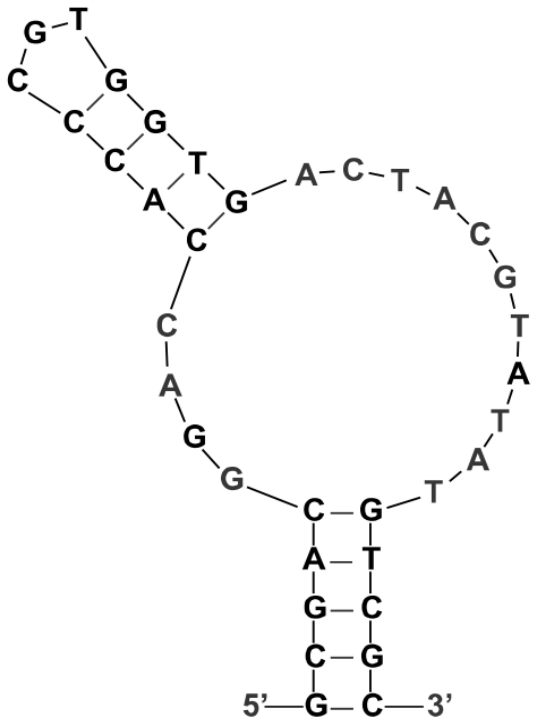

Figure 5.4.1. The predicted secondary structure of the SC-1b scandium binding aptamer which showcases a terminal stem region followed by a large loop region and another stem region.

The scandium-binding aptamer (Figure 5.4.1) provides an important example of the utility of NMR spectroscopy for studying aptamer interactions with targets that are difficult to monitor directly. Unlike many organic small molecules, metal ions do not possess extensive proton networks or distinctive NMR-active functional groups that can be readily followed using conventional ligand-observed NMR experiments. In addition, metal ion binding can be influenced by hydration, electrostatics, competing buffer components, and coordination with nucleobase or backbone functional groups. These factors make ion tracking and direct characterization of ion–aptamer interactions experimentally challenging. As a result, structural readouts from the aptamer itself become especially valuable.

In this context, the imino proton region of the ^{1}H-NMR spectrum provides an indirect but highly informative measure of Sc^{3+}-dependent aptamer folding. The free scandium-binding aptamer displays several intense resonances in the downfield Watson–Crick region, indicating that portions of the aptamer are already structured in the absence of metal ion (Figure 5.4.2). These signals likely correspond to pre-

formed base-paired regions that act as a structural scaffold. In contrast, weak and broad resonances in the non-Watson–Crick region suggest the presence of dynamic or weakly populated non-canonical structures in the free state. Upon titration with Sc^{3+}, several existing resonances sharpen and increase in intensity, while additional signals emerge in the non-Watson–Crick region. These changes indicate that Sc^{3+} binding stabilizes the pre-existing aptamer scaffold and promotes formation of additional non-canonical interactions. The concentration-dependent emergence of new imino resonances suggests that metal ion binding shifts the aptamer ensemble toward a more ordered and structurally defined state. This behavior is consistent with a model in which the aptamer is partially pre-structured before ligand addition but undergoes further conformational refinement upon Sc^{3+} binding.

This example highlights an important advantage of NMR spectroscopy in the study of small-molecule and ion-binding aptamers. Even when the target itself is difficult to observe directly, NMR can reveal binding-induced structural changes by monitoring the nucleic acid response. For metal ions, where direct detection of the bound species can be challenging, changes in aptamer imino proton resonances provide a valuable structural proxy for binding. Peak sharpening, chemical shift changes, and the emergence of new resonances can collectively reveal whether target association stabilizes existing base pairs, induces new secondary or tertiary contacts, or reduces conformational heterogeneity.

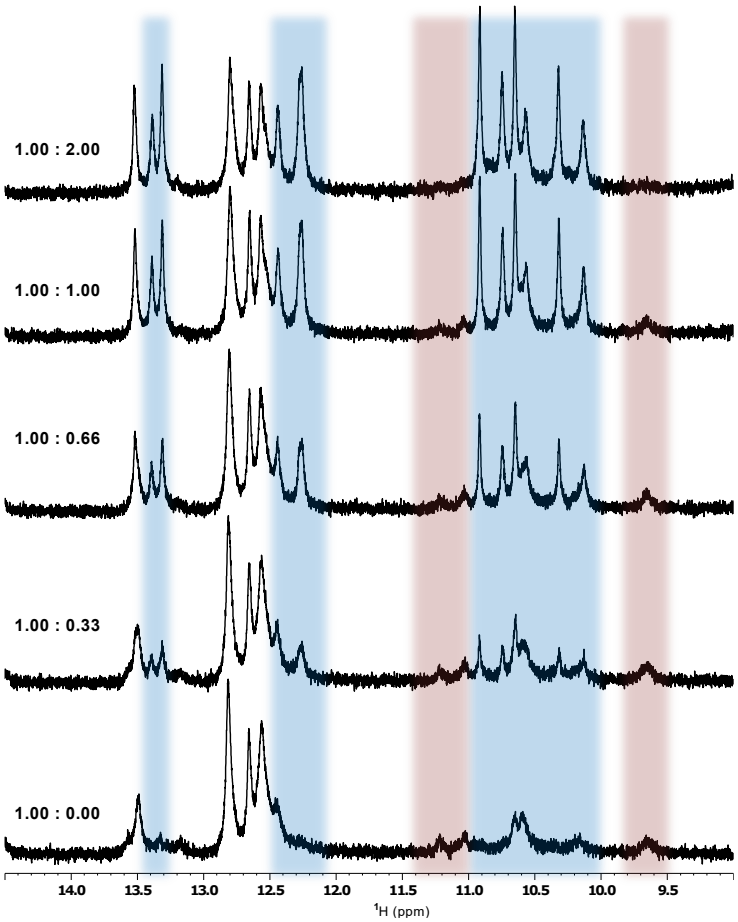

Figure 5.4.2. ^{1}H-NMR titration of the scandium (III)-binding aptamer with increasing equivalents of Sc^{3+}. The free aptamer displays several intense resonances in the downfield Watson–Crick imino proton region, indicating the presence of pre-formed secondary structure. Weak and broad signals in the non-Watson–Crick region suggest additional dynamic or weakly populated non-canonical interactions. Upon addition of increasing Sc^{3+}, several existing resonances sharpen and increase in intensity, while new peaks emerge and intensify in the non-Watson–Crick region. These spectral changes indicate that Sc^{3+} binding stabilizes pre-existing structural elements and promotes formation of additional non-canonical interactions, consistent with metal ion-induced ordering of the aptamer into a more defined bound-state conformation. Peaks that appear with ligand addition are highlighted in blue whereas peaks that disappear with ligand addition are highlighted in red.

The scandium-binding aptamer therefore demonstrates that NMR is not limited to detecting ligand binding through direct observation of the ligand. Rather, it can define how ligand binding affects the aptamer structural ensemble. This is particularly important for small-molecule and ion-binding aptamers, where binding may involve subtle conformational changes that are difficult to interpret using affinity measurements alone. In this case, the NMR data suggest that Sc^{3+} recognition is coupled to both preorganization and metal-induced structural ordering, reinforcing the broader theme that aptamer function

is governed by the relationship between ligand binding, conformational dynamics, and structural stabilization.

5.5 NMR Characterization of a Tris-Binding Tris1Δ4 Aptamer

Small-molecule aptamer selection is complicated by the fact that many selection experiments are performed in buffers containing high concentrations of background molecules. These buffer components are often assumed to be chemically inert; however, they can be present at concentrations far exceeding those of the intended target. As a result, there is a possibility that nucleic acid sequences may become enriched against buffer components rather than the intended ligand, particularly in selections where target binding is weak, nonspecific, or difficult to validate. This concern is especially relevant for small-molecule SELEX because small targets often present limited chemical surface area for recognition and may compete poorly against abundant buffer molecules present throughout the selection process.[174,200]

Tris is one of the most widely used biological buffer molecules and is frequently used in biochemical assays, nucleic acid handling, and aptamer selection workflows. Although commonly treated as a background reagent, recent work has demonstrated that DNA aptamers can be isolated against Tris, highlighting the possibility that buffer molecules may interact with nucleic acid libraries under selection conditions.[200] This finding has important implications for aptamer selection and validation, as it suggests that buffer composition can influence the sequences enriched during SELEX. Therefore, characterizing aptamer interactions with buffer molecules such as Tris is important not only for understanding the binding properties of individual aptamers, but also for evaluating potential sources of buffer interference in aptamer discovery. NMR spectroscopy provides a useful approach for examining such interactions because it can directly monitor structural changes in the aptamer upon ligand addition. In particular, the imino proton region of the one-dimensional ^{1}H-NMR spectrum is highly sensitive to nucleic acid secondary and tertiary structure. Imino proton resonances are typically observed when exchangeable protons are protected from solvent exchange through stable hydrogen bonding, such as Watson–Crick base pairs, non-canonical interactions, or tertiary contacts.[70,72] Therefore, changes in peak number, intensity, linewidth, and chemical

shift can reveal whether ligand binding stabilizes existing structure, promotes formation of new base pairs, or induces conformational ordering. Figure 5.5.1 shows the predicted secondary structure of the Tris1Δ4 as well as the chemical structure for Tris·HCl.

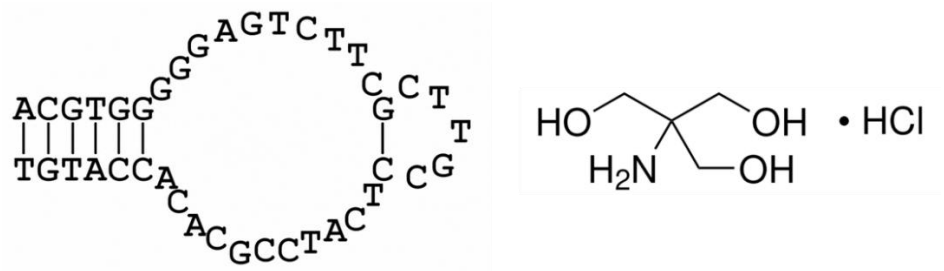

Figure 5.5.1. On the left is the predicted secondary structure of Tris1Δ4. On the right is the chemical structure of Tris-HCl.

In the free state, the Tris1Δ4 aptamer displays three partially resolved imino proton resonances and one broader peak (Figure 5.5.2). This suggests that the aptamer contains a limited amount of pre-formed secondary structure in the absence of ligand, but also retains some conformational heterogeneity. The presence of several observable peaks indicates that some imino protons are protected from solvent exchange, likely through base-pairing interactions. However, the broad feature suggests that other regions of the aptamer are dynamic or involved in exchange between multiple conformations. Thus, the free aptamer does not appear to be completely unfolded, but it also does not adopt a single highly ordered conformation in the absence of Tris.

Upon titration of Tris into the aptamer, substantial spectral changes are observed across the 9–15 ppm region. Several new imino proton resonances emerge as the concentration of Tris increases, while existing features become more defined. The appearance of new peaks throughout this region indicates that Tris binding promotes formation or stabilization of additional hydrogen-bonded structural elements. Resonances in the downfield Watson–Crick region are consistent with stabilization of canonical base-paired elements, whereas signals appearing in other regions of the imino spectrum may reflect non-canonical base pairs, tertiary contacts, or ligand-induced structural rearrangements. The progressive increase in peak number and intensity with increasing Tris concentration supports a concentration-dependent ligand-binding event rather than a random spectral fluctuation.

These data are consistent with a model in which the Tris1Δ4 aptamer contains a partially structured free-state ensemble that becomes more ordered upon ligand binding. In this model, Tris binding shifts the conformational equilibrium toward one or more folded states in which additional imino protons become protected from solvent exchange. The broad peak observed in the free aptamer may represent conformational exchange or structural heterogeneity that is reduced upon ligand addition. As Tris is titrated into the sample, the emergence of sharper resonances suggests that ligand binding stabilizes specific secondary or tertiary interactions and reduces conformational averaging on the NMR timescale.

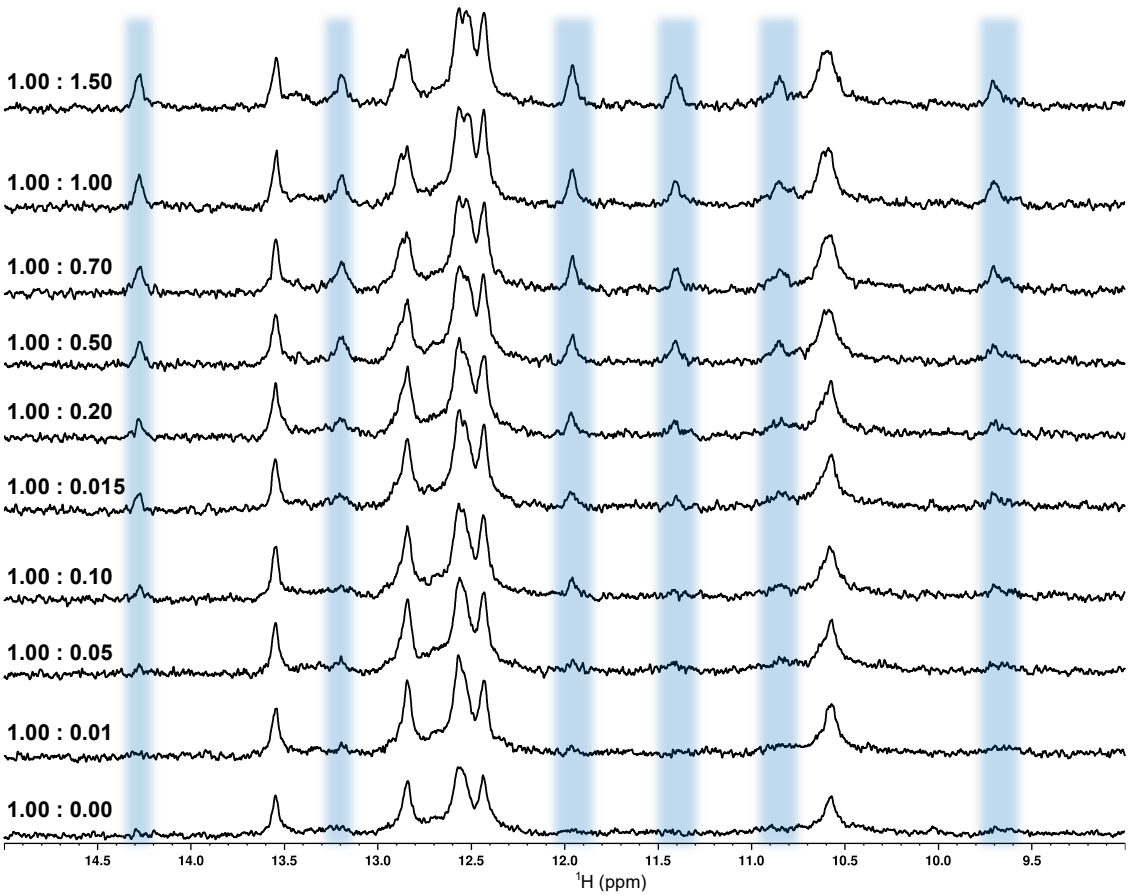

Figure 5.5.2. ^{1}H-NMR titration of the Tris1Δ4 aptamer with increasing equivalents of Tris. The free aptamer displays three partially resolved imino proton resonances and one broader feature, consistent with limited pre-formed secondary structure and conformational heterogeneity. Upon titration with Tris, several new resonances emerge throughout the 9–15 ppm region and increase in intensity with increasing Tris concentration. These ligand-dependent spectral changes indicate that Tris binding promotes formation or stabilization of additional hydrogen-bonded structural elements, consistent with small-molecule-induced ordering of the aptamer. The peaks that appear with ligand addition are highlighted in blue.

Although the Tris1Δ4 aptamer exhibits weak affinity for Tris as seen with ITC[200], the interaction was still readily characterizable by NMR. This highlights a practical advantage of NMR spectroscopy in the study of weak aptamer–small molecule interactions. Unlike many techniques that require tight binding to generate a measurable response, NMR experiments are typically performed at relatively high aptamer and ligand concentrations, which can increase the population of the bound state even for weak interactions. As a result, ligand-dependent changes in the imino proton region can still be observed through peak emergence, sharpening, broadening, or chemical shift perturbations. In this case, increasing Tris concentration produced several new resonances across the 9–15 ppm region, indicating that even a weak interaction was sufficient to alter the aptamer conformational ensemble. These observations demonstrate that NMR can provide structural insight into low-affinity aptamer–ligand systems that may be difficult to characterize using methods optimized for stronger binding interactions.

Tris1Δ4 also emphasizes the importance of careful buffer selection and validation in aptamer research. Because buffer molecules are often present at high concentrations during SELEX and downstream characterization, their potential to interact with nucleic acid sequences should not be overlooked. NMR provides a direct way to evaluate whether such molecules affect aptamer structure, thereby helping distinguish target-specific interactions from buffer-induced folding or off-target stabilization. In this context, Tris1Δ4 serves as both a useful model for studying small-molecule-induced aptamer folding and a cautionary example of how selection conditions can influence aptamer discovery.

Collectively, the NMR titration indicates that Tris binding induces or stabilizes a more structured conformation of the aptamer. The free aptamer exhibits limited pre-formed structure, whereas increasing Tris concentrations lead to the emergence of multiple imino proton resonances across the 9–15 ppm range. These spectral changes suggest ligand-dependent stabilization of both canonical and non-canonical hydrogen-bonded interactions. More broadly, this example reinforces the value of NMR as a central tool for small-molecule aptamer characterization, particularly when the goal is to understand how ligand binding reshapes the aptamer conformational ensemble.

5.6 NMR Characterization of Bilirubin and Biliverdin Aptamers

Bilirubin and biliverdin are structurally related tetrapyrrolic bile pigments generated through heme catabolism. Biliverdin is produced during oxidative heme degradation and can be reduced to bilirubin, while bilirubin can also undergo oxidation back to biliverdin under certain conditions (Figure 5.6.1). Because these molecules are closely related in structure and chemical origin, selective molecular recognition between them presents a meaningful challenge for aptamer development. The ability to distinguish bilirubin from biliverdin is analytically important because both molecules are biologically relevant heme breakdown products, and their accurate detection may support applications in diagnostics, biosensing, and molecular switch development.[201]

Two aptamers were selected to recognize these related ligands (Figure 5.6.1), with BR3 showing selective binding toward bilirubin and Bili1 showing selective binding toward biliverdin. This pair of systems provides a useful model for examining how aptamers discriminate between structurally similar small molecules. Small-molecule selectivity is often difficult to establish using affinity measurements alone, particularly when ligands are chemically related or when one ligand can undergo partial chemical conversion into another. In this context, NMR spectroscopy provides a valuable solution-based method for evaluating whether ligand binding produces aptamer-specific structural responses. Rather than only measuring whether an interaction occurs, NMR can determine whether the interaction is accompanied by changes in aptamer folding, base-pair stabilization, or conformational exchange.[72,82]

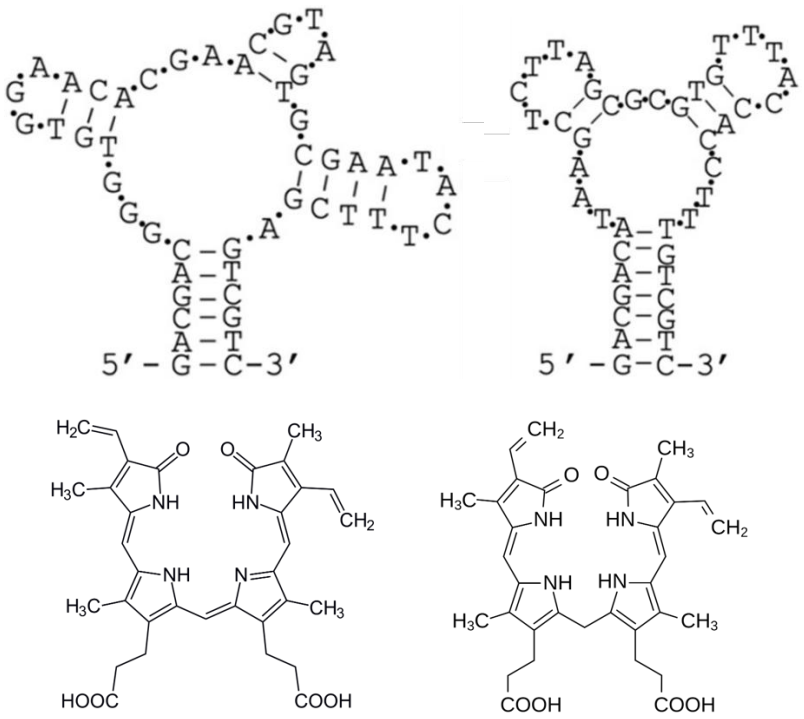

Figure 5.6.1. The predicted secondary structures of biliverdin-binding aptamer Bili1 on the left as well as the predicted secondary structure of the bilirubin-binding aptamer BR3 on the right. The chemical structures of both biliverdin and bilirubin are provided below each of their selected aptamers to which they bind.

For the Bili1 aptamer, titration with bilirubin produced little to no detectable change in the imino proton region (Figure 5.6.2). The absence of substantial peak emergence, sharpening, or chemical shift perturbation suggests that bilirubin does not meaningfully stabilize the Bili1 structure under the conditions tested. This lack of spectral response indicates that bilirubin does not induce the hydrogen-bonding network or conformational transition required for productive Bili1 folding. Therefore, the Bili1–bilirubin titration serves as an important negative control, demonstrating that the aptamer does not respond equivalently to both bile pigments. In contrast, titration of Bili1 with biliverdin produced clear ligand-dependent spectral changes (Figure 5.6.3). The emergence of new imino proton resonances and/or sharpening of existing peaks indicates that biliverdin binding promotes formation or stabilization of a more ordered aptamer structure. These changes are consistent with a cognate ligand-induced folding event in which biliverdin shifts the Bili1 conformational ensemble toward a defined bound state. The selective response of Bili1 to biliverdin,

but not bilirubin, indicates that the aptamer is capable of discriminating between these structurally related targets through a ligand-specific structural rearrangement.

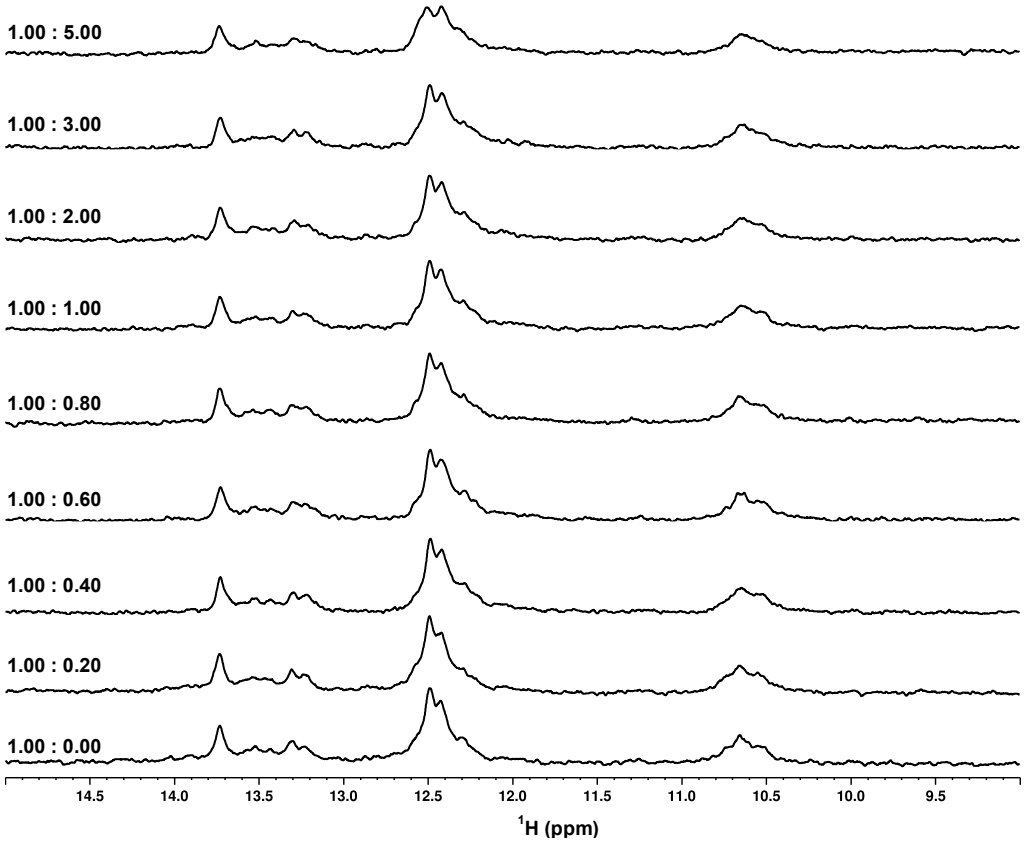

Figure 5.6.2. ^{1}H-NMR titration of the Bili1 aptamer with bilirubin. Stacked spectra show the imino proton region collected with increasing equivalents of bilirubin, with the aptamer:ligand molar ratio indicated beside each spectrum. Minimal changes in peak position, intensity and linewidth are observed upon bilirubin addition, indicating that bilirubin does not substantially alter the Bili1 aptamer structure. The absence of ligand-induced spectral changes suggests that bilirubin is not a binding ligand for Bili1 and does not stabilize a defined Bili1-bound conformation.

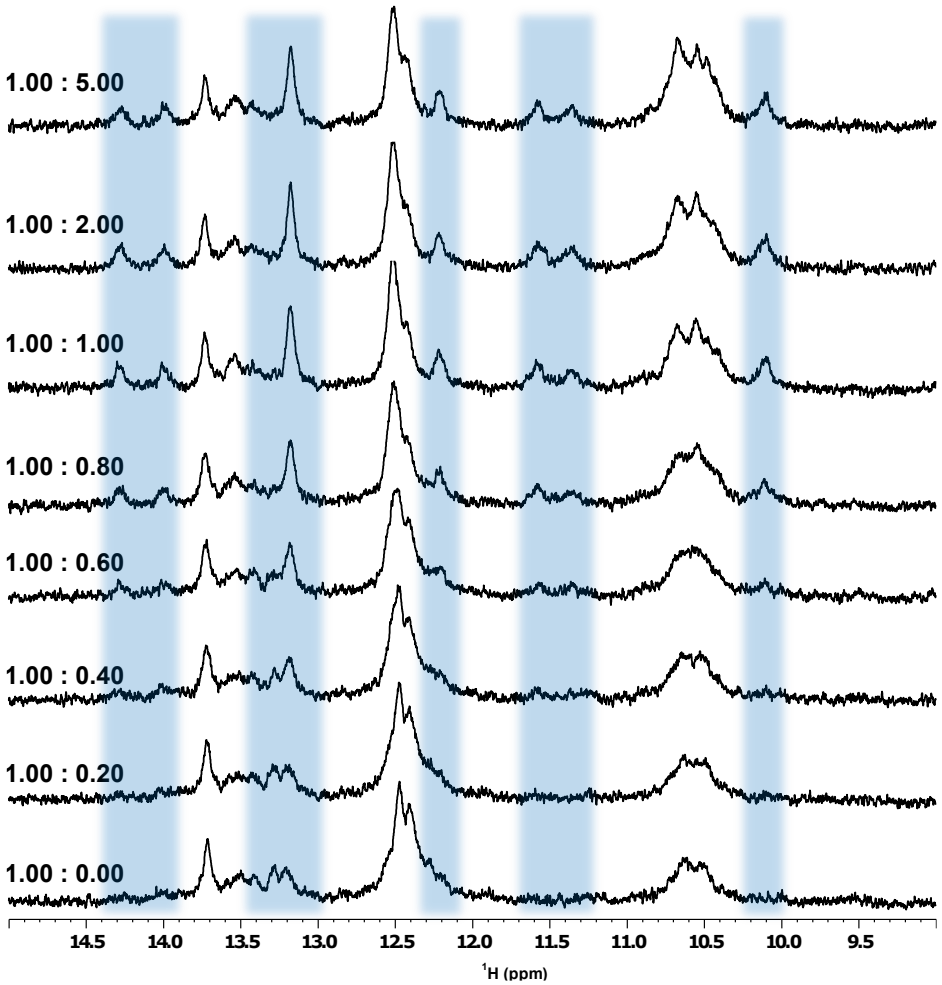

Figure 5.6.3. ^{1}H-NMR titration of the Bili1 aptamer with biliverdin. Stacked spectra show the imino proton region collected with increasing equivalents of biliverdin, with the aptamer:ligand molar ratio indicated beside each spectrum. Addition of biliverdin produces clear spectral changes, including the emergence of imino proton resonances, consistent with ligand-induced stabilization of hydrogen-bonded secondary or tertiary structure. These changes indicate that biliverdin is the cognate ligand for Bili1 and promotes formation of a more ordered aptamer-bound state. Peaks that appear with ligand addition are highlighted in blue.

A complementary pattern is observed for the bilirubin-binding aptamer BR3. Upon titration with bilirubin, BR3 displays clear changes in the imino proton spectrum, indicating that bilirubin binding alters the aptamer structure (Figure 5.6.4). The appearance of new resonances and changes in peak intensity or linewidth are consistent with stabilization of hydrogen-bonded secondary or tertiary interactions in the ligand-bound state. These spectral changes suggest that bilirubin binding promotes a defined structural response in BR3 and supports the assignment of BR3 as a bilirubin-selective aptamer. When BR3 is titrated with biliverdin, however, the NMR spectra show little to no structural response relative to the free aptamer

(Figure 5.6.5). The absence of significant imino proton changes suggests that biliverdin does not productively engage the BR3 binding pocket or stabilize the BR3 folded state. This cross-reactivity experiment is especially important because biliverdin is structurally related to bilirubin and could plausibly interact nonspecifically with nucleic acid sequences. The lack of a comparable spectral response indicates that the bilirubin-dependent changes observed for BR3 are not simply due to nonspecific interaction with a hydrophobic tetrapyrrole scaffold, but instead reflect ligand-specific recognition.

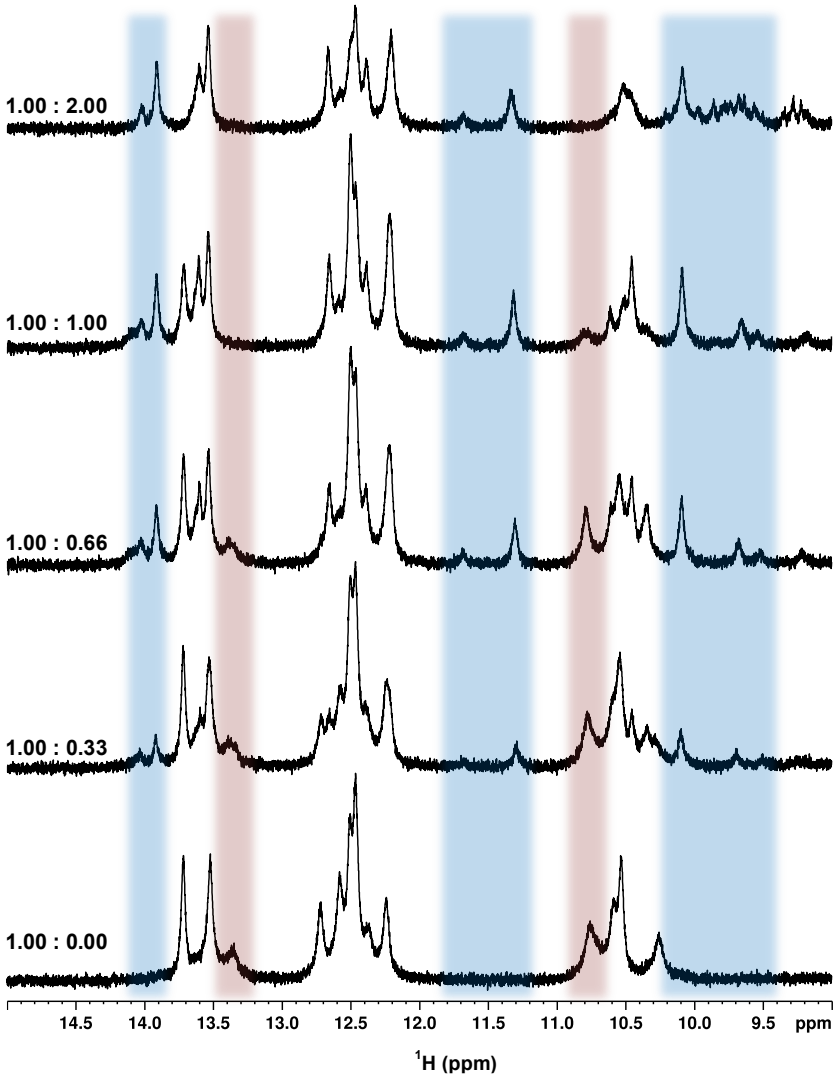

Figure 5.6.4. ^{1}H-NMR titration of the BR3 aptamer with bilirubin. Stacked spectra show the imino proton region collected with increasing equivalents of bilirubin, with the aptamer:ligand molar ratio indicated beside each spectrum. Bilirubin addition induces distinct changes in the imino proton region, including changes in resonance intensity, linewidth, and/or the appearance of new signals. These spectral changes are consistent with bilirubin-dependent stabilization or remodeling of the BR3 aptamer structure, supporting selective recognition of bilirubin by BR3. Peaks that appear with ligand addition are highlighted in blue. Peaks that disappear with ligand addition are highlighted in red.

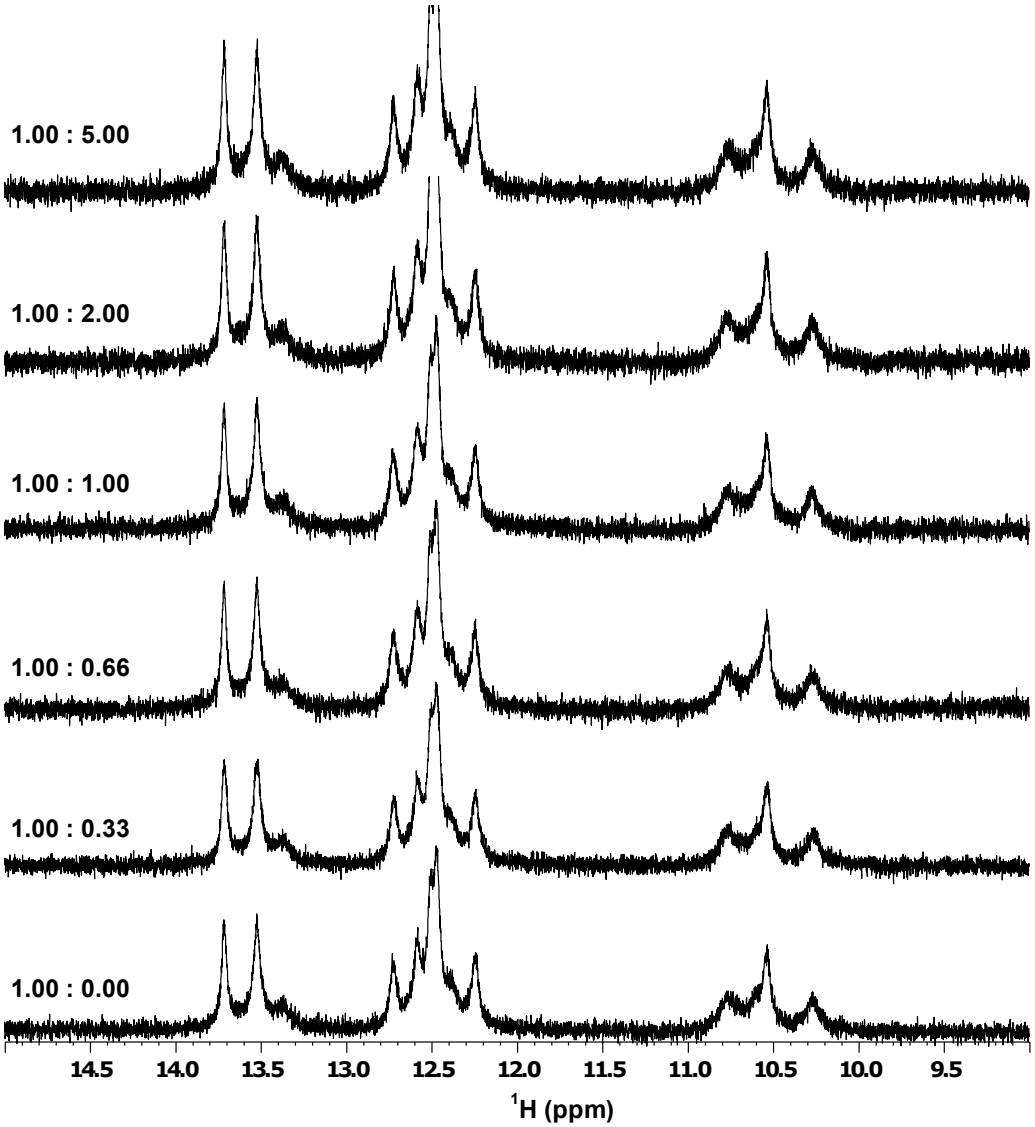

Figure 5.6.5. ^{1}H-NMR titration of the BR3 aptamer with biliverdin. Stacked spectra show the imino proton region collected with increasing equivalents of biliverdin, with the aptamer:ligand molar ratio indicated beside each spectrum. The absence of substantial ligand-induced spectral changes indicates that biliverdin does not strongly perturb or stabilize the BR3 aptamer structure under the conditions tested. This lack of structural response supports the conclusion that biliverdin is a non-cognate ligand for this bilirubin-binding aptamer and highlights the selectivity of the aptamer–ligand interaction.

Together, the four NMR titrations demonstrate reciprocal selectivity between the two aptamer–ligand pairs. Bili1 responds structurally to biliverdin but not bilirubin, whereas BR3 responds structurally to bilirubin but not biliverdin. These results show that NMR can provide a direct structural readout of aptamer selectivity. Importantly, the selectivity is not inferred solely from binding affinity or assay output,

but from the ability of each ligand to induce or stabilize a distinct aptamer conformation. This is particularly valuable for small-molecule aptamers, where structurally related ligands may produce ambiguous results in fluorescence, colorimetric, or displacement-based assays.

The bilirubin and biliverdin aptamer systems provide a clear example of how NMR spectroscopy can be used to assess aptamer selectivity at the structural level. Because bilirubin and biliverdin are chemically related heme catabolism products, distinguishing between them requires recognition elements that respond specifically to subtle differences in ligand structure. The NMR data show that Bili1 undergoes structural changes only in response to biliverdin, while BR3 undergoes structural changes only in response to bilirubin. In the cross-reactivity experiments, the non-cognate ligand fails to produce comparable spectral changes, indicating that the observed responses are ligand-specific rather than nonspecific effects of tetrapyrrole binding.

This example reinforces the importance of NMR in small-molecule aptamer characterization. Affinity measurements and sensor responses can identify promising aptamer candidates, but NMR provides direct evidence that binding is accompanied by selective structural stabilization. By comparing cognate and non-cognate ligand titrations, NMR can determine whether aptamer function arises from a specific ligand-induced fold or from broader nonspecific nucleic acid interactions. Thus, the bilirubin and biliverdin aptamers illustrate how NMR can be used not only to characterize aptamer binding, but also to validate the molecular basis of aptamer selectivity.

5.7 Using NMR to Distinguish Specific and Non-Specific DNA/Aptamer-Small Molecule Interactions

A challenge in small-molecule aptamer research is distinguishing specific target recognition from non-specific nucleic acid binding. This distinction is particularly important for ligands that can interact broadly with DNA through electrostatic interactions, base stacking, groove binding, or intercalation-like behavior. In these cases, an apparent binding event may not necessarily reflect recognition by a defined aptamer binding pocket but instead may arise from a heterogeneous collection of weak interactions distributed across different nucleic acid structures.

The cocaine-binding aptamer family provides a useful platform for evaluating this distinction. MN4 adopts a three-way junction architecture and has been widely used as a model system for studying aptamer–small molecule recognition. Previous studies have demonstrated that the cocaine-binding aptamer scaffold can bind several off-target ligands, including quinine and other structurally distinct small molecules, highlighting that aptamer recognition is not always limited to the ligand used during selection.[84,114,118] More recent work has shown that amodiaquine, a clinically relevant 4-aminoquinoline antimalarial compound, binds tightly to a range of duplex and junction-containing DNA constructs, supporting the conclusion that amodiaquine can engage nucleic acid structures through broad DNA-binding behavior (Figure 5.7.1).[166]

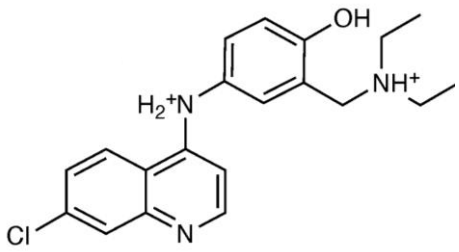

Amodiaquine

Figure 5.7.1. Chemical structure of amodiaquine, a 4-aminoquinoline antimalarial compound investigated for its interactions with MN4 and related DNA constructs. Amodiaquine contains a quinoline core and phenolic side chain that may contribute to its ability to associate with nucleic acid structures through aromatic stacking, electrostatic, and other non-specific DNA-binding interactions.

To evaluate whether amodiaquine binding reflects specific recognition, a series of MN4-derived constructs and unrelated DNA sequences were examined by ^{1}H-NMR spectroscopy. These constructs included the variants of the MN4 aptamer, the SS1 variant in which the two G–A mismatches were reversed, and three truncation variants: SS2, SS3, and SS4, in which stem 1, stem 2, or stem 3 were removed, respectively. Additional non-aptamer DNA controls, including a hexamer, the Dickerson–Drew dodecamer (DDD), and a generic three-way junction, were also tested. This panel allowed the effects of amodiaquine to be compared across both aptamer-derived sequences and unrelated DNA architectures (Figure 5.7.2).

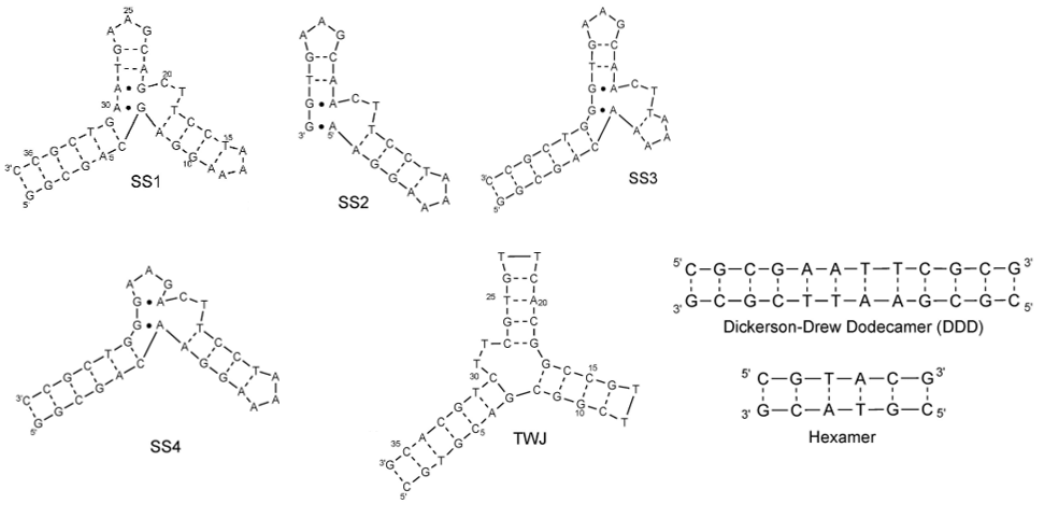

Figure 5.7.2. Structures of the nucleic acid constructs used in this study. Dashes indicate Watson-Crick base pairs while dots indicate non-Watson-Crick base pairs.

In a specific aptamer–ligand interaction, ligand binding often stabilizes a defined folded population. This can produce well-resolved spectral changes, including peak sharpening, chemical shift perturbations, or the appearance of new imino proton resonances. These features suggest that the ligand either selects or induces a discrete aptamer conformation. In contrast, non-specific binding may result in broadening or disappearance of resonances if the ligand promotes conformational heterogeneity, intermediate exchange, or multiple weakly populated binding modes.[202] Thus, the NMR response provides important information about the nature of the interaction, not simply whether binding occurs.

The bottom spectrum of Figure 5.7.3 shows free SS1 which has several broad, low intensity peaks in the 12 - 13.5 ppm range as well as even more broad and lower intensity peaks in the 9 – 11 ppm range. This indicates poorly formed structure compared to the parent MN4. Thus, swapping the two mismatched G-A base pairs introduced destabilization to the free MN4 structure. The addition of amodiaquine resulted in a progressive reduction of imino proton signal intensity. Rather than producing a new set of well-resolved ligand-bound resonances, the existing imino signals broadened and eventually disappeared into baseline noise.

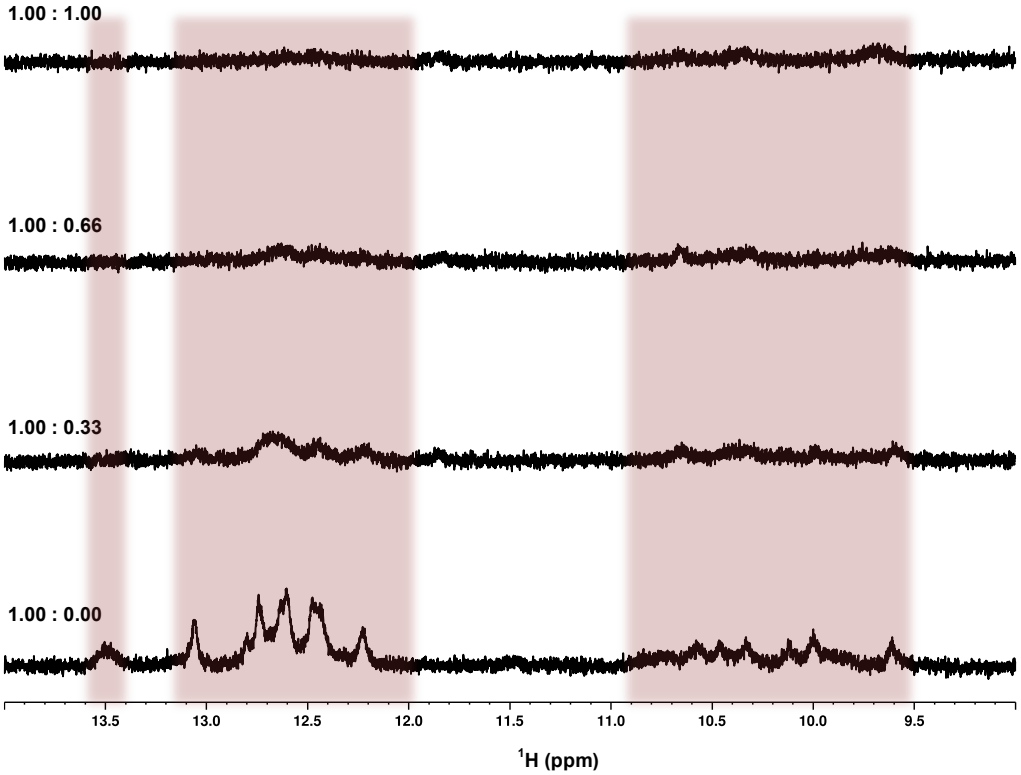

Figure 5.7.3. ^{1}H-NMR titration of the SS1 aptamer with amodiaquine. Stacked spectra show the imino proton region collected with increasing equivalents of amodiaquine, with the aptamer:ligand molar ratio indicated beside each spectrum. This was performed in 10 mM phosphate buffer, pH 7.4, 140 mM NaCl, 10% ^2H_2O – 90% ^1H_2O at 5°C. Peaks that disappear with ligand addition are highlighted in red.

The bottom spectrum of Figure 5.7.4 shows free SS2 which has two sharper peaks in the more downfield region between 12 – 13.5 ppm as well as some low intensity, broad peaks. Additionally, there are also some peaks that appear in the upfield region between 9 – 11.5 ppm. This is indicative of some structure formed in the free state with clear signs of multiple conformations in exchange with one another. The addition of amodiaquine resulted in a progressive reduction of imino proton signal intensity however at a smaller extent compared to SS1 whereby a 1:1 ratio of DNA to amodiaquine results in all the imino signals broadening beyond visibility. This is likely due to the preformed structures of SS2 not being suitable for amodiaquine binding and thus higher concentrations are needed to push the equilibrium towards the unfolded MN4-variant.

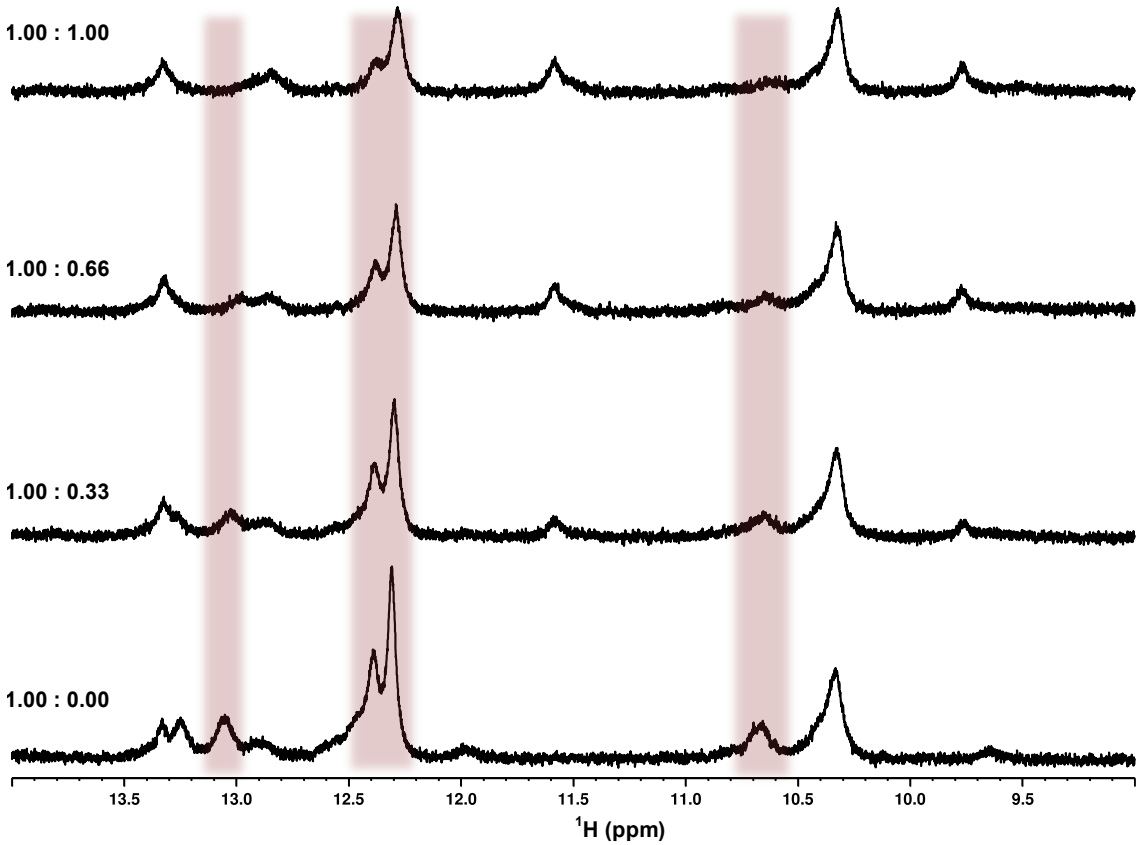

Figure 5.7.4. ^{1}H-NMR titration of the SS2 aptamer with amodiaquine. Stacked spectra show the imino proton region collected with increasing equivalents of amodiaquine, with the aptamer:ligand molar ratio indicated beside each spectrum. This was performed in 10 mM phosphate buffer, pH 7.4, 140 mM NaCl, 10% ^2H_2O – 90% ^1H_2O at 5°C. Peaks that disappear with ligand addition are highlighted in red.

The bottom spectrum of Figure 5.7.5 shows free SS3 where there are several sharp, high intensity peaks in the downfield region between 12 – 13.5 ppm. The presence of these signals indicate that SS3 has some preformed structure in the unbound state. Upon addition of amodiaquine, the imino proton spectrum changes substantially. At the 1.00 : 0.33 aptamer : amodiaquine ratio, several of the sharp resonances observed in the free aptamer broaden and decrease in intensity, especially the clustered peaks between approximately 12.5–13.5 ppm. Some signals remain visible, but the overall spectrum becomes less resolved. This indicates that amodiaquine perturbs the pre-existing base-paired structure of SS3 rather than stabilizing a single new folded conformation. Importantly, amodiaquine addition does not produce a new set of sharp, well-resolved resonances that would indicate formation of a discrete SS3–amodiaquine complex. Instead, the spectrum shows broadening and disappearance of the original peaks. This suggests

that amodiaquine does not bind SS3 through a single defined binding pocket that stabilizes a unique aptamer conformation. Rather, the ligand likely interacts with multiple sites or structural features within the DNA, producing an ensemble of ligand-associated conformations that exchange on the NMR timescale.

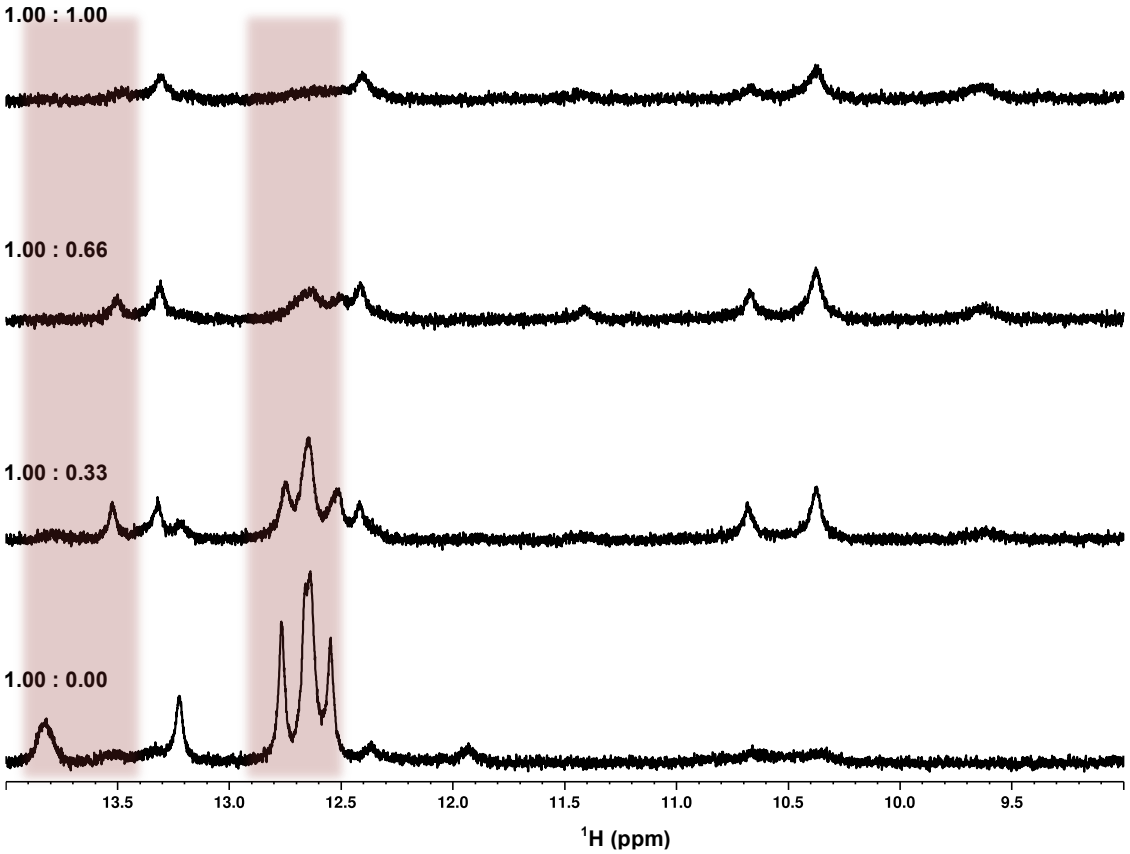

Figure 5.7.5. ^{1}H-NMR titration of the SS3 aptamer with amodiaquine. Stacked spectra show the imino proton region collected with increasing equivalents of amodiaquine, with the aptamer:ligand molar ratio indicated beside each spectrum. This was performed in 10 mM phosphate buffer, pH 7.4, 140 mM NaCl, 10% ^2H_2O – 90% ^1H_2O at 5°C. Peaks that disappear with ligand addition are highlighted in red.

The SS4 titration (Figure 5.7.6) shows that amodiaquine strongly perturbs the imino proton spectrum of the stem 3-deleted MN4 variant. In the free state, SS4 displays several resolved imino proton resonances, indicating that removal of stem 3 does not fully abolish secondary structure formation. The presence of these signals suggests that the remaining regions of the construct retain hydrogen-bonded base pairs or other protected imino environments in the absence of ligand. Upon addition of amodiaquine, the spectrum undergoes progressive broadening and loss of signal intensity. At lower amodiaquine equivalents, several resonances begin to decrease in intensity and broaden, indicating that ligand association perturbs

the pre-existing folded population. As the amodiaquine concentration increases, this effect becomes more pronounced, with many of the originally resolved imino peaks becoming weak, broadened, or disappearing into the baseline. This indicates that amodiaquine disrupts the observable structured state of SS4 rather than stabilizing a single, well-defined ligand-bound conformation.

Importantly, the titration does not produce a new set of sharp imino proton resonances that would be expected for formation of a discrete SS4–amodiaquine complex. Instead, the dominant spectral response is loss of resolution and signal broadening. This behavior is consistent with amodiaquine promoting a heterogeneous ensemble of DNA-bound states that are in exchange on the NMR timescale. Such exchange broadening suggests that amodiaquine may interact with multiple sites or structural features within SS4 rather than occupying one specific binding pocket.

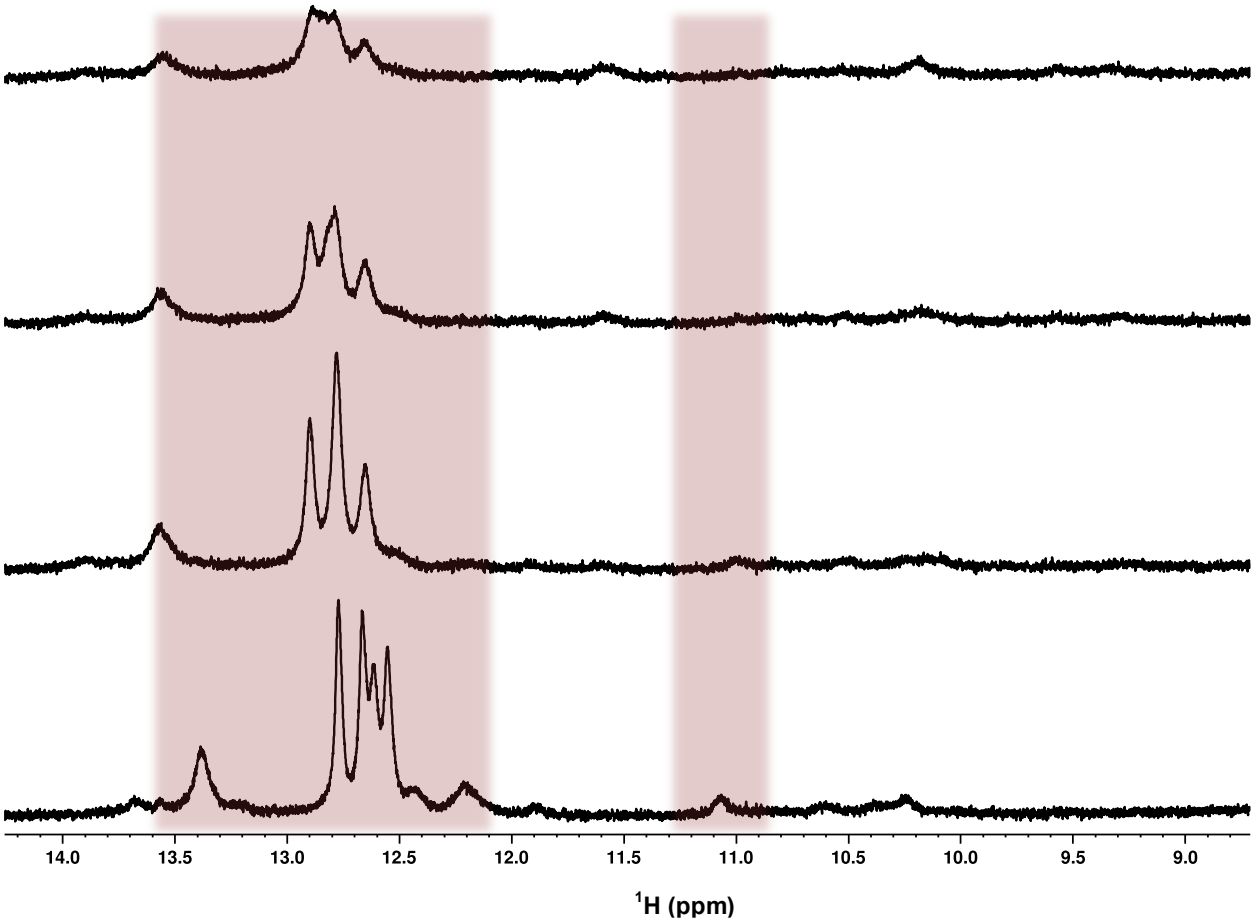

Figure 5.7.6. ^{1}H-NMR titration of the SS4 aptamer with amodiaquine. Stacked spectra show the imino proton region collected with increasing equivalents of amodiaquine, with the aptamer:ligand molar ratio indicated beside each spectrum. This was performed in 10 mM phosphate buffer, pH 7.4, 140 mM NaCl, 10% ^2H_2O – 90% ^1H_2O at 5°C. Peaks that disappear with ligand addition are highlighted in red.

This behavior observed for the MN4-derived variants, was also observed with the unrelated DNA constructs, indicating that the spectral response was not unique to single-stranded aptamers. A generic three-way junction nucleic acid sequence was also tested against amodiaquine (Figure 5.7.7). In the free state, the generic three-way junction displays several observable imino proton resonances, indicating that the construct forms hydrogen-bonded secondary structure prior to ligand addition. These signals are consistent with base-paired stem regions within the junction scaffold. Upon titration with amodiaquine, the imino proton signals progressively decrease in intensity and broaden. This indicates that amodiaquine perturbs the pre-existing structured state of the junction. Rather than producing a new set of well-resolved resonances corresponding to a defined ligand-bound structure, amodiaquine addition leads to a loss of spectral resolution. At higher amodiaquine concentrations, many of the imino resonances become substantially broadened or disappear into the baseline, suggesting that the DNA is sampling multiple ligand-associated conformations. This indicates that the interaction is not dependent on the selected MN4 aptamer binding pocket. Instead, amodiaquine appears capable of engaging general structural features of junction-containing DNA, potentially through aromatic stacking, groove association, electrostatic interactions, or interactions with partially flexible regions of the junction.

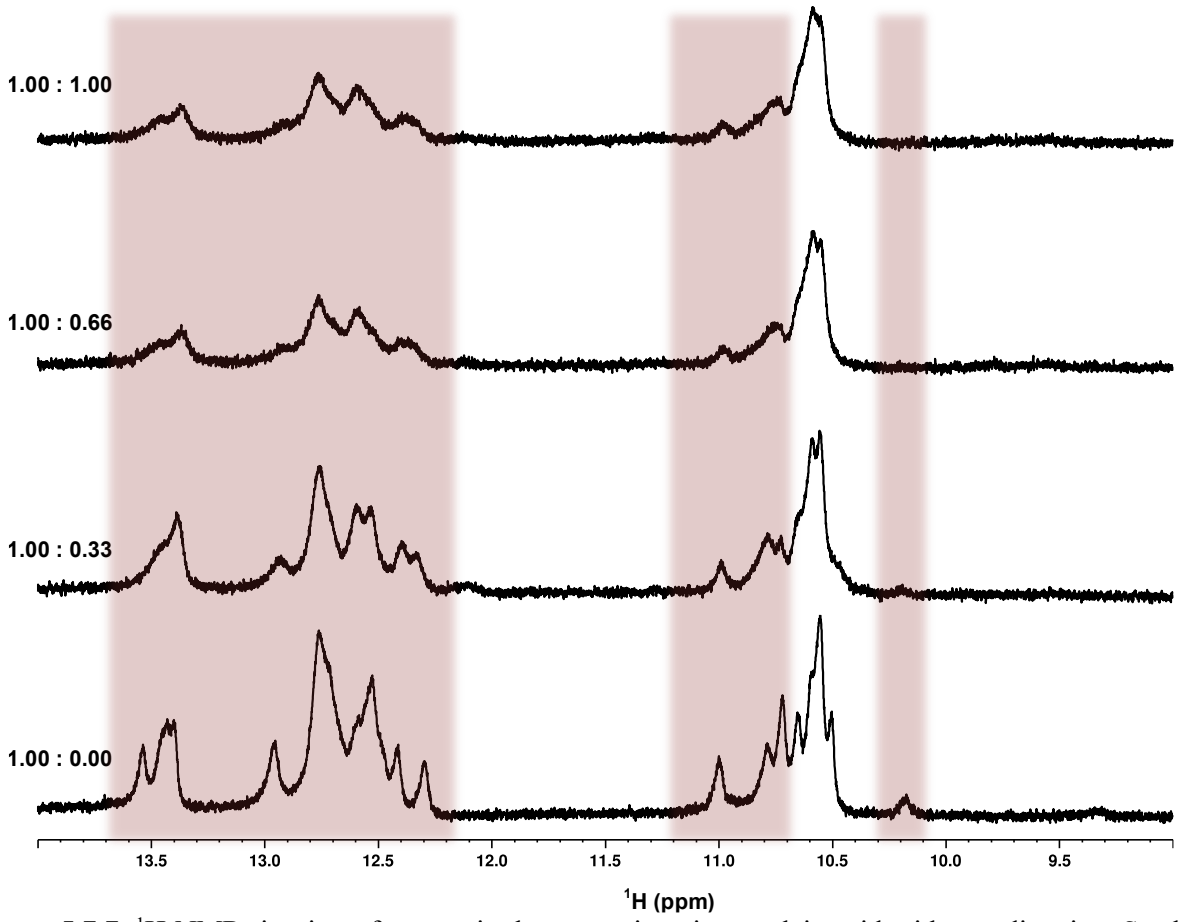

Figure 5.7.7. ^{1}H-NMR titration of a generic three-way junction nucleic acid with amodiaquine. Stacked spectra show the imino proton region collected with increasing equivalents of amodiaquine, with the DNA:ligand molar ratio indicated beside each spectrum. This was performed in 10 mM phosphate buffer, pH 7.4, 140 mM NaCl, 10% $^{2}H_2O$ – 90% $^{1}H_2O$ at 5°C. Peaks that disappear with ligand addition are highlighted in red.

The DDD titration provides another useful non-aptamer control for evaluating the binding behavior of amodiaquine (Figure 5.7.8). In the free state, the DDD duplex shows well-resolved imino proton resonances, consistent with a stable Watson–Crick base-paired duplex. As amodiaquine is titrated into the sample, these imino signals progressively broaden and decrease in intensity. Rather than producing new sharp peaks that would suggest formation of a defined bound complex, the spectrum gradually loses resolution. This indicates that amodiaquine perturbs the duplex structure and likely interacts with DDD through multiple weak or non-specific binding modes.

The fact that a simple duplex DNA sequence shows the same general loss of imino signal observed for MN4 and its variants supports the conclusion that amodiaquine binding is not specific to the MN4

aptamer. Instead, amodiaquine appears to broadly interact with DNA structures, producing a heterogeneous ensemble of complexes that exchange on the NMR timescale.

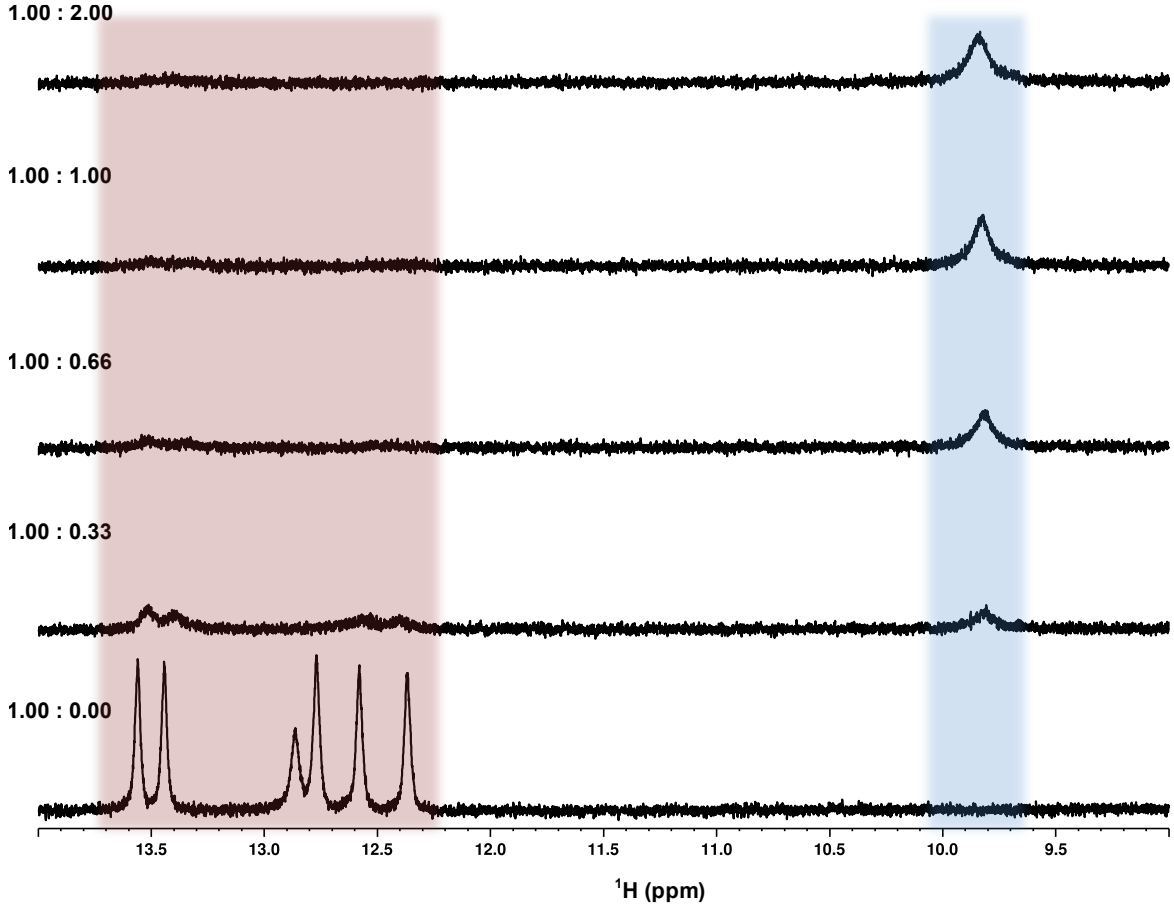

Figure 5.7.8. ^{1}H-NMR titration of the DDD dodecamer DNA with amodiaquine. Stacked spectra show the imino proton region collected with increasing equivalents of amodiaquine, with the DNA:ligand molar ratio indicated beside each spectrum. This was performed in 10 mM phosphate buffer, pH 7.4, 140 mM NaCl, 10% ^2H_2O – 90% ^1H_2O at 5°C. Peaks that disappear with ligand binding are highlighted in red. Peaks that appear with ligand addition are highlighted in blue.

The SJH hexamer duplex titration serves as another useful non-aptamer control for assessing whether amodiaquine binding is specific to aptamer structure or reflects more general DNA association (Figure 5.7.9). In the free state, the hexamer duplex shows observable imino proton resonances, consistent with formation of a short Watson–Crick base-paired duplex. With increasing amodiaquine, the imino signals progressively broaden and decrease in intensity. Similar to the DDD duplex, the titration does not produce a new set of sharp, well-resolved resonances that would indicate formation of a single defined bound complex. Instead, the gradual loss of signal suggests that amodiaquine perturbs the duplex through

heterogeneous or weakly defined interactions. The fact that even a short duplex DNA construct responds to amodiaquine supports the interpretation that amodiaquine is not binding exclusively to the MN4 aptamer or its three-way junction architecture. Rather, amodiaquine appears capable of interacting broadly with duplex DNA, likely through multiple non-specific binding modes. This reinforces the conclusion that the NMR signal loss observed across the DNA constructs reflects formation of dynamic, exchanging amodiaquine–DNA complexes rather than stabilization of a specific aptamer-bound state.

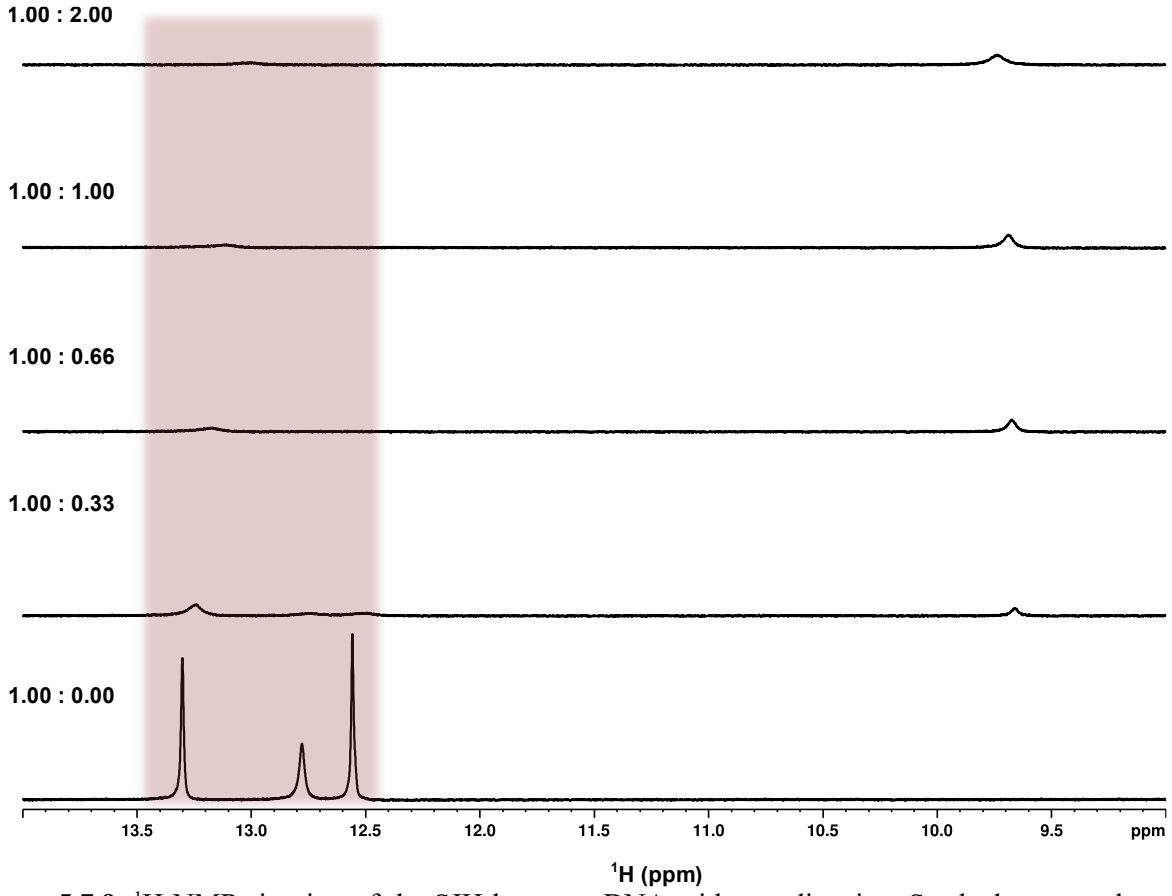

Figure 5.7.9. ^{1}H-NMR titration of the SJH hexamer DNA with amodiaquine. Stacked spectra show the imino proton region collected with increasing equivalents of amodiaquine, with the DNA:ligand molar ratio indicated beside each spectrum. This was performed in 10 mM phosphate buffer, pH 7.4, 140 mM NaCl, 10% $^{2}H_2O$ – 90% $^{1}H_2O$ at 5°C.

The rate at which imino resonances disappeared varied among the constructs. Some sequences lost their imino signals at lower amodiaquine concentrations, whereas others required higher ligand concentrations before broadening became complete. These differences likely reflect variation in the relative affinity or susceptibility of each DNA architecture to amodiaquine-induced perturbation. Constructs that

interact more strongly with amodiaquine may experience faster exchange broadening or more rapid disruption of observable base-paired states. However, the shared pattern of signal loss across all constructs indicates that the dominant interaction is not a unique MN4-specific recognition event, but rather a broader DNA-binding behavior.

The MN4 variant series was particularly informative. If amodiaquine recognition depended on a specific MN4 binding pocket, removal of individual stems or reversal of the G–A mismatches would be expected to produce a qualitatively distinct NMR response. For example, disruption of a required binding pocket might eliminate ligand-induced structural changes or prevent formation of a defined bound-state spectrum. Instead, all MN4-derived constructs displayed progressive imino signal broadening upon amodiaquine addition. This indicates that amodiaquine binding is not strictly dependent on the intact MN4 three-way junction or on a single arrangement of the G–A mismatches.

The non-aptamer controls further support this interpretation. The observation that the hexamer, DDD duplex, and generic three-way junction also undergo imino signal reduction upon amodiaquine addition demonstrates that amodiaquine-induced broadening is not exclusive to aptamer-derived sequences. The response of DDD is especially notable because this construct lacks the selected MN4 aptamer architecture and is commonly used as a model duplex DNA sequence. Signal broadening in DDD indicates that amodiaquine can interact with canonical duplex DNA, consistent with reports that amodiaquine binds double-stranded DNA structures.[166] Similarly, broadening in the generic three-way junction suggests that junction architecture may provide additional binding surfaces or conformational flexibility, but does not confer aptamer-specific recognition.

These results illustrate an important distinction between specific and non-specific aptamer–ligand interactions. Specific interactions often stabilize a discrete structural state, resulting in sharper or newly resolved NMR signals that correspond to an ordered ligand-bound complex. Non-specific interactions, by contrast, can generate many structurally related but non-identical complexes that interconvert on the NMR timescale. When this exchange is sufficiently rapid or occurs in the intermediate exchange regime, the corresponding imino resonances broaden and may disappear from the spectrum altogether.

This interpretation is further supported by ITC measurements of amodiaquine binding, which did not produce a simple one-site binding isotherm. Instead, the binding profiles were more consistent with multi-site behavior, suggesting that amodiaquine interacts with multiple binding sites on the DNA rather than forming a single discrete aptamer–ligand complex. This is consistent with the NMR data, where amodiaquine addition did not generate a new set of well-resolved resonances corresponding to a defined bound state. Instead, the imino proton signals progressively broadened and disappeared, indicating conformational heterogeneity and exchange among multiple ligand-associated states. Together, the ITC and NMR data support a model in which amodiaquine binds DNA through non-specific or broadly structure-dependent interactions involving multiple sites.[166]

The ability to make this distinction is a major strength of NMR spectroscopy in aptamer–small molecule studies. Affinity measurements alone may indicate that a ligand binds tightly to an aptamer, but they cannot necessarily determine whether the interaction is structurally specific. NMR provides a direct structural readout of the binding event. When binding stabilizes a defined aptamer fold, this is reflected in the emergence or sharpening of imino proton resonances. When binding produces heterogeneous interactions or conformational exchange, this is reflected in resonance broadening and signal loss.

A similar NMR response was observed in the methylene blue studies described in Chapter 4, where addition of methylene blue to polynucleotide DNA constructs resulted in a progressive loss of imino proton resonances. Methylene blue is a well-established DNA-binding dye that can intercalate into duplex DNA and interact with nucleic acids in a non-specific manner. The disappearance of imino signals upon methylene blue addition was therefore interpreted as non-specific DNA binding, structural perturbation, and rapid exchange rather than stabilization of a single well-defined complex. The amodiaquine titrations show a comparable spectral behavior, where imino resonances progressively broaden and disappear across MN4 variants, and unrelated duplex or junction DNA constructs. This similarity supports the interpretation that amodiaquine, like methylene blue, can engage DNA through broadly non-specific interactions that generate an ensemble of exchanging ligand-bound states. Thus, the parallel between the methylene blue

and amodiaquine data further reinforces the utility of NMR for distinguishing specific aptamer recognition from general small-molecule binding to DNA.

5.8 Characterization of Cobalt- and Zinc-Binding Aptamers

Metal ion-binding aptamers represent a distinct class of nucleic acid receptors because their targets are small, highly solvated, and often lack the extended molecular surfaces typically used for recognition of organic small molecules or proteins. Unlike aromatic or heterocyclic ligands, metal ions do not generally provide proton-rich structural features that can be directly followed by conventional ligand-observed ^{1}H-NMR experiments. Their interactions with DNA are instead governed by charge density, ionic radius, hydration, coordination geometry, and electrostatic interactions with nucleobases or the phosphate backbone. As a result, determining whether a metal ion binds specifically to an aptamer, rather than interacting nonspecifically with the negatively charged DNA backbone, remains an important challenge in aptamer selection for small metal ligands.[203–205]

The Co-1 and Zn-1 aptamers were selected to bind cobalt and zinc ions, respectively, and provide useful model systems for examining how DNA aptamers recognize divalent transition metals. Cobalt and zinc are chemically important metal ions with distinct coordination preferences and biological relevance. Zinc plays essential roles in nucleic acid-binding proteins and metalloenzymes, while cobalt-containing complexes and cobalt-binding systems are relevant in coordination chemistry, environmental monitoring, and bioinorganic applications. Because divalent metal ions can associate with nucleic acids through both specific coordination sites and more diffuse electrostatic interactions, structural validation is required to determine whether aptamer binding is coupled to a defined metal-dependent fold.[203,206] This distinction is especially important for cobalt- and zinc-binding aptamers because metal ion interactions can be difficult to interpret using affinity measurements alone. A binding assay may demonstrate that an aptamer complexes with a metal ion, but it does not necessarily reveal whether the interaction produces a single structured complex, multiple weakly bound states, or nonspecific charge-mediated association. NMR provides an orthogonal structural perspective by showing how the aptamer conformational ensemble changes upon

ligand titration. For example, the emergence or sharpening of imino proton resonances would support metal-induced stabilization of a more ordered aptamer fold, whereas broadening or disappearance of signals would suggest exchange, heterogeneity, or disruption of existing structure.

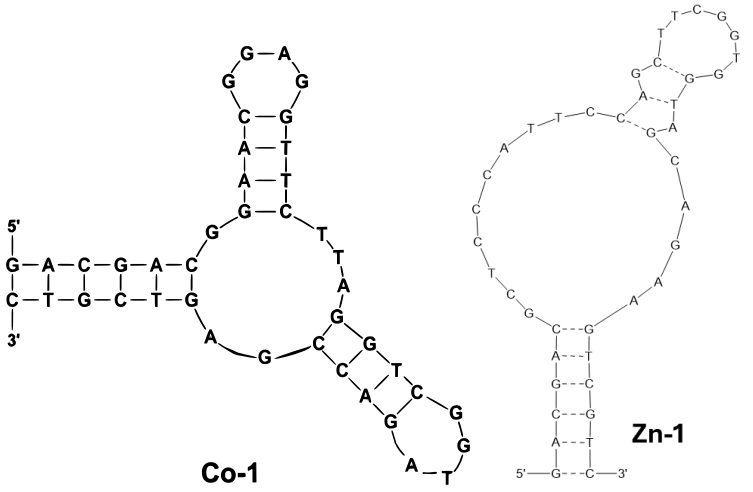

Figure 5.8.1. The predicted secondary structures of the Co-1 and Zn-1 aptamers.

The ^{1}H-NMR titration of Zn-1 with Zn^{2+} shows clear zinc-dependent changes in the imino proton region, indicating that metal binding perturbs and stabilizes the aptamer structure. In the absence of added Zn^{2+}, the free Zn-1 aptamer already displays several observable imino proton resonances between approximately 9.8 and 13.7 ppm. The presence of these peaks indicates that Zn-1 is not fully unfolded in the free state but instead contains pre-formed hydrogen-bonded structural elements. However, several peaks in the free spectrum are broad and partially overlapped, particularly in the 12.5–13.1 ppm and 10.3–10.8 ppm regions, suggesting that the free aptamer samples multiple conformations or contains dynamic structural elements (Figure 5.8.2).

Upon addition of Zn^{2+}, several existing resonances increase in intensity and become better resolved. This is most apparent in the downfield region near 13.6 ppm, the cluster between approximately 12.5 and 13.1 ppm, and the group of resonances between approximately 10.3 and 10.8 ppm. These changes indicate that Zn^{2+} binding stabilizes structural features that are already partially populated in the free aptamer. Rather than generating an entirely new spectrum immediately, zinc appears to shift the conformational ensemble toward a more ordered state.

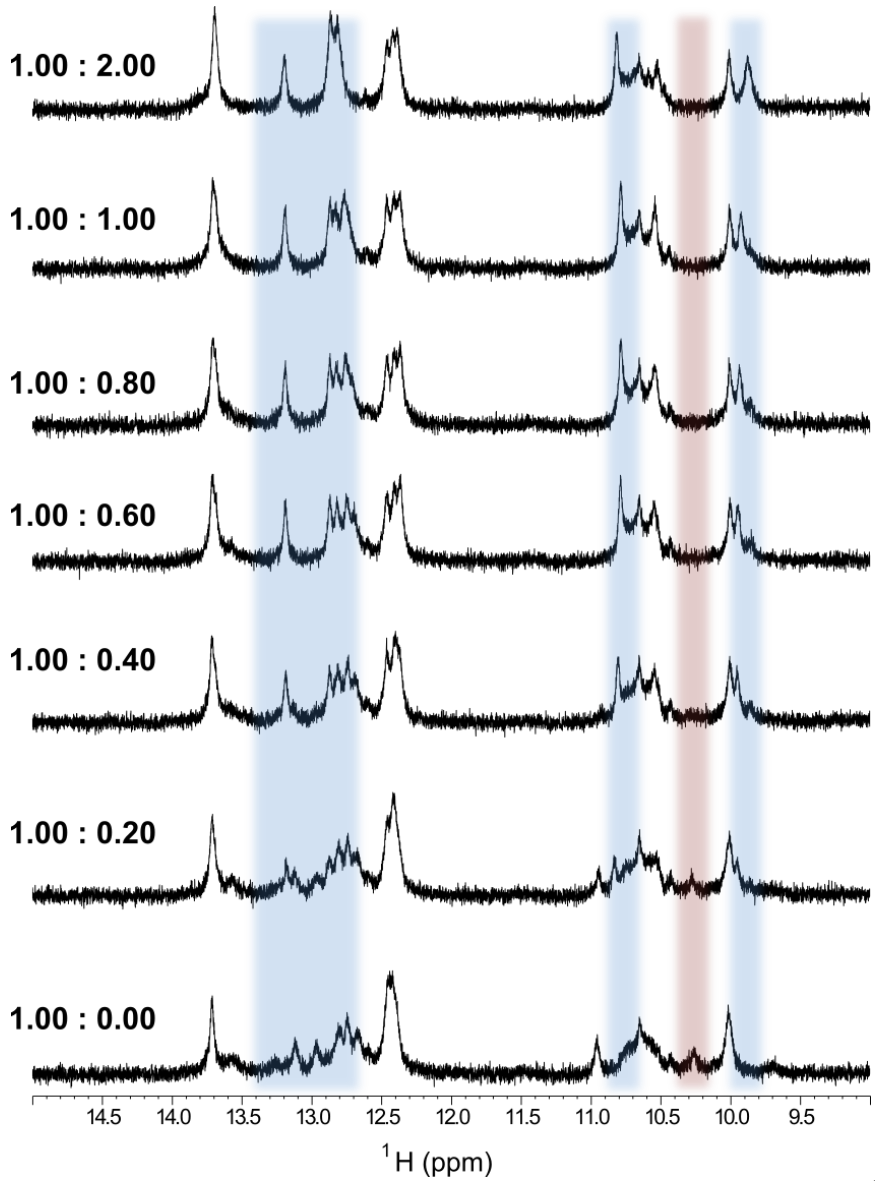

Figure 5.8.2. ^{1}H-NMR titration of the Zn-1 aptamer with increasing equivalents of Zn^{2+}. Spectra were collected with 500 µM Zn-1 in 100 mM NaCl, 2 mM $MgCl_2$, and 10% $^{2}H_2O$ – 90% $^{1}H_2O$ at 5 °C, with aptamer:Zn^{2+} molar ratios indicated beside each spectrum. Peaks that appear with ligand addition are highlighted in blue. Peaks that disappear with ligand addition are highlighted in red.

The titration of Co-1 was also done with zinc ions as cobalt (II) ions are paramagnetic and cause substantial line-broadening in the NMR spectra collected. Similar to the Zn-1 aptamer, the ^{1}H-NMR titration of Co-1 with Zn^{2+} shows a strong metal-dependent structural response, indicating that cobalt binding substantially alters the conformational ensemble of the aptamer. In the absence of added Zn^{2+}, the free Co-1 aptamer already displays several well-resolved imino proton resonances across approximately 9.7–14.1 ppm. This indicates that Co-1 is not fully unfolded in the free state but contains pre-formed

hydrogen-bonded secondary structure. The relatively sharp resonances near 13.6–13.8 ppm, 12.4–12.7 ppm, and 10.5–10.8 ppm suggest that both Watson–Crick and non-Watson–Crick or tertiary-like interactions are present before cobalt addition.

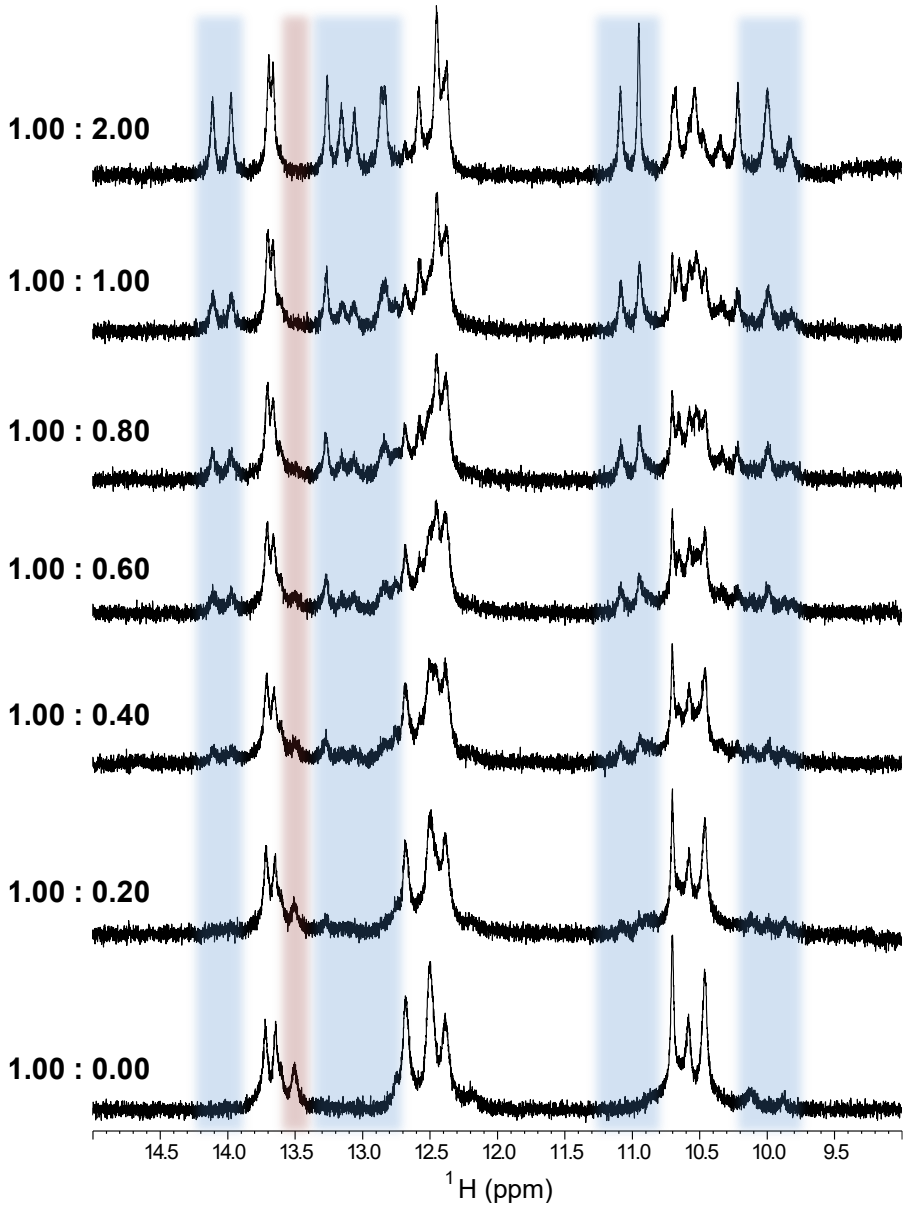

Figure 5.8.3. ^{1}H-NMR titration of the Co-1 aptamer with increasing equivalents of Zn^{2+}. Spectra were collected with 500 μM Zn-1 in 100 mM NaCl, 2 mM $MgCl_2$, and 10% $^{2}H_2O$ – 90% $^{1}H_2O$ at 5 °C, with aptamer:Zn^{2+} molar ratios indicated beside each spectrum. Peaks that appear with ligand addition are highlighted in blue. Peaks that disappear with ligand addition are highlighted in red.

Upon addition of Zn^{2+}, the spectrum changes progressively. Several of the original peaks decrease in intensity or broaden, while new or more pronounced resonances begin to appear. The changes are especially evident in the 12.3–12.8 ppm region and the 10.3–10.8 ppm region. This suggests that cobalt binding perturbs the free-state structure and shifts the aptamer toward a different conformational population rather than simply strengthening the original fold without rearrangement. At a 1:1 aptamer to ligand ratio, the spectrum becomes more resolved, with numerous sharper imino resonances emerging across both the Watson–Crick and non-Watson–Crick regions. This is particularly notable because cobalt addition does not simply eliminate the imino signals, which would suggest nonspecific disruption or extensive paramagnetic broadening. Instead, the high-equivalent spectrum contains many defined peaks, indicating that cobalt promotes or stabilizes a more ordered Co-1 conformation. The appearance of multiple resolved resonances between approximately 10.0 and 11.0 ppm is especially suggestive of cobalt-dependent stabilization of non-canonical interactions or tertiary contacts.

These findings highlight why NMR is particularly valuable for metal ion-binding aptamer characterization. Metal ions such as Zn^{2+} are difficult to monitor directly using conventional ligand-observed ^{1}H-NMR because they lack proton-rich structural features. However, the aptamer itself provides a sensitive structural readout through changes in the imino proton region. By monitoring the appearance of new peaks, peak sharpening, peak broadening, and changes in resonance distribution, NMR can reveal whether metal binding stabilizes a defined aptamer conformation, induces conformational exchange, or causes nonspecific structural perturbation. In the case of Zn-1 and Co-1, the data validates that metal binding is associated with specific structural organization of the selected aptamers, reinforcing the broader theme of this chapter that aptamer function is directly linked to ligand-dependent changes in nucleic acid structure and dynamics.

5.9 NMR Characterization of the Kanamycin-Binding Kan 6.1 Aptamer

Kanamycin is an aminoglycoside antibiotic that has been widely studied as a target for aptamer-based detection because of its clinical relevance, narrow safety margin, and importance in food and environmental monitoring. Aminoglycosides such as kanamycin and tobramycin are structurally related, highly functionalized, and polycationic molecules, which makes selective molecular recognition challenging. Their shared amino-sugar architecture and positive charge allow them to engage nucleic acids through electrostatic interactions and hydrogen bonding, but specific aptamer recognition requires discrimination between closely related ligand structures.[207–209] The Kanamycin 6.1 aptamer was selected to recognize kanamycin, and its reported specificity makes it a useful system for examining whether selective aminoglycoside binding is coupled to a major ligand-induced structural transition or instead occurs through a largely preorganized aptamer fold (Figure 5.9.1)[210,211]

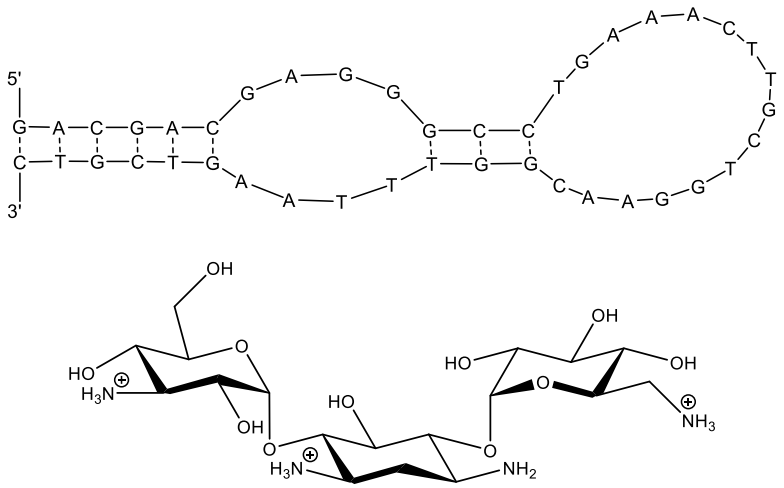

Figure 5.9.1. The predicted secondary structure of the Kan 6.1 aptamer. Solid lines are covalent bonds and dashed lines are hydrogen bonds. Below is the chemical structure of kanamycin A in its positively charged state which predominates at the pH used throughout this study.

This distinction is important because aptamer function does not always require a large-scale ligand-induced folding event. While some aptamers are weakly structured in the free state and become ordered only after ligand binding, others may exist as pre-folded or partially preorganized structures in the absence of target. In such cases, ligand recognition can occur through subtle stabilization of an existing binding pocket rather than through global restructuring. NMR is especially useful for identifying these cases

because a largely unchanged imino proton fingerprint across a titration indicates that the overall hydrogen-bonded architecture is maintained even when ligand binding occurs.

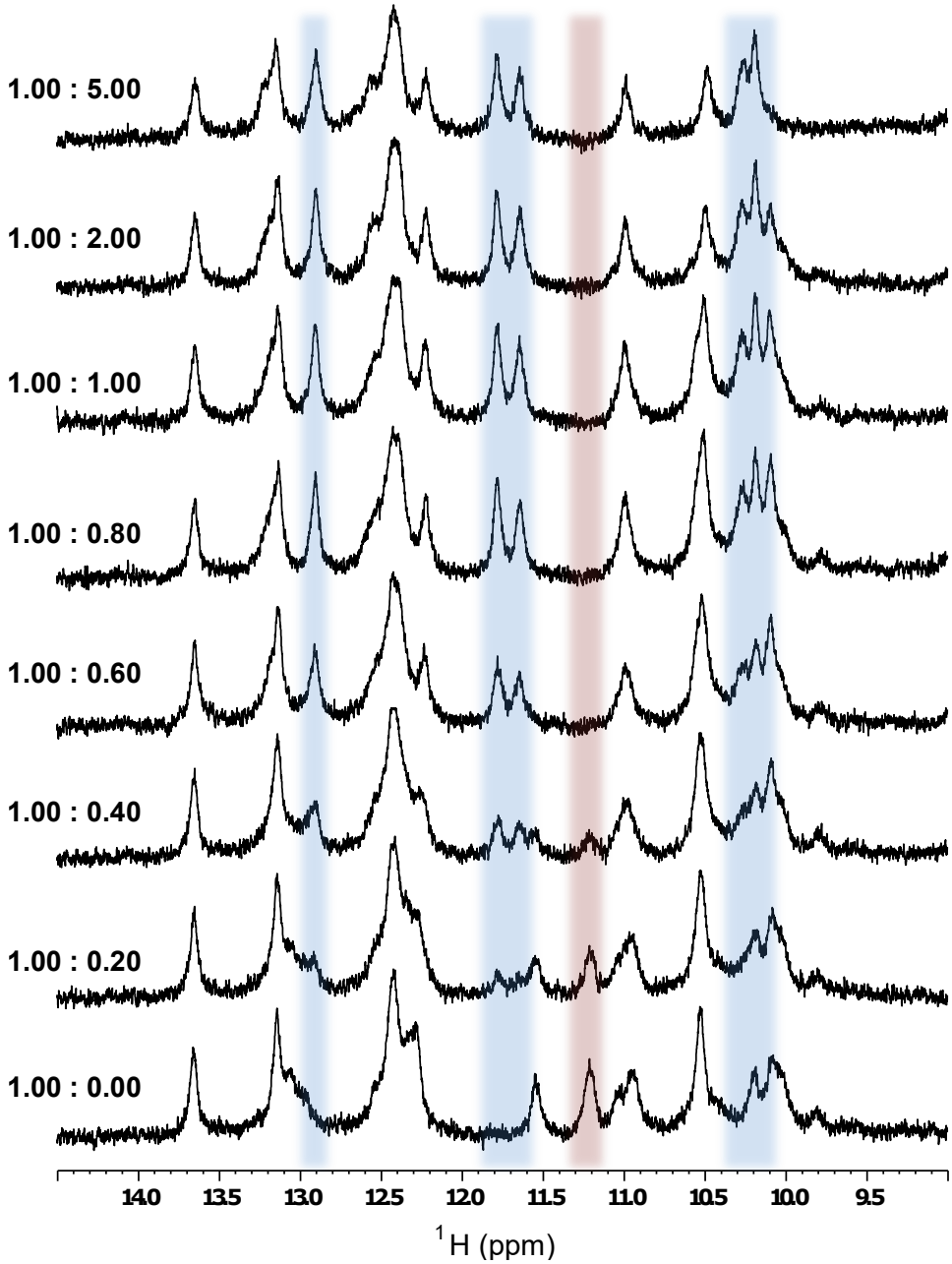

Figure 5.9.2. ^{1}H-NMR titration of the Kanamycin 6.1 aptamer with increasing equivalents of kanamycin. Stacked spectra show the imino proton region collected at the indicated aptamer:kanamycin molar ratios. Data was collected with an aptamer concentration of 500 μM prepared in 50 mM $NaHPO_4$, 300 mM NaCl, 10 mM $MgCl_2$, 5 mM KCl, pH 6.0, 10% ^2H_2O – 90% ^1H_2O at 5 °C. Peaks that appear with ligand addition are highlighted in blue. Peaks that disappear with ligand addition are highlighted in red.

The ^{1}H-NMR titration of Kanamycin 6.1 with kanamycin shows that the aptamer is already highly structured in the absence of ligand (Figure 5.9.2). The free aptamer spectrum displays numerous imino proton resonances across approximately 9.5–14.0 ppm, including several sharp peaks in the Watson–Crick region and additional resonances in the non-Watson–Crick region. This indicates that many imino protons are protected from solvent exchange before kanamycin addition, consistent with a pre-formed or highly populated folded state. Visual inspection of the free spectrum shows approximately 15–18 observable imino resonances, indicating that the aptamer contains substantial secondary and/or tertiary structure prior to ligand binding. Upon titration with kanamycin, the overall spectral profile remains broadly similar. Across the titration series, from the free aptamer to the 1.00:2.00 aptamer ratio, the same major resonance pattern is retained. There are modest changes in peak intensity, linewidth, and relative distribution, particularly in the clustered regions near approximately 12.0–13.5 ppm and 10.0–11.0 ppm. The two resonances between approximately 11.2 and 11.6 ppm in the free aptamer appear to be in slow exchange with two newly emerging resonances between approximately 11.5 and 11.8 ppm in the kanamycin-bound state. The simultaneous observation of both sets of peaks at intermediate kanamycin concentrations indicates that the free and bound aptamer populations coexist in solution prior to ligand saturation. This behavior is consistent with slow exchange on the NMR chemical-shift timescale, where separate resonances are observed for the free and ligand-bound conformations rather than a single peak that shifts gradually during the titration. Although the overall imino proton fingerprint remains largely conserved, these localized changes suggest that kanamycin binding produces specific structural perturbations within an otherwise pre-folded aptamer.

This example highlights an important utility of NMR in aptamer–small molecule characterization. NMR can identify not only systems where ligand binding produces obvious folding or stabilization, but also systems where binding is associated with minimal global structural change. This is critical because the absence of dramatic spectral rearrangement should not be interpreted as absence of binding. Rather, when the free aptamer is already highly structured, ligand binding may only produce subtle but functionally meaningful perturbations. In the case of Kanamycin 6.1, the retention of a similar imino proton fingerprint

across the kanamycin titration indicates that ligand binding is not coupled to extensive refolding, distinguishing this system from aptamers that undergo pronounced ligand-induced folding.

5.10 NMR Characterization of the Q1 Quinine-Binding Aptamer

Quinine is a biologically and pharmacologically important small molecule best known for its historical use as an antimalarial compound. It is also structurally relevant in aptamer research because it has been shown to bind the classical cocaine-binding DNA aptamer with unexpectedly high affinity. Although the cocaine-binding aptamer was originally selected for cocaine, subsequent work demonstrated that it binds quinine more tightly than cocaine, with reported quinine affinity approximately 30–40-fold stronger than cocaine binding.[114] This unusual cross-reactivity highlights an important challenge in small-molecule aptamer research: aptamers selected for one ligand may also recognize structurally distinct off-target molecules if the aptamer binding pocket can accommodate shared chemical features or alternative binding interactions.

The Q1 aptamer was selected to bind quinine selectively rather than cocaine, making it a useful system for evaluating how aptamer selection can generate molecular receptors with improved ligand discrimination (Figure 5.10.1). This is particularly relevant because quinine and cocaine have both been studied using the cocaine-binding aptamer scaffold, yet the desired functional outcome for Q1 is different from that scaffold. Rather than binding both molecules, Q1 is intended to distinguish quinine from cocaine. Therefore, characterization of Q1 provides an opportunity to examine how aptamer specificity can be assessed at the structural level and how ligand-dependent folding responses differ between cognate and non-cognate targets. The Q1 aptamer therefore provides a useful final example in this chapter for demonstrating how NMR can be used to evaluate both aptamer specificity and selectivity. By comparing the NMR response of Q1 upon addition of quinine and cocaine, it becomes possible to determine whether quinine selectively stabilizes or perturbs the Q1 structure in a manner that is not reproduced by cocaine. In this way, NMR provides information beyond simple binding detection: it can show whether ligand

recognition is structurally specific and whether the selected aptamer distinguishes between related or historically cross-reactive ligands through a defined conformational response.[212]

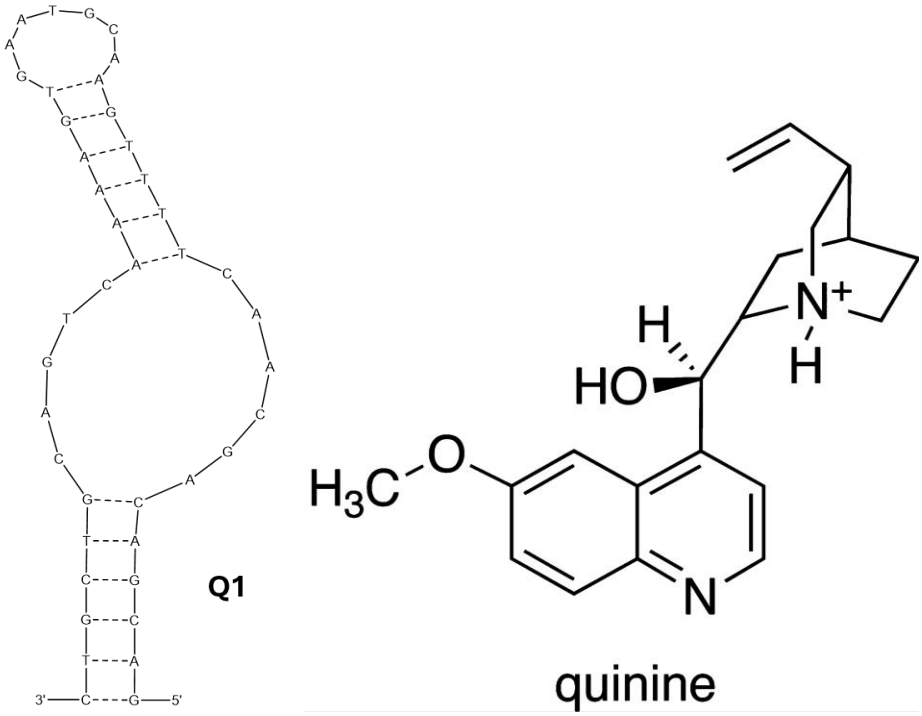

Figure 5.10.1. The predicted secondary structure of the Q1 aptamer. Dashed lines represent hydrogen bonds whereas solid lines represent covalent bonds. To the right is the chemical structure of quinine.

The ^{1}H-NMR titration of the Q1 aptamer with quinine shows clear ligand-dependent changes in the imino proton region, indicating that quinine binding is coupled to substantial structural organization of the aptamer. In the absence of ligand, the free Q1 aptamer already displays several sharp imino proton resonances across the 10.0–14.0 ppm region. Prominent peaks are observed near approximately 13.7, 13.4, 13.2, 12.5, 12.3, 10.6, and 10.1 ppm, demonstrating that Q1 contains pre-formed structural elements before ligand addition. These free-state resonances indicate that the aptamer is not fully unfolded in solution, but instead samples one or more partially folded conformations with protected imino protons.

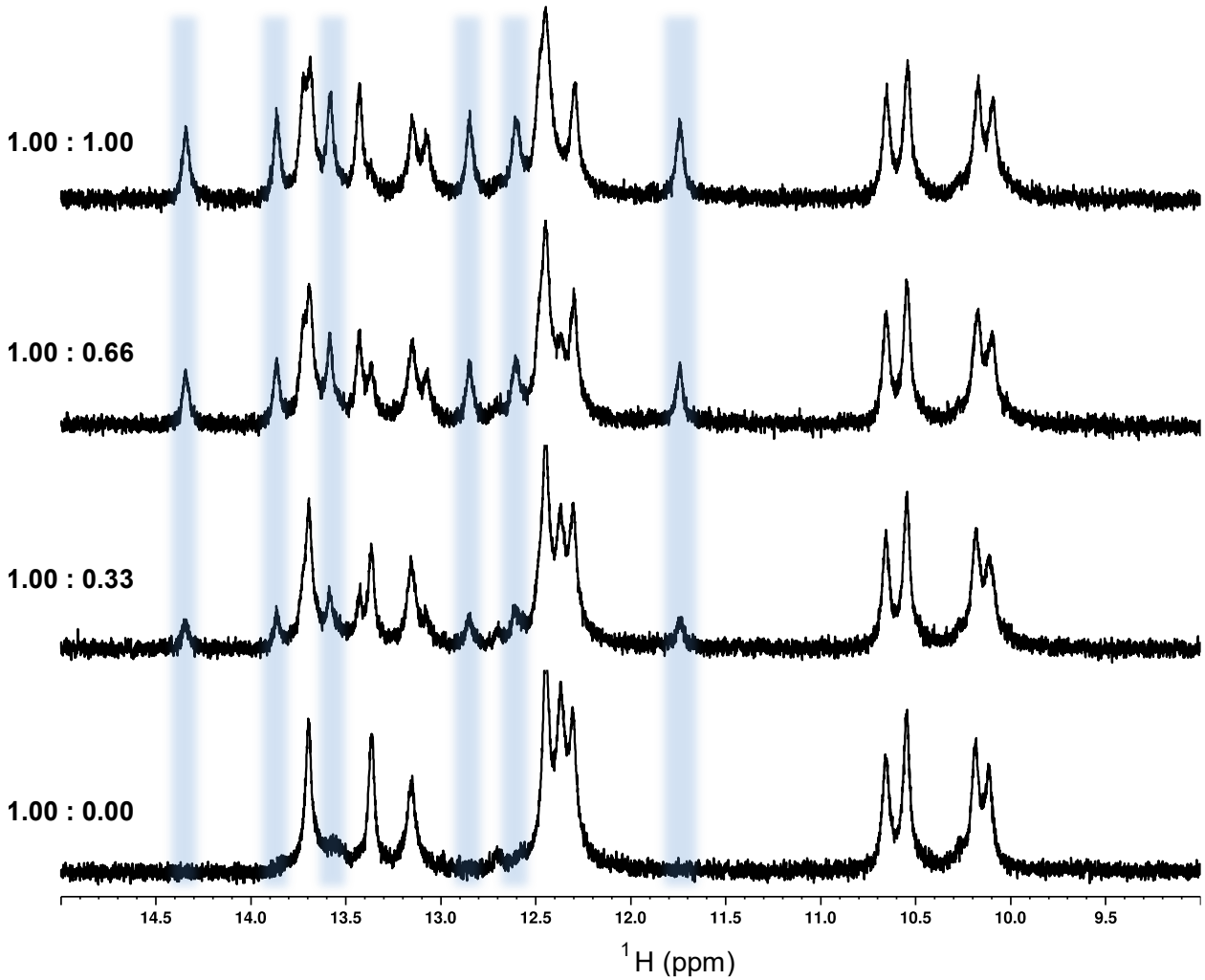

Figure 5.10.2. ^{1}H-NMR titration of the Q1 aptamer with increasing equivalents of quinine. Stacked spectra show the imino proton region collected at the indicated aptamer:quinine molar ratios. Data was collected with an aptamer concentration of 500 µM prepared in 140 mM NaCl, 10 mM sodium phosphate (pH 6.8) in 10 % ^{2}H2O - 90 % ^{1}H2O at 5 °C. Peaks that appear with ligand addition are highlighted in blue.

Upon titration with quinine, the imino proton spectrum changes substantially. At the 1.0:0.33 aptamer ratio, several new resonances begin to emerge, particularly in the downfield Watson–Crick region between approximately 13.0 and 14.0 ppm. Additional changes are also observed around 12.0–12.7 ppm and in the 10.0–10.8 ppm region. These spectral changes become more pronounced as the quinine concentration increases to 1.0:0.66 and 1.0:1.0, where the spectrum contains a greater number of resolved imino proton signals relative to the free aptamer. The emergence of numerous new peaks upon quinine addition indicates that ligand binding promotes the formation or stabilization of additional hydrogen-bonded interactions within the aptamer. This is consistent with a ligand-induced structure formation, where

quinine shifts the conformational ensemble of Q1 toward a more structured bound state. Importantly, the ligand-bound spectrum does not simply show broad disappearance of the free-state resonances. Instead, the number and definition of observable imino signals increase, supporting the formation of a more ordered aptamer–quinine complex rather than nonspecific ligand-induced disruption.

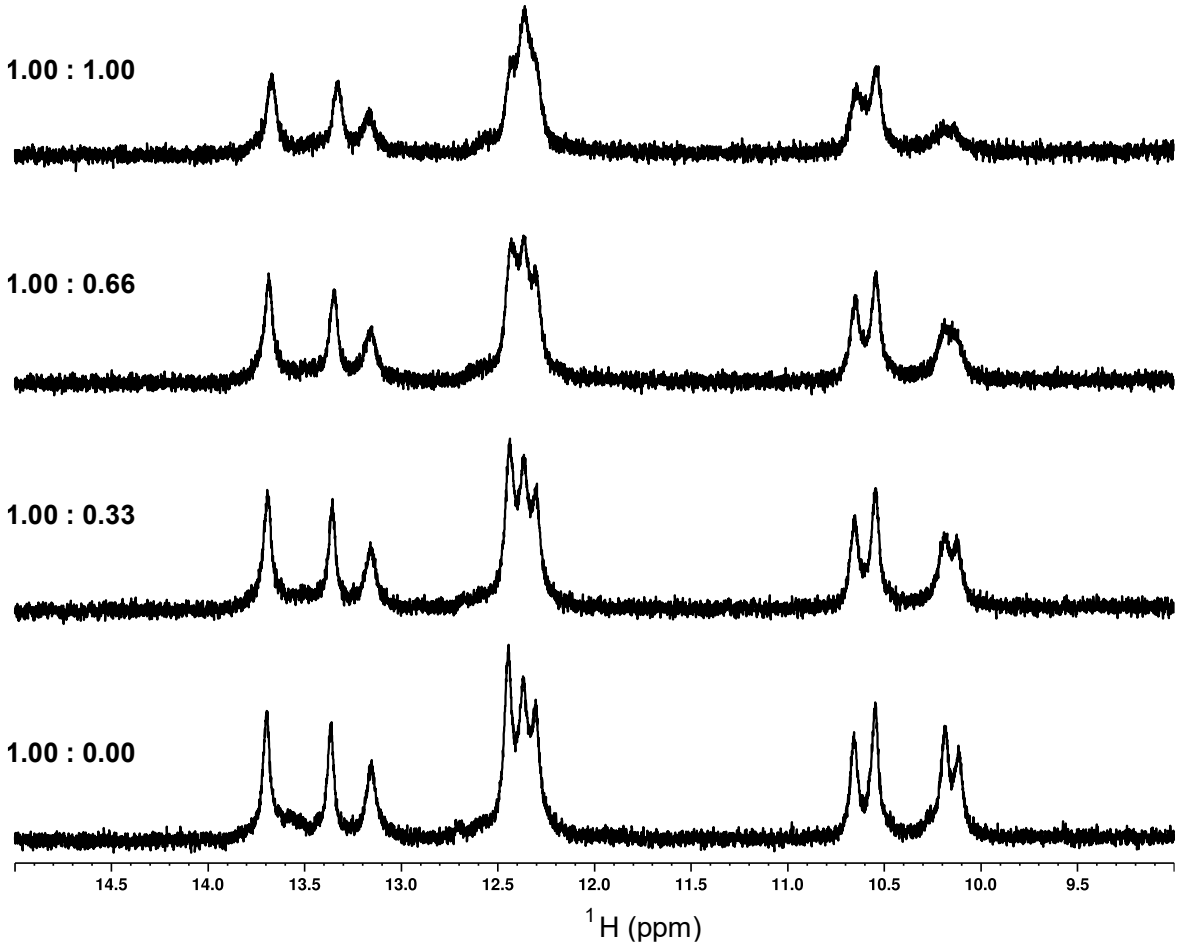

Figure 5.10.3. ^{1}H-NMR titration of the Q1 aptamer with increasing equivalents of cocaine. Stacked spectra show the imino proton region collected at the indicated aptamer:cocaine molar ratios. Data was collected with an aptamer concentration of 500 µM prepared in 140 mM NaCl, 10 mM sodium phosphate (pH 6.8) in 10 % ^{2}H2O - 90 % ^{1}H2O at 5 °C.

The ^{1}H-NMR titration of the Q1 aptamer with cocaine shows little evidence of ligand-induced structural change. Upon addition of cocaine, the overall spectral profile remains largely unchanged. At aptamer: cocaine ratios of 1.0:0.5, 1.0:1.0, and 1.0:3.0, the same major resonances remain visible with only minor changes in intensity and linewidth. The dominant peaks near approximately 13.6, 13.3, 13.1, 12.4, 10.6, and 10.1 ppm persist throughout the titration, and no substantial new imino proton resonances emerge.

Similarly, there is no widespread peak sharpening, disappearance, or chemical shift redistribution that would suggest formation of a new cocaine-bound structural state. At higher concentrations of cocaine, some line broadening that occurs may be due to weak, non-specific interactions taking place between the ligand and the aptamer.

Together, the Q1 titrations with quinine and cocaine demonstrate the utility of NMR spectroscopy for evaluating aptamer selectivity at the structural level. The free Q1 aptamer is already partially structured, as shown by the presence of multiple sharp imino proton resonances in the absence of ligand. However, the response of this pre-formed structural ensemble differs substantially depending on the ligand added. Quinine titration produces numerous new imino proton resonances and a more complex bound-state spectrum, indicating that quinine binding promotes additional hydrogen-bonded structure formation and stabilizes a more ordered aptamer conformation. In contrast, cocaine titration produces little to no change in the imino proton spectrum, indicating that cocaine does not substantially interact with or structurally stabilize Q1.

This finding is particularly meaningful given the known behavior of the traditional cocaine-binding aptamer, which can bind both cocaine and quinine. In contrast, Q1 appears to avoid this cross-reactivity, responding structurally to quinine but not to cocaine. The NMR data therefore support the conclusion that Q1 is a quinine-selective aptamer whose ligand recognition is coupled to formation of a distinct quinine-bound structural state.

More broadly, this highlights the value of NMR in small-molecule aptamer characterization. NMR can distinguish productive, structure-stabilizing ligand binding from non-cognate ligand exposure that produces little or no structural response. For Q1, the direct comparison between quinine and cocaine shows that NMR can validate aptamer specificity by monitoring whether each ligand induces a defined conformational change. This reinforces the central theme of this chapter: aptamer function is governed not only by whether a ligand can associate with the nucleic acid, but by whether that interaction stabilizes a specific structural ensemble required for molecular recognition.

5.11 Conclusions

Collectively, the systems examined in this chapter demonstrate the broad utility of NMR spectroscopy for characterizing aptamer–small molecule and aptamer–ion interactions. Across a diverse set of targets, including organic small molecules, metal ions, buffer molecules, antibiotics, and structurally related ligand pairs, ^{1}H-NMR spectroscopy provided direct insight into how ligand binding influences aptamer structure, conformational dynamics, and molecular recognition. In particular, analysis of the imino proton region enabled comparison of free and ligand-bound aptamer states by monitoring changes in peak number, intensity, linewidth, and chemical shift. These spectral features provided structural information that could not be obtained from binding affinity measurements alone. A major theme that emerged from these studies is that aptamer binding is not governed by a single universal mechanism. Some aptamers, such as the serotonin-binding aptamer, showed ligand-induced structural organization, where the free aptamer was largely dynamic or weakly structured and ligand addition promoted the appearance of new imino proton resonances. The potassium-dependent enhancement of these resonances further supported the formation of a G-quadruplex or G-quadruplex-like folded state. This demonstrated the value of NMR for identifying ligand-induced folding and for probing structural motifs, such as G-quadruplexes.

In contrast, other aptamers showed evidence of preorganization prior to ligand binding. The scandium-, zinc-, cobalt-, and kanamycin-binding aptamers all displayed imino proton resonances in the free state, indicating the presence of pre-formed hydrogen-bonded structure. In these systems, ligand addition did not necessarily create structure from a fully unfolded state, but instead refined, stabilized, or reorganized an existing conformational ensemble. The Zn-1 aptamer showed zinc-dependent sharpening and stabilization of existing imino resonances, while Co-1 displayed a more extensive cobalt-dependent structural reorganization. The Kanamycin 6.1 aptamer retained a largely similar spectral fingerprint upon kanamycin addition, indicating that ligand binding was not coupled to a major global rearrangement. These examples illustrate that NMR can distinguish between ligand-induced folding, conformational refinement, and binding to a largely pre-folded aptamer structure.

The metal-binding aptamer systems further highlight the importance of NMR for targets that are difficult to observe directly. Metal ions such as Sc^{3+} and Zn^{2+} lack the proton-rich features typically used in ligand-observed ^{1}H-NMR experiments, and their interactions with nucleic acids can be difficult to separate from nonspecific electrostatic association. By monitoring the structural response of the aptamer rather than the ion itself, NMR provided an indirect but highly informative readout of metal-dependent folding and stabilization. The observation of ligand-dependent imino proton changes showed that metal binding was coupled to specific structural responses within the aptamer, supporting the conclusion that these systems form more ordered metal-associated states rather than undergoing nonspecific structural disruption.

NMR was also valuable for identifying weak aptamer–ligand interactions. The Tris-binding aptamer provided an important example of a weak interaction that could still be characterized under the relatively high sample concentrations typically used for NMR experiments. Although the Tris aptamer displayed weak affinity, titration with Tris produced detectable changes in the imino proton region, including the emergence of new resonances across the 9–15 ppm range. This demonstrated that NMR can provide structural insight even for low-affinity systems that may be challenging to analyze using methods optimized for stronger binding interactions. In this context, NMR is particularly useful because weak binding can still shift the aptamer conformational ensemble sufficiently to generate observable spectral changes.

Another important application of NMR in this chapter was the distinction between specific and nonspecific ligand binding. The amodiaquine studies demonstrated that not all binding interactions result in formation of a defined aptamer–ligand complex. Across MN4 variants, duplex DNA controls, and generic junction constructs, amodiaquine titration caused progressive broadening and disappearance of imino proton signals rather than the emergence of new well-resolved peaks. This was consistent with DNA binding and exchange among multiple ligand-bound states. The interpretation was further supported by ITC data showing multi-site binding behavior. Similar spectral behavior was observed in the methylene blue studies, where a known DNA intercalator caused loss of imino resonances in polynucleotide constructs.

Together, these examples show that NMR can distinguish structure-stabilizing aptamer recognition from nonspecific DNA interactions that generate dynamic, poorly defined ensembles.

NMR also proved useful for validating aptamer specificity and selectivity. The bilirubin and biliverdin aptamer systems demonstrated that cognate ligands can produce clear structural responses while structurally related non-cognate ligands produce little or no change. Similarly, the Q1 aptamer showed a strong structural response to quinine, with numerous new imino resonances emerging upon titration, while cocaine produced little to no spectral change. These comparisons demonstrate that NMR can validate selectivity by directly monitoring whether each ligand induces or stabilizes a specific aptamer structure. This is particularly important for small-molecule aptamers, where structurally related ligands may produce ambiguous results in fluorescence, colorimetric, or affinity-based assays.

Overall, the studies presented in this chapter reinforce the central role of NMR spectroscopy in aptamer characterization. NMR does not simply indicate whether a ligand binds; it reveals how binding affects aptamer structure and dynamics. It can identify pre-formed structure, ligand-induced folding, conformational exchange, G-quadruplex formation, weak binding, nonspecific DNA association, and ligand-specific structural stabilization. Across the systems examined here, NMR provided a direct solution-state readout of the relationship between aptamer structure and function. These findings support the broader conclusion that aptamer performance is governed not only by ligand affinity, but by the ability of ligand binding to stabilize, reorganize, or selectively preserve specific nucleic acid conformations.

Chapter 6 Conclusions and Future Works

6.1 Conclusions

Aptamers are often described by the ligands they bind. A dopamine aptamer binds dopamine, a cocaine-binding aptamer binds cocaine, and a kanamycin aptamer binds kanamycin. However, the work presented in this thesis shows that this description is incomplete. An aptamer is not simply a sequence that binds a target. It is a dynamic nucleic acid system whose function depends on how it folds, how stable that fold is, how ligand binding reshapes the conformational landscape, and whether that structural response is specific enough to be useful.

This thesis examined that relationship between structure and function across several aptamer–small molecule and aptamer–ion systems. These systems did not all behave in the same way. In some cases, ligand binding induced folding. In others, the aptamer was already structured, and the ligand refined or stabilized a pre-existing conformation. Some ligands destabilized the aptamer, while others interacted broadly and non-specifically with DNA. Together, these examples demonstrate that binding affinity alone is not sufficient to explain aptamer function. The structural consequence of binding is equally important.

Chapter 2 focused on the dopamine-binding aptamer and established ligand-induced folding as a central mechanism of molecular recognition. In the absence of dopamine, the aptamer showed limited stable structure, whereas dopamine addition promoted formation of a more ordered conformation as observed by CD and NMR spectroscopy. Truncation of the terminal stem reduced dopamine affinity, indicating that regions outside of the immediate binding site contribute to formation and stabilization of the binding-competent fold. These results support a model in which dopamine recognition depends on the ability of the aptamer to adopt the correct three-dimensional structure, rather than on isolated ligand contacts alone.

Chapter 3 presented a contrasting view of aptamer–ligand interactions through studies of MN4 and a series of local anesthetics. While ligand binding is often assumed to stabilize aptamer structure, the MN4 system demonstrated that this is not always the case. Binding of local anesthetics produced ligand-dependent destabilization of the aptamer, with benzocaine and tetracaine representing the extremes of the

thermal effects observed by DSC and complementary methods. These findings showed that a ligand can bind an aptamer while weakening aspects of the folded structure. This chapter therefore expanded the interpretation of aptamer function by demonstrating that ligand binding and structural stabilization are not necessarily synonymous.

Chapter 4 examined methylene blue and leucomethylene blue, a redox pair directly relevant to electrochemical aptamer-based sensing. Methylene blue is widely used as a redox reporter in E-AB sensors and is known to interact with nucleic acids. In contrast, leucomethylene blue, the reduced form of methylene blue, had been less thoroughly characterized. Structural analysis revealed that leucomethylene blue adopts a bent "butterfly" conformation, unlike the more planar structure of methylene blue. Binding studies using ITC, NMR, UV–vis absorbance, and fluorescence showed that methylene blue binds generic single-stranded and duplex DNA, whereas leucomethylene blue shows little to no DNA binding.

This finding has important implications for biosensor design. It shows that ligand conformation can strongly influence nucleic acid recognition, even when the chemical difference between two states appears subtle. In the context of E-AB sensors, where signal generation depends on redox cycling and the positioning of the reporter relative to the electrode surface, the structural difference between methylene blue and leucomethylene blue may directly influence sensor behavior.

Chapter 5 focused on the broader utility of NMR spectroscopy for studying aptamer–small molecule and aptamer–ion interactions. Across a diverse set of systems, NMR provided a direct solution-state view of how ligand binding affects aptamer structure. The imino proton region was particularly informative because it reported on hydrogen-bonded base pairs, non-canonical interactions, and tertiary contacts. By monitoring changes in peak number, intensity, linewidth, and chemical shift, NMR revealed whether ligand binding induced new structure, stabilized existing structure, caused conformational exchange, or produced non-specific perturbation.

Several distinct binding mechanisms were observed. The serotonin- and quinine-binding aptamers showed evidence of ligand-induced structural organization, where ligand addition generated new imino proton resonances and stabilized more ordered bound-state conformations. The serotonin system also

provided evidence for potassium-dependent stabilization of a G-quadruplex or G-quadruplex-like structure, highlighting the ability of NMR to probe specific structural motifs involved in aptamer function.

Other systems were more preorganized. The scandium-, zinc-, cobalt-, and kanamycin-binding aptamers all displayed imino proton resonances in the free state, indicating that substantial structure existed prior to ligand addition. In these cases, ligand binding did not necessarily build structure from an unfolded state. Instead, it refined, stabilized, or reorganized existing conformational ensembles. The Zn-1 aptamer showed zinc-dependent sharpening and stabilization of resonances, while Co-1 underwent a more extensive cobalt-dependent conformational rearrangement. The Kanamycin 6.1 aptamer retained a largely similar imino proton fingerprint upon kanamycin addition, indicating that binding was not coupled to a major global structural change.

This distinction is important. Aptamers can function through induced folding, conformational selection, local structural refinement, or stabilization of a pre-formed binding pocket. NMR was able to distinguish among these possibilities.

The chapter also showed that NMR is valuable for weakly binding systems and difficult ligand classes. The Tris-binding aptamer, despite its weak affinity, produced detectable ligand-dependent changes in the imino proton spectrum. This was possible because NMR experiments are typically performed at relatively high concentrations, allowing weak interactions to become observable. Similarly, metal ions such as Sc^{3+} and Zn^{2+} are difficult to monitor directly by conventional ligand-observed ^{1}H-NMR because they lack proton-rich structures. By observing the aptamer instead of the ion, NMR provided an indirect but highly informative readout of metal-dependent folding and stabilization.

NMR was also essential for distinguishing specific from non-specific binding. The amodiaquine studies showed that ligand addition caused broad disappearance of imino proton resonances across MN4 variants, duplex DNA, and generic three-way junction controls. Rather than forming a well-resolved aptamer-bound spectrum, amodiaquine produced signal loss consistent with heterogeneous DNA binding and conformational exchange. This interpretation was further supported by ITC data showing multi-site

binding behavior. Similar loss of imino signals was observed in the methylene blue studies, consistent with its known ability to bind DNA broadly and non-specifically.

In contrast, specificity validation experiments demonstrated how NMR can confirm selective aptamer recognition. The bilirubin and biliverdin aptamers showed structural responses only with their corresponding cognate ligands. Likewise, the Q1 aptamer responded strongly to quinine but showed little to no structural response upon cocaine addition. These comparisons showed that NMR can validate aptamer selectivity at the structural level by asking a direct question: does the ligand stabilize or induce a specific aptamer conformation?

Taken together, the systems studied in this thesis show that aptamer–small molecule recognition is highly context-dependent. Some ligands induce folding. Some stabilize pre-existing structures. Some destabilize the aptamer. Some bind weakly but detectably. Others interact broadly with DNA without producing a defined complex. These outcomes cannot be understood from affinity measurements alone. For aptamer development, this has practical consequences. A high-affinity aptamer is not necessarily a useful sensor if ligand binding does not produce a reproducible structural or dynamic response. Conversely, an aptamer with a modest binding affinity may still be valuable if binding produces a clear conformational change that can be coupled to signal transduction. Understanding structure–function relationships is therefore essential for rational aptamer optimization, biosensor design, and the development of electrochemical aptamer-based sensing platforms.

Overall, this thesis demonstrates that aptamer function is governed by the interplay between sequence, structure, ligand chemistry, and conformational dynamics. The combined use of NMR, ITC, DSC, CD, UV–vis absorbance, fluorescence, and structural analysis provided complementary views of these interactions, but NMR was especially powerful because it directly monitored how aptamers respond structurally in solution. These findings support a central conclusion: aptamers should not be evaluated solely by whether they bind a ligand, but by what ligand binding causes them to become.

6.2 Future Work

The findings presented in this thesis highlight the importance of understanding aptamer function through the lens of structure, dynamics, and ligand-dependent conformational change. Although this work provides insight into several aptamer–small molecule and aptamer–ion systems, it also opens several future directions that could further clarify the mechanisms governing aptamer recognition and improve the rational design of aptamer-based sensors.

One important future direction is the high-resolution structural characterization of aptamers that undergo ligand-induced folding. In Chapter 2, the dopamine-binding aptamer was shown to adopt a more ordered structure upon dopamine binding, while Chapter 5 identified similar ligand-induced folding behavior in systems such as the serotonin- and quinine-binding aptamers. Future work could focus on determining high-resolution structures of these aptamers in their ligand-bound states using multidimensional NMR spectroscopy, X-ray crystallography, or cryo-EM where applicable. Structural models of the bound complexes would help identify the specific nucleotides involved in ligand recognition, the organization of the binding pocket, and the structural transitions required for folding. Comparing free, partially folded, and ligand-bound states would provide a more complete view of the folding pathway and clarify whether these aptamers bind through induced-fit, conformational selection, or a combination of both mechanisms.

The ligand-induced destabilization observed for MN4 in Chapter 3 also raises important questions for future investigation. Aptamer–ligand binding is often assumed to stabilize nucleic acid structure, yet the local anesthetic studies showed that ligands can instead destabilize the aptamer to different extents. Future work should aim to determine the structural basis of this destabilization. High-resolution NMR studies, molecular dynamics simulations, and additional thermal-melt experiments could be used to identify whether destabilizing ligands disrupt specific stems, alter junction geometry, weaken non-canonical interactions, or shift the aptamer toward alternative conformations. Comparing destabilizing ligands such as benzocaine with less destabilizing ligands such as tetracaine could clarify which ligand features control the

thermodynamic outcome of binding. This would be particularly valuable for understanding cases where ligand affinity and thermal stability are not directly correlated.

Another important future direction is to further examine the relationship between ligand binding thermodynamics and structural stability. In several systems, binding affinity alone did not fully explain the structural response observed by NMR or DSC. Future work could combine ITC, DSC, and NMR across larger ligand series to compare binding free energy, enthalpy, entropy, melt temperature shifts, and structural changes. This type of analysis would help determine whether particular thermodynamic signatures are associated with ligand-induced folding, stabilization of pre-existing structure, destabilization, or nonspecific binding. Such studies could also help clarify why some ligands bind favourably but produce limited structural stabilization, while others cause substantial changes in aptamer structure despite weaker affinity.

The methylene blue and leucomethylene blue studies in Chapter 4 also provide several future directions, particularly in the context of electrochemical aptamer-based sensors. The finding that methylene blue binds generic single-stranded and duplex DNA while leucomethylene blue shows little to no DNA binding suggests that the redox state and three-dimensional conformation of the reporter can strongly influence nucleic acid interactions. Future work could examine how repeated redox cycling between methylene blue and leucomethylene blue affects aptamer structure, reporter positioning, and sensor signal generation. This could include electrochemical studies using surface-bound aptamers, combined with solution-state NMR or fluorescence experiments to determine whether reporter–DNA interactions influence aptamer folding or ligand responsiveness. Understanding how the redox reporter interacts with the nucleic acid scaffold may improve the design of E-AB sensors with lower background signal and more predictable performance.

Finally, future work should aim to translate structural insights into improved aptamer and biosensor design. The results of this thesis show that an aptamer's usefulness depends not only on whether it binds a ligand, but on whether binding produces a reproducible structural or dynamic response. Future aptamer selection and optimization strategies should therefore incorporate structural screening methods, such as

NMR, CD, or thermal-melt analysis, alongside affinity-based assays. Aptamers that show clear ligand-induced folding, selective stabilization, or predictable conformational switching may be better candidates for sensor development than aptamers that bind without structural response or interact nonspecifically. Applying these principles could improve the rational design of aptamers for electrochemical sensing, diagnostics, environmental monitoring, and molecular recognition applications.

References

(1) Garst, A. D.; Edwards, A. L.; Batey, R. T. Riboswitches: Structures and Mechanisms. *Cold Spring Harb. Perspect. Biol.* 2011, 3 (6), a003533. https://doi.org/10.1101/cshperspect.a003533.

(2) Serganov, A.; Nudler, E. A Decade of Riboswitches. *Cell* 2013, 152 (1–2), 17–24. https://doi.org/10.1016/j.cell.2012.12.024.

(3) Ge, H.; Marchisio, M. A. Aptamers, Riboswitches, and Ribozymes in S. cerevisiae Synthetic Biology. *Life* 2021, 11 (3), 248. https://doi.org/10.3390/life11030248.

(4) Famulok, M.; Mayer, G. Aptamers as Tools in Molecular Biology and Immunology. In *Combinatorial Chemistry in Biology*; Famulok, M.; Mörl, M., Eds.; *Curr. Top. Microbiol. Immunol.*; Springer: Berlin, Heidelberg, 1999; Vol. 243, pp 123–136. https://doi.org/10.1007/978-3-642-60142-2_7.

(5) Tuerk, C.; Gold, L. Systematic Evolution of Ligands by Exponential Enrichment: RNA Ligands to Bacteriophage T4 DNA Polymerase. *Science* 1990, 249 (4968), 505–510. https://doi.org/10.1126/science.2200121.

(6) Ellington, A. D.; Szostak, J. W. In Vitro Selection of RNA Molecules That Bind Specific Ligands. *Nature* 1990, 346 (6287), 818–822. https://doi.org/10.1038/346818a0.

(7) Robertson, D. L.; Joyce, G. F. Selection In Vitro of an RNA Enzyme That Specifically Cleaves Single-Stranded DNA. *Nature* 1990, 344 (6265), 467–468. https://doi.org/10.1038/344467a0.

(8) Shaw, J.-P.; Kent, K.; Bird, J.; Fishback, J.; Froehler, B. Modified Deoxyoligonucleotides Stable to Exonuclease Degradation in Serum. *Nucleic Acids Res.* 1991, 19 (4), 747–750. https://doi.org/10.1093/nar/19.4.747.

(9) White, R. R.; Sullenger, B. A.; Rusconi, C. P. Developing Aptamers into Therapeutics. *J. Clin. Invest.* 2000, 106 (8), 929–934. https://doi.org/10.1172/JCI11325.

(10) Zhu, Q.; Liu, G.; Kai, M.; Miller, A. O. A. DNA Aptamers in the Diagnosis and Treatment of Human Diseases. *Molecules* 2015, 20 (12), 20979–20997. https://doi.org/10.3390/molecules201219739.

(11) Germer, K.; Leonard, M.; Zhang, X. RNA Aptamers and Their Therapeutic and Diagnostic Applications. *Int. J. Biochem. Mol. Biol.* 2013, 4 (1), 27–40.

(12) Orava, E. W.; Cicmil, N.; Gariépy, J. Delivering Cargoes into Cancer Cells Using DNA Aptamers Targeting Internalized Surface Portals. *Biochim. Biophys. Acta Biomembr.* 2010, 1798 (12), 2190–2200. https://doi.org/10.1016/j.bbamem.2010.02.004.

(13) Ilgu, M.; Nilsen-Hamilton, M. Aptamers in Analytics. *Analyst* 2016, 141 (5), 1551–1558. https://doi.org/10.1039/c5an01824b.

(14) Kulabhusan, P. K.; Hussain, B.; Yüce, M. Current Perspectives on Aptamers as Diagnostic Tools and Therapeutic Agents. *Pharmaceutics* 2020, 12 (7), 1–23. https://doi.org/10.3390/pharmaceutics12070646.

(15) Ni, X.; Castanares, M.; Mukherjee, A.; Lupold, S. E. Nucleic Acid Aptamers: Clinical Applications and Promising New Horizons. *Curr. Med. Chem.* 2011, 18 (27), 4206–4214. https://doi.org/10.2174/092986711797189600.

(16) Kohlberger, M.; Gadermaier, G. SELEX: Critical Factors and Optimization Strategies for Successful Aptamer Selection. *Biotechnol. Appl. Biochem.* 2022, 69 (5), 1771–1792. https://doi.org/10.1002/bab.2244.

(17) Mencin, N.; Šmuc, T.; Vraničar, M.; Mavri, J.; Hren, M.; Galeša, K.; Krkoč, P.; Ulrich, H.; Šolar, B. Optimization of SELEX: Comparison of Different Methods for Monitoring the Progress of In Vitro Selection of Aptamers. *J. Pharm. Biomed. Anal.* 2014, 91, 151–159. https://doi.org/10.1016/j.jpba.2013.12.031.

(18) Xu, Y.; Jiang, X.; Zhou, Y.; Ma, M.; Wang, M.; Ying, B. Systematic Evolution of Ligands by Exponential Enrichment Technologies and Aptamer-Based Applications: Recent Progress and Challenges in Precision Medicine of Infectious Diseases. *Front. Bioeng. Biotechnol.* 2021, 9, 704077. https://doi.org/10.3389/fbioe.2021.704077.

(19) McKeague, M.; Bradley, C. R.; de Girolamo, A.; Visconti, A.; David Miller, J.; de Rosa, M. C. Screening and Initial Binding Assessment of Fumonisin B 1 Aptamers. *Int. J. Mol. Sci.* 2010, 11 (12), 4864–4881. https://doi.org/10.3390/ijms11124864.

(20) Hünniger, T.; Wessels, H.; Fischer, C.; Paschke-Kratzin, A.; Fischer, M. Just In Time-Selection: A Rapid Semiautomated SELEX of DNA Aptamers Using Magnetic Separation and BEAMing. *Anal. Chem.* 2014, 86 (21), 10940–10947. https://doi.org/10.1021/ac503261b.

(21) Hong, S. L.; Xiang, M. Q.; Tang, M.; Pang, D. W.; Zhang, Z. L. Ebola Virus Aptamers: From Highly Efficient Selection to Application on Magnetism-Controlled Chips. *Anal. Chem.* 2019, 91 (5), 3367–3373. https://doi.org/10.1021/acs.analchem.8b04623.

(22) Aquino-Jarquin, G.; Toscano-Garibay, J. D. RNA Aptamer Evolution: Two Decades of Selection. *Int. J. Mol. Sci.* 2011, 12 (12), 9155–9171. https://doi.org/10.3390/ijms12129155.

(23) Kim, Y. S.; Hyun, C. J.; Kim, I. A.; Gu, M. B. Isolation and Characterization of Enantioselective DNA Aptamers for Ibuprofen. *Bioorg. Med. Chem.* 2010, 18 (10), 3467–3473. https://doi.org/10.1016/j.bmc.2010.03.074.

(24) Jenison, R. D.; Gill, S. C.; Pardi, A.; Polisky, B. High-Resolution Molecular Discrimination by RNA. *Science* 1994, 263 (5152), 1425–1429. https://doi.org/10.1126/science.7510417.

(25) Mendonsa, S. D.; Bowser, M. T. In Vitro Evolution of Functional DNA Using Capillary Electrophoresis. *J. Am. Chem. Soc.* 2004, 126 (1), 20–21. https://doi.org/10.1021/ja037832s.

(26) Mendonsa, S. D.; Bowser, M. T. In Vitro Selection of High-Affinity DNA Ligands for Human IgE Using Capillary Electrophoresis. *Anal. Chem.* 2004, 76 (18), 5387–5392. https://doi.org/10.1021/ac049857v.

(27) Berezovski, M. V.; Musheev, M. U.; Drabovich, A. P.; Jitkova, J. V.; Krylov, S. N. Non-SELEX: Selection of Aptamers Without Intermediate Amplification of Candidate Oligonucleotides. *Nat. Protoc.* 2006, 1 (3), 1359–1369. https://doi.org/10.1038/nprot.2006.200.

(28) Berezovski, M.; Krylov, S. N. Nonequilibrium Capillary Electrophoresis of Equilibrium Mixtures: A Single Experiment Reveals Equilibrium and Kinetic Parameters of Protein-DNA Interactions. *J. Am. Chem. Soc.* 2002, 124 (46), 13674–13675. https://doi.org/10.1021/ja028212e.

(29) Berezovski, M.; Krylov, S. N. Thermochemistry of Protein-DNA Interaction Studied with Temperature-Controlled Nonequilibrium Capillary Electrophoresis of Equilibrium Mixtures. *Anal. Chem.* 2005, 77 (5), 1526–1529. https://doi.org/10.1021/ac048577c.

(30) Daniels, D. A.; Chen, H.; Hicke, B. J.; Swiderek, K. M.; Gold, L. A Tenascin-C Aptamer Identified by Tumor Cell SELEX: Systematic Evolution of Ligands by Exponential Enrichment. *Proc. Natl. Acad. Sci. U.S.A.* 2003, 100 (26), 15416–15421. https://doi.org/10.1073/pnas.2136683100.

(31) Lyu, C.; Khan, I. M.; Wang, Z. Capture-SELEX for Aptamer Selection: A Short Review. *Talanta* 2021, 229, 122274. https://doi.org/10.1016/j.talanta.2021.122274.

(32) Kou, Q.; Wu, P.; Sun, Q.; Li, C.; Zhang, L.; Shi, H.; Wu, J.; Wang, Y.; Yan, X.; Le, T. Selection and Truncation of Aptamers for Ultrasensitive Detection of Sulfamethazine Using a Fluorescent Biosensor Based on Graphene Oxide. *Anal. Bioanal. Chem.* 2021, 413 (3), 901–909. https://doi.org/10.1007/s00216-020-03044-2.

(33) Özyurt, C.; Canbay, Z. Ç.; Dinçkaya, E.; Evran, S. A Highly Sensitive DNA Aptamer-Based Fluorescence Assay for Sarcosine Detection Down to Picomolar Levels. *Int. J. Biol. Macromol.* 2019, 129, 91–97. https://doi.org/10.1016/J.IJBIOMAC.2019.02.030.

(34) Kim, S. H.; Lee, J.; Lee, B. H.; Song, C. S.; Gu, M. B. Specific Detection of Avian Influenza H5N2 Whole Virus Particles on Lateral Flow Strips Using a Pair of Sandwich-Type Aptamers. *Biosens. Bioelectron.* 2019, 134, 123–129. https://doi.org/10.1016/J.BIOS.2019.03.061.

(35) Wang, H.; Zhang, Y.; Yang, H.; Qin, M.; Ding, X.; Liu, R.; Jiang, Y. In Vivo SELEX of an Inhibitory NSCLC-Specific RNA Aptamer from PEGylated RNA Library. *Mol. Ther. Nucleic Acids* 2018, 10, 187–198. https://doi.org/10.1016/j.omtn.2017.12.003.

(36) Huang, X.; Zhong, J.; Ren, J.; Wen, D.; Zhao, W.; Huan, Y. A DNA Aptamer Recognizing MMP14 for In Vivo and In Vitro Imaging Identified by Cell-SELEX. *Oncol. Lett.* 2019, 18 (1), 265–274. https://doi.org/10.3892/ol.2019.10282.

(37) Mayer, G. The Chemical Biology of Aptamers. *Angew. Chem., Int. Ed.* 2009, 48 (15), 2672–2689. https://doi.org/10.1002/anie.200804643.

(38) Eaton, B. E.; Gold, L.; Zichi, D. A. Let's Get Specific: The Relationship between Specificity and Affinity. *Chem. Biol.* 1995, 2 (10), 633–638. https://doi.org/10.1016/1074-5521(95)90023-3.

(39) Garvie, C. W.; Wolberger, C. Recognition of Specific DNA Sequences. *Mol. Cell* 2001, 8 (5), 937–946. https://doi.org/10.1016/S1097-2765(01)00392-6.

(40) Westhof, E.; Fritsch, V. RNA Folding: Beyond Watson–Crick Pairs. *Structure* 2000, 8 (3), R55–R65. https://doi.org/10.1016/S0969-2126(00)00112-X.

(41) Ruff, K. M.; Snyder, T. M.; Liu, D. R. Enhanced Functional Potential of Nucleic Acid Aptamer Libraries Patterned to Increase Secondary Structure. *J. Am. Chem. Soc.* 2010, 132 (27), 9453–9464. https://doi.org/10.1021/ja103023m.

(42) Roxo, C.; Kotkowiak, W.; Pasternak, A. G-Quadruplex-Forming Aptamers—Characteristics, Applications, and Perspectives. *Molecules* 2019, 24 (20), 3781. https://doi.org/10.3390/molecules24203781.

(43) Bochman, M. L.; Paeschke, K.; Zakian, V. A. DNA Secondary Structures: Stability and Function of G-Quadruplex Structures. *Nat. Rev. Genet.* 2012, 13 (11), 770–780. https://doi.org/10.1038/nrg3296.

(44) Murat, P.; Balasubramanian, S. Existence and Consequences of G-Quadruplex Structures in DNA. *Curr. Opin. Genet. Dev.* 2014, 25 (1), 22–29. https://doi.org/10.1016/j.gde.2013.10.012.

(45) Dolot, R.; Lam, C. H.; Sierant, M.; Zhao, Q.; Liu, F. W.; Nawrot, B.; Egli, M.; Yang, X. Crystal Structures of Thrombin in Complex with Chemically Modified Thrombin DNA Aptamers Reveal the Origins of Enhanced Affinity. *Nucleic Acids Res.* 2018, 46 (9), 4819–4830. https://doi.org/10.1093/nar/gky268.

(46) Nakatsuka, N.; Yang, K.-A.; Abendroth, J. M.; Cheung, K. M.; Xu, X.; Yang, H.; Zhao, C.; Zhu, B.; Rim, Y. S.; Yang, Y.; Weiss, P. S.; Stojanović, M. N.; Andrews, A. M. Aptamer-Field-Effect Transistors Overcome Debye Length Limitations for Small-Molecule Sensing. *Science* 2018, 362 (6412), 319–324. https://doi.org/10.1126/science.aao6750.

(47) Xu, G.; Zhao, J.; Yu, H.; Wang, C.; Huang, Y.; Zhao, Q.; Zhou, X.; Li, C.; Liu, M. Structural Insights Into the Mechanism of High-Affinity Binding of Ochratoxin A by a DNA Aptamer. *J. Am. Chem. Soc.* 2022, 144 (17), 7731–7740. https://doi.org/10.1021/jacs.2c00478.

(48) Esguerra, M.; Nilsson, L.; Villa, A. Triple Helical DNA in a Duplex Context and Base Pair Opening. *Nucleic Acids Res.* 2014, 42 (18), 11329–11338. https://doi.org/10.1093/nar/gku848.

(49) Bing, T.; Zheng, W.; Zhang, X.; Shen, L.; Liu, X.; Wang, F.; Cui, J.; Cao, Z.; Shangguan, D. Triplex-Quadruplex Structural Scaffold: A New Binding Structure of Aptamer. *Sci. Rep.* 2017, 7 (1), 15467. https://doi.org/10.1038/s41598-017-15797-5.

(50) Patel, M.; Dutta, A.; Huang, H. A Selective Adenosine Sensor Derived from A Triplex DNA Aptamer. *Anal. Bioanal. Chem.* 2011, 400 (9), 3035–3040. https://doi.org/10.1007/s00216-011-4996-1.

(51) Yoon, S.; Rossi, J. J. Future Strategies for the Discovery of Therapeutic Aptamers. *Expert Opin. Drug Discov.* 2017, 12 (4), 317–319. https://doi.org/10.1080/17460441.2017.1290077.

(52) Ng, E. W. M.; Shima, D. T.; Calias, P.; Cunningham, E. T.; Guyer, D. R.; Adamis, A. P. Pegaptanib, A Targeted Anti-VEGF Aptamer for Ocular Vascular Disease. *Nat. Rev. Drug Discov.* 2006, 5 (2), 123–132. https://doi.org/10.1038/nrd1955.

(53) Bunka, D. H. J.; Platonova, O.; Stockley, P. G. Development of Aptamer Therapeutics. *Curr. Opin. Pharmacol.* 2010, 10 (5), 557–562. https://doi.org/10.1016/j.coph.2010.06.009.

(54) Han, K. H.; Li, Y. C.; Parveen, R.; Venkataraman, S.; Lin, C. W. Technologies for Monoclonal Antibody Discovery and Development. *Int. J. Mol. Sci.* 2025, 26 (21), 10470. https://doi.org/10.3390/ijms262110470.

(55) Ansar, W.; Ghosh, S. Monoclonal Antibodies: A Tool in Clinical Research. *Indian J. Clin. Med.* 2013, 4, 9–21. https://doi.org/10.4137/ijcm.s11968.

(56) Köhler, G.; Milstein, C. Continuous Cultures of Fused Cells Secreting Antibody of Predefined Specificity. *Nature* 1975, 256 (5517), 495–497. https://doi.org/10.1038/256495a0.

(57) Emerson, J. F.; Lai, K. K. Y. Endogenous Antibody Interferences in Immunoassays. *Lab. Med.* 2013, 44 (1), 69–73. https://doi.org/10.1309/lmmurcfqhksb5yec.

(58) Pusuluri, A.; Krishnan, V.; Lensch, V.; Sarode, A.; Bunyan, E.; Vogus, D. R.; Menegatti, S.; Soh, H. T.; Mitragotri, S. Treating Tumors at Low Drug Doses Using an Aptamer–Peptide Synergistic Drug Conjugate. *Angew. Chem.* 2019, 131 (5), 1451–1455. https://doi.org/10.1002/ange.201812650.

(59) Zhu, H.; Zhang, L.; Liu, Y.; Zhou, Y.; Wang, K.; Xie, X.; Song, L.; Wang, D.; Han, C.; Chen, Q. Aptamer-PEG-Modified Fe3O4 @Mn as a Novel T1-and T2-Dual-Model MRI Contrast Agent Targeting Hypoxia-Induced Cancer Stem Cells. *Sci. Rep.* 2016, 6, 39245. https://doi.org/10.1038/srep39245.

(60) Mallikaratchy, P.; Stahelin, R. V.; Cao, Z.; Cho, W.; Tan, W. Selection of DNA Ligands for Protein Kinase C-δ. *Chem. Commun.* 2006, No. 30, 3229–3231. https://doi.org/10.1039/b604778e.

(61) Dauphin-Ducharme, P.; Yang, K.; Arroyo-Currás, N.; Ploense, K. L.; Zhang, Y.; Gerson, J.; Kurnik, M.; Kippin, T. E.; Stojanovic, M. N.; Plaxco, K. W. Electrochemical Aptamer-Based Sensors for Improved Therapeutic Drug Monitoring and High-Precision, Feedback-Controlled Drug Delivery. *ACS Sens.* 2019, 4 (10), 2832–2837. https://doi.org/10.1021/acssensors.9b01616.

(62) Grabowska, I.; Sharma, N.; Vasilescu, A.; Iancu, M.; Badea, G.; Boukherroub, R.; Ogale, S.; Szunerits, S. Electrochemical Aptamer-Based Biosensors for the Detection of Cardiac Biomarkers. *ACS Omega* 2018, 3 (9), 12010–12018. https://doi.org/10.1021/acsomega.8b01558.

(63) Radko, S.; Ptitsyn, K.; Novikova, S.; Kiseleva, Y.; Moysa, A.; Kurbatov, L.; Mannanova, M.; Zgoda, V.; Ponomarenko, E.; Lisitsa, A.; Archakov, A. Evaluation of Aptamers as Affinity Reagents for an Enhancement of SRM-Based Detection of Low-Abundance Proteins in Blood Plasma. *Biomedicines* 2020, 8 (5), 133. https://doi.org/10.3390/biomedicines8050133.

(64) Zhou, W.; Xu, F.; Li, D.; Chen, Y. Improved Detection of HER2 by A Quasi-Targeted Proteomics Approach Using Aptamer–Peptide Probe and Liquid Chromatography–Tandem Mass Spectrometry. *Clin. Chem.* 2018, 64 (3), 526–535. https://doi.org/10.1373/clinchem.2017.274266.

(65) Ahn, J. Y.; Lee, S. W.; Kang, H. S.; Jo, M.; Lee, D. K.; Laurell, T.; Kim, S. Aptamer Microarray Mediated Capture and Mass Spectrometry Identification of Biomarker in Serum Samples. *J. Proteome Res.* 2010, 9 (11), 5568–5573. https://doi.org/10.1021/pr100300t.

(66) Ge, K.; Peng, Y.; Lu, Z.; Hu, Y.; Li, G. Aptamer-Gold Nanoparticle Doped Covalent Organic Framework Followed by Matrix-Assisted Laser Desorption/Ionization Time-of-Flight Mass Spectrometry for Selective Enrichment and Detection of Human Insulin. *J. Chromatogr. A* 2020, 1615, 460741. https://doi.org/10.1016/j.chroma.2019.460741.

(67) Krylov, S. N.; Krylova, S. M.; Le, A. T. H.; Johnson, P. E.; Hili, R.; Wilson, D. J.; Kim, S. B.; Stovall, G. M.; Xu, G.; Dzantiev, B. B.; DeRosa, M.; Bueno, P. R.; Dauphin-Ducharme, P.; Tanner, J.

A.; Whitehouse, W. L.; Zhao, Q.; Zhu, J. J.; Crous, A.; Ferapontova, E. Widespread Omission of Aptamer-Target Binding Verification in Aptasensor Development: Consequences for Sensor Performance and the Need for a Kd Gate. *Biosens. Bioelectron.* 2026, 308, 118807. https://doi.org/10.1016/j.bios.2026.118807.

(68) Slavkovic, S.; Johnson, P. E. Isothermal Titration Calorimetry Studies of Aptamer-Small Molecule Interactions: Practicalities and Pitfalls. *Aptamers* 2018, 2, 45–51.

(69) Marion, D. An Introduction to Biological NMR Spectroscopy. *Mol. Cell. Proteomics* 2013, 12 (11), 3006–3025. https://doi.org/10.1074/mcp.O113.030239.

(70) Thompson, R. D.; Baisden, J. T.; Zhang, Q. NMR Characterization of RNA Small Molecule Interactions. *Methods* 2019, 167, 66–77. https://doi.org/10.1016/j.ymeth.2019.05.015.

(71) Hulse, S. G. *Estimation of NMR Signals in the Time Domain: Methodology, Applications and Software*; Ph.D. Thesis, University of Oxford, Oxford, United Kingdom, 2023. https://doi.org/10.5287/ora-bpdg8rr9k.

(72) Churcher, Z. R.; Johnson, P. E. NMR for Non-Experts: A Practical Guide for Applying NMR Methods in Studies of Aptamer-Ligand Interactions. *Aptamers* 2020, 4, 3–9.

(73) IUPAC-IUBMB-IUPAB Inter-Union Task Group on the Standardization of Data Bases of Protein and Nucleic Acid Structures Determined by NMR Spectroscopy. Recommendations for the Presentation of NMR Structures of Proteins and Nucleic Acids. Pure Appl. *Chem.* 1998, 70 (1), 117–142. https://doi.org/10.1351/pac199870010117.

(74) Bhattacharya, P. K.; Cha, J.; Barton, J. K. 1H NMR Determination of Base-Pair Lifetimes in Oligonucleotides Containing Single Base Mismatches. *Nucleic Acids Res.* 2002, 30 (21), 4740–4750. https://doi.org/10.1093/nar/gkf601.

(75) Gill, P.; Moghadam, T. T.; Ranjbar, B. Differential Scanning Calorimetry Techniques: Applications in Biology and Nanoscience. *J. Biomol. Tech.* 2010, 21 (4), 167–193.

(76) Bruylants, G.; Wouters, J.; Michaux, C. Differential Scanning Calorimetry in Life Science: Thermodynamics, Stability, Molecular Recognition and Application in Drug Design. *Curr. Med. Chem.* 2005, 12 (17), 2011–2020. https://doi.org/10.2174/0929867054546564.

(77) Kaiyum, Y. A.; Chao, E. H. P.; Dhar, L.; Shoara, A. A.; Nguyen, M.-D.; Mackereth, C. D.; Dauphin-Ducharme, P.; Johnson, P. E. Ligand-Induced Folding in a Dopamine-Binding DNA Aptamer. *ChemBioChem* 2024, 25 (23), e202400493. https://doi.org/10.1002/cbic.202400493.

(78) Yang, L. F.; Ling, M.; Kacherovsky, N.; Pun, S. H. Aptamers 101: Aptamer Discovery and In Vitro Applications in Biosensors and Separations. *Chem. Sci.* 2023, 14 (19), 4961–4978. https://doi.org/10.1039/d3sc00439b.

(79) Arroyo-Currás, N.; Somerson, J.; Vieira, P. A.; Ploense, K. L.; Kippin, T. E.; Plaxco, K. W. Real-Time Measurement of Small Molecules Directly in Awake, Ambulatory Animals. *Proc. Natl. Acad. Sci. U.S.A.* 2017, 114 (4), 645–650. https://doi.org/10.1073/pnas.1613458114.

(80) Neves, M. A. D.; Reinstein, O.; Johnson, P. E. Defining a Stem Length-Dependent Binding Mechanism for the Cocaine-Binding Aptamer. A Combined NMR and Calorimetry Study. *Biochemistry* 2010, 49 (39), 8478–8487. https://doi.org/10.1021/bi100952k.

(81) Wolfe, M.; Cramer, A.; Webb, S.; Goorskey, E.; Chushak, Y.; Mirau, P.; Arroyo-Currás, N.; Chávez, J. L. Rational Approach to Optimizing Conformation-Switching Aptamers for Biosensing Applications. *ACS Sens.* 2024, 9 (2), 717–725. https://doi.org/10.1021/acssensors.3c02004.

(82) Nakatsuka, N.; Abendroth, J. M.; Yang, K. A.; Andrews, A. M. Divalent Cation Dependence Enhances Dopamine Aptamer Biosensing. *ACS Appl. Mater. Interfaces* 2021, 13 (8), 9425–9435. https://doi.org/10.1021/acsami.0c17535.

(83) Liu, X.; Hou, Y.; Chen, S.; Liu, J. Controlling Dopamine Binding by the New Aptamer for a FRET-Based Biosensor. *Biosens. Bioelectron.* 2021, 173, 112798. https://doi.org/10.1016/j.bios.2020.112798.

(84) Douaki, A.; Stuber, A.; Hengsteler, J.; Momotenko, D.; Rogers, D. M.; Rocchia, W.; Hirst, J. D.; Nakatsuka, N.; Garoli, D. Theoretical Analysis of Divalent Cation Effects on Aptamer Recognition of Neurotransmitter Targets. *Chem. Commun.* 2023, 59 (99), 14713–14716. https://doi.org/10.1039/d3cc04334g.

(85) Liu, X.; He, F.; Zhang, F.; Zhang, Z.; Huang, Z.; Liu, J. Dopamine and Melamine Binding to Gold Nanoparticles Dominates Their Aptamer-Based Label-Free Colorimetric Sensing. *Anal. Chem.* 2020, 92 (13), 9370–9378. https://doi.org/10.1021/acs.analchem.0c01773.

(86) Hwang, T. L.; Shaka, A. J. Water Suppression That Works. Excitation Sculpting Using Arbitrary Wave-Forms and Pulsed-Field Gradients. *J. Magn. Reson. A* 1995, 112 (2), 275–279. https://doi.org/10.1006/JMRA.1995.1047.

(87) Turnbull, W. B.; Daranas, A. H. On the Value of c: Can Low Affinity Systems Be Studied by Isothermal Titration Calorimetry? *J. Am. Chem. Soc.* 2003, 125 (48), 14859–14866. https://doi.org/10.1021/ja036166s.

(88) Reinstein, O.; Neves, M. A. D.; Saad, M.; Boodram, S. N.; Lombardo, S.; Beckham, S. A.; Brouwer, J.; Audette, G. F.; Groves, P.; Wilce, M. C. J.; Johnson, P. E. Engineering a Structure Switching Mechanism into a Steroid-Binding Aptamer and Hydrodynamic Analysis of the Ligand Binding Mechanism. *Biochemistry* 2011, 50 (43), 9368–9376. https://doi.org/10.1021/bi201361v.

(89) Zhang, Z.; Oni, O.; Liu, J. New Insights into a Classic Aptamer: Binding Sites, Cooperativity and More Sensitive Adenosine Detection. *Nucleic Acids Res.* 2017, 45 (13), 7593–7601. https://doi.org/10.1093/nar/gkx517.

(90) Neves, M. A. D.; Shoara, A. A.; Reinstein, O.; Abbasi Borhani, O.; Martin, T. R.; Johnson, P. E. Optimizing Stem Length to Improve Ligand Selectivity in a Structure-Switching Cocaine-Binding Aptamer. *ACS Sens.* 2017, 2 (10), 1539–1545. https://doi.org/10.1021/acssensors.7b00619.

(91) Slavkovic, S.; Eisen, S. R.; Johnson, P. E. Designed Alteration of Binding Affinity in Structure-Switching Aptamers through the Use of Dangling Nucleotides. *Biochemistry* 2020, 59 (5), 663–670. https://doi.org/10.1021/acs.biochem.9b00630.

(92) Swensen, J. S.; Xiao, Y.; Ferguson, B. S.; Lubin, A. A.; Lai, R. Y.; Heeger, A. J.; Plaxco, K. W.; Soh, H. T. Continuous, Real-Time Monitoring of Cocaine in Undiluted Blood Serum via a Microfluidic, Electrochemical Aptamer-Based Sensor. *J. Am. Chem. Soc.* 2009, 131 (12), 4262–4266. https://doi.org/10.1021/ja806531z.

(93) Rahbarimehr, E.; Chao, H. P.; Churcher, Z. R.; Slavkovic, S.; Kaiyum, Y. A.; Johnson, P. E.; Dauphin-Ducharme, P. Finding the Lost Dissociation Constant of Electrochemical Aptamer-Based Biosensors. *Anal. Chem.* 2023, 95 (4), 2229–2237. https://doi.org/10.1021/acs.analchem.2c03566.

(94) Nguyen, M. D.; Osborne, M. T.; Prevot, G. T.; Churcher, Z. R.; Johnson, P. E.; Simine, L.; Dauphin-Ducharme, P. Truncations and in Silico Docking to Enhance the Analytical Response of Aptamer-Based Biosensors. *Biosens. Bioelectron.* 2024, 265, 116680. https://doi.org/10.1016/j.bios.2024.116680.

(95) Downs, A. M.; Gerson, J.; Ploense, K. L.; Plaxco, K. W.; Dauphin-Ducharme, P. Subsecond-Resolved Molecular Measurements Using Electrochemical Phase Interrogation of Aptamer-Based Sensors. *Anal. Chem.* 2020, 92 (20), 14063–14068. https://doi.org/10.1021/acs.analchem.0c03109.

(96) Xiao, Y.; Uzawa, T.; White, R. J.; DeMartini, D.; Plaxco, K. W. On the Signaling of Electrochemical Aptamer-Based Sensors: Collision- and Folding-Based Mechanisms. *Electroanalysis* 2009, 21 (11), 1267–1271. https://doi.org/10.1002/elan.200804564.

(97) Chao, E. H. P.; Largy, E.; Kaiyum, Y. A.; Nguyen, M.-D.; Vialet, B.; Dauphin-Ducharme, P.; Johnson, P. E.; Mackereth, C. D. Unconventional DNA Architecture in a Dopamine–Bound Aptamer Complex. *bioRxiv* 2025. https://doi.org/10.1101/2025.11.27.690961.

(98) Dunn, M. R.; Jimenez, R. M.; Chaput, J. C. *Analysis of Aptamer Discovery. Nat. Rev. Chem.* 2017, 1, 0076. https://doi.org/10.1038/s41570-017-0076.

(99) Ding, Y.; Liu, J. Pushing Adenosine and ATP SELEX for DNA Aptamers with Nanomolar Affinity. *J. Am. Chem. Soc.* 2023, 145 (13), 7540–7547. https://doi.org/10.1021/jacs.3c00848.

(100) Lauhon, C. T.; Szostak, J. W. RNA Aptamers That Bind Flavin and Nicotinamide Redox Cofactors. *J. Am. Chem. Soc.* 1995, 117 (4), 1246–1257. https://doi.org/10.1021/ja00109a008.

(101) Mannironi, C.; Scerch, C.; Fruscoloni, P.; Tocchini-Valentini, G. P. Molecular Recognition of Amino Acids by RNA Aptamers: The Evolution into an L-Tyrosine Binder of a Dopamine-Binding RNA Motif. *RNA* 2000, 6 (4), 520–527. https://doi.org/10.1017/S1355838200992321.

(102) Cobbert, J. D.; DeMott, C.; Majumder, S.; Smith, E. A.; Reverdatto, S.; Burz, D. S.; McDonough, K. A.; Shekhtman, A. Caught in Action: Selecting Peptide Aptamers against Intrinsically Disordered Proteins in Live Cells. *Sci. Rep.* 2015, 5, 9402. https://doi.org/10.1038/srep09402.

(103) Thi Tran, T. D.; Nguyen, H. L.; Ngoc Hoa, P. T.; Pham, T. T.; Thanh Huyen, N. T.; Huong, G. D.; Hoang, H. T.; Wagner, P.; Charrier, A.; Lien, T. T. N.; Nguyen, P. H.; Toan, N. T. Accelerated Aptamer Selection via SELEX and Molecular Simulations for Lipopolysaccharide Detection. *RSC Adv.* 2025, 15 (55), 46790–46806. https://doi.org/10.1039/d5ra06759f.

(104) Guérin, M.; Vandevenne, M.; Matagne, A.; Aucher, W.; Verdon, J.; Paoli, E.; Ducrotoy, J.; Octave, S.; Avalle, B.; Maffucci, I.; Padiolleau-Lefèvre, S. Selection and Characterization of DNA Aptamers Targeting the Surface Borrelia Protein CspZ with High-Throughput Cross-over SELEX. *Commun. Biol.* 2025, 8 (1). https://doi.org/10.1038/s42003-025-08034-7.

(105) Alkhamis, O.; Byrd, C.; Canoura, J.; Bacon, A.; Hill, R.; Xiao, Y. Exploring the Relationship between Aptamer Binding Thermodynamics, Affinity, and Specificity. *Nucleic Acids Res.* 2025, 53 (6), gkaf219. https://doi.org/10.1093/nar/gkaf219.

(106) Sokoloski, J. E.; Dombrowski, S. E.; Bevilacqua, P. C. Thermodynamics of Ligand Binding to a Heterogeneous RNA Population in the Malachite Green Aptamer. *Biochemistry* 2012, 51 (1), 565–572. https://doi.org/10.1021/bi201642p.

(107) Sakamoto, T.; Ennifar, E.; Nakamura, Y. Thermodynamic Study of Aptamers Binding to Their Target Proteins. *Biochimie* 2018, 145, 91–97. https://doi.org/10.1016/J.BIOCHI.2017.10.010.

(108) Neves, M. A. D.; Reinstein, O.; Saad, M.; Johnson, P. E. Defining the Secondary Structural Requirements of a Cocaine-Binding Aptamer by a Thermodynamic and Mutation Study. *Biophys. Chem.* 2010, 153 (1), 9–16. https://doi.org/10.1016/J.BPC.2010.09.009.

(109) Reinstein, O.; Yoo, M.; Han, C.; Palmo, T.; Beckham, S. A.; Wilce, M. C. J.; Johnson, P. E. Quinine Binding by the Cocaine-Binding Aptamer. Thermodynamic and Hydrodynamic Analysis of High-Affinity Binding of an off-Target Ligand. *Biochemistry* 2013, 52 (48), 8652–8662. https://doi.org/10.1021/bi4010039.

(110) Slavkovic, S.; Altunisik, M.; Reinstein, O.; Johnson, P. E. Structure–Affinity Relationship of the Cocaine-Binding Aptamer with Quinine Derivatives. *Bioorg. Med. Chem.* 2015, 23 (10), 2593–2597. https://doi.org/10.1016/J.BMC.2015.02.052.

(111) Xia, T.; Yuan, J.; Fang, X. Conformational Dynamics of an ATP-Binding DNA Aptamer: A Single-Molecule Study. *J. Phys. Chem. B* 2013, 117 (48), 14994–15003. https://doi.org/10.1021/jp4099667.

(112) Bishop, G. R.; Ren, J.; Polander, B. C.; Jeanfreau, B. D.; Trent, J. O.; Chaires, J. B. Energetic Basis of Molecular Recognition in a DNA Aptamer. *Biophys. Chem.* 2007, 126 (1–3), 165–175. https://doi.org/10.1016/J.BPC.2006.07.009.

(113) Churcher, Z. R.; Garaev, D.; Hunter, H. N.; Johnson, P. E. Reduction in Dynamics of Base Pair Opening upon Ligand Binding by the Cocaine-Binding Aptamer. *Biophys. J.* 2020, 119 (6), 1147–1156. https://doi.org/10.1016/j.bpj.2020.08.012.

(114) Shoara, A. A.; Slavkovic, S.; Donaldson, L. W.; Johnson, P. E. Analysis of the Interaction between the Cocaine-Binding Aptamer and Its Ligands Using Fluorescence Spectroscopy. *Can. J. Chem.* 2017, 95 (12), 1253–1260. https://doi.org/10.1139/cjc-2017-0380.

(115) Nguyen, M. D.; Tavakoli, S.; Mittelstedt, S.; Johnson, P. E.; Dauphin-Ducharme, P. Solution-Based Biophysical Methods for Guiding Design of Aptamers into Electrochemical Biosensors. *Analysis Sens.* 2025. https://doi.org/10.1002/anse.202500077.

(116) Batchelor, R. H.; Kaiyum, Y. A.; Chao, E. H. P.; Tenorio, N.; Ofori, C.; Bird, S. A.; Brand, H. E. A.; Auckett, J. E.; Karouei, M. H.; Richardson, K.; Vlcek, V.; Johnson, P. E.; Gooding, J. J.; Bonham, A. J. The Butterfly Structure of Leucomethylene Blue Results in Weak Binding to Single- or Double-Stranded DNA. *J. Phys. Chem. B* 2025, 129 (47), 12110–12119. https://doi.org/10.1021/acs.jpcb.5c05704.

(117) Cwalinski, T.; Polom, W.; Marano, L.; Roviello, G.; D'Angelo, A.; Cwalina, N.; Matuszewski, M.; Roviello, F.; Jaskiewicz, J.; Polom, K. Methylene Blue—Current Knowledge, Fluorescent Properties, and Its Future Use. *J. Clin. Med.* 2020, 9 (11), 3538. https://doi.org/10.3390/jcm9113538.

(118) Papich, M. G. *Saunders Handbook of Veterinary Drugs: Small and Large Animal*, 4th ed.; Elsevier: St. Louis, MO, 2016.

(119) Nedu, M. E.; Tertis, M.; Cristea, C.; Georgescu, A. V. Comparative Study Regarding the Properties of Methylene Blue and Proflavine and Their Optimal Concentrations for In Vitro and In Vivo Applications. *Diagnostics* 2020, 10 (4), 223. https://doi.org/10.3390/diagnostics10040223.

(120) Caro, H. Ueber Methylenblau. *Ber. Dtsch. Chem. Ges.* 1876, 9 (1), 969–970. https://doi.org/10.1002/cber.187600901248.

(121) Bernthsen, A. Zur Kenntniss Des Methylenblau Und Verwandter Farbstoffe. *Ber. Dtsch. Chem. Ges.* 1883, 16 (2), 2896–2904. https://doi.org/10.1002/cber.188301602249.

(122) Dauphin-Ducharme, P.; Churcher, Z. R.; Shoara, A. A.; Rahbarimehr, E.; Slavkovic, S.; Fontaine, N.; Boisvert, O.; Johnson, P. E. Redox Reporter - Ligand Competition to Support Signaling in the Cocaine-Binding Electrochemical Aptamer-Based Biosensor. *Chem. Eur. J.* 2023, 29 (35). https://doi.org/10.1002/chem.202300618.

(123) Mahlum, J. D.; Pellitero, M. A.; Arroyo-Currás, N. Chemical Equilibrium-Based Mechanism for the Electrochemical Reduction of DNA-Bound Methylene Blue Explains Double Redox Waves in Voltammetry. *J. Phys. Chem. C* 2021, 125 (17), 9038–9049. https://doi.org/10.1021/acs.jpcc.1c00336.

(124) Wang, Y.; Jie, H.; Ye, H.; Zhang, Y.; Li, N.; Zhuang, J. Methylene Blue-Stained Single-Stranded DNA Aptamers as a Highly Efficient Electronic Switch for Quasi-Reagentless Exosomes Detection: An Old Dog with New Tricks. *Anal. Chem.* 2023, 95 (49), 18166–18173. https://doi.org/10.1021/acs.analchem.3c03715.

(125) Batchelor, R. H.; Dief, E. M.; Bonham, A. J.; Gooding, J. J. A Review of Methylene Blue's Interactions with DNA and Their Relevance for DNA-Based Sensors. *ACS Sens.* 2025, 10 (6), 3854–3877. https://doi.org/10.1021/acssensors.5c00336.

(126) Bellin, J. S.; Oster, G. Photodynamic Inactivation of Transforming Principle. *Biochim. Biophys. Acta* 1960, 42 (C), 533–535. https://doi.org/10.1016/0006-3002(60)90835-0.

(127) Comings, D. E.; Avelino, E. Mechanisms of Chromosome Banding VII. Interaction of Methylene Blue with DNA and Chromatin. *Chromosoma* 1975, 51 (4), 365–379. https://doi.org/10.1007/BF00326323.

(128) Hu, Z.; Tong, C. Synchronous Fluorescence Determination of DNA Based on the Interaction between Methylene Blue and DNA. *Anal. Chim. Acta* 2007, 587 (2), 187–193. https://doi.org/10.1016/J.ACA.2007.01.050.

(129) Baranovskii, S. F.; Bolotin, P. A.; Evstigneev, M. P. Aggregation of 1,3,7-Trimethylxanthine with Methylene Blue in Aqueous Solution. *J. Appl. Spectrosc.* 2006, 73 (2), 171–177. https://doi.org/10.1007/s10812-006-0054-8.

(130) Tong, C.; Hu, Z.; Wu, J. Interaction between Methylene Blue and Calfthymus Deoxyribonucleic Acid by Spectroscopic Technologies. *J. Fluoresc.* 2010, 20 (1), 261–267. https://doi.org/10.1007/s10895-009-0549-9.

(131) Vardevanyan, P. O.; Antonyan, A. P.; Parsadanyan, M. A.; Shahinyan, M. A.; Hambardzumyan, L. A. Mechanisms for Binding between Methylene Blue and DNA. *J. Appl. Spectrosc.* 2013, 80 (4), 595–599. https://doi.org/10.1007/s10812-013-9811-7.

(132) Rohs, R.; Sklenar, H. Methylene Blue Binding to DNA with Alternating AT Base Sequence: Minor Groove Binding Is Favoured over Intercalation. *J. Biomol. Struct. Dyn.* 2004, 21 (5), 699–711. https://doi.org/10.1080/07391102.2004.10506960.

(133) Rohs, R.; Bloch, I.; Sklenar, H.; Shakked, Z. Molecular Flexibility in Ab Initio Drug Docking to DNA: Binding-Site and Binding-Mode Transitions in All-Atom Monte Carlo Simulations. *Nucleic Acids Res.* 2005, 33 (22), 7048–7057. https://doi.org/10.1093/nar/gki1008.

(134) Jähnchen, J.; Purwanto, M. G. M.; Weisz, K. NMR Studies on Self-Complementary Oligonucleotides Conjugated with Methylene Blue. *Biopolymers* 2005, 79 (6), 335–343. https://doi.org/10.1002/bip.20363.

(135) Purwanto, M. G. M.; Weisz, K. NMR Studies on Oligonucleotide – Methylene Blue Conjugates Targeting Double-Helical Nucleic Acids. *Biophys. Chem.* 2020, 257, 106314. https://doi.org/10.1016/J.BPC.2019.106314.

(136) Vardevanyan, P. O.; Antonyan, A. P.; Parsadanyan, M. A.; Shahinyan, M. A.; Petrosyan, N. H. Study of Interaction of Methylene Blue with DNA and Albumin. *J. Biomol. Struct. Dyn.* 2022, 40 (17), 7779–7785. https://doi.org/10.1080/07391102.2021.1902397.

(137) Rohs, R.; Sklenar, H.; Lavery, R.; Röder, B. Methylene Blue Binding to DNA with Alternating GC Base Sequence: A Modeling Study. *J. Am. Chem. Soc.* 2000, 122 (12), 2860–2866. https://doi.org/10.1021/ja992966k.

(138) Fujimoto, B. S.; Clendenning, J. B.; Delrow, J. J.; Heath, P. J.; Schurr, M. Fluorescence and Photobleaching Studies of Methylene Blue Binding to DNA. *J. Phys. Chem.* 1994, 98 (26), 6633–6643. https://doi.org/10.1021/j100077a033.

(139) Pal, M. K.; Ghosh, A. K. Stoichiometry of Metachromatic Dye Binding by Deoxyribonucleic Acid. *Histochemie* 1973, 36 (1), 29–33. https://doi.org/10.1007/BF00310118.

(140) Kelly, J. M.; van der Putten, W. J. M.; McConnell, D. J. Laser Flash Spectroscopy of Methylene Blue with Nucleic Acids. *Photochem. Photobiol.* 1987, 45 (2), 167–175. https://doi.org/10.1111/j.1751-1097.1987.tb05360.x.

(141) Tomita, G. Absorption and Fluorescence Properties of Some Basic Dyes Complexing with Nucleosides or Nucleic Acids. *Z. Naturforsch. B* 1968, 23 (7), 922–925. https://doi.org/10.1515/znb-1968-0707.

(142) Erdem, A.; Kerman, K.; Meric, B.; Ozsoz, M. Methylene Blue as a Novel Electrochemical Hybridization Indicator. *Electroanalysis* 2001, 13 (3), 219–223. https://doi.org/10.1002/1521-4109(200103)13:3<219::AID-ELAN219>3.0.CO;2-7.

(143) Ehrlich, P. Zur Biologischen Verwertung Des Methylenblau. *Centralbl. Med. Wiss.* 1885, 23, 113–117.

(144) Brdička, R. Measurements of Quantities Concerning the Adsorption of Certain Reducible Compounds or Their Reduction Products at the Dropping Mercury Electrode. *Collect. Czech. Chem. Commun.* 1947, 12, 522–540.

(145) Kelner, M. J.; Alexander, N. M. Methylene Blue Directly Oxidizes Glutathione Without the Intermediate Formation of Hydrogen Peroxide. *J. Biol. Chem.* 1985, 260 (28), 15168–15171. https://doi.org/10.1016/S0021-9258(18)95717-0.

(146) Hiraku, Y.; Goto, H.; Kohno, M.; Kawanishi, S.; Murata, M. Metal-Mediated Oxidative DNA Damage Induced by Methylene Blue. *Biochim. Biophys. Acta, Gen. Subj.* 2014, 1840 (9), 2776–2782. https://doi.org/10.1016/J.BBAGEN.2014.04.020.

(147) Olajire, A. A.; Olajide, A. J. Kinetic Study of Decolorization of Methylene Blue with Sodium Sulphite in Aqueous Media: Influence of Transition Metal Ions. *J. Phys. Chem. Biophys.* 2014, 2 (2), 1000136. https://doi.org/10.4172/2161-0398.1000136.

(148) Dutta, G.; Lillehoj, P. B. An Ultrasensitive Enzyme-Free Electrochemical Immunosensor Based on Redox Cycling Amplification Using Methylene Blue. *Analyst* 2017, 142 (18), 3492–3499. https://doi.org/10.1039/c7an00789b.

(149) Lee, S. K.; Mills, A. Novel Photochemistry of Leuco-Methylene Blue. *Chem. Commun.* 2003, 3 (18), 2366–2367. https://doi.org/10.1039/b307228b.

(150) Lee, S.-K.; Mills, A. Luminescence of Leuco-Thiazine Dyes. *J. Fluoresc.* 2003, 13 (5), 375–377. https://doi.org/10.1023/A:1026341420942.

(151) Furst, A. L.; Hill, M. G.; Barton, J. K. Electrocatalysis in DNA Sensors. *Polyhedron* 2014, 84, 150–159. https://doi.org/10.1016/J.POLY.2014.07.005.

(152) Papadopoulou, E.; Gale, N.; Thompson, J. F.; Fleming, T. A.; Brown, T.; Bartlett, P. N. Specifically Horizontally Tethered DNA Probes on Au Surfaces Allow Labelled and Label-Free DNA Detection Using SERS and Electrochemically Driven Melting. *Chem. Sci.* 2016, 7 (1), 386–393. https://doi.org/10.1039/c5sc03185k.

(153) Boon, E. M.; Barton, J. K.; Bhagat, V.; Nersissian, M.; Wang, W.; Hill, M. G. Reduction of Ferricyanide by Methylene Blue at a DNA-Modified Rotating-Disk Electrode. *Langmuir* 2003, 19 (22), 9255–9259. https://doi.org/10.1021/la030266u.

(154) Xu, P.; Wang, J.; Xu, Y.; Chu, H.; Shen, H.; Zhang, D.; Zhao, M.; Liu, J.; Li, G. Binding Modes and Interaction Mechanism between Different Base Pairs and Methylene Blue Trihydrate: A Quantum Mechanics Study. In *Advance in Structural Bioinformatics*; Wei, D., Xu, Q., Zhao, T., Dai, H., Eds.; *Adv. Exp. Med. Biol.*; Springer: Dordrecht, 2015; Vol. 827, pp 187–203. https://doi.org/10.1007/978-94-017-9245-5_12.

(155) Karunakaran, S. C.; Cafferty, B. J.; Jain, K. S.; Schuster, G. B.; Hud, N. V. Reversible Transformation of a Supramolecular Hydrogel by Redox Switching of Methylene Blue-A Noncovalent Chain Stopper. *ACS Omega* 2020, 5 (1), 344–349. https://doi.org/10.1021/acsomega.9b02785.

(156) Mayer, G.; Menger, M. M., Eds. *Nucleic Acid Aptamers: Selection, Characterization, and Application*, 2nd ed.; Methods Mol. Biol.; Springer: New York, NY, 2023; Vol. 2570. https://doi.org/10.1007/978-1-0716-2695-5.

(157) Barile, E.; Pellecchia, M. NMR-Based Approaches for the Identification and Optimization of Inhibitors of Protein-Protein Interactions. *Chem. Rev.* 2014, 114 (9), 4749–4763. https://doi.org/10.1021/cr500043b.

(158) Furukawa, A.; Konuma, T.; Yanaka, S.; Sugase, K. Quantitative Analysis of Protein–Ligand Interactions by NMR. *Prog. Nucl. Magn. Reson. Spectrosc.* 2016, 96, 47–57. https://doi.org/10.1016/J.PNMRS.2016.02.002.

(159) Williamson, M. P. Using Chemical Shift Perturbation to Characterize Ligand Binding. *Prog. Nucl. Magn. Reson. Spectrosc.* 2013, 73, 1–16. https://doi.org/10.1016/J.PNMRS.2013.02.001.

(160) Johnston, Y.; Leupin, W.; Washington, S.; Denny, W. A.; Wüthrich, K. NMR Studies of the Complex between the Decadeoxynucleotide d-(GCATTAATGC)2 and a Minor-Groove-Binding Drug. *Biochemistry* 1986, 25 (20), 5902–5910.

(161) Slavkovic, S.; Shoara, A. A.; Kaiyum, Y. A.; Churcher, Z. R.; Liu, T.; Simine, L.; Johnson, P. E. Amodiaquine Nonspecifically Binds Double Stranded and Three-Way Junction DNA Structures. *ChemBioChem* 2024, 25 (14), e202400116. https://doi.org/10.1002/cbic.202400116.

(162) Bastos, M.; Abian, O.; Johnson, C. M.; Ferreira-da-Silva, F.; Vega, S.; Jimenez-Alesanco, A.; Ortega-Alarcon, D.; Velazquez-Campoy, A. Isothermal Titration Calorimetry. *Nat. Rev. Methods Primers* 2023, 3 (1), 17. https://doi.org/10.1038/s43586-023-00199-x.

(163) Buurma, N. J.; Haq, I. Advances in the Analysis of Isothermal Titration Calorimetry Data for Ligand–DNA Interactions. *Methods* 2007, 42 (2), 162–172. https://doi.org/10.1016/J.YMETH.2007.01.010.

(164) Hossain, M.; Suresh Kumar, G. DNA Intercalation of Methylene Blue and Quinacrine: New Insights into Base and Sequence Specificity from Structural and Thermodynamic Studies with Polynucleotides. *Mol. BioSyst.* 2009, 5 (11), 1311–1322. https://doi.org/10.1039/B909563B.

(165) Hossain, Maidul; Giri, Prabal; Kumar, Gopinatha Suresh. DNA Intercalation by Quinacrine and Methylene Blue: A Comparative Binding and Thermodynamic Characterization Study. *DNA Cell Biol.* 2008, 27 (2), 81–90. https://doi.org/10.1089/dna.2007.0652.

(166) Xie, Y.; Kaiyum, Y. A.; Gu, L.; Liu, Y.; Johnson, P. E.; Liu, J. A Pair of DNA Aptamers That Can Selectively Bind to Bilirubin and Biliverdin. ACS *Chem. Biol.* 2025, 20 (8), 2028–2037. https://doi.org/10.1021/acschembio.5c00438.

(167) Eisen, S. R.; Dauphin-Ducharme, P.; Johnson, P. E. Solution-Based Biophysical Characterization of Conformation Change in Structure-Switching Aptamers. *Q. Rev. Biophys.* 2024, 57, e7. https://doi.org/10.1017/S0033583524000076.

(168) Yu, H.; Alkhamis, O.; Canoura, J.; Liu, Y.; Xiao, Y. Advances and Challenges in Small-Molecule DNA Aptamer Isolation, Characterization, and Sensor Development. *Angew. Chem., Int. Ed.* 2021, 60 (31), 16800–16823. https://doi.org/10.1002/anie.202008663.

(169) McKeague, M.; Derosa, M. C. Challenges and Opportunities for Small Molecule Aptamer Development. *J. Nucleic Acids* 2012, 2012, 748913. https://doi.org/10.1155/2012/748913.

(170) Slavkovic, S.; Zhu, Y.; Churcher, Z. R.; Shoara, A. A.; Johnson, A. E.; Johnson, P. E. Thermodynamic Analysis of Cooperative Ligand Binding by the ATP-Binding DNA Aptamer Indicates a Population-Shift Binding Mechanism. *Sci. Rep.* 2020, 10 (1). https://doi.org/10.1038/s41598-020-76002-8.

(171) Patel, D. J.; Shapiro, L.; Hare, D. DNA and RNA: NMR Studies of Conformations and Dynamics in Solution. *Q. Rev. Biophys.* 1987, 20 (1–2), 35–112. https://doi.org/10.1017/S0033583500004224.

(172) Szulik, M. W.; Voehler, M.; Stone, M. P. NMR Analysis of Base-Pair Opening Kinetics in DNA. *Curr. Protoc. Nucleic Acid Chem.* 2014, 2014, 7.20.1-7.20.18. https://doi.org/10.1002/0471142700.nc0720s59.

(173) Williamson, M. P. Using Chemical Shift Perturbation to Characterise Ligand Binding. *Prog. Nucl. Magn. Reson. Spectrosc.* 2013, 73, 1–16. https://doi.org/10.1016/J.PNMRS.2013.02.001.

(174) Dieckmann, T.; Suzuki, E.; Nakamura, G. K.; Feigon, J. Solution Structure of an ATP-Binding RNA Aptamer Reveals a Novel Fold. *RNA* 1996, 2 (7), 628–640.

(175) Jiang, F.; Kumar, R. A.; Jones, R. A.; Patel, D. J. Structural Basis of RNA Folding and Recognition in an AMP–RNA Aptamer Complex. *Nature* 1996, 382 (6587), 183–186. https://doi.org/10.1038/382183a0.

(176) Jiang, F.; Patel, D. J.; Zhang, X.; Zhao, H.; Jones, R. A. Specific Labeling Approaches to Guanine and Adenine Imino and Amino Proton Assignments in the AMP–RNA Aptamer Complex. *J. Biomol. NMR* 1997, 9 (1), 55–62. https://doi.org/10.1023/A:1018623601946.

(177) Nonin, S.; Jiang, F.; Patel, D. J. Imino Proton Exchange and Base-Pair Kinetics in the AMP-RNA Aptamer Complex. *J. Mol. Biol.* 1997, 268 (2), 359–374. https://doi.org/10.1006/JMBI.1997.0986.

(178) Wang, K. Y.; McCurdy, S.; Shea, R. G.; Swaminathan, S.; Bolton, P. H. Thrombin-Binding DNA Aptamer Forms a Unimolecular Quadruplex Structure in Solution. *Proc. Natl. Acad. Sci. U.S.A.* 1993, 90 (8), 3746–3750. https://doi.org/10.1073/pnas.90.8.3746.

(179) Schultze, P.; Macaya, R. F.; Feigon, J. Three-Dimensional Solution Structure of the Thrombin-Binding DNA Aptamer d(GGTTGGTGTGGTTGG). *J. Mol. Biol.* 1994, 235 (5), 1532–1547. https://doi.org/10.1006/JMBI.1994.1105.

(180) Kelly, J. A.; Feigon, J.; Yeates, T. O. Reconciliation of the X-Ray and NMR Structures of the Thrombin-Binding Aptamer d(GGTTGGTGTGGTTGG). *J. Mol. Biol.* 1996, 256 (3), 417–422. https://doi.org/10.1006/JMBI.1996.0097.

(181) Shoara, A. A.; Reinstein, O.; Borhani, O. A.; Martin, T. R.; Slavkovic, S.; Churcher, Z. R.; Johnson, P. E. Development of a Thermal-Stable Structure-Switching Cocaine-Binding Aptamer. *Biochimie* 2018, 145, 137–144. https://doi.org/10.1016/J.BIOCHI.2017.08.010.

(182) Shoara, A. A.; Churcher, Z. R.; Slavkovic, S.; Johnson, P. E. Weak Binding of Levamisole by the Cocaine-Binding Aptamer Does Not Interfere with an Aptamer-Based Detection Assay. *ACS Omega* 2021, 6 (37), 24209–24217. https://doi.org/10.1021/acsomega.1c03781.

(183) Schoukroun-Barnes, L. R.; Macazo, F. C.; Gutierrez, B.; Lottermoser, J.; Liu, J.; White, R. J. Reagentless, Structure-Switching Electrochemical Aptamer-Based Sensors. *Annu. Rev. Anal. Chem.* 2016, 9 (1), 163–181. https://doi.org/10.1146/annurev-anchem-071015-041446.

(184) Bottari, F.; Daems, E.; de Vries, A.-M.; Van Wielendaele, P.; Trashin, S.; Blust, R.; Sobott, F.; Madder, A.; Martins, J. C.; De Wael, K. Do Aptamers Always Bind? The Need for a Multifaceted Analytical Approach When Demonstrating Binding Affinity between Aptamer and Low Molecular Weight Compounds. *J. Am. Chem. Soc.* 2020, 142 (46), 19622–19630. https://doi.org/10.1021/jacs.0c08691.

(185) Nakatsuka, N.; Faillétaz, A.; Eggemann, D.; Forró, C.; Vörös, J.; Momotenko, D. Aptamer Conformational Change Enables Serotonin Biosensing with Nanopipettes. *Anal. Chem.* 2021, 93 (8), 4033–4041. https://doi.org/10.1021/acs.analchem.0c05038.

(186) Lin, C.; Dickerhoff, J.; Yang, D. NMR Studies of G-Quadruplex Structures and G-Quadruplex-Interactive Compounds. In *G-Quadruplex Nucleic Acids: Methods and Protocols*; Yang, D.; Lin, C., Eds.; *Methods Mol. Biol.*; Springer: New York, NY, 2019; Vol. 2035, pp 157–176. https://doi.org/10.1007/978-1-4939-9666-7_9.

(187) Oh, K. I.; Kim, J.; Park, C. J.; Lee, J. H. Dynamics Studies of DNA with Non-Canonical Structure Using NMR Spectroscopy. *Int. J. Mol. Sci.* 2020, 21 (8), 2673. https://doi.org/10.3390/ijms21082673.

(188) Ambrus, A.; Chen, D.; Dai, J.; Bialis, T.; Jones, R. A.; Yang, D. Human Telomeric Sequence Forms a Hybrid-Type Intramolecular G-Quadruplex Structure with Mixed Parallel/Antiparallel Strands in Potassium Solution. *Nucleic Acids Res.* 2006, 34 (9), 2723–2735. https://doi.org/10.1093/nar/gkl348.

(189) Dai, J.; Punchihewa, C.; Ambrus, A.; Chen, D.; Jones, R. A.; Yang, D. Structure of the Intramolecular Human Telomeric G-Quadruplex in Potassium Solution: A Novel Adenine Triple Formation. *Nucleic Acids Res.* 2007, 35 (7), 2440–2450. https://doi.org/10.1093/nar/gkm009.

(190) Kuryavyi, V.; Phan, A. T.; Patel, D. J. Solution Structures of All Parallel-Stranded Monomeric and Dimeric G-Quadruplex Scaffolds of the Human C-Kit2 Promoter. *Nucleic Acids Res.* 2010, 38 (19), 6757–6773. https://doi.org/10.1093/nar/gkq558.

(191) Zhou, W.; Saran, R.; Liu, J. Metal Sensing by DNA. *Chem. Rev.* 2017, 117 (12), 8272–8325. https://doi.org/10.1021/acs.chemrev.7b00063.

(192) Qu, H.; Csordas, A. T.; Wang, J.; Oh, S. S.; Eisenstein, M. S.; Soh, H. T. Rapid and Label-Free Strategy to Isolate Aptamers for Metal Ions. *ACS Nano* 2016, 10 (8), 7558–7565. https://doi.org/10.1021/acsnano.6b02558.

(193) Andrałojć, W.; Wieruszewska, J.; Pasternak, K.; Gdaniec, Z. Solution Structure of a Lanthanide-Binding DNA Aptamer Determined Using High Quality Pseudocontact Shift Restraints. *Chem. Eur. J.* 2022, 28 (66), e202202114. https://doi.org/10.1002/chem.202202114.

(194) Wang, J.; Kaiyum, Y. A.; Li, X.; Lei, H.; Johnson, P. E.; Liu, J. Kinetic and Affinity Profiling Rare Earth Metals Using a DNA Aptamer. *J. Am. Chem. Soc.* 2025, 147 (2), 1831–1839. https://doi.org/10.1021/jacs.4c13768.

(195) Ding, Y.; Zhang, Z.; Kaiyum, Y. A.; Heng, Y.; Johnson, P. E.; Liu, J. DNA Aptamers for Common Buffer Molecules: Possibility of Buffer Interference in SELEX. *Org. Biomol. Chem.* 2024, 22 (41), 8337–8343. https://doi.org/10.1039/d4ob00622d.

(196) Xie, Y.; Kaiyum, Y. A.; Gu, L.; Liu, Y.; Johnson, P. E.; Liu, J. A Pair of DNA Aptamers That Can Selectively Bind to Bilirubin and Biliverdin. ACS *Chem. Biol.* 2025, 20 (8), 2028–2037. https://doi.org/10.1021/acschembio.5c00438.

(197) Shortridge, M. D.; Hage, D. S.; Harbison, G. S.; Powers, R. Estimating Protein-Ligand Binding Affinity Using High-Throughput Screening by NMR. *J. Comb. Chem.* 2008, 10 (6), 948–958. https://doi.org/10.1021/cc800122m.

(198) Wang, J.; Kaiyum, Y. A.; Wang, S.; Li, X.; Lei, H.; Johnson, P. E.; Liu, J. A General Transition Metal Binding Aptamer Following the Irving-Williams Series. *Chem. Sci.* 2025, 16 (31), 14286–14294. https://doi.org/10.1039/d5sc02436f.

(199) Zhou, M.; Xu, T.; Xia, K.; Gao, H.; Li, W.; Zhai, T.; Gu, H. Small DNAs That Specifically and Tightly Bind Transition Metal Ions. *J. Am. Chem. Soc.* 2023, 145 (16), 8776–8780. https://doi.org/10.1021/jacs.3c01276.

(200) Hermann, T.; Westhof, E. Exploration of Metal Ion Binding Sites in RNA Folds by Brownian-Dynamics Simulations. *Structure* 1998, 6 (10), 1303–1314. https://doi.org/10.1016/S0969-2126(98)00130-0.

(201) Gao, Y.-G.; Sriram, M.; Wang, A. H.-J. Crystallographic Studies of Metal Ion–DNA Interactions: Different Binding Modes of Cobalt(II), Copper(II) and Barium(II) to N7 of Guanines in Z-DNA and a Drug-DNA Complex. *Nucleic Acids Res.* 1993, 21 (17), 4093–4101. https://doi.org/10.1093/nar/21.17.4093.

(202) Mehlhorn, A.; Rahimi, P.; Joseph, Y. Aptamer-Based Biosensors for Antibiotic Detection: A Review. *Biosensors* 2018, 8 (2), 54. https://doi.org/10.3390/bios8020054.

(203) Nikolaus, N.; Strehlitz, B. DNA-Aptamers Binding Aminoglycoside Antibiotics. *Sensors* 2014, 14 (2), 3737–3755. https://doi.org/10.3390/s140203737.

(204) Kraus, L.; Duchardt-Ferner, E.; Bräuchle, E.; Fürbacher, S.; Kelvin, D.; Marx, H.; Boussebayle, A.; Maurer, L. M.; Bofill-Bosch, C.; Wöhnert, J.; Suess, B. Development of a Novel Tobramycin Dependent Riboswitch. *Nucleic Acids Res.* 2023, 51 (20), 11375–11385. https://doi.org/10.1093/nar/gkad767.

(205) Zhao, Y.; Liu, J. pH-Directed Capture-SELEX for Nanomolar Affinity Aptamers for Kanamycin Detection. *Analysis Sens.* 2025, 5 (3), e202400099. https://doi.org/10.1002/anse.202400099.

(206) Ding, Y.; Chen, Q.; Heng, Y.; Chao, E. H. P.; Kaiyum, Y. A.; Johnson, P. E.; Liu, J. A High-Affinity but Low-Abundance Kanamycin Aptamer Reveals Hybridization-Limited Capture-SELEX. *Biochemistry* 2026, 65 (8), 1192–1201. https://doi.org/10.1021/acs.biochem.5c00778.

(207) Datta, M.; Kaiyum, Y. A.; Johnson, P. E.; Liu, J. An Ultrahigh Affinity DNA Aptamer for Quinine and Its Intrinsic Fluorescence Based Label-Free Detection. *Chem. Eur. J.* 2025, 31 (1), e202403435. https://doi.org/10.1002/chem.202403435.